ADPICAS Phase I & Phase II Final Report

SUBMITTED TO THE OFFICE OF NAVAL RESEARCH
Active Control Technology and Smart Structures Program

ADAPTIVE DAMPING AND POSITIONING USING INTELLIGENT COMPOSITE ACTIVE STRUCTURS (ADPICAS)

Phase I: May 2000 to May 2002
Phase II: June 2002 to May 2005

Grant No. N00014-00-1-0692

Principal Investigator:
Mehrdad Ghasemi Nejhad, Ph.D.
2540 Dole St., Holmes 302
Department of Mechanical Engineering
University of Hawaii, Honolulu, Hawaii 96822
Tel: 808-956-7560, Fax: 808-956-2373
E-mail: nejhad@wiliki.eng.hawaii.edu
URL: http://www.eng.hawaii.edu/~nejhad

October 2005

ADPICAS Phase I & Phase II Final Report

SUBMITTED TO THE OFFICE OF NAVAL RESEARCH
Active Control Technology and Smart Structures Program

ADAPTIVE DAMPING AND POSITIONING USING INTELLIGENT COMPOSITE ACTIVE STRUCTURS (ADPICAS)

Phase I: May 2000 to May 2002
Phase II: June 2002 to May 2005

Grant No. N00014-00-1-0692

Principal Investigator:
Mehrdad Ghasemi Nejhad, Ph.D.
2540 Dole St., Holmes 302
Department of Mechanical Engineering
University of Hawaii, Honolulu, Hawaii 96822
Tel: 808-956-7560, Fax: 808-956-2373
E-mail: nejhad@wiliki.eng.hawaii.edu
URL: http://www.eng.hawaii.edu/~nejhad

October 2005

TABLE OF CONTENTS

PART I (Phase I: May 2000 – May 2002) & PART II (Phase II: June 2002 – May 2005)

PART I (Phase I: May 2000 – May 2002)

ABSTRACT AND OBJECTIVES

The main objectives of this research are to design, analyze, fabricate, and test intelligent composite active structures and systems to provide simultaneous precision position and vibration suppression control capabilities for military and space structures to enhance their structural performance and reduce their fuel consumption. These simultaneous vibration suppression and precision positioning capabilities, for mission performance enhancement, are achieved by using well-integrated sensors/actuators/controllers where the host structures will be constructed mainly from composite materials that are lightweight and strong. Adaptive or intelligent structures which have the capability for sensing and responding to their environment promise a unique approach to solving numerous problems of spacecraft such as fighter jets and helicopters, smart rockets, satellites, space stations, unmanned underwater/aerial vehicles, and submarines. Intelligent sensors and actuators in combination with robust control system and composite materials as host structure are lightweight, increase structural efficiency, provide thermal stability, and monitor and respond dynamically to external stimuli. For spacecraft, these properties mean increased range, payload, and reduced fuel consumption as well as enhanced performance and reliability through internal control of the materials and host structures. The adaptive structures developed in this work can also be used for sensitive equipment and devices, e.g., aboard of aircraft and spacecraft as well as their structures to provide them with precision positioning as well as vibration suppression capabilities, and hence drastically improve their performance. More specifically, the objectives of ADPICAS Phase I were to develop a) Active Composite Strut (ACS) and b) Active Composite Panel (ACP) building blocks with well-integrated sensors/actuators and controllers with complete algorithms. These building blocks have simultaneous precision positioning and vibration suppression capabilities. In ADPICAS Phase II, the developed science and technology in Phase I for the ACS and ACP were employed to develop a Modified Stewart Platform (MSP) with simultaneous precision positioning and vibration suppression capabilities for Thrust Vector Control (TVC) application in spacecraft, in general, and satellites, in particular. The MSP has two in-plane rotational degrees of freedom with both SISO (Decentralized) and MIMO (Centralized) control capabilities.

The ACS, ACP, and MSP have the following attributes:

1. Simultaneous vibration suppression and precision position with SISO/MIMO Controls
2. Power off and hold capability (Struts)
3. Load bearing capability
4. DC-100 Hz band-width
5. Low power consumption
6. Well-integrated sensor/actuator with control system
7. Rapid response time
8. Compact and light weight
9. Milli/micro displacements with micro resolution/accuracy
10. Robust and versatile

The goals for ADPICAS Phase I and II of the project were to:

a) Develop (i.e., Design/Analyze/Manufacture) Active Composite Struts (ACSs) with integrated sensors/actuators/controllers and simultaneous vibration suppression and precision positioning capabilities with local and global control mode applications (Phase I)

b) Develop (i.e., Design/Analyze/Manufacture) Active Composite Panels (ACPs) with integrated sensors/actuators/controllers and simultaneous vibration suppression and precision positioning capabilities with local and global control mode applications (Phase I)

c) Perform ACS and ACP Local Mode Testing using single-input-single-output (SISO) control system (Phase I)

d) Perform ACS and ACP System Modifications/Refinements and Local Mode Testing as well as their Integration/Compactness (Phase II)

e) Integrate ACSs and ACPs into a Modified Stewart Platform for Thrust Vector Control application of spacecraft (Phase II).

f) Perform Local (SISO, Decentralized) and Global (MIMO, Centralized) Mode Testing of the developed Modified Stewart Platform (Phase II).

This report is summarized and divided into the following seven main sections: 1. General Introduction and overview of the ADPICAS project, 2. VSS (Vibration Suppression Schemes and Piezoelectric Effectiveness for ACPs with Surface-mounted and Embedded Sensors and Actuators), 3. ACS (Active Composite Struts), 4. ACP (Active Composite Panels), 5. MSP (Modified Stewart Platform) Design, Analysis, and Manufacturing, 6. MSP Control Strategies, and 7. MSP Testing.

1. GENERAL INTRODUCTION (Nejhad)

The primary system application of the ADPICAS Phase I and II project, for the use of ACS and ACP building blocks, is identified as the Thrust Vector Control (TVC) application for spacecraft, in consultation with the NRL and ONR. The TVC application with its corresponding specifications is explained here employing the following abbreviations:

1.1. Abbreviations:

ACS = Active Composite Strut
ACP = Active Composite Panel
VS = Vibration Suppression
PP = Precision Positioning
\+ = Simultaneous
SP = Stewart Platform
MSP = Modified Stewart Platform
2-DOF = Two Degrees of Freedom
6-DOF = Six Degrees of Freedom

1.2. Application: Thrust Vector Control (TVC):

The objectives of Phase II were to develop a predominately smart composite platform for the use in a spacecraft (such as a satellite) as a Thrust Vector Control (TVC) smart composite platform. The platform has simultaneous precision positioning and vibration suppression capabilities. The active strut members of the platform are the Active Composite Struts (ACSs) with simultaneous PP and VS capabilities. The top plate, where the thruster will be mounted, is a circular ACP with VS capability. The ACSs and ACP are selected and designed to suppress any lateral vibration from the thruster. The MSP central support is a high load bearing piezoelectric stack with VS capabilities selected to suppress any axial vibration from the thruster. The proposed thruster mount smart composite structure utilizes integrated sensors/actuators with controllers to provide fine tuning of position tolerance (PP + VS) for thruster alignment through the center of mass of the spacecraft preventing momentum buildup during thruster firing and to potentially isolate dynamic responses from the spacecraft bus. This smart system approach enhances the spacecraft mission performance by fine-tuning attitude control as well as eliminating the non-operational period during maneuvering.

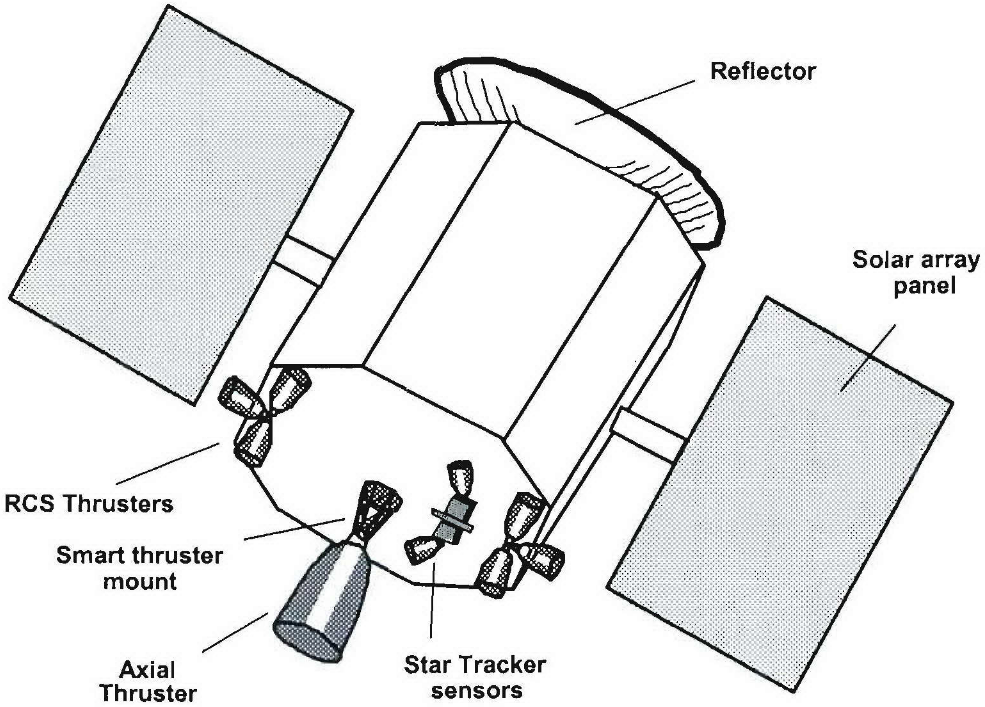

Figure 1.1. *Schematic of a Satellite.*

Figure 1.2. *The MSP solid model.*

Figure 1.1 shows the schematic of a satellite with smart thruster mount (i.e., the MSP in this design) in place. Figure 1.2 shows a solid model of such intelligent composite platform with simultaneous precision positioning and vibration suppression capabilities for the TVC application. The intelligent composite platform is a Modified Stewart Platform (MSP) with two rotational degrees of freedom (2-DOF) for the top plate (ACP) and has three active composite strut (ACS) legs. The bottom base plate is designed as a three-point star shape. The ACSs can extend or contract to tilt the top platform to a designated direction. Although the required top device plate tilt was set at plus/minus one degree, both the active composite struts and the top device plate range of motion are designed such that they can achieve up to plus/minus 15 degrees tilt of the top device plate if desired. Ghasemi-Nejhad and co-workers (Ghasemi Nejhad and Doherty, 2002; Ghasemi Nejhad, 2004; Doherty and Ghasemi Nejhad, 2005) have introduced the use of MSPs for the TVC application.

1.3. Specifications:

1.3.1: System: *2-DOF Modified Stewart Platform (MSP)*
1.3.2: Building Blocks Applications:
  1.3.2.1: High-Load Bearing, Low-Bandwidth ACS as the system struts (with PP + VS)
  1.3.2.2: High-Load Bearing, Low-Bandwidth, Thick ACP as top plate (with VS)
1.3.3: Angular Travel/Positioning Control of +/- 1 to 2 degrees of top plate
1.3.4: Angular Accuracy < 1 arcminute of top plate
1.3.5: Actuator (and system) Bandwidth DC to 100 Hz (DC to 10 HZ for PP and 10 to 100 Hz for VS)
1.3.6: ACS Load Bearing = 10 lbs. (for a thrust force of ~ 100 lbs.)
1.3.7: 2-DOF MSP Kinematics maps top plate motion to ACS motion (for design & simulations)
1.3.8: Control System Design:
  1.3.8.1: Based on combined spacecraft/system sensors and internal ACS/ACP sensors for the MSP SISO (Local/Decentralized) Controls.
  1.3.8.2: Based on spacecraft/system sensors (i.e., Star Trackers, Gyro, which feed into the Spacecraft Attitude Controller) for the MSP MIMO (Global/Centralized) Controls.

The Phase I concentrated on the development of ACSs and ACPs with control systems for PP + VS. Phase II modified, refined, and completed the ACS and ACP development and integrated the developed ACSs/ACPs into the MSP with control systems having local/SISO/Decentralized and Global/MIMIO/Centralized modes with PP + VS capabilities.

2. Active Vibration Suppression and Piezoelectric Performance Effectiveness for ACPs with Surface-Mounted and Embedded Sensors and Actuators Employing Vibration Suppression Schemes (Nejhad, Russ)

Effectiveness of the piezoelectric actuators either surface-mounted or embedded for different composite laminate thickness and distance to neutral axis have been studied and reported here.

This study focuses on the effectiveness of the surface-mounted or embedded piezoelectric patches for different composite laminate configurations. The considered composite laminates contain either constant number of constraint layers with variable thickness or laminates with different number of constraint layers and constant thickness. Primarily, three finite element models (FEMs) are considered for this study. The first FEM considered beams with varying thickness and non-collocated surface-mounted piezoelectric patches as sensor and actuator. Experimental and finite element results are compared for four, six, and eight layers graphite/epoxy composite laminates. The second FEM deals with embedded non-collocated piezoelectric patches as sensor and actuator for beams with varying thickness and constant number of constraint layers. For this embedded case, compared with a similar surface-mounted case, one extra layer is needed to cover the piezoelectric patch and one extra cut-out layer to fill the area around the piezoelectric patch, and hence the thickness between the piezo patches are the same. In this case, the number of constraint layers is constant and equal to a total of four while the beam thickness varies. Therefore, an embedded ACB with varying thickness in comparison with a surface-mounted ACB case has always four extra constraint layers. Typical results, for these two cases, are compared for the beams with the same number of inner layers. Experimental and finite element results were compared for six, eight, and total of twelve layers graphite/epoxy composite laminates. The third FEM focuses on beams having constant thickness and non-collocated piezoelectric patches that are embedded at different locations throughout the laminate thickness to produce beams with different number of constraint layers. A surface-mounted ACX piezoelectric patch acts as a shaker in all three FEMs. Numerical and experimental results from modal, harmonic analyses, and control voltages associated with different frequencies were compared and excellent comparisons were established. Cross-examinations between these three FEMs determined the following: 1) the effectiveness of piezoelectric patches acting as an actuator as a function of the laminate thickness and the actuator distance from the beam neutral axis for the three cases, 2) the influence of the constant and variable number of constraint layers on the effectiveness of the embedded piezoelectric patches for beams with variable or constant thickness, respectively, as well as the effects of the constraint layers as a function of thickness and the actuator distance from beam neutral axis.

Two composite beams each with one surface-mounted ACX piezoelectric patch and either two surface-mounted or embedded non-collocated CCC piezoelectric patches (CCC, 2002) are developed as Active Composite Beams (ACBs). These ACBs are employed to study the piezoelectric effectiveness as a function of beam thickness as well as the influence of the constraint layers on the embedded piezoelectric performance. Constant voltage (CV) technique developed in this project (explained later in this section) as a new direct methodology for active vibration suppression was employed to investigate the piezoelectric effectiveness. Direct vibration suppression schemes (i.e., CV, OV, COV, and TCOV) can be employed for active vibration suppression of adaptive structures. The piezoelectric patches used as sensors and actuators are both PZT (lead zirconate titanate) type with the designation of PZT-5A.

2.1. ACB Finite Element Models

Primarily, three Active Composite Beams (ACBs) were modeled employing the ANSYS finite element software (ANSYS, 2002). The first ACB model contained one surface-mounted ACX piezoelectric and two non-collocated surface-mounted CCC. The second ACB model contained one surface-mounted ACX and two non-collocated embedded CCC for beams with different thickness and constant number of constraint layers (i.e., four). The third ACB model contained one surface-mounted ACX and two non-collocated embedded CCC for beams with constant thickness and different number of constraint layers. Figure 2.1 shows the ACBs for surface-mounted and embedded cases. The material properties of PZT-5A patch and plain weave T300 carbon/934 epoxy "cross-ply" composite material were used for the ACBs in Figure 2.1. The ACBs are cantilevered structures. ANSYS SOLID5 element was used for the piezoelectric and composite parts with their respective properties. The use of SOLID73 for the composite using their respective properties yields the same results as SOLID5. ANSYS finite element analysis employing modal analysis for the surface-mounted and embedded ACB either for varying or constant thickness yields their first natural frequencies that are listed in Tables 2.1-2.3.

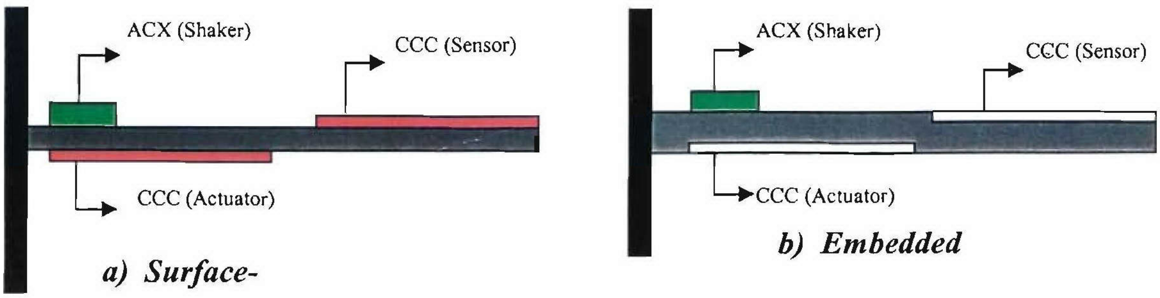

a) Surface-

b) Embedded

Figure 2.1. *FEA solid model of the active composite beams (ACBs) with a) surface-mounted and b) embedded piezoelectric flat patches with sensor at the tip and actuator at the clamped end.*

2.2. Finite Element Analysis Verification

In this study, ANSYS Finite Element Software is employed to investigate the dynamic behavior of Active Composite Beams (ACBs) with surface-mounted and embedded piezoelectric patches having different thickness with constant number of constraint layers as well as embedded with constant and varying number of constraint layers. For this work, dynamic behavior of ACBs were investigated through Modal and Harmonic analyses. Modal analysis can provide natural frequencies and modal shapes. Harmonic analysis determines the frequency response of the structure under a given harmonic load. To verify the accuracy of the finite element models and their solutions for the modal and harmonic analyses, the numerical solutions were compared with the experimental results. Modal and harmonic experimental data were obtained for the graphite/epoxy composite material ACBs with non-collocated surface-mounted and embedded piezoelectric sensor and actuator patches with four and eight inner layers. The ACX piezoelectric patch located near the clamped end (i.e., root) was used as a shaker and was surface-mounted for all cases. As a result, three primary Active Composite Beams (i.e., surface-mounted, embedded with varying thickness, and embedded with constant thickness) were modeled using the ANSYS Finite Element Program. ANSYS FEA was performed on these three primary models. All beams were modeled as a cantilevered beam with clamped boundary condition at one end as shown in Figure 2.1.

2.2.1. Modal Analysis Verification Study

As mentioned earlier, three primary ANSYS FEA models were employed. First and the second models define ACBs with surface-mounted and embedded piezoelectric patches with different thickness having constant number of constraint layers (i.e., four layers). The third model deals with ACB with constant thickness and embedded piezoelectric patches located at various places through the beam thickness. Each beam model has three piezoelectric patches (see Figure 2.1). The surface-mounted ACX piezoelectric patch located near the clamped end (i.e., root) acts as a shaker. One CCC piezoelectric patch located near the clamped end acts as an actuator and another one placed at the beam tip acts as a sensor. The two CCCs are either surface-mounted or embedded. Employing ANSYS FEA, natural frequencies and modal shapes were calculated for all beams with different thickness or constant thickness. To verify the accuracy of the ANSYS finite element modal analyses, the calculated natural frequencies were compared with those obtained from the experiments, and the results are given in Tables 2.1-2.3.

Table 2.1. *Modal analysis comparison between ANSYS FEA and experiment for the surface-mounted piezoelectric patches, Mode I*

Beam Thickness (m)	Total Number of Layers	ANSYS Natural Frequency (Hz)	Experimental Natural Frequency (Hz)	Error %
0.000470	2	7.665	7.63	0.46
0.000940	4	14.841	14.2	4.3
0.001390	6	21.912	21.5	1.88
0.001855	8	29.187	30.1	3.0
0.002319	10	36.483		
0.002780	12	43.749		
0.003710	16	58.435		

Table 2.2. *Modal analysis comparison between ANSYS FEA and experiment, embedded case, constant constraints, variable thickness, Mode I*

Beam Thickness (m)	Total Number of Layers	ANSYS Natural Frequency (Hz)	Experimental Natural Frequency (Hz)	Error %
0.00143	6	20.902	20.4	2.4
0.001888	8	27.956	27.8	0.56
0.002273	10	33.662		
0.002662	12	39.665	39.5	0.42
0.003051	14	45.705		
0.003440	16	51.770		
0.004218	20	63.947		

Table 2.3. *Modal analysis comparison between ANSYS FEA and experiment, embedded case, variable constraints, constant thickness, Mode I*

Beam Thickness (m)	Total Number of Layers	ANSYS Natural Frequency (Hz)	Experimental Natural Frequency (Hz)	Error %
0.00436	20	65.79		
0.00436	20	66.21		
0.00436	20	66.58		
0.00436	20	66.90		
0.00436	20	67.17		
0.00436	20	67.39		
0.00436	20	67.54		
0.00436	20	67.64		

Tables 2.1 and 2.2 reveal that ACBs with surface-mounted piezos are thicker/stiffer (since higher autoclave pressure was used during the manufacturing of the embedded ACBs). Also, it should be mentioned that the two beams with equal total number of layers has less mass for the embedded case since the embedded ones contain two cut-layers. Therefore, the surface-mounted ones have higher natural frequencies than those with embedded and with equal total number of layers. To demonstrate that the natural frequency is a linear function of the beam thickness an analytical equation for lateral vibration was selected (Thomson, 1988), as shown below.

$$\omega_n = (\beta_n L)^2 \sqrt{\frac{EI_0}{\rho_0 L^4}} \tag{2.1}$$

where β_n depends on boundary conditions, ρ_0 is mass per unit length, EI_0 is flexural rigidity, b is width, h is thickness, L is length, and $I_0 = \frac{bh^3}{12}$. β_n, L, and E are constants, hence:

$$\omega_n = (\beta_n L)^2 \sqrt{\frac{E}{L^4}} \sqrt{\frac{I_0}{\rho_0}} \tag{2.2}$$

Now, by doubling the beam thickness ($h = 2h_0$) new ρ will be doubled as well (i.e., $\rho = 2\rho_0$). Replace the new values for I_0 and ρ_0 (i.e., I and ρ) and simplify the formula, an extra coefficient of two will appears in the natural frequency formula (see Eq. (2.3)). As a result, doubling the beam thickness doubles the natural frequency indicating that a linear relation between the natural frequency and beam thickness exists. This can also be concluded from Tables 2.1 and 2.2.

$$\omega_n = (\beta_n L)^2 \sqrt{\frac{E}{L^4}} \sqrt{\frac{I}{\rho}} = (\beta_n L)^2 \sqrt{\frac{E}{L^4}} \sqrt{\frac{b(2h_0)^3}{12(2\rho_0)}} = (\beta_n L)^2 \sqrt{\frac{E}{L^4}} \left[2 * \sqrt{\frac{I_0}{\rho_0}} \right] \tag{2.3}$$

2.2.2. Harmonic Analysis Verification Study

ANSYS finite element harmonic analyses were performed for all the cases shown in Tables 2.1-2.3. To verify the accuracy of the finite element harmonic models, experimental harmonic analyses were also performed on selected cases. Frequency ranges for the harmonic analyses were chosen based on the natural frequencies obtained from the finite element modal analyses. For consistency, harmonic frequency range was chosen as twice of the natural frequency value for each specific case. The surface-mounted ACX piezoelectric patch located near the clamped end (i.e., root) acts as a shaker for all the cases. A peak voltage equal to seventy volts was supplied to the ACX in both experiments and finite element harmonic analyses. Closeness of the natural frequency values obtained from the finite element modal and harmonic analyses confirms the accuracy of the harmonic models. Harmonic analyses comparison between ANSYS FEA and the experiments were also performed on selected cases using ACX as a shaker or CCC as a shaker for either surface-mounted or embedded case. Representative results are shown in Figure 2.2. Overall, these results indicate that the results from finite element harmonic analyses and experiments are very close and confirm the accuracy of the harmonic analysis models for the three cases. DAs are damping factors in the graphs presented in Figure 2.2.

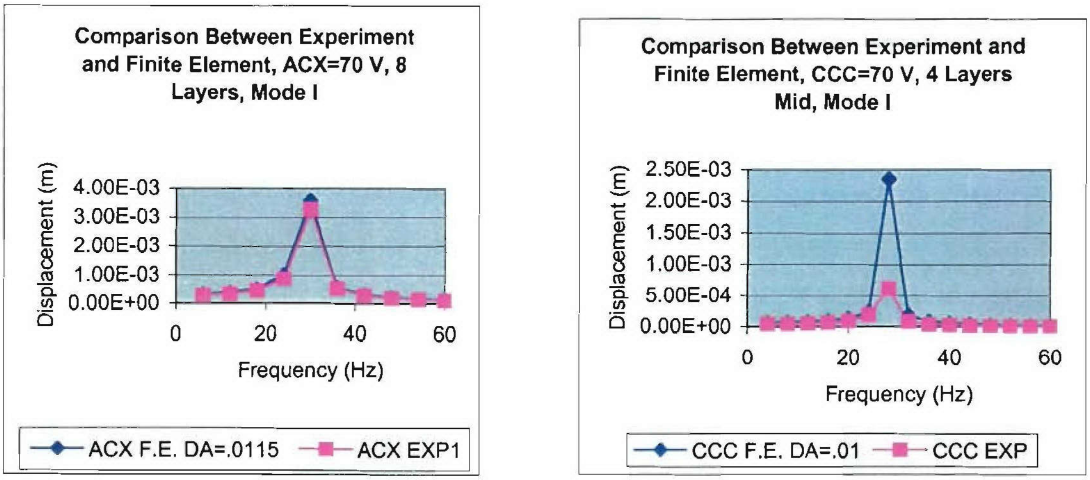

a) Surface-Mounted ***b) Embedded***

Figure 2.2. *FEA and Experimental Harmonic Analysis Comparisons.*

2.3. A Direct Approach for Active Vibration Suppression

Ghasemi-Nejhad and co-workers (Russ and Ghasemi-Nejhad, 2002a, 2002b, 2003, 2004a, 2004b; Ghasemi-Nejhad et al., 2005a, 2005b; Doherty and Ghasemi-Nejhad, 2005) introduced a direct methodology to determine the peak actuator voltage necessary to suppress a harmonic vibration imposed on a structure by a given peak external load at a particular frequency employing an ACB model similar to the ones used here. This direct technique was employed to develop direct constant voltage (CV), optimum voltage (OV), corresponding voltage (COV), and truncated corresponding voltage (TCOV) schemes for active vibration suppression of adaptive/intelligent structures over a wide range of frequency encompassing a natural frequency, directly without using trail-and-error and/or iteration approaches. The lateral displacement of the tip of the ACB was evaluated to develop a methodology for determining the appropriate actuator voltage to suppress a given mode shape for a known frequency and external load. In this work, it is assumed that the sensors and actuators are not co-located, and the piezoelectric material embedded at the beam tip is used as a sensor and the second piezoelectric embedded at the clamped end is used as an actuator. The following briefly explains the direct approach introduced by Ghasemi-Nejhad and co-workers.

2.3.1. Generating Displacement-Load (D-L) and Sensor Voltage-Load (S-L) Master Curves

1) Perform a modal analysis to determine the natural frequency of interest. ***2)*** Determine the range of frequency of interest that encompasses the natural frequency under consideration. ***3)***

Perform a harmonic analysis for the range of frequency of interest for an arbitrarily external load (ACX voltage as a shaker preferably in the neighborhood of the load of interest), and record the displacement and sensor voltage as a function of frequency. It should be noted that in this step there is only external load (i.e., ACX as shaker) without any internal load (i.e., actuator voltage). Use the absolute value of the displacement as well as sensor and actuator voltage curves versus frequencies. Also, *Dp* stands for the displacement due to the external load only. ***4)*** The *third* step can be repeated for various loads to cover the range of the load of interest to obtain Displacement-Frequency curves for various loads. ***5)*** Construct Displacement-Load "Master Curves" from the Displacement-Frequncy curves obtained in the harmonic analyses. It turns out that the Displacement-Load "Master Curves" are linear and they pass through the origin, and hence only one harmonic analysis is sufficient to generate the Displacement-Load "Master Curve," and step *forth* is not really needed. The mathematical form of Displacement-Load "Master Curve" for any frequency is given in Equation (2.4). ***6)*** While performing harmonic analysis for the range of frequency of interest for various arbitrarily external loads (ACX as a shaker) record the displacement and the sensor voltage as a function of frequency as well. The absolute value of the sensor voltage curves versus frequencies should be plotted. ***7)*** Similar to the Displacement-Load Master Curve and equation for any frequency, Sensor Voltage-Load Master Curve for any frequency can be constructed and its mathematical for is given in Equation (2.5).

$$D = (\Delta D/\Delta L = M_{DL})\ L \qquad \text{where } M_{DL} \text{ is the slope} \qquad (2.4)$$

$$S = (\Delta S/\Delta L = M_{SL})\ L \qquad \text{where } M_{SL} \text{ is the slope} \qquad (2.5)$$

2.3.2. Generating Displacement-Actuator Voltage (D-A) Master Curves

Steps in 2.3.2 are similar to steps in 2.3.1 except here the actuator voltage (i.e., internal load) is used instead of the external load to excite the structure. ***8)*** Perform a harmonic analysis for the range of frequency of interest (same as load) for an arbitrarily actuator voltage (i.e., internal load), say *V1*, but 180° out-of-phase with respect to the load only and record the displacement as a function of frequency. It should be noted that in this step there is only internal load (i.e., actuator voltage) without any external load. Also, *Dv* stands for the displacement due to the internal load (i.e., actuator voltage) only. ***9)*** The *eighth* step for various actuator voltages can be repeated to cover the range of the displacements generated for the external load and frequency of interest, which can be obtained from the Displacement-Load Master Curves to obtain Displacement-Frequency curves for various actuator voltages. ***10)*** Construct Displacement-Actuator Voltage "Master Curves". It turns out that the Displacement-Actuator Voltage "Master Curves" are also linear and they pass through the origin, and hence only one harmonic analysis is sufficient to generate the Displacement-Actuator Voltage "Master Curve," and step *ninth* is not really needed. The mathematical form of Displacement-Actuator Voltage "Master Curve" for any frequency is given in Equation (2.6).

$$D = (\Delta D/\Delta A = M_{DA})\ A \qquad \text{where } M_{DA} \text{ is the slope} \qquad (2.6)$$

2.3.3. Displacement-Load-Sensor Voltage-Actuator Voltage (D-L-S-A) Design Charts

Many control systems (particularly feed forward controls) for intelligent structures require a relationship between the sensor voltage and actuator voltage, which is usually not a one-to-one relationship. The direct approach explained here can be employed to establish this relationship as a function of the external load (ACX shaker) and displacement, in form of design chart master curves. To establish these master curves the results explained in previous sections can be employed. Rearranging S-L diagram by moving the Sensor Voltage axis (y-axis) to the right and by moving the Actuator Voltage axis (x-axis) to the top from D-A diagram, Figure 2.3 can be constructed to give Displacement-Load-Sensor Voltage-Actuator Voltage (D-L-S-A) Design Chart Master Curves for a given frequency. D-L-S-A charts can be generated for any specific frequency and provide interrelation between four parameters; namely, displacement (D), external load (L) (ACX as shaker), sensor voltage (S), and actuator voltage (A). Given the sensor voltage (S), external applied load (L), or displacement (D), the required actuator voltage can be determined from DLSA design chart of Figure 2.3. This technique constitutes the direct approach. The process of directly obtaining the required actuator voltage for active vibration suppression, which is usually different from and is larger than the sensor voltage for a given applied load at a given frequency, is explained in the following. a) Use the Displacement-Load (D-L) curve of Figure 2.3 to obtain the displacement response of the structure for a given frequency and applied external load, *Dp*. b) Use the Displacement-Actuator Voltage (D-A) Curve of Figure 2.3, *Dv*, and the obtained displacement from Figure 2.3, *Dp*, and assuming *Dp* = *Dv*, to obtain the required actuator voltage for the same frequency. Alternatively, if the information from the sensor is available, then Figure 2.3 can be used to determine the corresponding actuator voltage similar to steps a) and b). Steps a) and b) give the required actuator voltage (*Vact)* to obtain the same displacement as the external load only for a given frequency when applied individually. This level of actuator voltage can then suppress the vibration generated by the external load when applied simultaneously with the same frequency but 180° out-of-phase with respect to the applied external load, to give the suppressed displacement (*Dpv*). Figures 2.4 and 2.5 show two typical D-L-S-A control design chart for the four layers surface-mounted and four inner layers embedded (or eight layers total). "Sensor Root" in these figures means that the sensor information was taken from the root (i.e., clamped) side of the sensor. Alternatively, instead of using Figure 2.3, the actuator voltage (A) can be determined by simultaneously solving Equations (2.4) to (2.6) given the information from load (L), sensor (S), or displacement (D) for any given frequency.

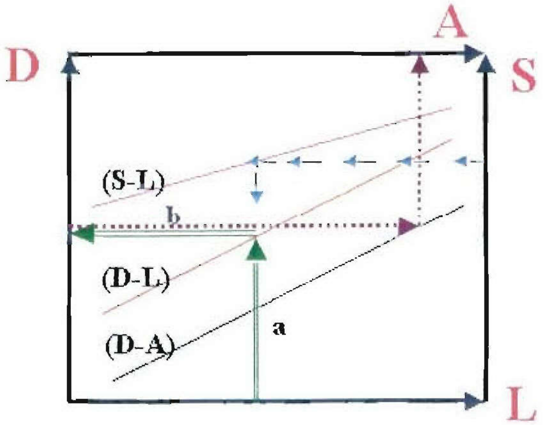

Figure 2.3. *D-L-S-A Design Chart for a given frequency.*

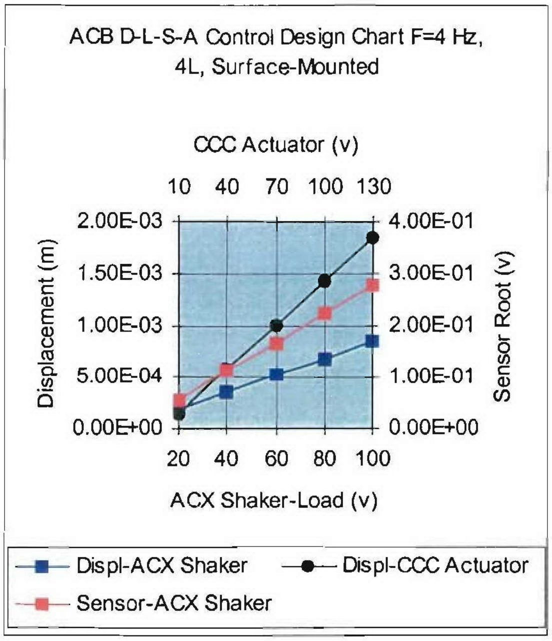

Figure 2.4. D-L-S-A Design Chart for 4 Layers, Surface-mounted, 4 Hz.

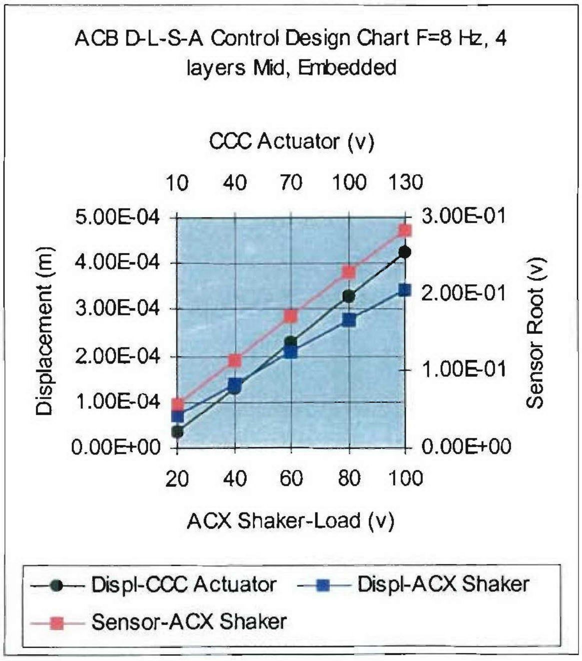

Figure 2.5. D-L-S-A Design Chart for 4 Inner Layers, Embedded, 8 Hz.

2.3.4. Constant Voltage (CV) Scheme

Employing (D-L-S-A) Design Chart Master Curves and assuming that the Displacement due to the ACX as a shaker is equal to that due to a CCC actuator voltage, find a constant voltage value (Vact) from the initial portion of the harmonic analysis, where the displacement is relatively constant for a range of frequency away from the natural frequency (see Figure 2.6, CV_I). Each natural frequency has its own constant voltage. Figures 2.7 and 2.8 show two typical ACB active vibration suppression using the direct Constant Voltage (CV) Scheme, one for the eight layer surface-mounted ACB and the other for the embedded ACB with four inner layers and varying thickness case (or a total of eight layers), respectively. For this work, the constant voltage technique is employed to investigate piezoelectric effectiveness for surface-mounted and embedded cases. As it will be explained later, for the surface-mounted case, the piezoelectric performance is influenced by the beam thickness and the distance from the neutral axis; for the embedded case with different thickness, the piezoelectric performance is influenced by the beam thickness, distance from the neutral axis, and the constant constraint layers; and for the embedded case with constant thickness, the piezoelectric performance is influenced by the distance from the neutral axis, and the different number of constraint layers. Finally, the influence of the constant constraint layers and the influence of varying constraint layers on the embedded piezoelectric performance was also investigated employing the constant voltage technique, which may be used as a tool to determine the piezoelectric effectiveness level.

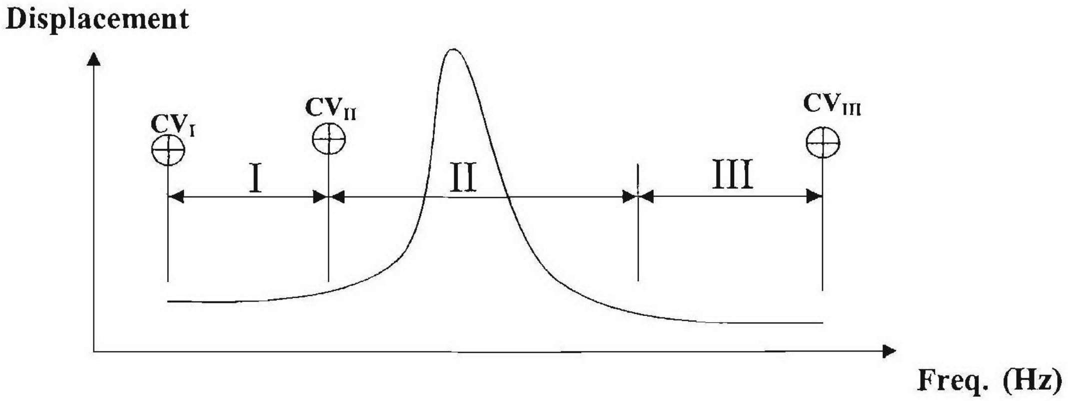

Figure 2.6. Schematic of vibration suppression schemes.

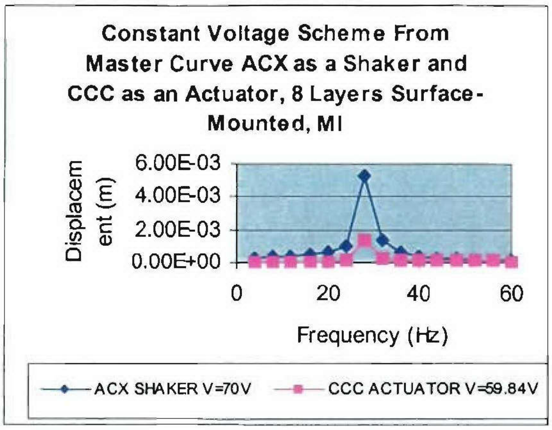

Figure 2.7. Active Vibration Suppression using CV for Surface-mounted ACB and 8 Layers.

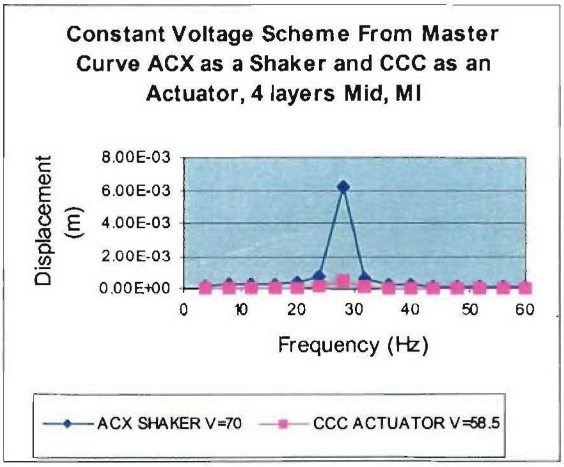

Figure 2.8. Active Vibration Suppression using CV for Embedded ACB and4 Inner Layers.

2.3.5. Optimum Voltage (OV) Scheme

Divide the frequency range encompassing a given natural frequency into three zones as shown in Figure 2.6. These three zones are I) the left relatively flat zone, II) the middle zone that includes the natural frequency, and III) the right relatively flat zone. These zones can be more precisely determined when the second derivative of the Sensor voltage versus Frequency curve in a harmonic analysis deviates from the zero slope line in Zones I and III. Next employing DLSA Charts, find three constant actuator voltage values ($A = Vact$) at three points shown schematically in Figure 2.6 and identified by CV_I, CV_{II}, CV_{III}. Here, to suppress the vibration for the whole range of the frequency in Figure 2.6, three constant *Vact* magnitudes determined at points CV_I,

CV_{II}, CV_{III} are applied to the actuator for frequencies within their respective zones with the corresponding frequency but 180° out-of-phase. Each natural frequency has its own three constant voltages called optimum voltage scheme.

2.3.6. Corresponding Voltage (COV) Scheme

Employing (D-L-S-A) Design Chart Master Curves and assuming that the Displacement due to the ACX as a shaker is equal to that due to a CCC actuator voltage, find the actuator voltage value (Vact) at any specific frequency over the frequency range of a harmonic analysis (see Figure 2.6). Figures similar to Figures 2.7 and 2.8 were obtained for two typical ACB active vibration suppression using the direct Corresponding Voltage (COV) Scheme, one for the eight layer surface-mounted ACB and the other for the embedded ACB with four inner layers or a total of eight layers, respectively. The corresponding voltage technique was employed to determine the correctness and the closeness of the finite element results in comparison with the experimental control voltages obtained at different frequency values using beams with different thickness either with surface-mounted or embedded piezoelectric patches. In the experimental section, control voltages from ANSYS FEA employing corresponding voltage technique have been compared with experimental control voltages utilizing typical samples either surface-mounted or embedded piezoelectric patches. The closeness of the finite element results to those of the experimental data verifies the correctness of the control voltage values calculated using the constant voltage technique in order to investigate the piezoelectric effectiveness for surface-mounted and embedded cases. These results are given later in Section 2.4.

2.3.7. Truncated Corresponding Voltage (TCOV) Scheme

It should be noted that in the vicinity of the natural frequencies the displacement and sensor voltage increase drastically (e.g., see Figure 2.6). Although not with a one-to-one relationship, the evaluated required "corresponding" actuator voltages (COV) also increase in the vicinity of the natural frequency. However, there may exist two principal limitations on the amount of the voltage that can be applied to an actuator: 1) the actuator voltage limit and 2) the spacecraft (or any other bus that uses the active structure) voltage limit. If the COVs in the vicinity of the natural frequency do not exceed the above-mentioned limits then the COV scheme can be applied. However, if the required "corresponding" actuator voltages in the vicinity of the natural frequencies (i.e., in Zone II) evaluated in the COV scheme exceed the two above-mentioned limits, first they should be "truncated" to the level of OV determined in the previous section, which is actually a CV in Zone II. Now, if this level of OV in real application, is still higher than the two limits mentioned above, then this OV/CV of Zone II should be reduced to the minimum of the two limiting voltages mentioned above and applied as a CV in Zone II. In this case, outside Zone II, the COV scheme is applied. This technique is called ***Truncated Corresponding Voltage (TCOV)*** scheme. It should be mentioned that the amount of voltage that COV is truncated to, in the TCOV scheme in this work, is the same amount of the OV used in Zone II, in the OV scheme section. Therefore, the TCOV scheme is a combination of the Corresponding Voltage (COV) scheme and the Optimum Voltage (OV) scheme, where the Corresponding Voltage values for the natural frequency zone (i.e., Zone II) will be replaced by the Optimum Voltage value for this zone. Once again, in reality this OV in Zone II should be the minimum of 1) OV for Zone II, 2) actuator voltage limit, and 3) spacecraft voltage limit.

2.3.8. Modified CV, OV, COV, and TCOV Schemes

The techniques described above are for direct CV, OV, COV, and TCOV schemes to obtain the required direct actuator voltage, $A=Vact$, employing DLSA Charts. This $Vact$ is then applied to the actuator as the internal load with the corresponding frequency but 180° out-of-phase (with respect to the sensor voltage or the evaluated displacement determined from the application of the external load only) and simultaneously with the external disturbance/load to actively suppress the imposed vibration with resulting residual displacement of Dpv, which should theoretically be zero. However, due to possible phase change complexity, particularly in the vicinity of the natural frequency, the 180° out-of-phase assumption may not always be accurate resulting in some non-zero residual vibration, Dpv. Ghasemi-Nejhad and co-workers (Russ and Ghasemi-Nejhad, 2002a, 2002b, 2003, 2004a, 2004b; Ghasemi-Nejhad et al., 2005a, 2005b; Doherty and Ghasemi-Nejhad, 2005) showed that when the Displacement versus Frequency curves due to the individual applications of the external load, Dp *curve*, and internal load (i.e., actuator voltage), Dv *curve*, obtained from their respective harmonic analysis are plotted in one figure, then Dp values are higher before the natural frequency and Dv values are higher after the natural frequency. It is believed that this phenomenon leads to having non-zero residual vibration, Dpv, using the proposed technique (albeit Dpv is often less than 10% of Dp). Ghasemi-Nejhad and co-workers (Russ and Ghasemi-Nejhad, 2002a, 2002b, 2003, 2004a, 2004b; Ghasemi-Nejhad et al., 2005a, 2005b; Doherty and Ghasemi-Nejhad, 2005) showed that to minimize the obtained residual vibration/displacement, Dpv, and maximize the vibration suppression the following equations should be used to determine the modified actuator voltage, $Vact'$, that should lead to a minimum modified residual vibration, Dpv'.

$$Vact' = Vact\,(1+Dpv/Dp) \qquad \text{For Frequencies} \le \text{Natural Frequency} \tag{2.7}$$

$$Vact' = Vact\,(1-Dpv/Dp) \qquad \text{For Frequencies} > \text{Natural Frequency} \tag{2.8}$$

Dpv is the residual vibration of the controlled displacement after the simultaneous application of the external load, L, and the actuator voltage, $A=Vact$ (determined from DLSA Charts), with the corresponding frequency but 180° out-of-phase, while Dp is the uncontrolled displacement due to the application of the external load, L, only. Ghasemi-Nejhad and co-workers (Russ and Ghasemi-Nejhad, 2002a, 2002b, 2003, 2004a, 2004b; Ghasemi-Nejhad et al., 2005a, 2005b; Doherty and Ghasemi-Nejhad, 2005) showed that while $Vact$ curve over a natural frequency range has a spike around the natural frequency, $Vact'$ is a smooth curve with no spike over the same frequency range. Also, the 180° out-of-phase assumption is reasonable for structures with low structural damping, such as those used here.

Ghasemi-Nejhad and co-workers (Russ and Ghasemi-Nejhad, 2002a, 2002b, 2003, 2004a, 2004b; Ghasemi-Nejhad et al., 2005a, 2005b; Doherty and Ghasemi-Nejhad, 2005) showed that the Vibration Suppression Schemes (i.e., CV, OV, COV, and TCOV) discussed here are applicable to both axial (such as ACSs) and lateral (such as ACPs) vibration applications.

2.4. Comparison between Experimental and Finite Element Results employing Corresponding Voltage Technique

To use constant voltage technique as a versatile tool to determine piezoelectric effectiveness, influence of different number of constraint layers on the embedded piezoelectric performance, and give insight into the effects of thickness and distance to neutral axis, good correlations must be established between the experiments and finite element analyses. Excellent agreement was established in terms of modal and harmonic analysis as explained in previous sections. For further assurance experimentally obtained actuator voltages needed for the active vibration suppression were compared with numerically calculated actuator voltages that constitute the constant voltage technique. Experimental and numerical required actuator voltages were compared at different frequencies. The experimental system, as shown in Figure 2.9, consists of two 601B-4 amplifiers from Trek, Inc., an MT600-800 laser displacement sensor from MTI Instruments, Inc., whose sensitivity is 2.54 *mm*/V, and the active composite panel (ACP). A harmonic disturbance through one of the amplifiers is sent to the ACX piezoelectric patch to vibrate the ACP, and the control signal through another amplifier is then sent to the CCC piezoelectric patch to suppress the disturbance-induced vibration. The laser displacement sensor senses the displacement at the tip of the cantilevered ACP. For the sake of easily tuning the amplitude and phase of the control signal and monitoring the suppressed vibration signal, a *dSPACE* real time system and a SR785 2-channel dynamic signal analyzer are also employed in this experiment. Figure 2.10 shows a typical vibration suppression for a harmonic disturbance at the frequency of 10 Hz, demonstrating that the uncontrolled vibration is 137.23 V, and it decreases to almost zero after an optimal constant control voltage is applied.

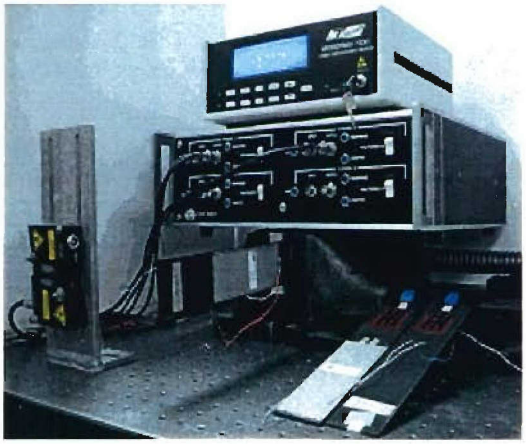

Figure 2.9. Experimental setup.

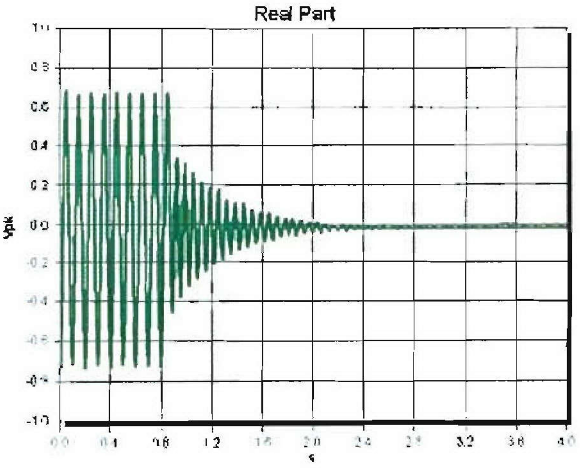

Figure 2.10. Uncontrolled and controlled displacements.

Experimental data and finite element results were compared for beams of graphite/epoxy composite laminates having four, six, and eight layers with surface-mounted piezoelectric patches. For the embedded case, experiment and finite element results were compared for beams having two, four, and eight inner layers (i.e., 6, 8, and 12 total layers). Representative comparison of experimental and numerical required corresponding actuator control voltage values as a function of frequency needed for active vibration suppression are shown in Figures 2.11 a and b. For the surface-mounted case, the peak voltage equals to seventy volts, and for the embedded case, the peak voltage equals to twenty volts and was supplied to the ACX patch to perform experimental and finite element analyses harmonic tests. The peak voltage of twenty volts for the embedded case was due to the amplifier voltage limitation. In the experiment, the actuator voltage value, supplied to CCC piezoelectric patch either surface-mounted or embedded, was measured at a specific frequency when active vibration suppression was reached. The percentage of discrepancy between the experiment and finite element results for the surface-mounted case was less than 5 percent, whereas that for the embedded case was about 10 percent. But, in general, a good agreement between experimental data and finite element results were established as shown in Figures 2.11 a and b. Representative results for the eight layers surface-mounted and four inner layers embedded confirm the accuracy of the ANSYS finite element models. More importantly, the closeness of the actuator voltage values from the experiments and finite element analyses verifies the validity of the proposed constant and corresponding voltage techniques for active vibration suppression.

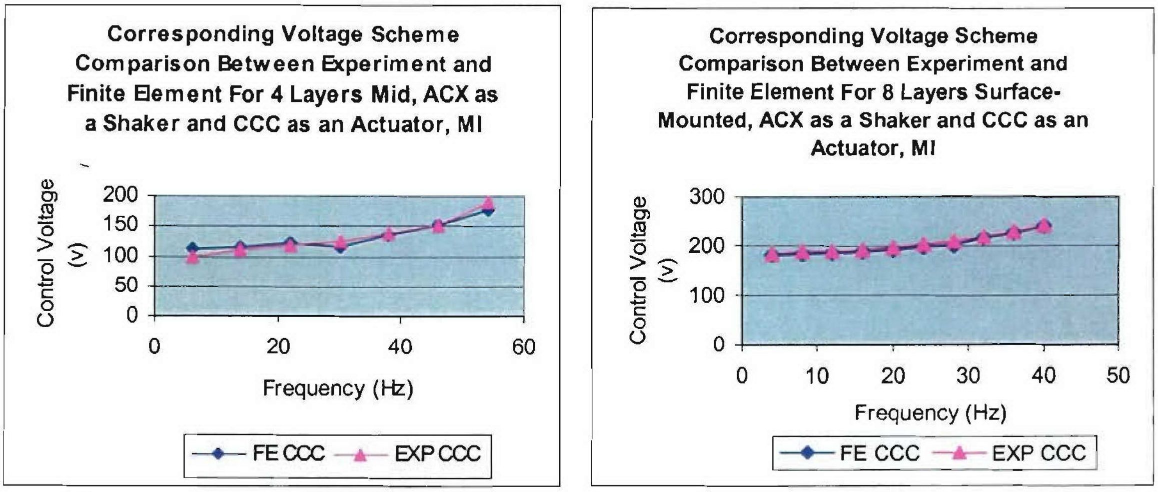

a) Four inner layers embedded, varying thickness b) Eight layers surface-mounted

Figure 2.11. *Comparing experimental data with finite element results using corresponding voltage technique.*

2.5. Piezoelectric Actuator Effectiveness

The Constant Voltage technique was employed to address three very important and complex issues; namely, effectiveness of piezoelectric patch acting as an actuator as a function of the beam thickness and the actuator distance from the beam neutral axis, as well as the influence of the constraint layers (either constant number of constraints or variable number of constraints) on the performance of the embedded piezoelectric patches. Due to the complexity of the subject matters three cases were considered for this study. 1) Case I focuses on beams having various thickness with non-collocated and surface-mounted piezoelectric patches acting as a sensor and an actuator. Beams with surface-mounted piezoelectric patches can be considered as the simplest case. In this case, the piezoelectric effectiveness is influenced by the beam thickness and the actuator distance from the beam neutral axis. For the surface-mounted case, the actuator distance from the beam neutral axis is half of the beam total thickness. 2) Case II considers beams with embedded piezoelectric sensor/actuator patches with varying thickness having constant number of total constraint layers, equal to four. The embedded and non-collocated piezoelectric patches act as a sensor and an actuator. The embedded case with varying beam thickness compared to the surface-mounted one is considered to be more complex. For this embedded case, the piezoelectric effectiveness is influenced by three coupling factors; namely, beam thickness, the actuator distance from the beam neutral axis, and the constant number of constraint layers. Case II focuses on the influence of the constant number of constraint layers on the embedded piezoelectric effectiveness. Once again, the Constant Voltage technique was employed to study the performance of the embedded piezoelectric patches, and the results are compared with Case I with the same ACX voltage. As mentioned earlier, each embedded beam contains four extra constraint layers compared to a surface-mounted one. Therefore, if the total number of layers for the surface-mounted case is selected as N, then the total number of inner layers for the embedded case would be N and the total number of layers would be N+4. 3) Case III deals with embedded ACBs having different number of constraint layers and constant thickness. The embedded and non-collocated piezoelectric patches are located at different places through the composite laminate thickness and act as a sensor and an actuator. For this case, i.e., constant composite laminate thickness, the piezoelectric effectiveness is influenced by only two coupling factors; namely, the actuator distance from the beam neutral axis, and the existence of different number of constraint layers. Finally, constant voltage technique was employed to investigate the influence of various number of constraint layers on the embedded piezoelectric performance. The selected maximum displacement values are associated with the initial frequency of four hertz.

2.5.1. Case I: Piezoelectric Effectiveness versus the Beam Thickness and Actuator Distance from Neutral Axis for Surface-mounted

The Constant Voltage (CV) technique was employed to investigate the piezoelectric effectiveness as a function of the beam thickness and the actuator distance from the beam neutral axis, for ACBs with surface-mounted piezo patches. The ACX piezoelectric patch acts as a shaker and a CCC piezoelectric patch acts as the actuator. Constant peak voltage equivalent to seventy volts was supplied to the ACX piezoelectric patch for all beams with different thickness over the range of frequency under consideration. Using D-L-S-A charts for each beam, the required actuator voltages, as explained earlier, necessary for active vibration suppression, were obtained employing the Constant Voltage technique. The finite element natural frequency versus the beam thickness is found to be linear. However, the constant voltage values show non-linear behavior as a function of the beam thickness. The piezoelectric performance, employing constant voltage technique as a function of the beam thickness (or actuator distance from beam neutral axis) is shown graphically in Figure 2.12.

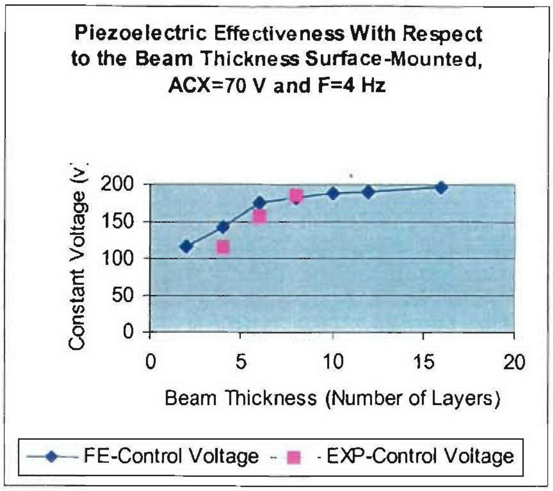

Figure 2.12. Comparing experimental data with finite element Control Voltage as a function of beam thickness using CV, Surface-mounted.

The experimental control voltages were obtained for four, six, and eight layers composite beams with surface-mounted piezoelectric patches. Therefore, the comparison between the experimental and finite element control voltages as a function of the beam thickness and actuator distance at four Hertz are shown in Figure 2.12. For this case, the piezoelectric performance is influenced by the beam thickness (also, noting that the actuator distance from the beam neutral axis is half of the beam thickness). Figure 2.12 shows that higher actuator voltage values are required for active vibration suppression as the beam thickness increases. It also shows that the actuator voltage increases non-linearly with increasing beam thickness. The rate of the constant voltage in terms of the beam thickness (i.e., the slope) is much higher in the beginning and rapidly reduces till it reaches near a platue as the beam thickness increases. For the surface-mounted case, the lower level of actuator voltage as the beam thickness decreases indicates that the piezoelectric performance is more effective and more sensitive to the thickness at lower beam thickness. When the beam thickness increases change of slope decrease and actuator voltage approaches near a constant value which means that the piezoelectric effectiveness reduces but approaches to that of the external piezo (i.e., the ACX). As a result, for the surface-mounted case, the piezoelectric effectiveness decreases as the beam thickness and the actuator distance from the beam neutral axis increases till it reaches a platue, meaning that the effect of the thickness increase is more dominant than the distance to neutral axis. It should be noted that for the given ACX and CCC actuator voltages, while the thickness increase reduces the effect of the piezo, the increase in the distance to neutral axis increases the effect of the piezo in a lateral vibration, as those considered here. Finally, the non-linear behavior of the constant control voltage as a function of the beam thickness can be explained based on the definition of the Constant Voltage scheme. To determine the constant voltage value, it was assumed that *Dp* is equal to *Dv* as explained earlier. The following explains the non-linear behavior in Figure 2.12. In the harmonic analysis responses for beams with different thickness, zooming on the initial portion of the frequency range reveals that for any frequency before the natural frequency displacement values have non-linear growth as frequency increases. In the harmonic analysis, when constant voltage is supplied to the ACX piezoelectric, which acts as a shaker, thinner beams experience higher displacements, and hence by increasing the beam thickness displacement reduces in a non-linear fashion. To demonstrate non-linear displacement behavior as a function of the beam thickness due to the applied constant peak external load (i.e., ACX as a shaker), Figure 2.13 was extracted from various harmonic analyses for some initial frequency value of four hertz. Figure 2.13 shows that the rate of displacement as a function of the beam thickness (i.e., the slope) has negative slope and sharply decreases as the beam thickness increases. In addition, for beams with less number of layers, the slope is much higher in the beginning and reduces rapidly as the beam thickness increases. This non-linear behavior of the displacement repeats itself for any frequency value before reaching the natural frequency of the beams with various number of layers and natural frequencies. It is believed that this non-linearity of the displacement as a function of the beam thickness has an influence on the non-linear behavior of the constant voltage versus the beam thickness, as given in Figure 2.12. The Constant Voltage scheme uses these displacements to calculate the actuator voltages required for the active vibration suppression.

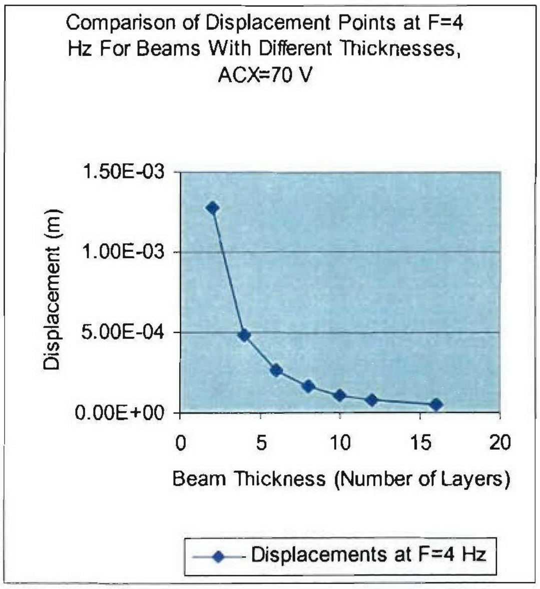

Figure 2.13. Displacement comparison at four hertz for beam with different thickness, surface-mounted.

2.5.2. Case II: Influence of the Constant Constraint Layers on the Piezoelectric Effectiveness for the Embedded Case with Variable Thickness ACBs

Once again, the Constant Voltage technique was employed to investigate the embedded piezoelectric effectiveness of beams having various thickness and constant number of constraint layers. For this case, surface-mounted ACX piezoelectric patch acts as a shaker and the embedded CCC piezoelectric patches act as a sensor and an actuator. Similar to Case I, the supplied peak voltage to the ACX piezoelectric patch was constant and equal to seventy volts for all the beams with different thickness and constant number of constraint layers. For this embedded case, the piezoelectric effectiveness is influenced by three coupling factors; namely, the beam thickness, the actuator distance from the beam neutral axis, and the constant number of constraint layers (i.e., four layers). The simultaneous interaction between these coupling factors contributes to the complexity of the problem. As it was mentioned earlier, for this embedded case one extra layer is needed to cover the piezoelectric element and one extra cut-out layer to fill the area around the piezoelectric patch (Ghasemi-Nejhad and Pourjalali, 2003; Ghasemi-Nejhad and Russ, 2003; Ghasemi-Nejhad et al., 2005c). Consequently for this embedded case, each beam has four extra constraint layers compared with its surface-mounted counterpart. In addition, the actuator distance from the beam neutral axis is not half of the beam thickness. Using D-L-S-A charts associated with each beam, the required actuator voltages were obtained. Figure 2.14 shows the constant voltage values for beams with different thickness and embedded sensor and actuator. Again, the natural frequencies were found to vary linearly with respect to the beam thickness. A comparison between the constant voltage values of Figures 2.12 and 2.14 shows about 35% increase in the required actuator voltage values for the embedded case, which are due to the additional 4 layers thickness and constraint layers effects. Note that if N is the number of inner layers, then the total thickness will be N+4 layers. The piezoelectric effectiveness which is influenced by three complex coupling factors, i.e., beam thickness, actuator distance from the beam neutral axis, and constant constraint layers was studied here by employing the Constant Voltage technique.

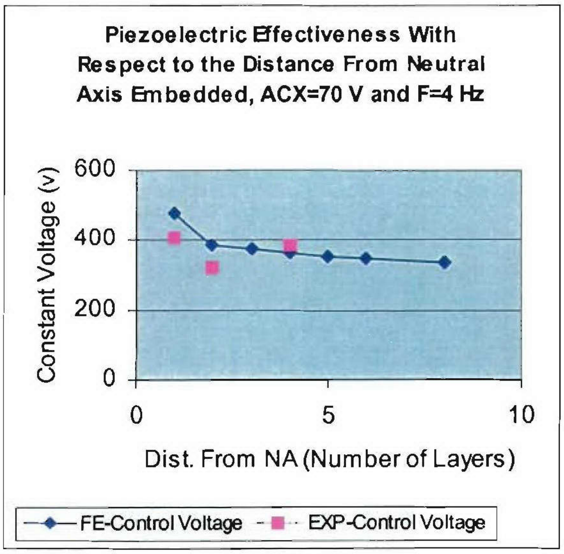

Figure 2.14. Comparing experimental data with finite element Control Voltage as a function of beam thickness using CV, Embedded

As a result, constant voltage values were plotted in term of the actuator distance from the beam neutral axis (NA) and are given in Figure 2.14. The corresponding experimental control voltages were also obtained for the embedded beams having total of six, eight, and twelve layers, and the results are also given in the same figure. Therefore, Figure 2.14 also shows the comparison between the experimental control voltages with the finite element results at four Hertz. Figure 2.14 shows that lower actuator voltage values are required for active vibration suppression as the beam thickness increases. Also, in contrast to Figure 2.12, Figure 2.14 shows negative slopes and that the constant voltage value reduces non-linearly when the beam thickness or the actuator distance from the beam neutral axis increases. In addition, the rate of constant voltage as a function of the actuator distance from NA (i.e., the slope) has larger negative value in the beginning and reaches near a platue value as the beam thickness increases. For the embedded case, the negative slope must be the influence of the constraint layers on the required actuator voltage needed for the active vibration suppression. For the embedded case, high change of the negative slope and the higher actuator voltage as the beam thickness decreases indicates that the influence of the constraint layers on the piezoelectric effectiveness is high for thinner beams. As the beam thickness increases, the change of the negative slope decreases and the actuator voltage approaches near a constant value indicating that the influence of the constraint layers on the piezoelectric effectiveness decreases (and hence the piezoelectric effectiveness increases) as the beam thickness increases. It should also be noted that the ratio of the constraint layer thickness over the beam overall thickness decreases as the beam thickness increases. The comparison between the constant voltage value as a function of the actuator distance from the neutral axis for surface-mounted and embedded beams are shown in Figure 2.15. As the beam thickness decreases the constant voltage reaches higher values for embedded case due to the effects of the constraint layers (i.e., four, in this study). However, the surface-mounted case demonstrated that as the beam thickness decreases the piezoelectric effectiveness increases and lower control voltage is needed. In fact, Figure 2.15 shows that at a lower thickness, surface-mounted performs better than embedded, but as the beam thickness increases the performances of both beams approach each other, which can be attributed to the fact that the constraint layer thickness compared to the overall beam thickness decreases as the beam thickness increases.

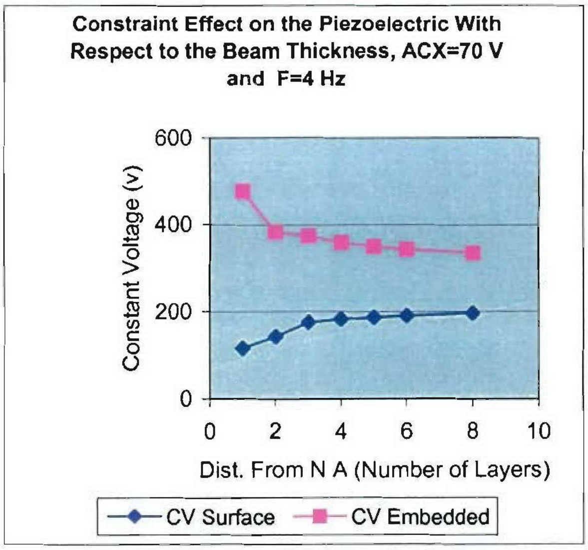

Figure 2.15. Comparing Control Voltage as a function of Distance to Neutral Axis using CV, Surface-mounted and Embedded

2.5.3. Case III: Influence of Various Number of Constraint Layers on the Embedded Piezoelectric Effectiveness for Beams with Constant Thickness

Case III focuses on employing the Constant Voltage technique to study the embedded piezoelectric effectiveness for beams with different number of constraint layers and constant thickness. The location of the embedded and non-collocated piezoelectric sensor and actuator changes with respect to the beam neutral axis while the beam thickness remains constant. For this embedded case, the goal is to demonstrate that the ratio of the total number of constraint layers over the beam overall thickness can provide useful information in terms of the constant voltage values which are influenced by the beam thickness, actuator distance from beam neutral axis, and different number of constraint layers. Constant voltage values associated with different number of constraint layers may give insight into the threshold limit of the constraint layer thickness or piezoelectric selection. Therefore, all beams with constant thickness and variable constraint layers contain twenty layers and the surface-mounted ACX piezoelectric patch acts as a shaker. Similar to Cases I and II, the supplied peak voltage to the ACX piezoelectric patch was constant and equal to seventy volts. Because of the beam constant thickness (i.e., 20 layers) the embedded piezoelectric performance is influenced by only two coupling factors, i.e., the actuator distance from the beam neutral axis, and the existence of different number of constraint layers. In the first finite element model, the embedded piezoelectric patches are located one lamina below the skin with total of four constraint layers and the largest actuator distance from the beam neutral axis. Whereas in the subsequent models, the embedded piezoelectric patches move one lamina at a time toward the beam neutral axis, causing higher number of constraint layers and smaller actuator distance from the beam neutral axis. It is clear that due to the beam constant thickness, as the number of the constraint layers increases the corresponding actuator distance decreases and visa versa. In addition, the actuator distance from the beam neutral axis is not half of the beam total thickness. Once again, using D-L-S-A charts associated with each beam, the required actuator voltages were obtained. The control voltage as a function of the distance to neutral axis of the embedded beam is given in Figure 2.16. The constant voltage value increases rapidly as the number of constraint layers increases or the associated actuator distance from the beam neutral axis decreases. It is important to mention that in Case III, constant voltage values are influenced by two interacting factors, i.e., actuator distance to the beam neutral axis and the variable constraint thickness in comparison with Case II where the constant voltage values were affected by the actuator distance to the beam neutral axis and the beam thickness. Much higher constant voltage values for Case III in comparison to Case II are mainly associated with higher number of constraint layers as well as higher beam thickness.

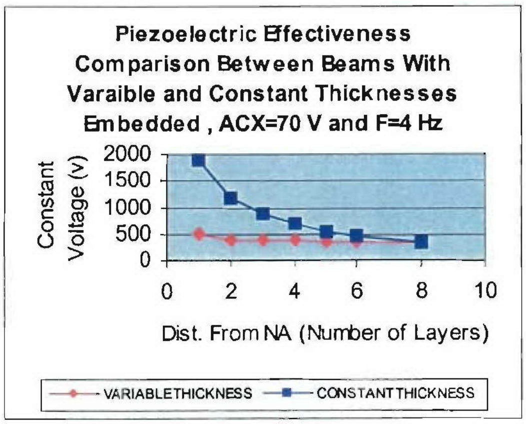

__Figure 2.16.__ Comparing Control Voltage as a function of Distance to Neutral Axis using CV, for Embedded with Variable Thickness (Case II) and Constant Thickness (Case III).

Once again, employing the Constant Voltage technique, the piezoelectric effectiveness was investigated based on the required actuator voltage values needed for the active vibration suppression. As expected, Figure 2.16 of Case III shows similar characteristic to Figure 2.14 of Case II such as having negative slopes and non-linear behavior of the constant voltage values. In addition, Figure 2.16 of Case III shows much higher constant voltage values as well as much sharper rate of negative slopes as the actuator distance from beam neutral axis decreases. As a result, similar to Case II, Case III shows that lower constant voltage values are required for active vibration suppression as the actuator distance increases or number of constraint layer decreases. On the other hand, constant voltage value and associated rate of negative slope sharply increases as the actuator distance decreases or number of constraint layers increases. A comparison between constant voltage values as a function of the actuator distance to the beam neutral axis for Case II and Case III is also shown in Figure 2.16. The higher constant voltage values in Case III, compared to Case II, was expected and is due to the higher thickness of the beam and constraint layers in Case III. In Case II, a constant number of constraint layers influenced the piezoelectric performance whereas in Case III piezoelectric performance was influenced by different number of constraint layers. As a result, the increase in the constant voltage values for Case III as the actuator distance decreases must be attributed not only to a higher thickness but also to the increase in the number of constraint layers. The two curves associated with Case II and Case III, in Figure 2.16, approach each other as the actuator distance increases and finally intercept where the samples become identical. The intercept point presents beams having same thickness, same actuator distance, and same number of constraint layers for Case II and Case III.

In summary, in embedded cases, the piezoelectric effectiveness had been influenced by three coupling factors: beam thickness, actuator distance to beam neutral axis, and number of constraint layers. The simultaneous interacting effects between these three factors make it impossible to determine the individual effect on the piezoelectric performance. Due to the combined effects of the beam thickness, the actuator distance, and the constraint layers on the piezoelectric performance, useful information may be obtained by considering the ratio of the total number of constraint layers over the beam overall thickness (called the *constraint ratio*, here) in conjunction with the constant voltage as a function of the actuator distance from the beam neutral axis. It seems that the value of this ratio can provide some insight to the degree of their influences on the piezoelectric effectiveness due to the beam thickness, the actuator distance, and the number of constraint layers. It is clear that, the value of this ratio is controlled by the total number of constraint layers and the beam overall thickness. It is worth noting that the effect of the actuator distance from the beam neutral axis is linked either to the beam overall thickness (such as Case II where the number of the constraint layer is fixed and the beam thickness varies) or to the total number of constraint layers (such as Case III where the number of the constraint layer varies and the beam thickness is fixed). In addition, the value of this ratio can provide useful information with regard to the level of the constant voltage needed for the active vibration suppression. In Case II, the total number of constraint layers was kept constant and equal to four whereas the beam thickness was variable. The influence of the actuator distance on the piezoelectric performance was reflected in the beam overall thickness. It is reminded that in Case II, the numerator of the *constraint ratio* was constant and equal to four as the denominator indicating the beam thickness was changed. The value of this ratio, changes from 0.67 to 0.2 as the beam overall thickness or the actuator distance from the beam neutral axis increases. In Case III, the number of the constraint layers varied as the beam overall thickness was kept constant. For this case, the effect of actuator distance on the piezoelectric performance was merged within the influence of the total number of constraint layers. As it was explained in Section 2.5.1, for the surface-mounted and variable thickness, the piezoelectric effectiveness increases as the beam thickness and the actuator distance from the beam neutral axis decreases. For the surface-mounted case (i.e., Case I), the piezoelectric effectiveness reaches its maximum as the beam thickness reaches its minimum (see Figure 2.12). On the other hand, as it was discussed in Section 2.5.2, for the embedded beams having constant number of constraint layers and variable thickness (i.e., Case II), the influence of the constant number of constraint layers on the piezoelectric effectiveness increases as the beam thickness decreases (see Figure 2.14). Similar result was obtained in Case III, for the embedded beams having variable number of constraint layers and constant thickness (see Figure 2.16). Finally, a *constraint ratio* (i.e., the value of the constraint layers thickness over the beam thickness) was introduced such that as the this ratio increased the *piezoelectric effectiveness* decreased. For Case III, the *constraint ratio* varied from 0.9 to 0.2 as the thickness of the constraint layers decreased (and the actuator distance to the beam neutral axis increased). Also in general, a higher *constraint ratio* value indicates that a higher constant control voltage value is needed for the active vibration suppression leading to a lower *piezoelectric effectiveness.*

2.6. CONCLUSIONS

A comparative study on the piezoelectric effectiveness employing the Constant Voltage technique was performed for active composite beams with surface-mounted and embedded piezoelectric sensors and actuators. To ensure the accuracy of the calculated actuator control voltages, evaluated employing the Constant Voltage technique, comparisons between finite element and experimental results for modal and harmonic analyses as well as required actuator control voltages needed for active vibration suppression at different frequencies were performed. Excellent agreement between the finite element and experimental data were established which confirmed the correctness of the finite element models and the obtained results.

The ACX piezoelectric patch was surface-mounted and used as a shaker in all cases. Two CCC piezoelectric patches, used as a sensor and an actuator, were non-collocated either surface-mounted or embedded. For the surface-mounted case (i.e., Case I) the following results were obtained for the beams with varying thickness. The piezoelectric effectiveness is influenced primarily by the beam thickness and the actuator distance from the beam neutral axis which for this case is half of the beam thickness. The Constant (Control) Voltage increases non-linearly with positive slopes as the beam thickness increases. The high variation of the positive slope in the actuator voltage as the beam thickness decreases indicates that the piezoelectric performance is more effective due to the lower values of constant control voltage in this region. On the other hand, as the beam thickness increases the variation in the slope decreases and the actuator voltage approaches near a constant value indicating that the piezoelectric performance approaches that of the shaker. As a result, for the surface-mounted case the piezoelectric effectiveness increases as the beam thickness or actuator distance from beam neutral axis decreases, indicating that the effect of thickness is stronger than that of the actuator distance to the beam neutral axis in this case, since these two factors have competing effects on the level of the constant control voltage value.

For an embedded case (i.e., Case II), the piezoelectric effectiveness is influenced by three coupling factors; namely, beam thickness, actuator distance from the beam neutral axis, and the constraint layers. For this case, the actuator distance from the beam neutral axis is not half of the beam thickness. The total number of the constraint layers is fixed, at four, and the beam thickness increases (and so does the actuator distance to the beam neutral axis). The Constant (Control) Voltage decreases non-linearly with negative slopes as the beam thickness increases. The higher constant voltage values for the embedded case are expected since in comparison to the surface-mounted each beam has four extra layers as the constraint layers. The negative slope must be the influence of the constraint layers on the actuator voltage needed for the active vibration suppression. The high change of the negative slope and higher actuator voltage as the beam thickness decreases indicates that the influence of the constant constraint thickness on the piezoelectric performance is high at lower thickness. On the other hand, as the beam thickness increases the variation of the negative slope decreases and the actuator voltage approaches near a constant value indicating that the influence of the constraint layers on the piezoelectric performance is diminished. As a result, the influence of the constant number of constraint layers (i.e., four here) on the piezoelectric effectiveness increases as the beam thickness or the actuator distance from the beam neutral axis decreases. In general, for the embedded case with constant constraint layers thickness, as the beam thickness increases (or the actuator distance from the beam neutral axis increases) the influence of the constraint layers on the piezoelectric performance decreases.

For Case III, beams with constant thickness and variable constraint layers and actuator distance to the beam neutral axis need much higher constant voltages and have sharper rate of negative slopes as the number of the constraint layers increases and the actuator distance from the beam neutral axis decreases. Otherwise, the general trends in Case II and III were similar.

A *constraint ratio* (i.e., the thickness of the constraint layers over the beam overall thickness) was introduced here for the beams with embedded piezoelectric actuators. The *constraint ratio* is the inverse of the *piezoelectric effectiveness*. The effects of the *constraint ratio* and *piezoelectric effectiveness* and their inverse relationship can clearly be seen in Figures 2.14 to 2.16.

3. ACTIVE COMPOSITE STRUT (ACS) AND ACTIVE COMPOSITE CENTRAL SUPPORT (ACCS) (Nejhad, Ma, Bletcha)

3.1. Specifications

Our objectives have been to develop active composite struts (ACSs) that will be used for simultaneous precision positioning and active vibration suppression (Ghasemi Nejhad, 2002). The main application for this strut is its use in a 2-DOF Tripod intelligent/adaptive MSP for a Thrust Vector Control (TVC) application in ADPICAS Phase II. The bandwidth for the TVC is DC-100 Hz and the load capability is 10 lbs. per strut for a thruster force of 100 lbs. The platform requires +/- 1 degree of tilt with an accuracy of +/- 1 arc-minute. The overall dimensions of the Modified Stewart Platform, MSP, is based on a mid-to-small size satellite (similar to Clamentine Satellite) and will be given in the MSP section in this report:

3.2. ACS and ACCS Design

A solid model of the ACS assembly with its components is shown in Figure 3.1 and consists of the following components from left-to-right and bottom-to-top:

1. Actuator motor for PP (in brown)
2. Piezoelectric translator actuator for active VS + PP (in blue)
3. Sensor and sensor clamps (in red)
4. Bearings (in yellow)
5. Connecting rod (in silver)

The ACS is housed in a composite tubular housing (in dotted black) and has joints at both ends to be connected to the MSP.

Figure 3.1. Active Composite Strut (ACS).

3.2.1. ACS Actuator Motor

The actuator chosen is currently an M-235 High Resolution Closed-Loop DC-Mike Actuator Motor manufactured by Physik Instrumente. This motor is an ultra-high resolution linear actuator providing linear motion up to 50 mm with 0.0035-micrometer resolution (the nano accuracy is when moving in one direction) and 30 mm/sec speed, with a push/pull force of 100 N, driven by a closed-loop DC motor/gearhead combination with motor shaft mounted high-resolution encoder with a repeatability of 0.5 μm. To control the actuator, the C-842 DC Motor Controller PC Board, also manufactured by Physik Instrumente, was used. The M-235 actuator motor is shown in Figure 3.2.

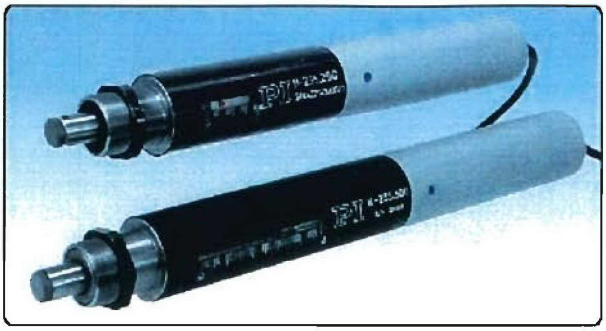

Figure 3.2. *M-235 High Resolution Closed-Loop DC-Mike Actuator used in the ACS.*

3.2.2. ACS Piezoelectric Translator

The piezoelectric translator used for ACS active vibration suppression is the PZT stack actuator (see Figure 3.3) manufactured by Physik Instrumente. This translator offers displacement up to 90 μm at 100 volts, sub-nanometer resolution of 0.9 nm, and a pushing/pull capacity of 800/300 N. This piezoelectric is capable of displacement off-setting while generating a vibration, hence participating in a simultaneous precision positioning (PP) and vibration suppression (VS). In addition, to the piezo participation in the PP, the motor actuator can also participate in the milli/micro/nano positioning simultaneously. The piezo stack actuator is assembled on the motor actuator and will be explained further in this part of the resport.

Figure 3.3. *Physik Instrumente PZT Stack Actuator used in the ACS.*

3.2.3. ACS Sensor and Load Cell

In the early version of the ACS a sensor capable of precision positioning and vibration measurements was introduced (see Figure 3.1). Its accuracy was 0.001 mm. One side of the sensor was clamped to the base of the motor and its other side clamped to the telescoping rod, and hence could measure total displacements for PP and VS. However, in the final version of the ACS this sensor was eliminated and the motor encoder was used for the PP and a load cell was used for VS. Therefore, in the final version of the ACS, the Motor is responsible for PP and the Piezo Stack responsible for the VS and they are controlled simultaneously to provide the possibility of simultaneous vibration suppression and precision positioning for the ACS as well as MSP. The load cell used for the ACS is an Entran ELPM force sensor and is shown in Figure 3.4.

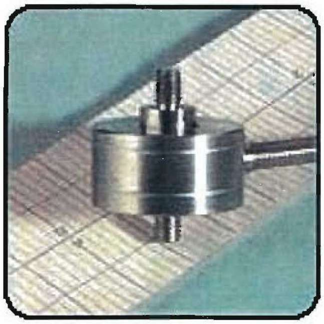

Figure 3.4. *Entran ELPM Force Sensor used in the ACS.*

3.2.4. ACS Composite Housing

The ACS composite housing is made of woven carbon/epoxy plain weave composite prepreg using a roll-wrapping technique and shrink taping with a total thickness of 1 mm (0.040"). In Figure 3.1, only half of the composite tube housing is shown schematically as a break away to depict the ACS internal components. The actual composite tubular housing are in three segments as shown in Figure 3.5.

3.2.5. ACS Rod, Joints, and Bearing

Joints for the struts are designed to allow the two in-plane degrees-of-freedom for the platform top device-plate. These joints are ball-and-socket precision joints at the top for the ACSs to connect to the MSP, and they are universal precision joints at the bottom of the ACSs to connect to the pivot joints on the bottom star plate. Necessary bearings and connecting rods are used for the ACSs (see Figures 3.1 and 3.5).

3.2.6. ACS Assembly

The ACS assembly with its composite tubular housing is shown in Figure 3.5. The lower and upper composite housing are only protective covers, while the middle part is both a protective cover and a load bearing component. All wiring is contained within the main middle composite housing. As a result of the ACS component characteristics, the platform will have 10 Hz band for precision positioning of 1 to 2 degrees tilts and 300 Hz band for vibration suppression.

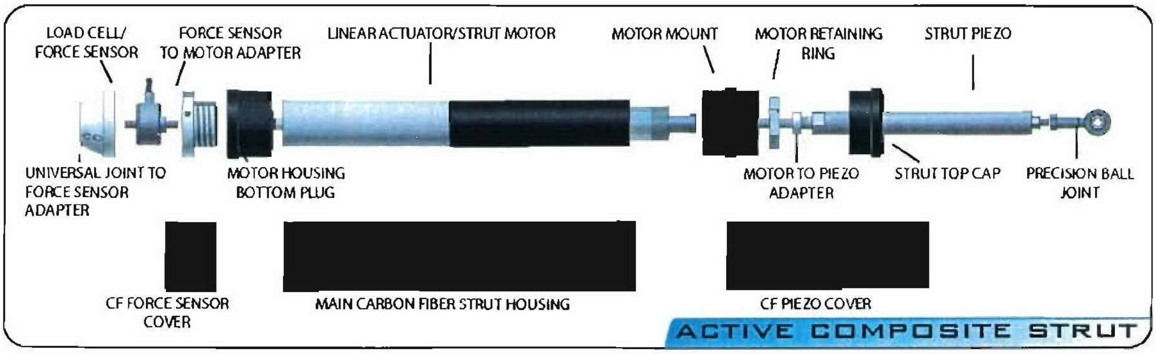

Figure 3.5. The ACS Assembly.

3.2.7. ACCS Design and Assembly

The ACS and ACP are designed to suppress the lateral vibration caused by the thruster on the top device plate. While ACS has VS+PP capabilities, the ACP has primarily a VS capability. It should also be noted that the ACS VS capability is axial but due to its arrangement designed in the MSP, it can participate in the MSP top plate lateral VS. To suppress the axial vibration caused by the thruster, ACCS is designed for axial VS only. The joints for the ACCS are designed to allow the two in-plane degrees-of-freedom for the platform top device-plate. The ACCS connects the top device-plate to the bottom star plate. The ACCS bottom is bolted into the center of the star bottom plate, and it is joined to the top device-plate using a universal precision joint to restrict the rotation of the top device-plate of the MSP to two rotational degrees of freedom about the in-plane axes with no out-of-plane axis rotation. All translation degrees of freedom are restricted due to the MSP ACCS design (see Figure 3.6).

A high-load capacity PZT stack actuator with 80 μm motion at 1000 volts and 30,000/3,500 N push/pull force-carrying capability was used in the ACCS. This piezo stack actuator was purchased from Piezomechanics, GmbH (see Figure 3.6). An Entran ELPM load cell, with higher load capabilities that those used in the ACS and shown in Figure 3.4, was used here at the bottom of the central support to monitor the vibration suppression (see Figure 3.6). The ACCS composite housing was manufactured similar to the ACS composite housing. The ACCS composite housing bears no structural loading and is strictly in place to provide protection for the ACCS internals. The housing is easily removable and uses a floating rubber seal provide a complete seal while not passing on any vibration (see Figure 3.6).

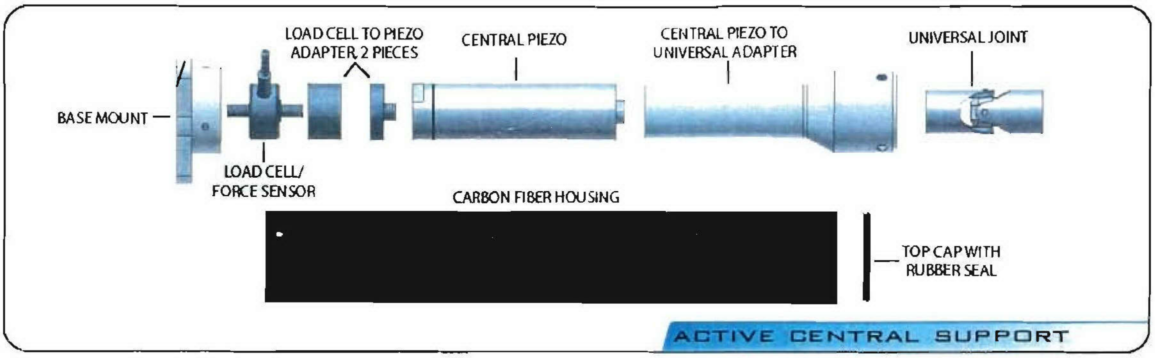

Figure 3.6. *The ACCS Assembly.*

3.3. ACS Analysis

The accuracy of the ANSYS FEA results was tested against available analytical solution. For this purpose, an aluminum rod with the diameter of 0.0127 *m*, length of 0.184912 *m*, Young's modulus of 6.8E10 Pa, density of 2,690 kg/m^3, and Poisson's ratio of 0.345 was modeled as a cantilevered beam. Its fundamental axial natural frequency was found to be 6794 Hz analytically (Meirovitch, 1967). This rod was modeled in ANSYS and its fundamental natural frequency was found to be 6,823 Hz when the whole rod was modeled using modal analysis, and it was 6,821 when only a quarter of the rod (i.e., 90-degree angle of the circular rod) was modeled in modal analysis. This difference was about 0.40%. This model was also studied by harmonic analysis and the results were the same.

Finite element analysis using ANSYS was conducted for vibration suppression of the Active Composite Strut. Modal, harmonic, and transient analyses were conducted on a model of the complete strut. The model consisted of the motor actuator, piezoelectric stack actuator, and the strut shaft/rod (see Figure 3.5). Modal, harmonic, and transient finite element analyses were performed on the model and the results from the three analyses were in agreement. Also, CV and COV vibration suppression schemes introduced in Section 2 of this report was also successfully applied to the ACS and near complete vibration suppression was achieved using the COV technique.

3.4. ACS VS and PP+VS Testing

This section explains the ACS VS as well as PP+VS testing using the Fuzzy Logic Control. For the PP+VS experiments, the ACSs were attached to a flexible beam where the motion of the ACS motor induces a vibration into the flexible beam. Two setups were used for the PP+VS. First, a laser sensor was used to monitor the vibration of a polymer flexible beam and the ACS piezo stack was used to suppress the vibration. Second, two Active Fiber Composite piezoelectric patches were surface-mounted onto a composite flexible beam, non-collocated (one at the beam tip as the sensor and one at the beam root as the actuator). Once again, the ACS motor motion induced the vibration and either the ACS piezo stack actuator or the beam piezo patch actuator suppressed the vibration.

3.4.1. ACS VS Testing

The ACS precision positioning tests using a digital micrometer were performed and the results were in agreement with the Motor encoder. Vibration suppression tests were conducted on the complete strut assembly using an ET-132 Electrodynamic Transducer as an input. The back end of the strut was clamped in a vice and bolted to the vibration table. A D100 fiber-optic sensor made by Philtec was used to measure the displacement of the strut shaft tip. This test setup is shown in Figure 3.7. The fiber optic sensor was calibrated using the same test setup. The actuator motor was displaced 1 micron at a time and the voltage output of the fiber optic sensor was recorded. Tests were performed while applying 1, 2, 5, and 10V signals to the piezo at 100Hz. The amplitude of the shaker displacement was adjusted to match the piezo displacement. Measurements were taken for the shaker displacement and the displacement with the piezo suppression. The output of the shaker was also measured using the piezo as a sensor. Figure 3.8 shows the ACS vibration suppression test.

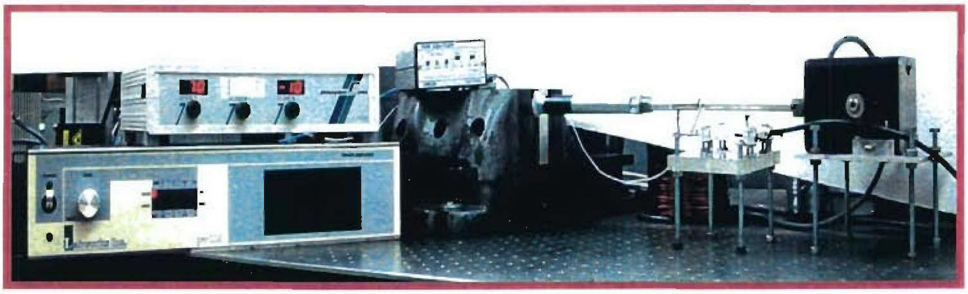

Figure 3.7. *ACS Vibration Suppression Test Set-up.*

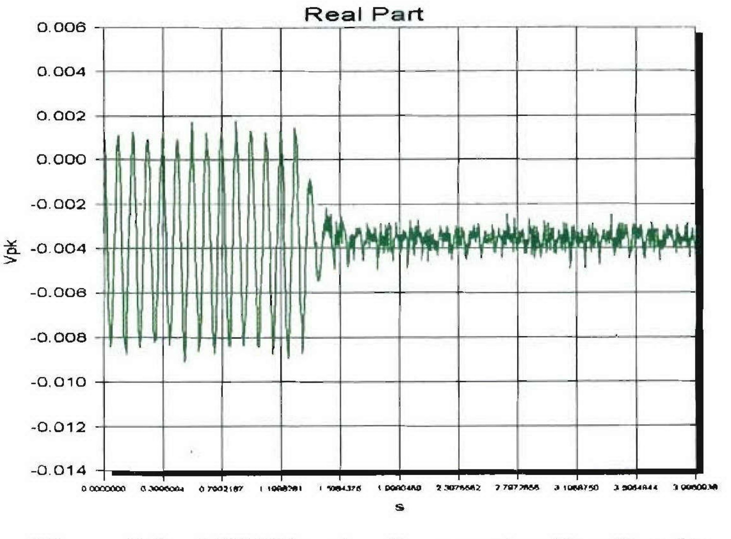

Figure 3.8. *ACS Vibration Suppression Test Results.*

3.4.2. ACS PP+VS Testing using a Laser Sensor

The PP+VS test set-up in this case is shown in Figure 3.9. A polymer flexible beam was attached to the end of the ACS, and the ACS motor was exited to generate positioning, and a low frequency vibration. A Fuzzy Logic Control (FLC) (Ma and Ghasemi-Nejhad, 2004a, 2005a) was developed for the ACS PP+VS. The motor actuator is used for the PP and the piezoelectric stack actuator is used for the VS. Figure 3.10 shows the ACS PP+VS test results in this case. The ACS motor (50 mm stroke and 1 mm/sec speed) and piezo (40 microns at 150 volts) in this case were the older components used in the initial version of the ACS developed in the ADPICAS.

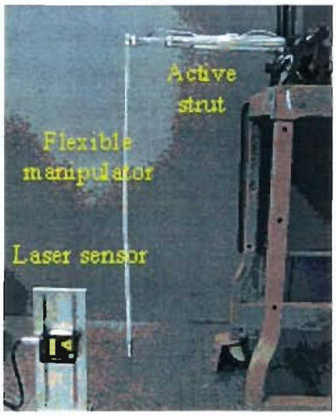

Figure 3.9. *ACS PP + VS Test Set-up using a Laser Sensor.*

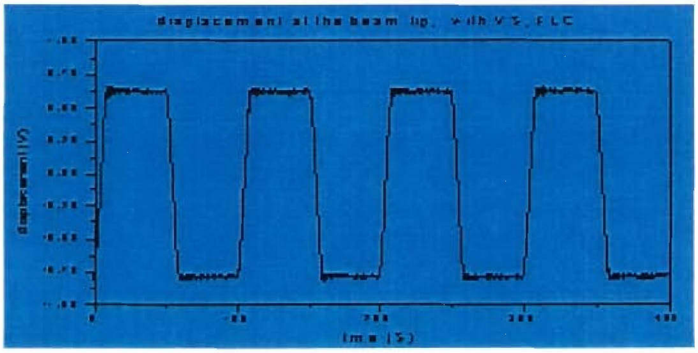

Figure 3.10. *ACS PP + VS Test Results using a Laser Sensor.*

3.4.3. ACS PP+VS Testing using a Piezo Patch Sensor

The PP+VS test set-up in this case is shown in Figure 3.11. A composite flexible beam was attached to the end of the ACS, and the ACS motor was exited to generate positioning, and a low frequency vibration. A Fuzzy Logic Control (FLC) (Ma and Ghasemi-Nejhad, 2004a, 2005a, 2005b) was developed for the ACS PP+VS. The motor actuator is used for the PP and the ACS piezoelectric stack actuator or the ACP piezoelectric patch actuator can be used for the VS in this case. The ACS motor (50 mm stroke and 30 mm/sec speed) and piezo (90 microns at 150 volts) in this case were the new components used in the final version of the ACS developed in the ADPICAS.

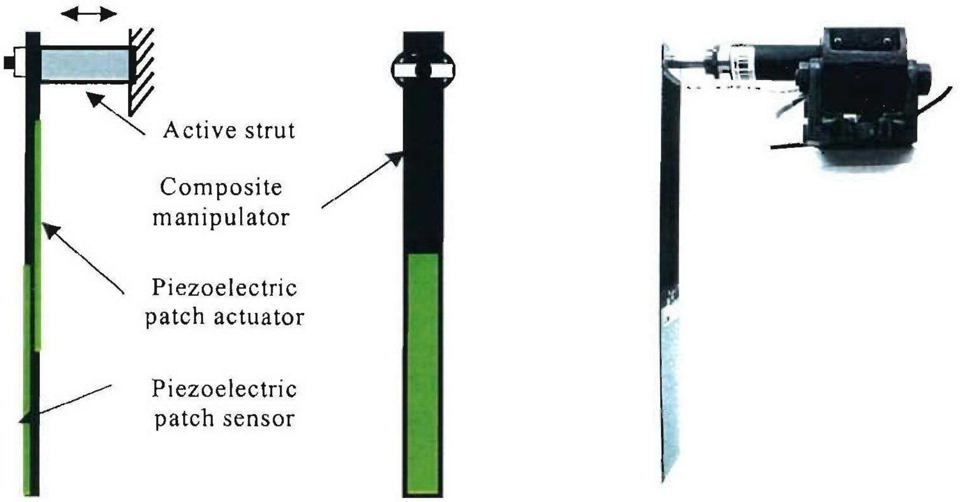

***Figure 3.11.** Setup for the SPPVS of the new strut and composite beam.*

In addition to the updating of the ACS hardware, all amplifiers were updated including DC-motor amplifiers, amplifiers for PZT stack actuators, and amplifiers for the PZT patch actuators. In addition, a new DC-motor amplifier has been fabricated and successfully tested with the new motor in our laboratory. Figure 3.12 illustrates the block-diagram of the DC-motor control loop employing incremental encoder to measure the displacement of the motor. This closed loop contains an amplifier, a DC-motor, an encoder, a decoder board, and a controller.

The step response and frequency response of this control loop are given in Figure 3.13, indicating that it takes 0.18 second to position the motor to 5 mm with the steady state error of 2 μm and for 0.5 mm input, the bandwidth of the loop is 17 Hz (-3 dB). The modeling of the ACS, composite beam, and the PZT patch sensor/actuator are performed, and a control strategy, as shown in Figure 3.14, is proposed, which includes a motion controller for the ACS and a vibration controller for the PZT actuator bonded onto the composite (Ma and Ghasemi-Nejhad, 2005b).

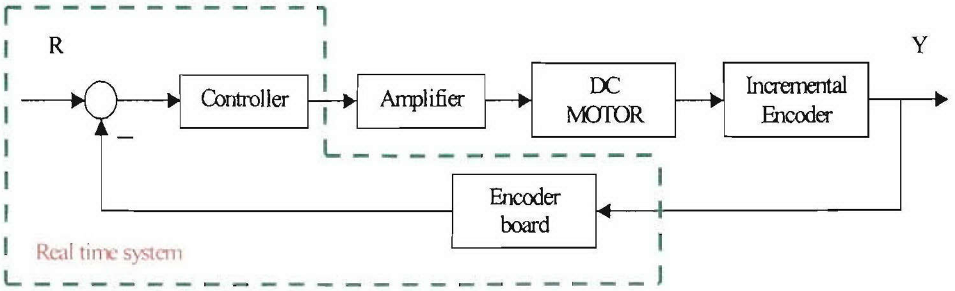

***Figure 3.12.** The ACS Motor control loop.*

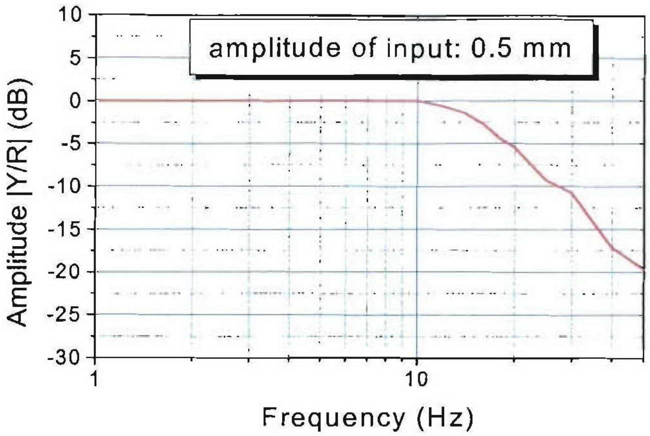

Figure 3.13. Bode plot of the ACS.

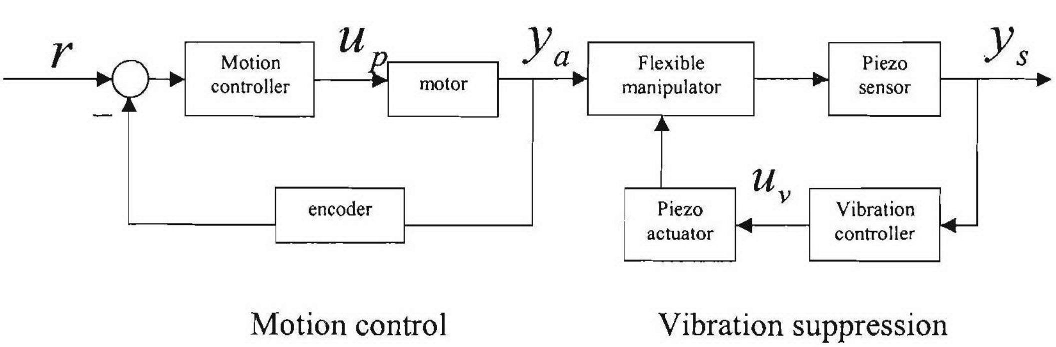

Figure 3.14. ACS control strategy.

The motion controller employed is a fuzzy logical controller (Ma and Ghasemi-Nejhad, 2005b). The Fuzzy Logic Control (FLC) is the latest development in machine intelligence that enables computers and controllers to determine a wider range of responses. Computers and controllers manipulate precise facts that have been reduced to strings of zeros and ones or statements that are either true or false, although they do not have the reasoning capability of human mind. Controllers with fuzzy logic emulate human thinking by assisting the instrument to determine responses of two values. A fuzzy logic controller is robust, operates in real time, accommodates nonlinearities, and provides the high degree of accuracy required by high-performance systems, without the need for the detailed mathematical models. It is a rule-based control scheme in which a set of so-called fuzzy rules represents a control decision mechanism to adjust the effects of certain system stimuli. The goal of the fuzzy logic control is normally to replace experienced human operator with a fuzzy rule-based system based on expert knowledge. A FLC is comprised of four primary components: (1) fuzzifier (the values of the state variables monitored during the process are fuzzified into fuzzy linguistic terms), (2) a knowledge base that contains fuzzy IF-THEN rules and membership functions, (3) fuzzy reasoning (the result of which is a fuzzy output for each rule), and (4) a defuzzification interface. A number of fuzzy sets for each of the input variables are chosen to represent the drive system under study. In the motion controller, seven input fuzzy sets and five output fuzzy sets are defined. The seven input fuzzy sets are Negative Large (NL), Negative Medium (NM), Negative Small (NS), Zero (Z), Positive Small (PS), Positive Medium (PM), and Positive Large (PL); and the five output fuzzy sets are Negative Large (NL), Negative Small (NS), Zero (Z), Positive Small (PS), and Positive Large (PL). Tables 3.1 and 3.2 list the fuzzy sets and their membership functions for the inputs and outputs of the motion controller, respectively. The defined varying ranges are [–2, 2] for the input variable and [-10, 10] for the output variable. In Tables 3.1 and 3.2, MF, GAUSS, TRAP, and TRI stand for Membership Function, Gaussian, Trapezoidal, and Triangular, respectively. Based on the IF-THEN rules mentioned earlier and the MFs given in Tables 3.1 and 3.2, the following characteristics between the input and output of the FLC were obtained (Ma and Ghasemi-Nejhad, 2005b): (1) the control signal is large (i.e., the strut moves fast) when the position error is large in order to rapidly reduce the position error; (2) as the position error becomes smaller, the control signal becomes smaller as well, but the control signal is maintained at a certain level such that it can overcome the existing friction in the strut with a certain speed to decrease the position error; and (3) the control signal is zero when the position error is zero.

The vibration controller is an independent modal space adaptive controller (IMSAC), as shown in Figure 3.15, which is based on conventional independent modal space control with new developed adaptive control scheme. Since the IMSAC vibration controller is a feedback controller and the manipulator reciprocates, the controller may become unstable after a long-time running. To avoid this situation, a switch strategy of the convergence factors is developed based on the modal damping ratio estimation. The switch strategy includes the following three steps (Ma and Ghasemi-Nejhad, 2005b): (a) sampling the modal response $y_i(t)$ and capturing its maximums designated A_1 and A_2 and the period number (N) between the maximums A_1 and A_2; (b) estimating the damping ratio of each mode using the formula shown in Equation (3.1) in which $\hat{\xi}_i$ is the estimated damping ratio of the i-th mode; and (c) switching the convergence factors according to the rules as described below. If $\hat{\xi}_i$ is greater than a desired damping ratio that represents a desired vibration attenuation, then the convergence factor μ_i is set to zero; otherwise, μ_i remains at its initial value determined experimentally. The adaptation for each mode of the structure is listed in Equation (3.2).

Table 3.1. *Input fuzzy sets and membership functions.*

Fuzzy Sets	Membership Functions
NL	GAUSS_MF (x, 0.5, -2)
NM	TRAP_MF (x, -1.95, -1.57, -1.13, -0.757)
NS	TRAP_MF (x, -1, -0.64, -0.49, -0.08)
Z	TRI_MF (x, -0.0688, 0.0265, 0.0688)
PS	TRAP_MF (x, 0.058, 0.534, 0.725, 1)
PM	TRAP_MF (x, 0.77, 1.25, 1.54, 1.98)
PL	GAUSS_MF (x, 0.5, 2)

***Table 3.2.** Output fuzzy sets and membership functions.*

Fuzzy Sets	Membership Functions
NL	GAUSS_MF (*x*, 1.8, -10)
NS	TRAP_MF (*x*, -9.34, -5, -3, -0.556)
Z	TRI_MF (*x*, -0.556, 0.082, 0.503)
PS	TRAP_MF (*x*, 1.93, 3.78, 6.06, 9.29)
PL	GAUSS_MF (*x*, 1.8, 10)

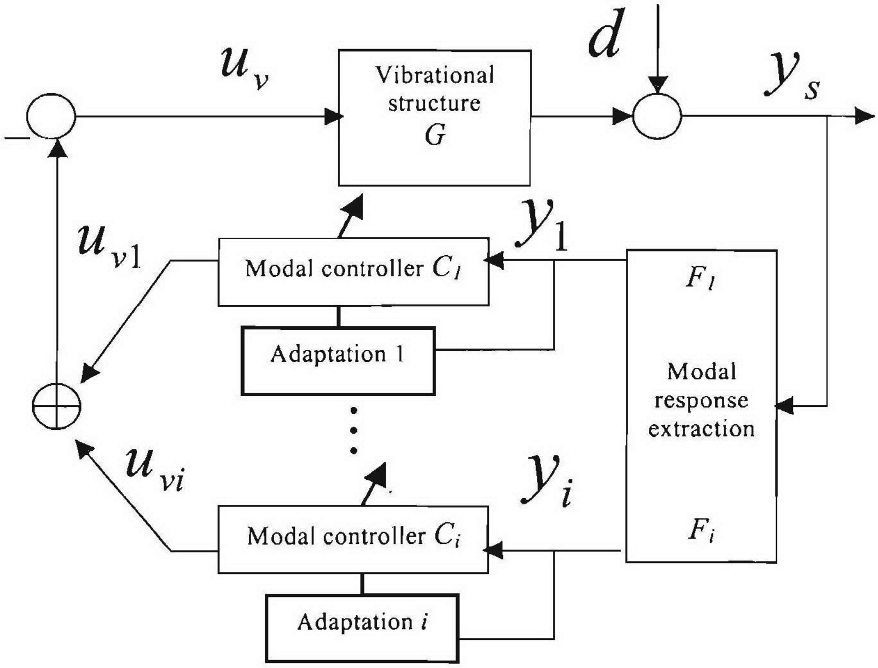

***Figure 3.15).** Independent modal space adaptive control (IMSAC).*

$$\delta = \ln (A_1/A_2)$$

$$\hat{\xi}_i = \delta (4 \pi^2 n^2 + \delta^2)^{-1/2}$$

(3.1)

$$Y_s(z) = \frac{1}{1 + G(z)\sum_i C_i(z)F_i(z)} D(z)$$

$$C_i(z, k+1) = C_i(z, k) + 2\mu_i Y_s(z, k) F_{xi}(z, k)$$

$$F_{xi}(z,k) = \frac{G(z)F_i(z)}{1 + G(z)\sum_i C_i(z,k)F_i(z)} Y_s(z,k)$$

(3.2)

The experiments are performed. The first two modes of the structure are controlled to alleviate the manipulator vibrations. The sampling rate is 1,000 Hz. The control code is programmed in Matlab-Simulink, compiled, and downloaded to the real time control system. For vibration control, two modal adaptive controllers are FIR filters with lengths of 500 each (Ma and Ghasemi-Nejhad, 2004a, 2005a, 2005b). The initial values of the coefficients of the two modal adaptive controllers are zeros. The two convergence factors for the two IMSACs are 1×10^{-5} and 1×10^{-4}.

Sample results are shown in Figures 3.16 to 3.18. Figure 3.16 shows the strut displacement and error, showing that it takes 0.2 s to move the strut from –3 mm to 3 mm and the average steady state error is 1.8 μm, i.e., the average relative steady state error is 0.06%, etc. Figure 3.17 shows the uncontrolled and controlled vibrations of the piezoelectric sensor surface-mounted on the composite beam. It takes 4.9 s and 0.83 s for the uncontrolled and controlled vibration of the piezoelectric sensor to reduce to 0.06 V of steady state error tolerance, respectively, and the damping ratio increases from 0.0018 to 0.0213. Figure 3.18 illustrates the spectra of the uncontrolled and controlled vibrations of the piezoelectric sensor. The vibration amplitudes of the first two modes of the flexible manipulator decrease from uncontrolled –16.90 dB and –28.36 dB to controlled –35.26 dB and –38.37 dB, resulting in 18.36 dB and 10.01 dB vibration reductions, respectively. Figure 3.19 shows the impulse responses of the two modal adaptive controllers (i.e., the coefficients of the FIR filters) after the adaptation is finished. It demonstrates that the predominate frequency of the first modal adaptive controller is the first modal frequency of the manipulator, and the same is true for the second modal adaptive controller. The Bode plot of the vibration controller is plotted in Figure 3.20 showing that the controller has large magnitudes at the first two modal frequencies of the manipulator and thus providing good vibration reduction at these frequencies. Table 3.3 summarizes the positioning and vibration reduction of the experimental flexible composite manipulator.

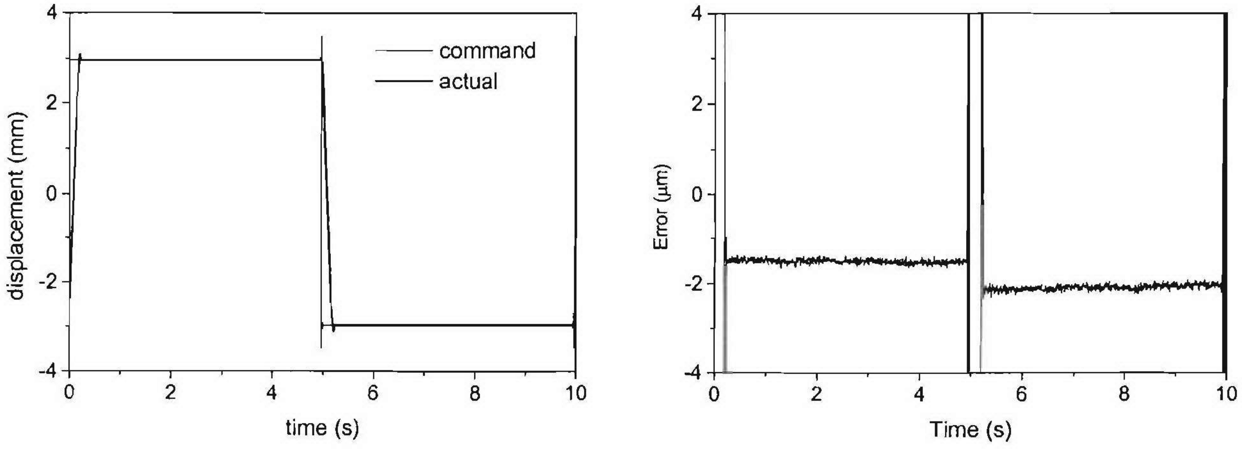

(a) position

(b) error

Figure 3.16. *Position and error of the ACS.*

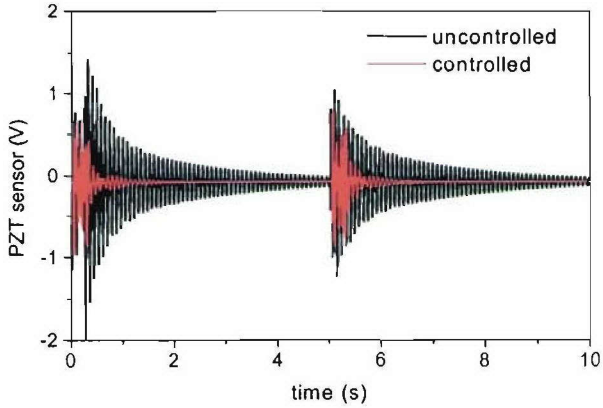

Figure 3.17. *Uncontrolled/controlled vibration of the composite beam using the piezoelectric patches one as a sensor and the other as an actuator (time history).*

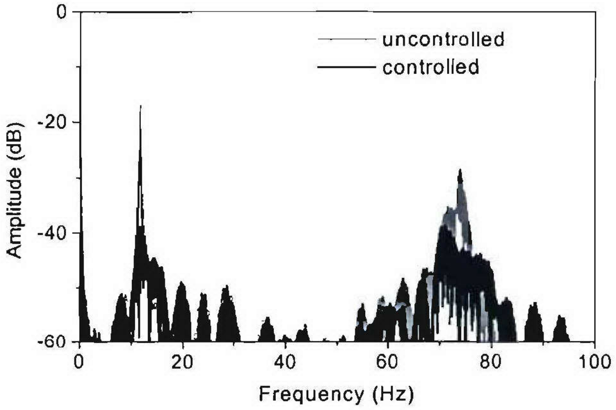

Figure 3.18. Uncontrolled/controlled vibration of the composite suing the piezoelectric sensor (spectra).

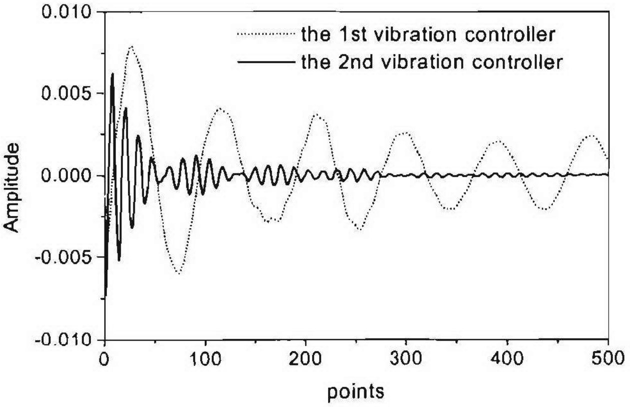

Figure 3.19. Weights of adaptive vibration control for the composite beam first two modes.

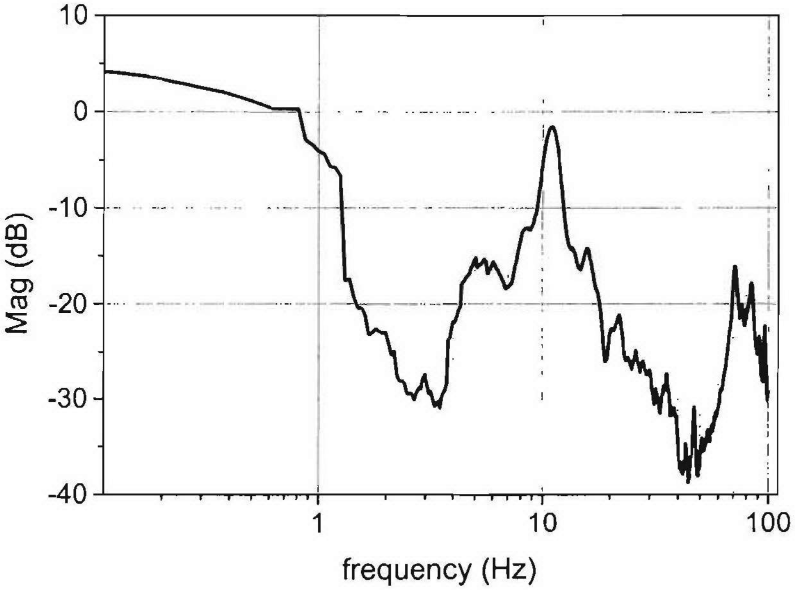

Figure 3.20. *Bode plot of adaptive vibration controller.*

Table 3.3. *Summary of PP+VS of new ACS and flexible composite manipulator.*

Motion	Steady state error (µm)			1.8	
	Relative steady state error			0.06%	
Vibration			uncontrolled	controlled	reduction
	Damping ratio		0.0018	0.0213	
	Amplitude (dB)	1st mode	-16.9	-35.26	18.36
		2nd mode	-28.36	-38.37	10.01

4. ACTIVE COMPOSITE PANELS (ACPs)

(Nejhad, Russ, Pourjalali, Ma, Yan, Sakagawa)

4.1. ACPs Design and Configurations

Active composite panels with piezoelectric patches are fundamental building-blocks for many structures (Ghasemi Nejhad, 2002). In the ADPICAS project, different panels are investigated in terms of manufacturing, location of piezoelectric patches, control schemes, and their experiments. Figure 4.1 gives ACP samples covering active composite beams, active rectangular composite plates, active circular composite plates, and active composite tubes. All of these ACPs are either with surface-mounted or embedded piezoelectric patches. The used piezoelectric patches are large-size active fiber composites (CCC, 2002) employing PZT-5A piezoelectric material and performing as extension motors. Their dimensions are 0.33 *mm* in thickness, 55 *mm* in width, and 135 *mm* in length. The composite panels are made of plain weave fabric graphite/epoxy prepreg with a ply thickness of about 0.30 *mm*. Three techniques are introduced in the ADPICAS project for embedding the active fiber composite piezoelectric ceramic patches in the ACPs and for taking the piezoelectric patch lead wires out, and they are: a) cut-out holes, b) molded-in holes, and c) embedding techniques shown in Figure 4.2 (Ghasemi-Nejhad and Poujalali, 2003; Ghasemi-Nejhad and Russ, 2003; Ghasemi-Nejhad and Pourjalali, 2005; Ghasemi-Nejhad and Russ, 2005; Ghasemi-Nejhad et al., 2005c).

(a) Beams

(b) Rectangular plate

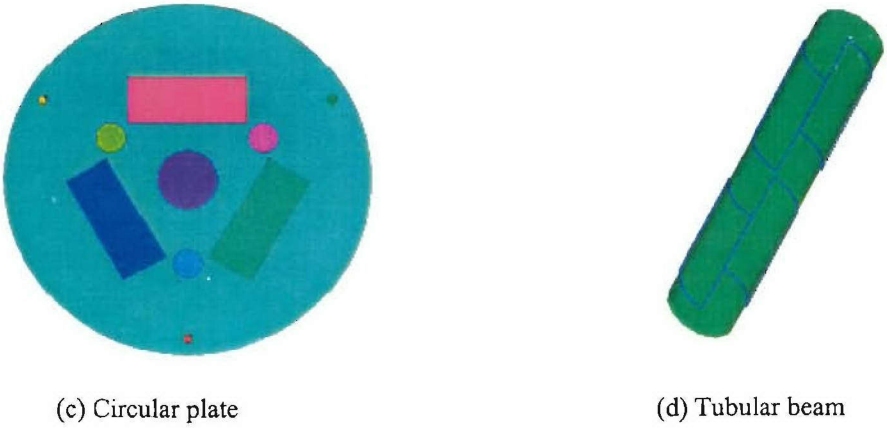

(c) Circular plate

(d) Tubular beam

Figure 4.1. *Active composite panels.*

(a) Cut-out holes (b) Molded-in holes (c) Embedding

Figure 4.2. Three techniques to take the lead wires out in ACPs with embedded piezo patches.

4.2. Manufacturing of ACPs with Embedded Active Fiber Composite Piezoelectric Patches

Active Fiber Composite (AFC) piezoelectric patches such as those shown in Figure 4.3 (CCC, 2002; MSI, 2003; Ghasemi-Nejhad et al., 2005c) were used here. Insulating materials such as Kepton tape, glass cloth electrical tape, and shrink tape were used to prevent short-circuit between the carbon fiber and the piezo patches. Plain weave graphite/epoxy composite prepregs (from Hexcel Co.) with a hand lay-up technique followed by a vacuum bagging and autoclave curing was used. The curing temperature of the composite (250° F here) should be well below the Curie temperature of the piezo patches (about 300° -350° F, here). The capacitance of the AFCs was measured before and after manufacturing to ensure consistent functionality of the AFCs. The as-received AFCs had a capacitance of 8 nF, while the capacitance of the AFCs embedded in the ACPs developed in this work varied between 6.5 and 7 nF. The difference between the capacitance measured for the as-received and embedded AFCs is believed to be due to different boundary conditions for these two cases. In addition, to avoid a possible current build-up in the piezo patch due to the high temperature manufacturing of the laminate, the leads were connected (i.e., short-circuited) during the laminate cure (Mall, 2002). Ghasemi-Nejhad and co-workers have reported on the manufacturing of the ACPs with embedded piezoelectric patches (Ghasemi-Nejhad and Poujalali, 2003; Ghasemi-Nejhad and Russ, 2003; Ghasemi-Nejhad and Pourjalali, 2005; Ghasemi-Nejhad and Russ, 2005; Ghasemi-Nejhad et al., 2005c). Here, the three technique stacking sequence are explained briefly.

Figure 4.4 shows the configuration of the embedded ACP with cut-out holes. As can be seen in this figure, the piezo patches are placed in pairs back-to-back. It should be noted that the composite layer within which the piezo patch is placed has cut-outs to the size of the piezos. These composite cut-out layers are necessary to fill the areas around the piezo patch to minimize the issues of ply drops in composites. Here, to take the wires out, the upper and lower surface layers are cut to take the wires out. Twelve layers of woven composite plies (0.30 mm thick each) were used here. Therefore, Figure 4.4 represents a plate with two pairs of back-to-back piezo patches. To obtain beams, the manufactured plates were cut to the size of the piezo patches to obtain two beams from Figure 4.4 (see Figure 4.5).

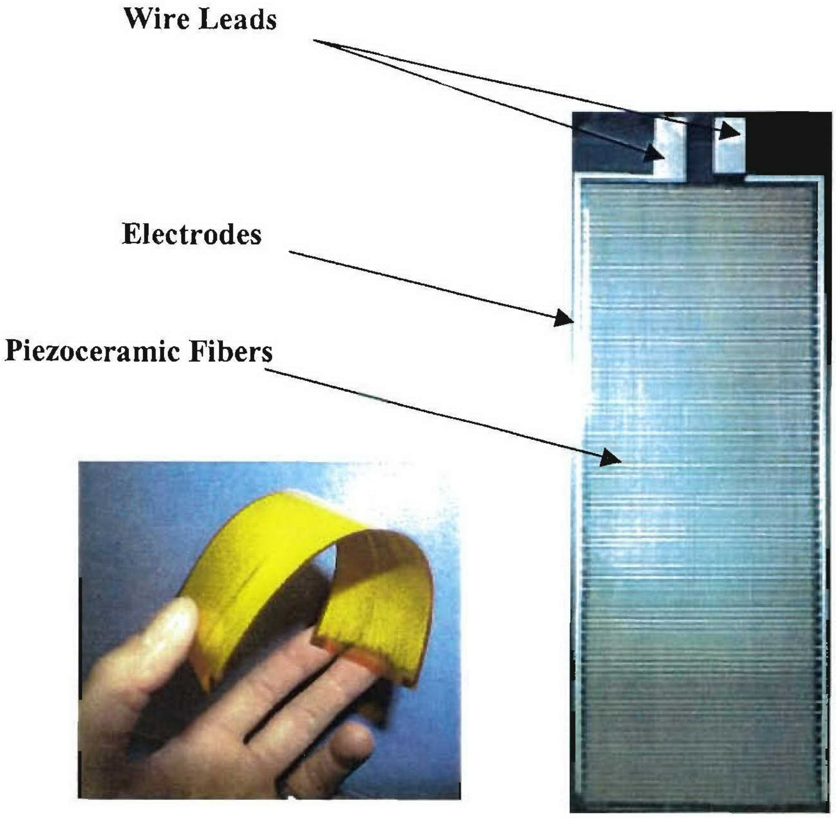

(a) **(b)**

Figure 4.3. *Active Fiber Composite PiezoFlex: a) CCC AFC (2002), b) MSI AFC (2003).*

If the piezo patches are placed near the surface as Figure 4.4, then cutting only one top and bottom layer of composite may not seriously affect the performance of the composites due to fiber end effects and stress concentrations. However, if for some reasons the piezopatches are embedded deeper into the composites, more layers have to be cut to take the wires out, and this may seriously affect the performance of the composite panel due to the fiber end effects and stress concentrations. In such cases or other reasons to be discussed later in the comparison of the three technique table, to solve such problems, either a molded-in hole or embedding technique to take the wires out are preferable (Ghasemi-Nejhad and Poujalali, 2003; Ghasemi-Nejhad and Russ, 2003; Ghasemi-Nejhad and Pourjalali, 2005; Ghasemi-Nejhad and Russ, 2005; Ghasemi-Nejhad et al., 2005c).

In the molded-in hole technique, since the composite layers are not cut to take the wires out, instead holes are gradually opened in the woven prepreg during the hand lay-up technique, the problems associate with the fiber cutting, fiber end effects, and stress concentrations have little to no effects in this case (Ghasemi-Nejhad and Chou, 1990a, 1990b). Figure 4.6 shows an AFC with wires soldered for the molded-in hole case, and Figure 4.7 shows the stacking configuration of the embedded ACP for this case. It is worth noting that while the wires can be taken out form top and bottom surfaces in case of cut-out holes, they have to come out from the top surface in case of molded-in hole due to its manufacturing requirements. Therefore, while still in Figure 4.7 the piezo patches are back-to-back, but they have been rotated 180° degrees so that the top and bottom piezo patches wires can come out from the top surface. Figure 4.8 and 4.9 show the embedded ACPs with wires out by molded-in holes. Figures 4.10 and 4.11 show the stacking sequence configuration and the manufactured embedded ACP with wires out by embedding. It should be noted that for all three manufacturing techniques proper templates should be used for proper placements of the piezo patches, the cut-outs, and the wires (Ghasemi-Nejhad and Poujalali, 2003; Ghasemi-Nejhad and Russ, 2003; Ghasemi-Nejhad and Pourjalali, 2005; Ghasemi-Nejhad and Russ, 2005; Ghasemi-Nejhad et al., 2005c).

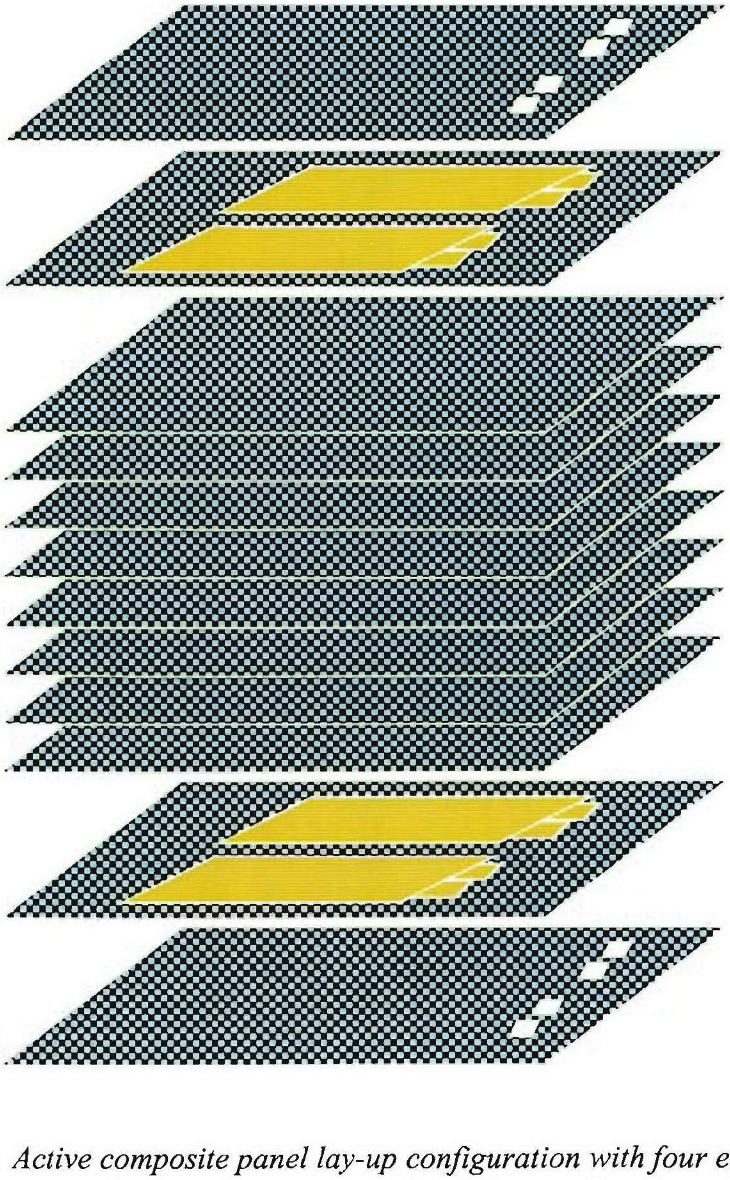

Figure 4.4. *Active composite panel lay-up configuration with four embedded AFC piezoceramic sensor/actuator patches, wires-out by cut-out holes.*

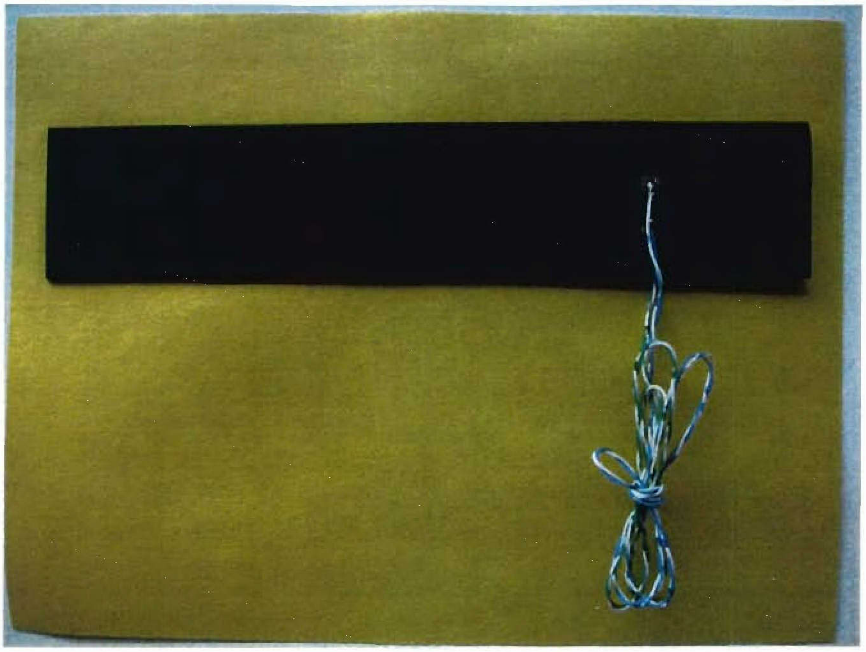

Figure 4.5. *Active composite panel with two embedded AFC piezoceramic sensors/actuators using wires out by cut-out holes technique.*

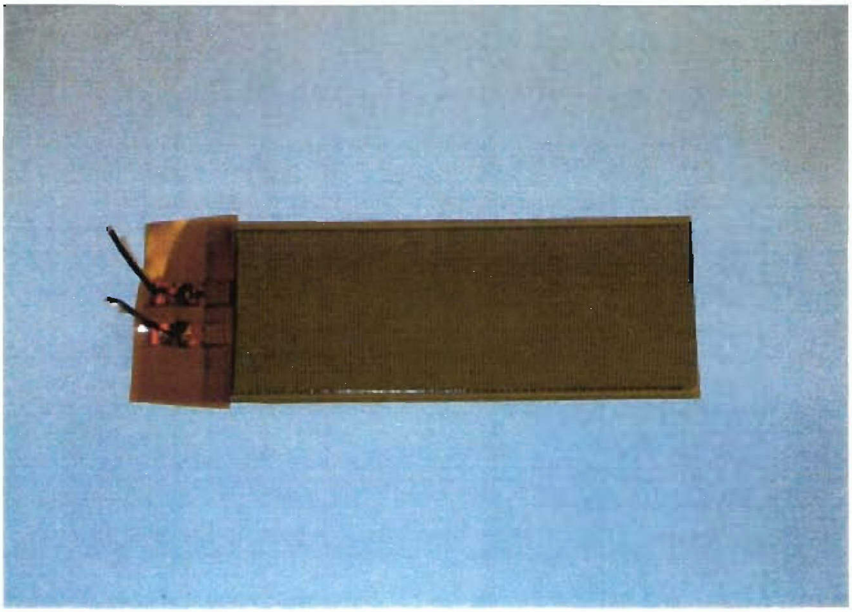

Figure 4.6. *AFC piezoceramic patch with soldered lead wires.*

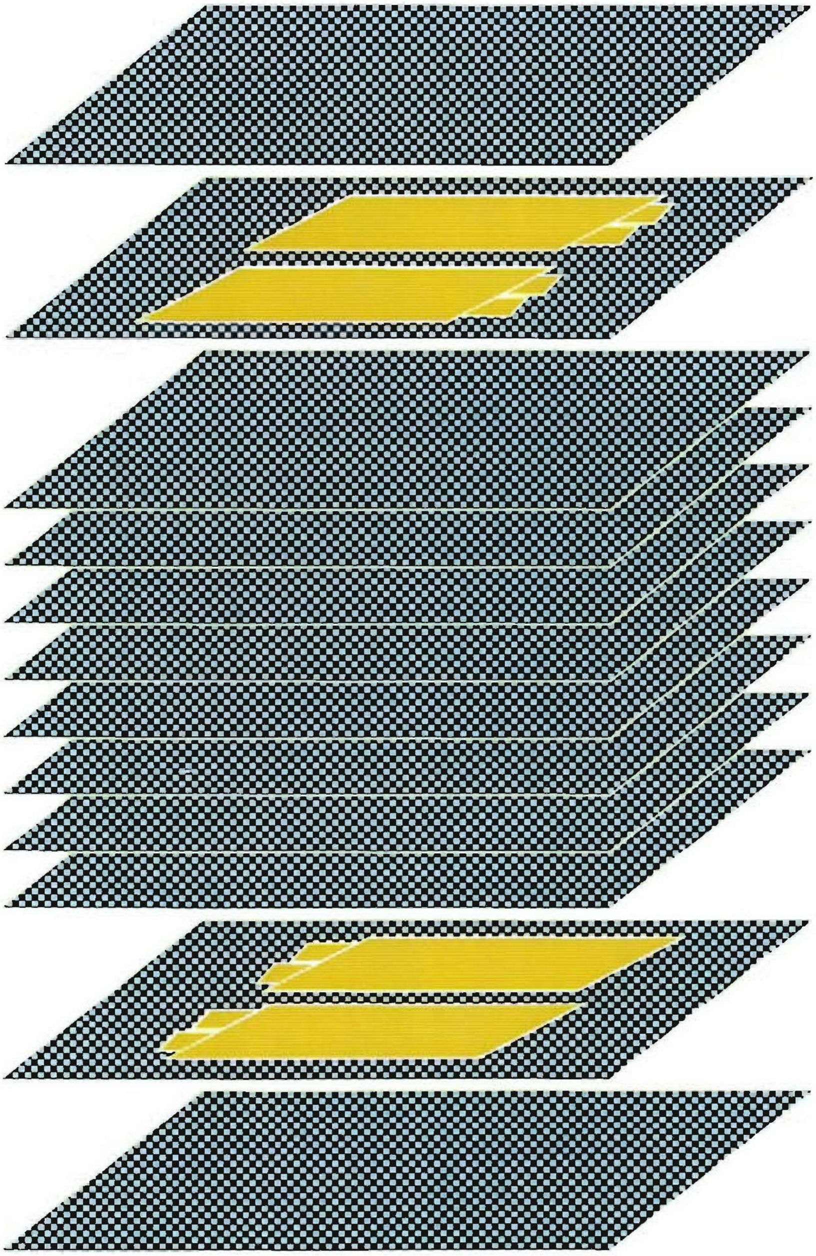

Figure 4.7. *Active composite panel lay-up configuration with four embedded AFC piezoceramic sensor/actuator patches, wires out by molded-in holes.*

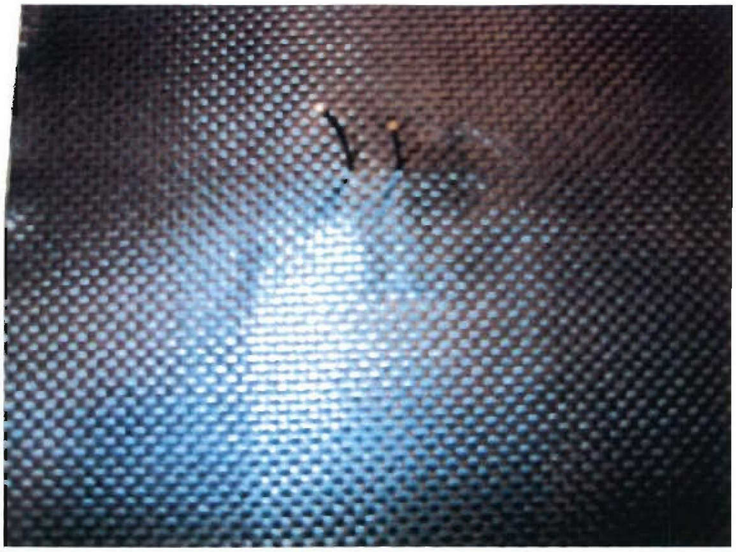

Figure 4.8. Wires out by molded-in holes.

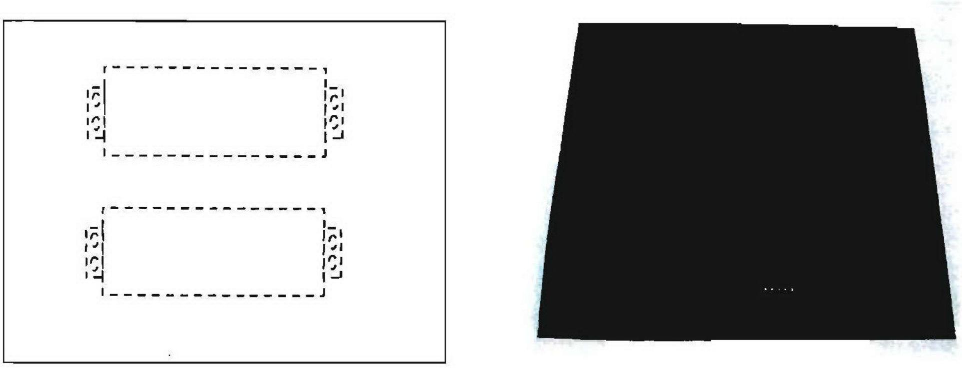

(a) (b)

Figure 4.9. ACPs for wires out by molded-in holes: a) schematic of the embedded back-to-back piezo patch sensors/actuators, b) the actual panel

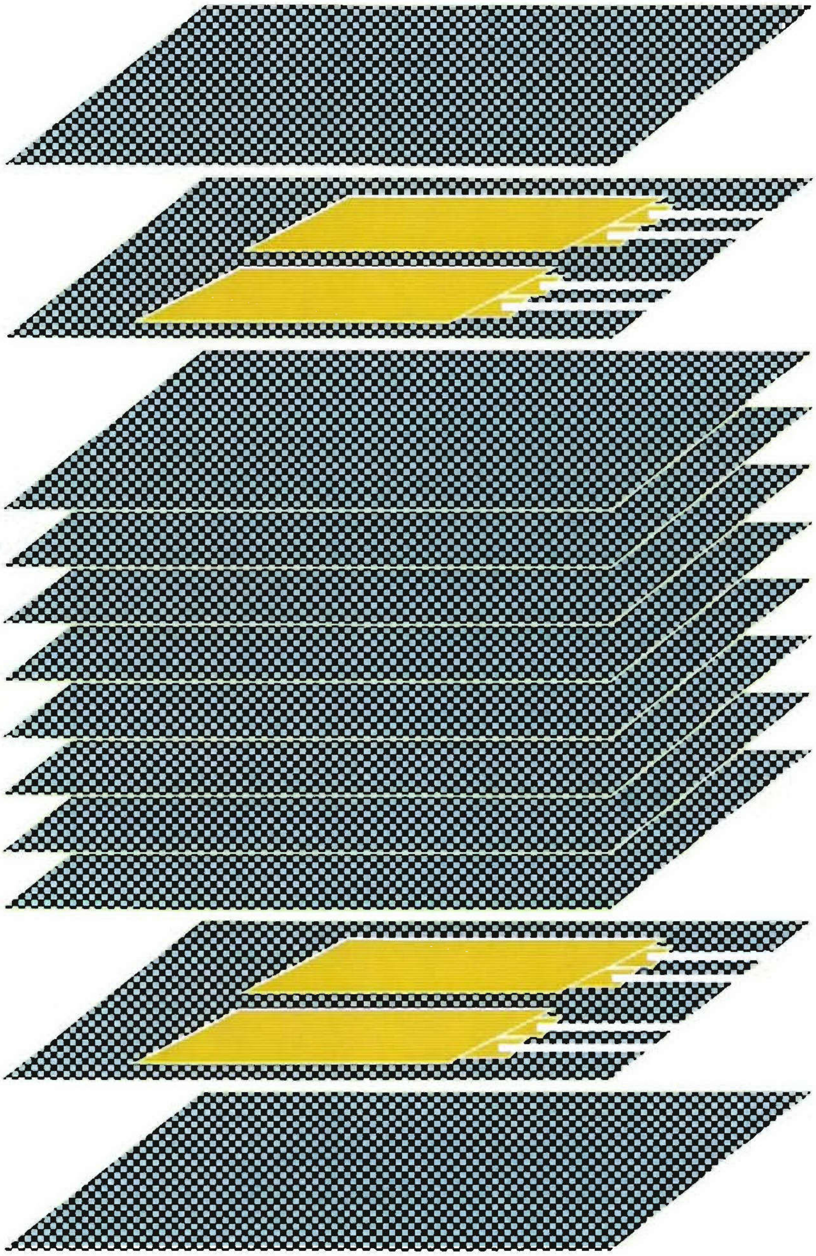

Figure 4.10. *Active composite panel lay-up configuration with four embedded AFC piezoceramic sensor/actuator patches, wires out by embedding.*

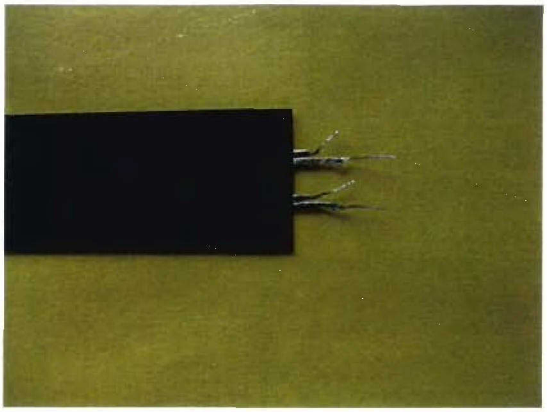

Figure 4.11. Active composite panel with embedded AFC piezoceramic patch sensors/actuators using wires out by embedding technique.

4.3. Static and Dynamics Testing of ACPs with Embedded Active Fiber Composite Piezoelectric Patches

Precision positioning of the beam tip static as well as modal and harmonic dynamic finite element analyses were performed and the results were compared with the experimental data were excellent agreements were achieved (Ghasemi-Nejhad et al., 2005c). First, the free expansion of the AFC piezo patches under the voltage application were modeled using ANSYS finite element method (FEM). These results were compared with the manufacturer's supplied experimental results, and they are given in Figure 4.12 with a very good agreement. Next, a static test set-up (see Figure 4.13) was devised to experimentally measure the beam tip displacement of the ACPs under voltage application using a laser sensor. These results were compared with the FEM results and again very good agreements were achieved (see Figure 4.14). Finally, the experimental set-up of Figure 4.13 was used again in a modal and harmonic testing and the results were compared with the FEM results for these dynamic cases and once again very good agreements were achieved. Figure 4.15 shows the results of the harmonic study. The results from the modal study were consistent with the harmonic study.

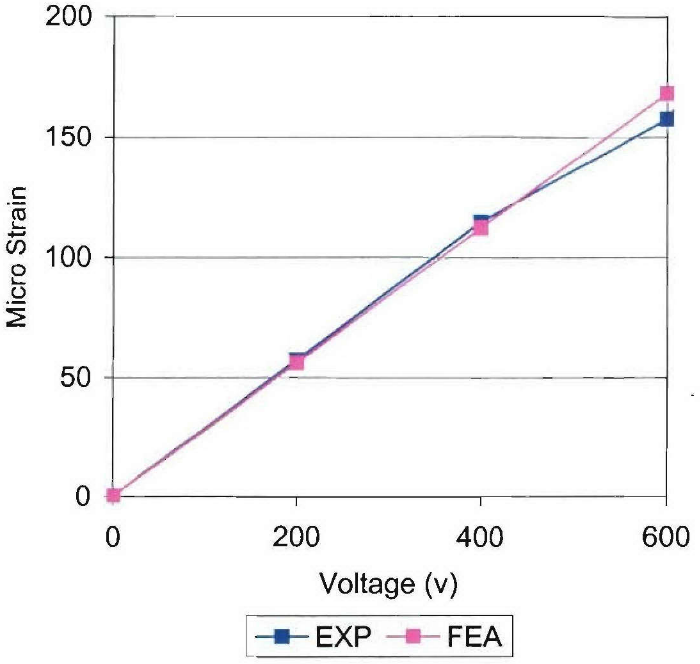

Figure 4.12. *Experimental and FEA comparison of the free extension strain of the AFC piezoceramic patch sensors/actuators as a function of applied DC voltage*

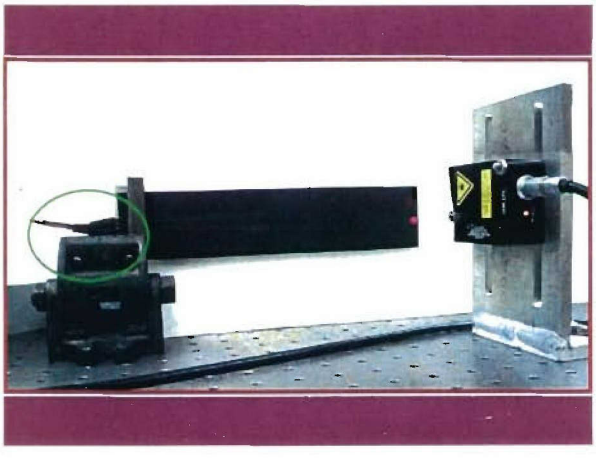

Figure 4.13. *Experimental set-up with a laser system for the beam tip deflection measurements.*

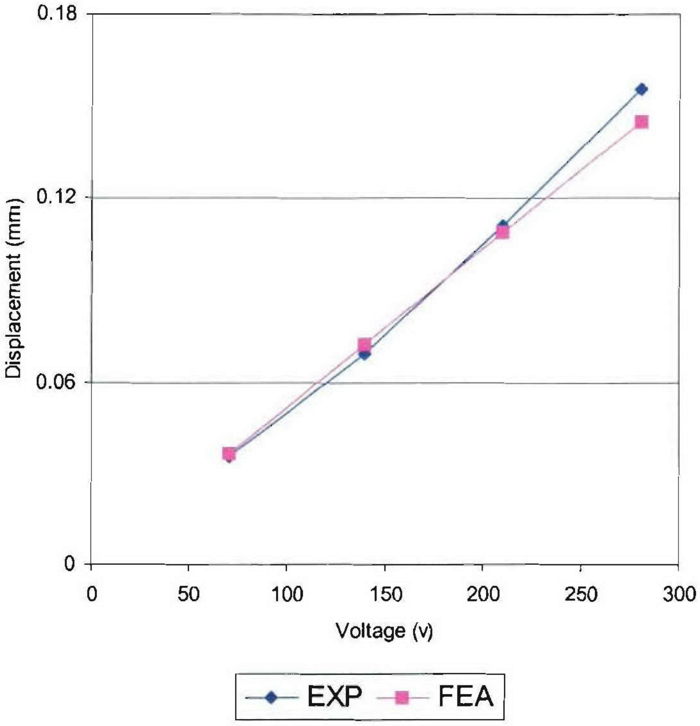

Figure 4.14. Experimental and FEA comparison of the beam tip deflection as a function of applied DC voltage

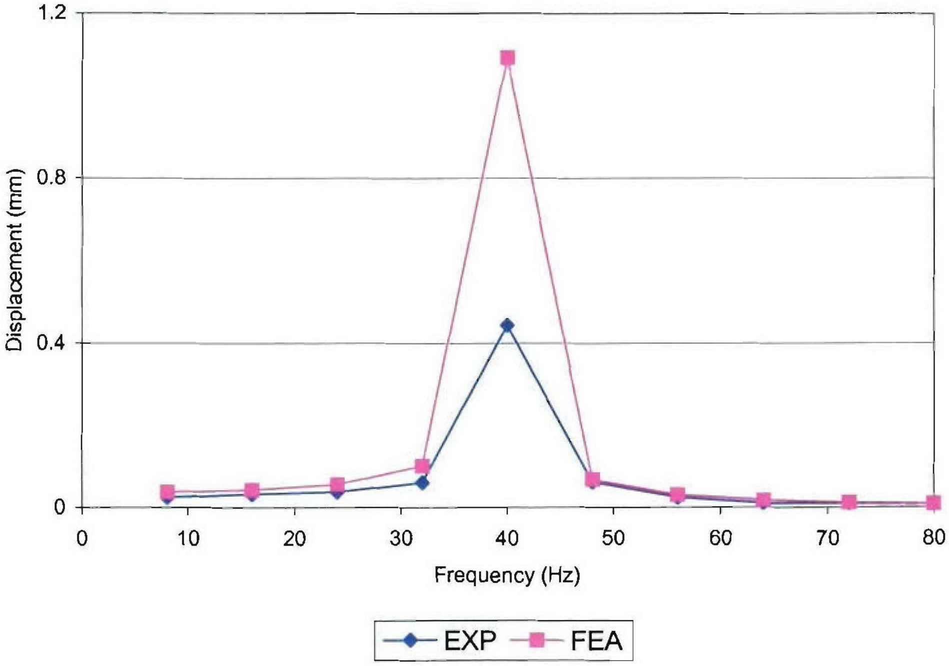

Figure 4.15. Experimental and FEA comparison of the beam tip deflection versus frequency.

4.4. ACP Adaptive Control Techniques

Four adaptive control techniques were developed for the ACPs in this work. The following explains these techniques. Figure 4.16 shows the schematics of three adaptive control algorithms; namely, adaptive feedforward control (AFC), adaptive internal model control (AIMC), and hybrid adaptive control (HAC) for simultaneous precision positioning and vibration suppression (Ma and Ghasemi-Nejhad, 2003b, 2005d). In these diagrams, $P_0(z)$ and $P(z)$ represent the impulse transfer functions of the disturbance path and control path of a controlled structure, respectively. f, y, and r are the external disturbance, the displacement of the ACP, and command, respectively. $C_v(z)$ and $C_p(z)$ are the impulse transfer functions of two adaptive feedforward controllers for vibration suppression and precision positioning, respectively, and $C_b(z)$ is the impulse transfer function of an adaptive feedback controller for vibration suppression and precision positioning. $E(z)=Y(z)-R(z)$ is defined as the tracking error between the command and the displacement at the tip of the ACP.

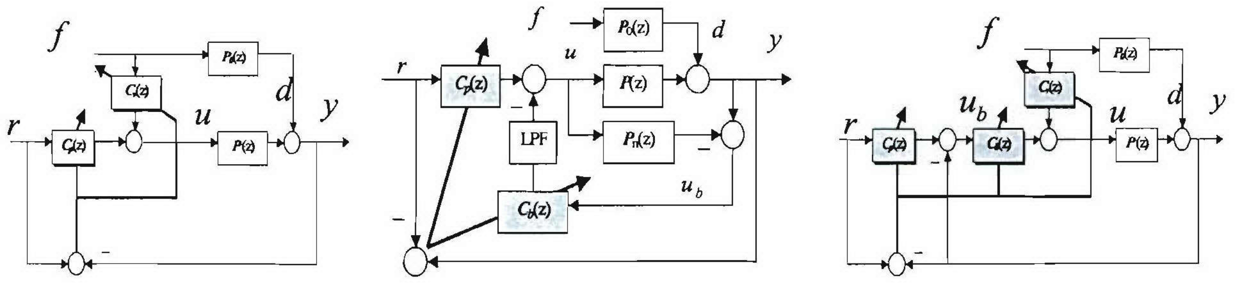

(a) AFC (b) AIMC (c) HAC

Figure 4.16. Three adaptive control schemes.

4.4.1. Adaptive Feedforward Control (AFC) (Ma and Ghasemi-Nejhad, 2002b, 2003b, 2005d)

AFC consists of two feedforward controllers, where one of them is related to the external disturbance and the other is related to the command. It is obvious that this scheme strongly depends on the external disturbance information (see Figure 4.16 (a) for the AFC block-diagram). If the disturbance can be known correctly and completely or be observed and constructed then this scheme can perform well; otherwise, a good performance is hardly achieved. The detailed adaptation algorithm of this scheme can be found in Ma and Ghasemi-Nejhad (2002b). The optimal controllers in Ma and Ghasemi-Nejhad (2002b) indicate that the tracking error will be zero if $C_v(z)=-P^{-1}(z)P_0(z)$ and $C_p(z)=P^{-1}(z)$.

4.4.2. Adaptive Internal Model Control (AIMC) (Ma and Ghasemi-Nejhad, 2003a, 2003b, 2005d)

Compared with feedforward control, feedback control can provide better performance in the case of unknown external disturbance. To achieve high precision, internal model control has been considered in structural vibration suppression and high precision mechanical systems to enhance the vibration reduction and disturbance rejection. Figure 4.16 (b) shows the block-diagram of a two-degree-of-freedom internal model control, in which $P_n(z)$ is the nominal impulse response function of the control path $P(z)$. Suppose that the nominal model $P_n(z)$ equals to $P(z)$, the signal u_b is then exactly the same as the response due to the external disturbance, i.e., the unknown external disturbance response d can be reconstructed or observed by introducing an internal model $P_n(z)$. The detailed adaptation algorithm of this scheme can be found in Ma and Ghasemi-Nejhad (2003a). The optimal controllers in Ma and Ghasemi-Nejhad (2003a) indicate that the tracking error will be zero if $C_b(z) = C_p(z) = P_n^{-1}(z)$.

4.4.3 Hybrid Adaptive Control (HAC) (Ma and Ghasemi-Nejhad, 2002a, 2003b, 2004b, 2005c, 2005d)

HAC takes advantage of both feedforward control and feedback control. It consists of a feedback controller and two feedforward controllers. The two feedforward controllers are related to the external disturbance and command to individually achieve vibration suppression and precision positioning, respectively, and the feedback controller takes care of both vibration suppression and precision positioning, as well (see Figure 4.16 (c) for the HAC block-diagram). The detailed adaptation algorithm of this scheme can be found in Ma and Ghasemi-Nejhad (2002a, 2005c). The optimal controllers in Ma and Ghasemi-Nejhad (2002a, 2005c) indicate that the tracking error will be zero if $C_v(z) = -P^{-1}(z)P_0(z)$ and $C_p(z) = 1 + C_h^{-1}(z)P^{-1}(z)$. Compared with the optimal controller of the AFC, $C_p(z)$ in HAC is not only related to the inverse of the controlled path, but also to the introduced feedback controller, giving more flexibility to the design of the feedforward controller in HAC. A frequency-weighted HAC can also be found in Ma and Ghasemi-Nejhad (2004b) that considers signal fusion of different sensors. A summary and comparison of these three adaptive control schemes can be found in Ma and Ghasemi-Nejhad (2003b, 2005d).

Figure 4.17 illustrates the experimental results of the vibration suppression (VS) only, for an active composite beam with two back-to-back surface-mounted piezoelectric patches (see Figure 4.1 (a)). The beam is clamped at its end close to the piezo patches and a laser system is used as a sensor to monitor the ACP tip displacements (one of the piezo patches can also be used as the sensor). The experimental set-up is similar to the one shown in Figure 4.13. The beam is vibrating with its first natural frequency. For AFC, the displacement at the tip of the beam decreases from uncontrolled 0.7 V to controlled 0.053 V after the control works for 20 seconds, to controlled 0.01 V after the control works for 40 seconds, and dies out along with the controller action, but the convergent process is slow. For AIMC, the uncontrolled vibration amplitude of the displacement is 0.76 V and attenuates to 0.03 V after the controller works for 0.7 seconds. For HAC, the amplitude of the displacement decreases almost to zero from uncontrolled 0.7 V after the controller works for 5 seconds.

Figure 4.18 shows the SPPVS experimental results of the active composite beam of Figure 4.17. The steady state relative errors, in Figure 4.18, for each control scheme are calculated and found to be 3.3%, 1.2%, and 0.7% for the AFC, AIMC, and HAC, respectively. Also, it can be observed that the relative error diminishes along with the control action, demonstrating the adaptation of the three adaptive control schemes.

Summarizing the experimental results, it can be seen that (a) for vibration suppression, the AFC and HAC can eventually suppress the entire vibration, the HAC generates a faster reduction, and the AIMC can provide the fastest vibration reduction but some small residual vibration still remains; (b) for SPPVS, the AFC, AIMC, and HAC sequentially produce more accurate positioning, and the HAC makes the best tradeoff between the fastness of the positioning and vibration suppression as well as the accuracy of the position. It should be mentioned that, in these control techniques, the filtered-input LMS (Least Mean Square) algorithms Ma and Ghasemi-Nejhad (2002a, 2004b, 2005c) are employed to update the controllers.

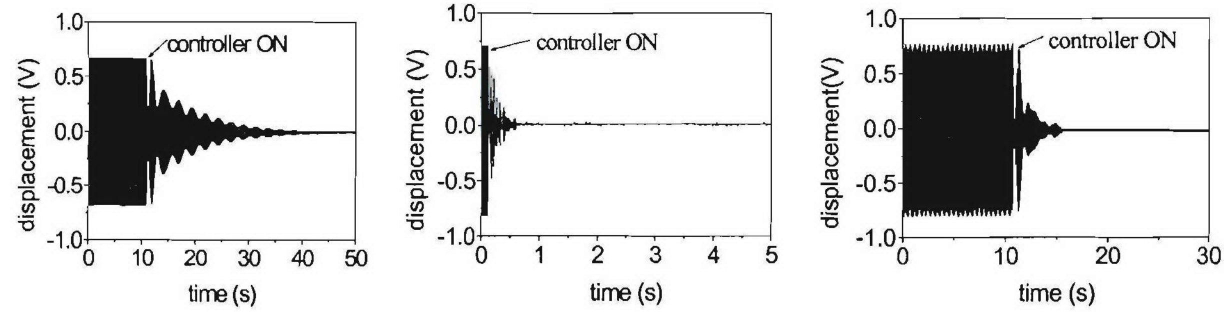

(a) AFC (b) AIMC (c) HAC

Figure 4.17. *Displacement at the panel tip of an active composite beam for VS.*

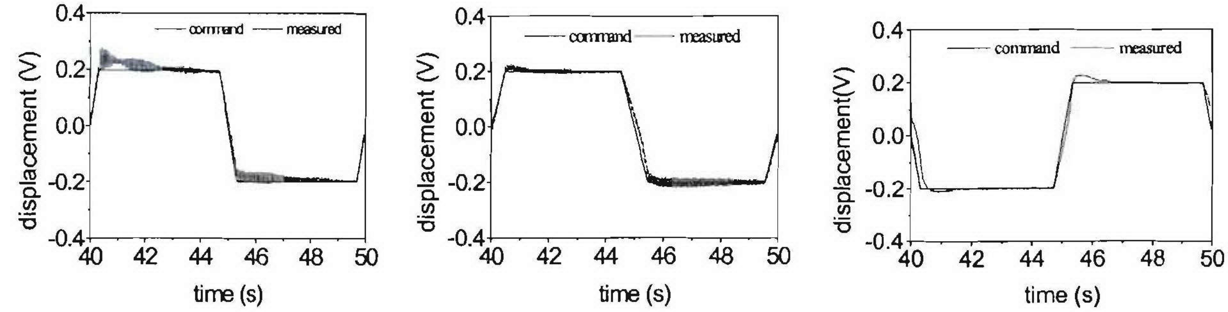

(a) AFC (b) AIMC (c) HAC

Figure 4.18. *Displacement at the panel tip of an active composite beam for SPPVS.*

4.4.4. Adaptive Disturbance Observer Control (DOB) (Yan and Ghasemi-Nejhad, 2004a)

This section introduces an Adaptive Disturbance Observer Controller for the ACP with co-located sensors/actuators as a SISO system.

Researchers have tried to use various controllers for rejecting the vibration or positioning of the intelligent systems. The typical ones are proportional integral derivative (PID) control, internal model control (IMC), feed-forward controller, independent modal space control (IMSC), linear quadratic regulator (LQR), robust control, $H\infty$ optimal control, sliding mode control, intelligent control using the neural network and genetic algorithms and so on.

The adaptive disturbance observer for simultaneously vibration suppression and precision positioning of an ACP has been adopted here. First, as to how the disturbance observer observes and rejects the vibration caused by the external disturbance is introduced here. Meanwhile, to compare the performance of the DOB, we used the internal model controller for the same task.

Internal model control (IMC) was introduced as an alternative to the classic feedback structure. The main advantage of IMC is that close-loop stability is assumed simply by choosing a stable IMC controller. Also, closed-loop performance characteristics are related directly to controller parameters, which make on-line tuning of the IMC controller very convenient. In addition, it is known that the IMC structure provides an effective framework for the analysis of the control system performance, especially for robust properties.

The basic structure of a standard internal model control system consists of P that is the plant, P_m a plant model, Q_m an IMC controller, and r is reference, e error, u control, y output, d disturbance, and ξ measurement noise. Here, it is required that both P_m and Q_m should be stable, and the plant is also assumed to be stable. From this, we can build the transfer functions from the reference, the disturbance and the measurement noise to the output.

$$y = G_{ry} \cdot u + G_{dy} \cdot d + G_{\xi y} \cdot \varsigma \qquad (4.1)$$

where

$$G_{ry} = \frac{PQ_m}{1+(P-P_m)Q_m},$$
$$G_{dy} = \frac{P(1-P_mQ_m)}{1+(P-P_m)Q_m},$$
$$G_{\xi y} = \frac{PQ_m}{1+(P-P_m)Q_m}. \qquad (4.2)$$

We can see and prove that assuming the model is perfect ($P = P_m$), and then the overall IMC will be internally stable if and only if both the plant P and the controller Q_m are stable. However, if the plant model P_m does not describe the plant P precisely, the resulting IMC system can be unstable, even when P, P_m and Q_m are stable. On the other hand, the IMC system is effectively open loop when there are no uncertainty, disturbance, and measurement noise.

The main idea of Disturbance Observer (DOB) is to estimate the equivalent disturbance by comparing the output of the real system with the output of the nominal model. The estimate is fed back as a cancellation signal, and then the whole system can behave like a nominal system. Therefore, it has been regarded as an effective tool in achieving control system robustness. The control diagram of DOB is shown in Figure 4.19.

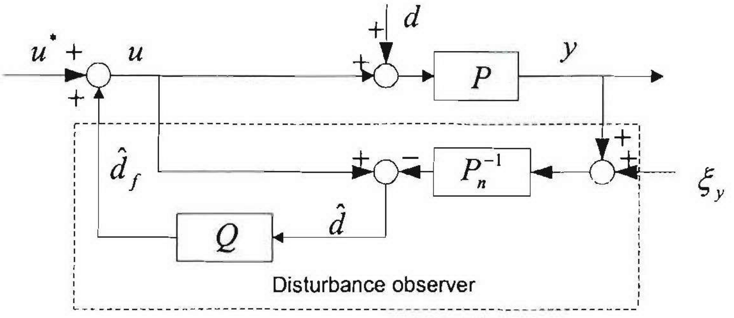

Figure 4.19. *DOB Control System*

where P is the real world system that to be controlled, P_n is the nominal model designed by the controller system designer, d is the external disturbance, u^* is the reference input of the system, u is the input of the system, y is the output of the system, ξ_y is the measurement noise, Q is the low-pass filter, $\hat{d}$ is the observed disturbance and $\hat{d}_f$ is the observed disturbance after the low-pass filter. Here Q has two functions. One is to make the inverse of the nominal model realizable; the other is to adjust the bandwidth of the DOB. Generally in mechanical systems, the nominal system is defined as two-order system. After using DOB, the low frequency disturbances are canceled and plant/model mismatch is compensated for command signals in the low frequency range. The actual system behaves as a nominal system, and this provides robustness to the control system. Through the input-output transfer function (Yan and Ghasemi-Nejhad, 2004a) for the low frequency range where $Q(s) \approx 1$ (in the bandwidth of Q) the following can be written:

$$H_{yu} \approx P_n(s), \quad H_{yd} \approx 0, \quad H_{y\xi} \approx 1 \tag{4.3}$$

This indicates that low frequency disturbances are canceled and plant/model mismatch is compensated for command signals in the low frequency range. The actual system behaves as a nominal system, and this provides robustness to the control system. For the high frequency range $Q(s) \approx 0$ (above the bandwidth of Q) the following can be written:

$$H_{yu} \approx P(s), \quad H_{yd} \approx P(s), \quad H_{y\xi} \approx 0 \tag{4.4}$$

This indicates that the sensor noise is blocked ($H_{y\xi} = 0$). But the system behaves like an open-loop system. Therefore, a sensible choice for the design of $Q(s)$ is to let the low frequency dynamics of $Q(s)$ remain close to 1 for rejection of external disturbance and model uncertainties, while its high frequency dynamics must be close to 0 for sensor noise rejection.

The performances of IMC and DOB can be evaluated by experiments. The experimental system is a cantilevered beam surfaced with CCC (2002) and ACX (2002) piezo patches. In this system, one of the CCC PZTs patched on both sides of the beam, is used as the actuator. The Laser displacement sensor with 0.001 *mm* resolution measures the displacement of the tip of the beam.

The digital dynamic analyzer caused the disturbance, and was a sinusoid curve at first natural frequency. The test set-up was similar to that shown in Figure 4.13.

First, we built the system model, which is used as the nominal system in IMC, using the sinusoid scan. The transfer function of the beam from the actuator to the laser sensor is built experimentally, and its bode compared with the real system is shown in Figure 4.20. From the bode, one can see that the experimental function is a good approximation of the real system under 110Hz. The specifications of the project require the precision positioning and vibration suppression of the beam in the frequency range of 0~100Hz. Therefore, the experimental function can be regarded as the model of real system in the lower frequency period with excellent agreement.

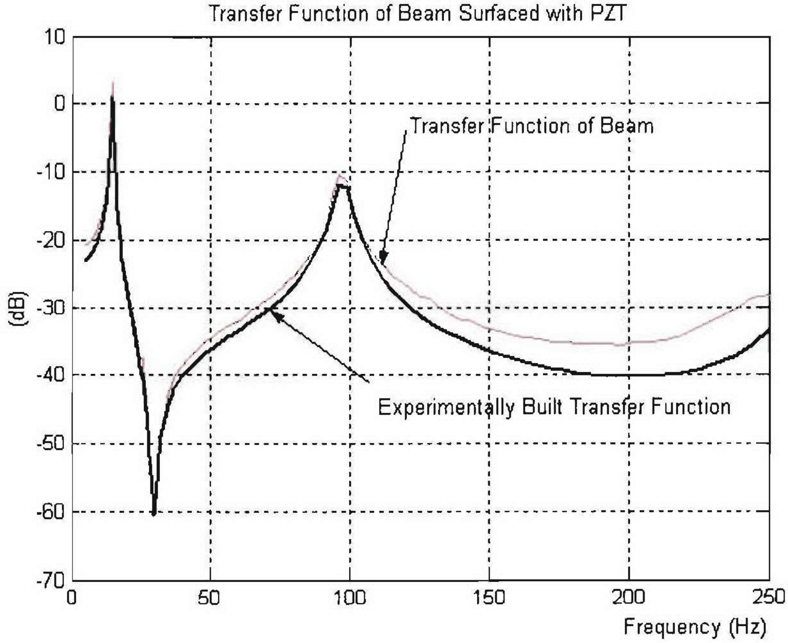

Figure 4.20. Bode Plot.

For DOB Case I, the nominal system of the DOB is designed as following:

$$G_n(s) = \frac{1}{s^2 + 100s + 10} \tag{4.5}$$

Also to make the QP_n^{-1} proper, the order of Q-filter is selected as:

$$Q(s) = \frac{1}{(\tau s)^2 + 2\tau s + 1} \tag{4.6}$$

Also, the cut-down frequency of the filter is 50Hz.

For IMC Case I:

$$P_m(s) = P(s) \tag{4.7}$$

Figures 4.21 and 4.22 show the Experimental Results of IMC and DOB for the vibration suppression of ACP for Case I and II, respectively.

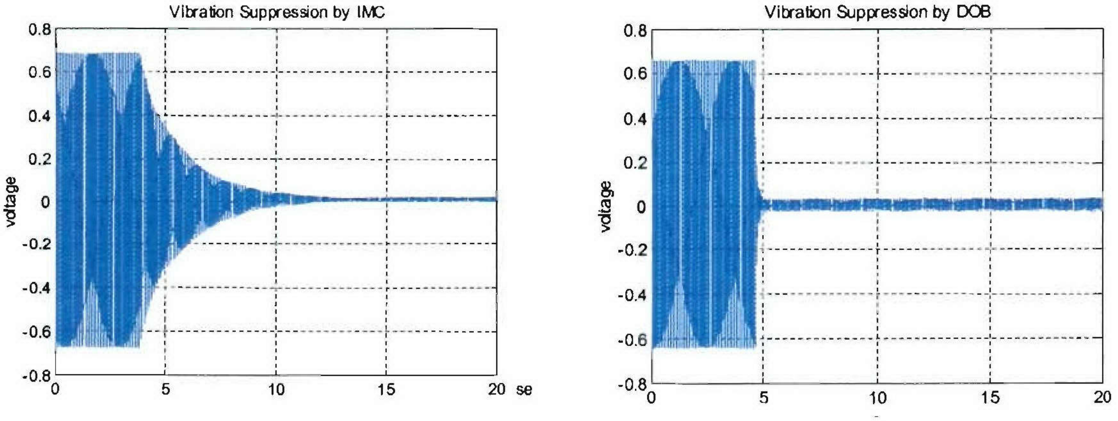

IMC DOB

Figure 4.21. *IMC and DOB Comparison of VS for ACP, Case I.*

DOB Case II:

$$P_n(s) = \frac{1}{s^2 + 20s + 100} \tag{4.8}$$

Also, Q(s) the same as Case I.

IMC Case II: $P_m(s) = 1/(s^2 + 20s+100)$

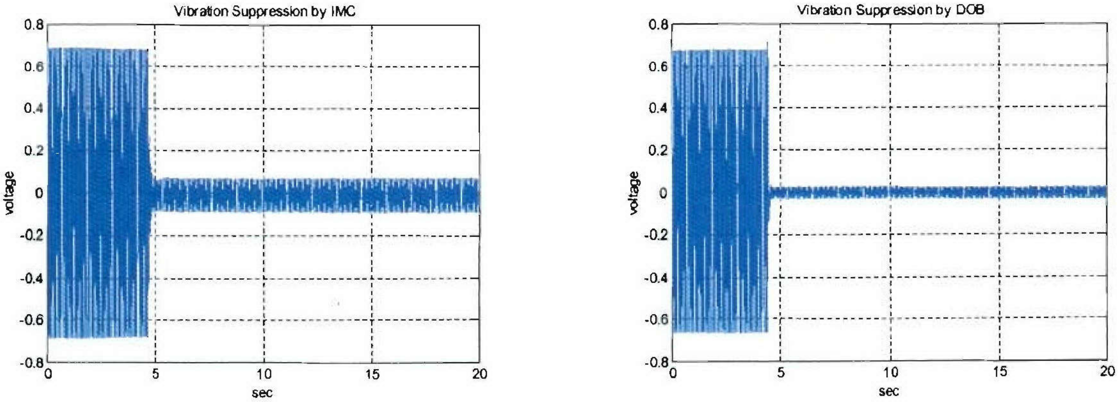

IMC DOB

Figure 4.22. *IMC and DOB Comparison of VS for ACP, Case II.*

Although IMC is simple for implementation and can successfully reject the vibration of the beam, the model uncertainties can seriously degrade the performance of IMC. While the closed-loop control system is designed by employing disturbance observer (DOB) to reject modeling uncertainties as well as the external disturbances. Disturbance observer (DOB) is robust for modeling uncertainties and can reject the external disturbances.

The design of the low-pass filter is also the most important factor in achieving disturbance. It should be designed to satisfy the following conditions:

Disturbance suppression: $|Q(j\omega)| \approx 1$ at low frequency. (4.9)

Robust stability and sensor noise suppression: $|Q(j\omega)| \approx 0$ at high frequency. (4.10)

As the output-loop controller, a non-regressor-based adaptive controller is used for the precision positioning. Because of the compromise in the design of disturbance in achieving robustness and stability and the time delay of the low-pass filter, there are some errors between the nominal model and the model achieved by the disturbance observer. Also, due to the uncertainty of the external disturbance, the nominal model defined in the disturbance observer might not reflect its correct order. The outer-loop adaptive controller compensates the error generated for the reasons listed above. Adaptive control has been widely adopted as an effective means in robotic control. However, in the case of nonlinear systems with uncertain and unknown disturbance environments such as wing of plane, space station, where system dynamics is nonlinear and time-varying, and the spatial force is uncertain and impossible to model precisely, it is very difficult to derive the traditional regressor-based adaptive controller. Recently, a great deal of efforts have been spent onto the derivation of non-regressor-based adaptive controller. One approach is to use the bound estimation method that estimates the bounds of the parameter matrices of the nonlinear dynamic system or their combinations, and then use their estimates to adjust control gains. Among them, Choi and Yuh (1996) used four bound combinations of system parameter matrices or disturbance terms as the new parameters for estimation. Their estimates were used to adjust the control gains. Figure 4.19 shows the diagram of the adaptive DOB. Two controllers were used here: PID + DOB and Adaptive DOB in the simulation and experiment on two different systems in order to check the performance of the presented controller.

Mass-spring system simulations and its experimental results show that:

1. The cut-off frequency of the low-pass filter affects the performance of DOB.
2. The performance of Adaptive DOB is much better than that of PID + DOB.
3. The performance of Adaptive DOB is not changed significantly when the cut-off frequency is changed.

On the continuum system, i.e., ACB, Figures 4.23 and 4.24, show simulated and experimental results of PID + DOB and ADOB in term of changing the cut-off frequency of the filter.

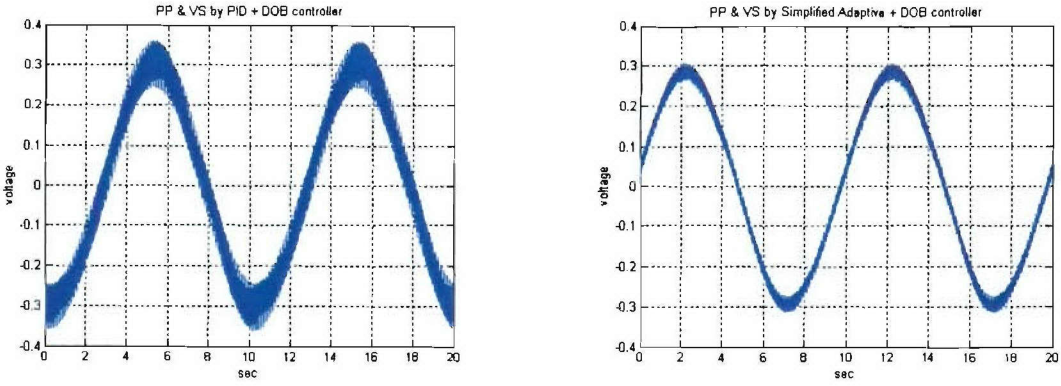

PID + DOB

Adaptive DOB

Figure 4.23. PID+DOB and Adaptive DOB Comparisons of VS + PP for ACP, Case I (τ_I=1/30).

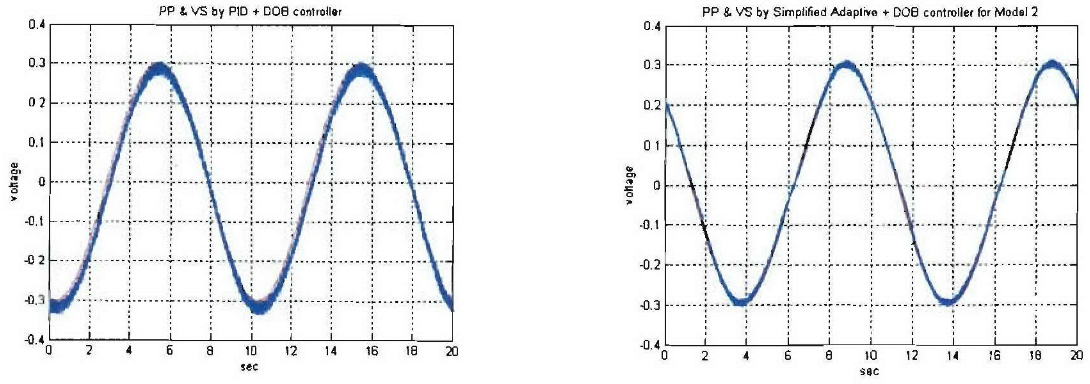

PID + DOB

Adaptive DOB

Figure 4.24.PID+DOB and Adaptive DOB Comparisons of VS + PP for ACP, Case II (τ_I=1/50).

From these results, one can see that the presented control system, i.e., the adaptive disturbance observer (ADOB) control system, is quite simple to implement, as it does not require any information about the system. The disturbance observer controller, which is used as the inner loop controller, compensates for the difference between the actual output and the output of the nominal model, and thus makes the actual system act as a nominal system. The adaptive controller that is used as the outer loop controller estimates control gains defined by the combinations of the bounded constants of parameter matrices of the nominal model. The ADOB adaptively tunes its control gains to compensate for tracking errors due to the disturbance and the low pass filter.

It is found that out of the four adaptive control techniques (i.e., AFC, AIMC, ADOB, and HAC), HAC and Frequency Weighted HAC are the most robust ones to handle a variety of cases.

4.5. Active Control Testing of ACPs with Embedded Active Fiber Composite (AFC) Piezoceramic Patches

The manufactured ACPs with embedded active fiber composite (AFC) piezoelectric patches were also tested for their vibration suppression as well as simultaneous vibration suppression and precision positioning capabilities measured at the beam tip. As explained in the previous sections, the Hybrid Adaptive Control (HAC) (Ma and Ghasemi-Nejhad, 2002a, 2003b, 2004b, 2005c, 2005d) technique was the best technique to perform simultaneous vibration control and precision positioning for the ACPs. Therefore, the HAC was employed and applied to the ACPs manufactured in this work using the three presented techniques for embedding the AFC piezoceramics for simultaneous vibration suppression and precision positioning tests. The following briefly explains the HAC technique.

Hybrid Adaptive Control (HAC) employed here is a combination of adaptive feedforward control and adaptive feedback control. The control scheme takes advantage of two adaptive feedforward controllers and an adaptive feedback controller to achieve vibration suppression as well as simultaneous precision positioning and vibration suppression of the active composite panels. One adaptive feedforward controller affects vibration suppression and the other affects the precision positioning. The feedback controller contributes to both vibration suppression and precision positioning. The combined adaptive feedback/feedforward control technique possessing the advantages of both feedback and feedforward control schemes was studied in active vibration control of smart rotor blades and beams with surface-bonded piezoelectric patches (Ma et al., 2000). The feedback part was fixed in those applications, and hence the adaptability of the controller came from its feedforward part. Saunders et al. (1996) considered the combination of DLQG-DM feedback control with adaptive feedforward control. Tseng et al. (1998) used the estimated disturbance response as the reference signal and suggested an optimization to compromise between the optimal weights of the feedforward part and the robust stability of the feedback part of the combined controller, concluding that a practical combined feedback-feedforward system could be a fixed feedback controller plus an adaptive feedforward controller. The following presents the functionality of the manufactured ACPs with embedded AFC PZTs for their vibration suppressions as well as simultaneous vibration suppression and precision positioning capabilities, employing the Hybrid Adaptive Control (HAC) technique.

4.5.1. Active Control Experiments of ACPs with Embedded AFCs PZTs

To demonstrate the vibration suppression as well as simultaneous vibration suppression and precision positioning capabilities of the manufactured ACPs, set-ups similar to those explained and showed in Figure 4.13 was used and are shown in Figures 4.25 through 4.27 for the three AFC PZT patch embedding techniques developed in this work. In these figures, the manufactured ACPs also have a surface-mounted ACX (2002) monolithic piezoelectric patch (behind the panel and near the clamped end) that functions as a controllable disturbance source in these experiments. All ACP beams developed in this work have two back-to-back AFC piezoceramic patches that one can function as a sensor and the other as an actuator. This is a straight-forward control approach since the information from one can easily be fed into another for the control purposes. Here, a more general control approach is used where the tip deflection data are found using a laser displacement sensor (explained earlier) and used for the control purposes. Hybrid Adaptive Control (HAC) was employed for the precision positioning and vibration control of the manufactured ACPs. Figures 4.28 through 4.30 show the vibration control of the ACPs. In the initial portions, the beams are vibrated by the surface-mounted ACX piezoelectric patch up to about 2.5, 5, and 2 seconds for Figures 4.28, 4.29, and 4.30, respectively, when the controller is turned on to actively suppress the vibration using the embedded Active Fiber Composite. Figures 4.31 through 4.33 show the simultaneous vibration control and precision positioning of the ACPs employing HAC. In these figures, the ACPs are vibrated by the surface-mounted ACX piezoelectric patch similar to Figures 4.28 through 4.30. Then, HAC is employed to suppress the vibration as well as position the tip of the beams based on a pre-determined path (called COMMAND in Figures 4.31 through 4.33), using the embedded Active Fiber Composite. The actual path taken by the beam tip (while the vibration is also suppressed) is called PRACTICAL in Figures 4.31 through 4.33.

4.5.2. Comparison of the Processing-Performance of the ACPs with Three AFC PZT Patch Embedding Techniques

Three techniques are introduced and explained in this work to embed piezoelectric patch Active Fiber Composites (AFCs) as sensors and actuators in composite structures: 1) wires-out by cut-out holes, 2) wires-out by molded-in holes, and 3) wires-out by embedding. Each AFC embedding technique has its own pros and cons, which are discussed here based on six criteria: 1) Manufacturing, 2) Complex Shape, 3) Structural Performance, 4) Durability, 5) Repairability, and 6) Dynamic Performance. Table 4.1 gives a summary of these qualitative comparisons. In this table, the three AFC embedding techniques are rated versus the six above-mentioned criteria, with "1" being the best and "0" being the worst, and are further explained in the following.

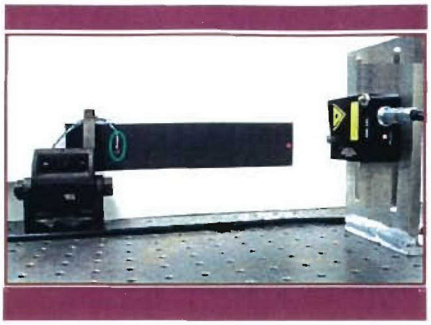

Figure 4.25. *Experimental set-up for precision positioning and vibration control for ACPs with cut-out hole wires-out.*

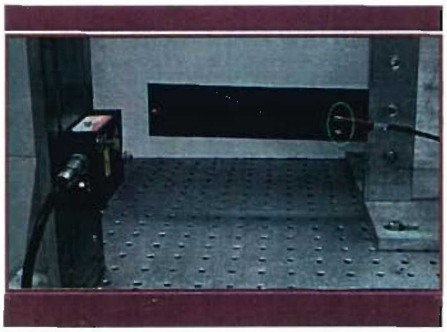

Figure 4.26. *Experimental set-up for precision positioning and vibration control for ACPs with molded-in hole wires-out.*

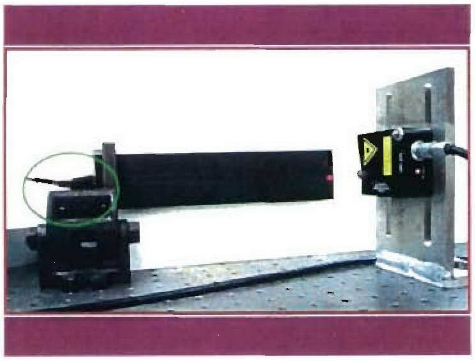

Figure 4.27. *Experimental set-up for precision positioning and vibration control for ACPs with embedding wires-out.*

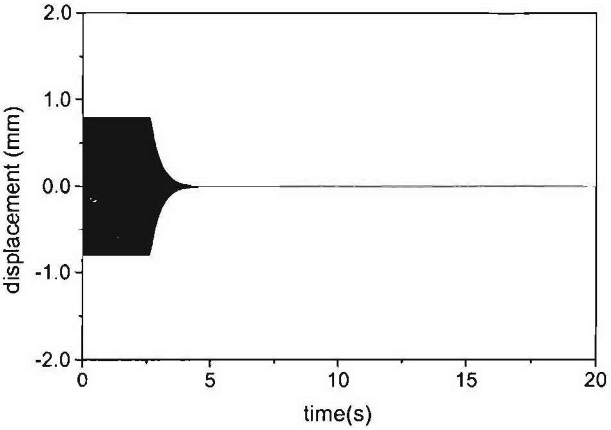

Figure 4.28. *Vibration control for the manufactured ACP of Figure 4.25 employing HAC.*

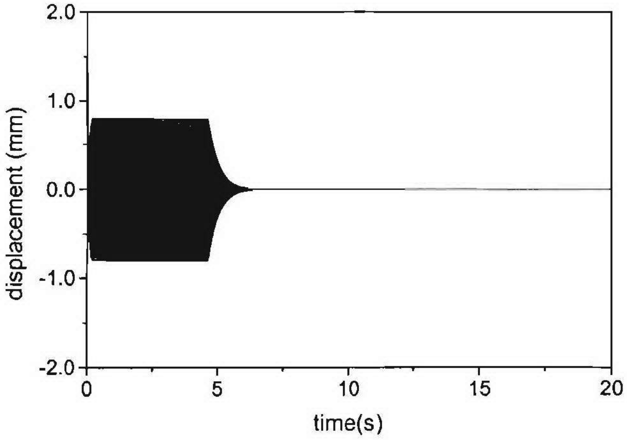

Figure 4.29. *Vibration control for the manufactured ACP of Figure 4.26 employing HAC.*

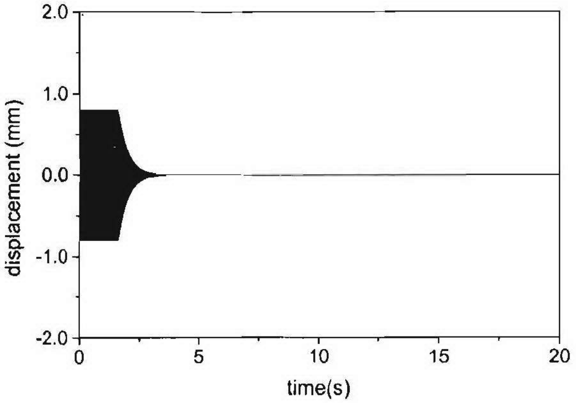

Figure 4.30. *Vibration control for the manufactured ACP of Figure 4.27 employing HAC.*

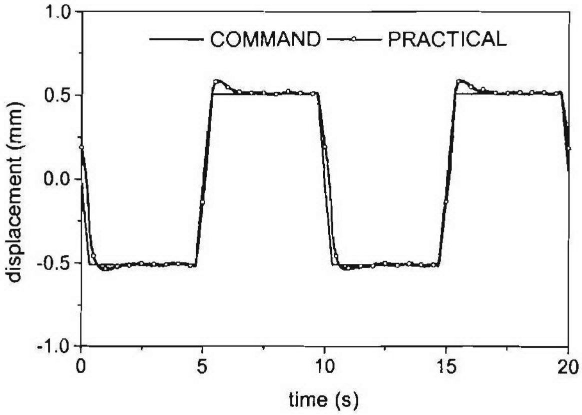

Figure 4.31. *Simultaneous vibration control and precision positioning for the manufactured ACP of Figure 4.25 employing HAC.*

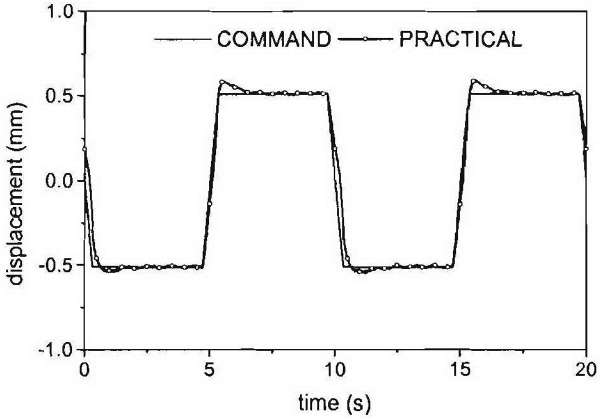

Figure 4.32. *Simultaneous vibration control and precision positioning for the manufactured ACP of Figure 4.26 employing HAC.*

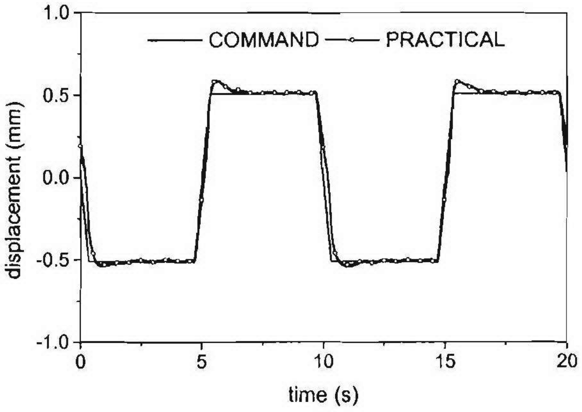

Figure 4.33. *Simultaneous vibration control and precision positioning for the manufactured ACP of Figure 4.27 employing HAC.*

Table 4.1. Comparison of the three AFC embedding techniques.

	Cut-out Hole	**Molded-in Hole**	**Embedding**
Manufacturing	1	0	1
Complex Shape	1	1	0
Structural Performance	0	1	1
Durability	0	0	1
Repairability	1	0	0
Dynamic Performance	0	0	1
Total/6	**3/6**	**2/6**	**4/6**

4.5.2.1. Manufacturing

Manufacturing of ACPs with embedded piezoelectric sensor and actuator patches is easier when the wires exit the panel by cut-out holes or embedding as compared with the molded-in holes. The molded-in hole process is more time consuming. While, the overall time of the lay-up does not increase substantially for cut-out hole and embedding technique as compared with laminates without embedded sensors and actuators, this time increases substantially for the molded-in hole technique. Therefore, both the cut-out hole and embedding techniques receive "1" and the molded-in hole technique receives "0" in this category.

4.5.2.2. Complex Shape

If the manufactured ACPs with embedded piezoelectric sensor and actuator patches need further edge cutting and machining to give geometries with more complex shapes, then the wires in the wires-out by embedding technique will be cut and post-wiring operations can be time consuming and costly. However, these problems do not exist for the other two techniques. As a result, both the cut-out hole and molded-in hole techniques receive "1" and the embedding technique receives "0" in this category.

4.5.2.3. Structural Performance

Since the cut-out hole technique causes fiber cuts and discontinuity, and hence introduces the fiber end effects and stress concentrations, it reduces the structural performance (Ghasemi-Nejhad and Chou, 1990a, 1990b), and receives "0", while the molded-in hole and embedding techniques do not have similar effects, and hence receive "1".

4.5.2.4. Durability

Since the location of the solder joint is embedded in the embedding technique, it is not subject to fatigue due to motion of the wires, and it receives "1". In the cut-out and molded-in hole techniques, the soldering location is subject to bending and fatigue due to wire motions, and hence receive "0".

4.5.2.5. Repairability

In the case of a failure of the solder joint, only the cut-out hole technique allows for repairs and thus receives "1". Hence, the molded-in hole and embedding techniques receive "0".

4.5.2.6. Dynamic Performance

In both the cut-out and molded-in hole techniques, the wires are taken out from the surface of the panel where the weight of the attached wires can interfere with dynamic performance, and hence receive "0". In case of the embedding, the wires are taken out from the edge and their influences on the dynamic performance are minimized, giving it "1" in this category.

4.5.2.7. Closure

Therefore, the total rating of the three techniques from Table 4.1 is 1) Embedding: 4/6, 2) Cut-out holes: 3/6, and 3) Molded-in holes: 2/6. It should be noted that the final selection of an embedding technique, in general, depends on the application which dictates various weighting factors for various criteria mentioned in Table 4.1. Therefore, the decision making matrix should be built based on Table 4.1 with the inclusion of the weighting factors to arrive at the best embedding technique for a particular application. It should be mentioned that the static, dynamic, vibration suppression, and the simultaneous vibration suppression and precision positioning performances of the manufactured ACPs using the three embedding techniques introduced here were the same for all practical purposes (see Figures 4.25 through 4.33). Patent applications are pending (Ghasemi-Nejhad and Pourjalali, 2005; Ghasemi-Nejhad and Russ, 2005) for the three techniques for the ACPs with embedded AFC PZT patches as sensors and actuators developed and introduced in the ADPICAS project.

4.6. Design and Optimization of the MSP Top Circular ACP

This section addresses the issues related to the design and optimization of the circular top device-plate ACP in terms of piezoelectric patch location and configuration as well as plate thickness employing (a) Genetic Algorithm (GA) in combination with analytical and Finite Element Modeling (FEM) as well as control algorithms such as LQR and DOB, and (b) the Vibration Suppression Schemes (VSS) developed in the ADPICAS project and explained in details in Section 2.

4.6.1. Optimization of the Circular ACP Using Analytical, FEA, and LQR Control

This section utilizes analytical, numerical, and control techniques to optimize the location and configuration of the AFC PZT patch locations on the top device-plate circular ACP.

4.6.1.1. Modeling

In the literature, the modeling methods are genetically categorized in two types. One modeling method, such as the Rayleigh-Ritz method (e.g. see Yan and Ghasemi-Nejhad, 2003), is based on the known analytical shape functions of smart structures. Using this method, the inertia and stiffness of actuators/sensors can be included in the model. Previous applications showed that this method was efficient and practical for simple structures, such as beams and rectangle plates, for which the analytical shape functions were available. For complex structures, most researchers assumed that piezoelectric actuators did not influence the dynamic characteristics of the structures. Therefore, the model of structures was built using the Finite Element Method (Piefort, 2000) without considerations of the location changes of actuators. In fact, this assumption is not always guaranteed because the inertia and stiffness of actuators are not the same as those of structures. Therefore, here, we developed a new more efficient and computationally less expensive approach to model a complex structure embedded or surfaced with piezoelectric actuators/sensors with various boundary conditions for the purpose of optimizing actuator configurations.

Figure 4.34.a shows such kind of the special case, the irregular panel with antisymmetric boundary conditions, that is, the top plate of the University of Hawaii Platform (UH Plateform) (Ghasemi-Nejhad and Doherty, 2002). Figure 4.34.b is the Adaptive Circular Composite Plate. It is assumed that the ACCP is synthesized of six layers of W3F 282 42" F593 graphite/epoxy plain weave fabric prepreg. The diameter of the ACCP is 0.42 meters and the thickness is 0.0024764 meters. It is assumed that there are one central joint support and three simply supports for the connection of the platform struts, as the boundary conditions.

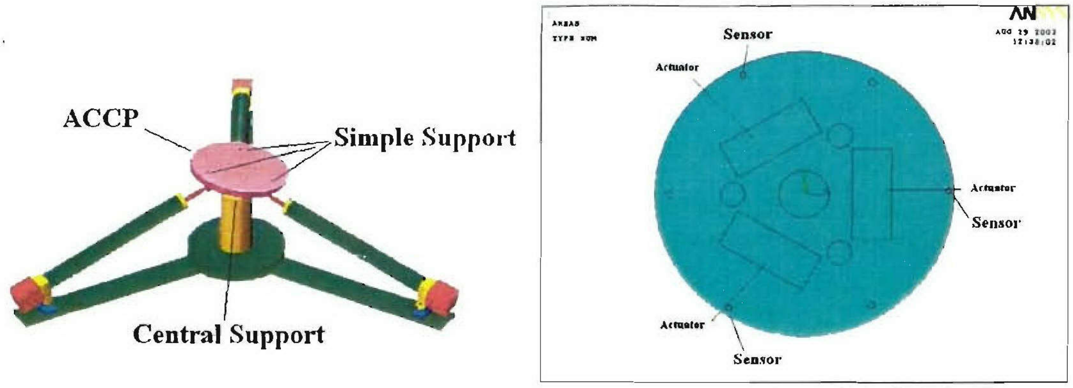

Figure 4.34. *(a) UH Platform.* ***Figure 4.34.*** *(b) Adaptive circular composite plate.*

Two modeling methods are proposed in this part of the study.

4.6.1.1.1. Modeling Method I

Harmonic response analysis from ANSYS FEA is a technique used to determine the steady-state response of a linear structure to loads that vary sinusoidally (harmonically) with time. The idea is to calculate the structure response at several frequencies and obtain a graph of a response quantity versus frequency. Using the harmonic analysis from ANSYS FEA, we could also obtain the frequency response of the ACCP from one actuator to certain node, shown in Figure 4.35.

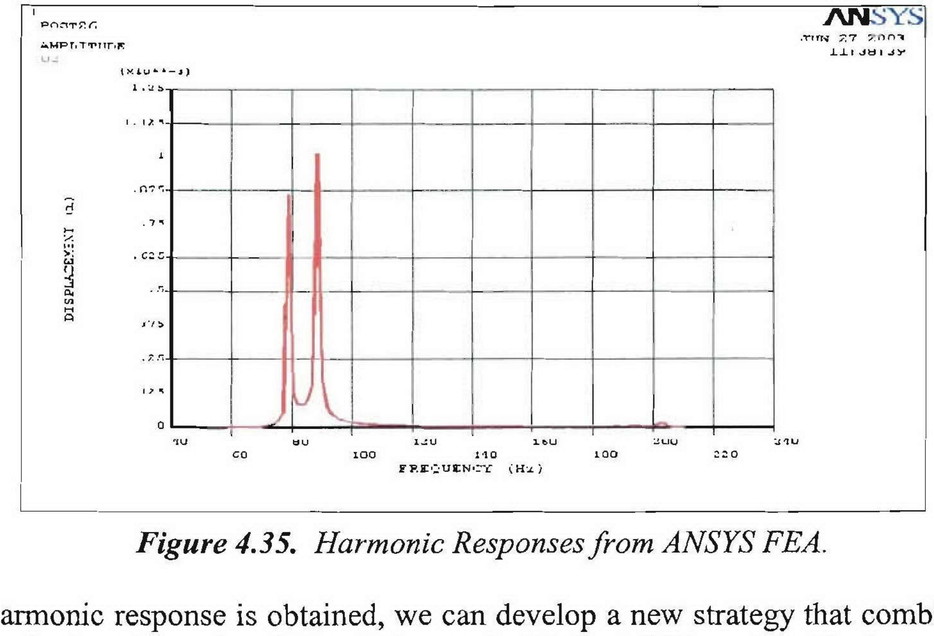

Figure 4.35. *Harmonic Responses from ANSYS FEA.*

Once the harmonic response is obtained, we can develop a new strategy that combines the FEM and the transfer function estimation technique to build the ACCP model. The harmonic response analysis of FEA can be employed to transfer the harmonic response values from meter into decibel, to build the transfer function in terms of the zero-pole-gain type for different actuators configurations. The poles, the denominator roots of the transfer function between actuators and the sensors, are consistent with the natural frequencies of the system. The zeros, the numerator roots of the transfer functions, are derived from the harmonic response analysis of FEA. Due to the 8 possible actuator configurations, a total of 78 transfer functions between three actuators and three sensors are estimated for the ACCP. Figure 4.36 shows the comparison of the estimated transfer function with the ANSYS FEA harmonic response, which demonstrates a very good estimation of the transfer function. Also, we noted that not all of the first three modes could be monitored when the actuator configuration is changed.

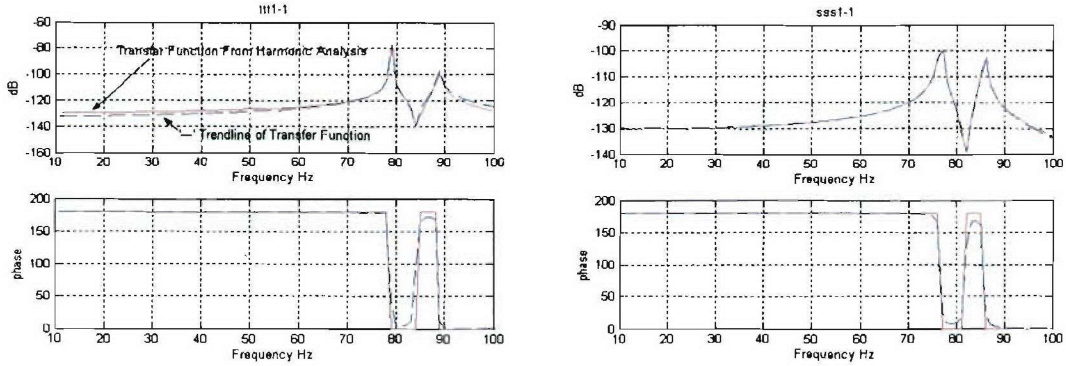

Figure 4.36. Harmonic responses from Transfer Function Estimation Technique and FEA.

Since the transfer functions from each actuator to each sensor have been obtained using the transfer function estimation technique, the whole system will be built as the three-input-three output system as given in Equation (4.11).

$$H_{TTT} = \begin{bmatrix} H_{11} & H_{12} & H_{13} \\ H_{21} & H_{22} & H_{23} \\ H_{31} & H_{32} & H_{33} \end{bmatrix} \tag{4.11}$$

where, H_{ij} is the transfer function from the ith sensor to the jth actuator.

4.6.1.1.2. Modeling Method II

When we tried to investigate the dynamic characteristics of the circular composite plate using the classic method, such as RR method, Method 1 revealed its weakness since the analytical mode shape function could not be obtained using this method. Generally, the modeling of the composite circular plate is complex due to the unknown analytical mode shape functions. Also, most papers studied the circular plates of one dimension (mainly in the radial direction due to the axisymmetry assumption which cannot be made here) which significantly simplifies the complexity of the analysis. For special circular plates with antisymmetric boundary conditions, the development of an analytical model is necessary and very important for various practical applications, such as the shape control of circular plates in satellite dishes, or the vibration control for platforms similar to that considered here.

The literature shows that the first studies on this topic are attributed to Poisson (1829) and Kirchoff (1850). Leissa (1965) has presented a thorough summary of the previously published literature up to the year 1965. In reference (Ruggiero, 2004), the free vibrations of the free-edge circular plates were studied. In particular, Asik (2004) studied the behavior of laminated circular glass plates in term of nonlinear characteristics.

Since the circular composite plate is employed as the top plate of the UH Platform, which can provide precision position control as well as vibration suppression capabilities simultaneously, the dynamic analyses of the circular plate with antisymmetric constraints in the angular/circumferential coordinate direction are investigated.

The governing equation of the thin circular plate undergoing free vibration is expressed by the following partial differential equation (Yan and Ghasemi-Nejhad, 2005):

$$\frac{\partial^2 u(x,t)}{\partial t^2} + c^2 \frac{\partial^4 u(x,t)}{\partial x^4} = 0 \tag{4.12}$$

where

$$u(x,t) = U(x)T(t) = R(r)\Theta(\theta)T(t) \tag{4.13}$$

and

$$c = \sqrt{\frac{EI}{\rho A}}$$

The boundary conditions at the UH Platform central support (where $r = 0$) and the ACS top connection to the top ACCP (where $r = R_1$) is assumed to be simply supported, and hence the displacement and moments should be zero. As a result, the boundary conditions at these points are:

$$u(0,\theta,t) = u(R_1,0,t) = u(R_1,\frac{2}{3}\pi,t) = u(R_1,\frac{4}{3}\pi,t) = 0 \tag{4.14}$$

$$M_r\Big|_{r=0,R_1,\theta=0,\frac{2}{3}\pi,\frac{4}{3}\pi} = 0 \text{ and } M_\theta\Big|_{r=0,R_1,\theta=0,\frac{2}{3}\pi,\frac{4}{3}\pi} = 0 \tag{4.15}$$

The initial conditions are:

$$u(R_1,\frac{1}{3}\pi,0) = u(R_1,\pi,0) = u(R_1,-\frac{1}{3}\pi,0) = f_1 \tag{4.16}$$

$$u_t(r,\theta,0) = 0 \tag{4.17}$$

The separation of variables method is use to solve Equation (4.12). By substituting (4.13) into (4.12), we have

$$\nabla^4 u = -\frac{1}{c^2}\frac{\partial^2 u}{\partial t^2} \tag{4.18}$$

In this equation, the left side is a function of x only and the right side is a function of t only. They must therefore be a constant equal to κ^4. Thus, the equation separates into two, as follows:

$$\nabla^2 T + c^2\kappa^4 T = 0 \tag{4.19}$$
$$\nabla^4 U - \kappa^4 U = 0 \tag{4.20}$$

where $\kappa^2 = \frac{\omega}{c}$.

The solution of (4.19) is:

$$T(t) = e^{-i\omega t} \tag{4.21}$$

As we know, $\nabla^4 = \nabla^2\nabla^2$ is the biharmonic operator, and hence Equation (4.20) takes the form of:

$$\nabla^4 U = \nabla^2\nabla^2 U = \kappa^4 U \tag{4.22}$$
$$\Rightarrow \begin{cases} \nabla^2 U = \kappa^2 U & (4.23) \\ \nabla^2 U = -\kappa^2 U & (4.24)' \end{cases}$$

Assuming that the thickness is much less than the radius of the circular plate, we can solve Equations (4.23) and (4.24) in the polar coordinates (Mathews and Walker, 1970). First, we solve the $\nabla^2 U = -\kappa^2 U$ equation. In two-dimensional polar coordinators:

$$\nabla^2 = \frac{1}{r}\frac{\partial}{\partial r}(r\frac{\partial}{\partial r}) + \frac{1}{r^2}\frac{\partial^2}{\partial\theta^2} \tag{4.25}$$

So that Equation (4.24) becomes:

$$\frac{1}{r}\frac{\partial}{\partial r}(r\frac{\partial U}{\partial r}) + \frac{1}{r^2}\frac{\partial^2 U}{\partial\theta^2} + \kappa^2 U = 0 \tag{4.26}$$

where

$$U(r,\theta) = R(r)\Theta(\theta) \tag{4.27}$$

Substituting (4.27) into (4.26), we obtain:

$$\frac{r^2}{R}\frac{d^2R}{dr^2} + \frac{r}{R}\frac{dR}{dr} + \kappa^2 r^2 + \frac{1}{\Theta}\frac{d^2\Theta}{d\theta^2} = 0 \tag{4.28}$$

Since the last term in this equation depends only on θ, while the rest depend only on r, then:

$$\frac{1}{\Theta}\frac{d^2\Theta}{d\theta^2}=-l^2 \Rightarrow \Theta(\theta)=E\cos(l\theta)+F\sin(l\theta) \qquad (4.29)$$

$$\frac{d^2R}{dr^2}+\frac{1}{r}\frac{dR}{dr}+(\kappa^2-\frac{l^2}{r^2})R=0 \qquad (4.30)$$

The R-Equation (4.30) is a Bessel's equation, so that the two solution of Equation (4.30) is Bessel's function of the first kind and the second kind, that is:

$$R(r)=AJ_l(\kappa r)+BY_l(\kappa r) \qquad (4.31)$$

When $\nabla^2U=\kappa^2U$, the same procedure is applied. Therefore, the corresponding equations are shown as follows:

$$\frac{1}{\Theta}\frac{d^2\Theta}{d\theta^2}=-l^2 \Rightarrow \Theta(\theta)=E\cos(l\theta)+F\sin(l\theta) \qquad (4.32)$$

$$\frac{d^2R}{dr^2}+\frac{1}{r}\frac{dR}{dr}+(-\kappa^2-\frac{l^2}{r^2})R=0 \qquad (4.33)$$

It should be noted that the difference in the sign of κ only resulted in the difference in the κ^2 sign in Equations (4.30) and (4.33). While the solution for Equation (4.30) Bessel's equation is in form of first kind and second kind Bessel's functions, the solution for Equation (4.33) modified Bessel's equation is in form of third kind and forth kind Bessel's functions and are given as follows:

$$R(r)=CI_l(\kappa r)+DK_l(\kappa r) \qquad (4.34)$$

It is easy to prove that Bessel's function of the first, the second, third, and the forth are linear independent. Therefore, combining with the solutions of the θ function, they are all solutions of the forth order PDE of the equation (5), shown as:

$$U(r,\theta)=\left[AJ_l(\kappa r)+BY_l(\kappa r)+CI_l(\kappa r)+DK_l(\kappa r)\right]\left[E\cos(l\theta)+F\sin(l\theta)\right] \qquad (4.35)$$

Applying the boundary conditions:

1. when $u(R_1,0,t)=u(R_1,\frac{2}{3}\pi,t)=u(R_1,\frac{4}{3}\pi,t)=0$,

$$\begin{cases} \left[AJ_l(\kappa R_1)+BY_l(\kappa R_1)+CI_l(\kappa R_1)+DK_l(\kappa R_1)\right]E=0 & (4.36) \\ \left[AJ_l(\kappa R_1)+BY_l(\kappa R_1)+CI_l(\kappa R_1)+DK_l(\kappa R_1)\right]\left[E\cos(\frac{2}{3}\pi l)+Fin(\frac{2}{3}\pi l)\right]=0 & (4.37) \\ \left[AJ_l(\kappa R_1)+BY_l(\kappa R_1)+CI_l(\kappa R_1)+DK_l(\kappa R_1)\right]\left[E\cos(\frac{4}{3}\pi l)+F\sin(\frac{4}{3}\pi l)\right]=0 & (4.38) \end{cases}$$

$$\Rightarrow \begin{cases} E=0 \\ \left[E\cos(\frac{2}{3}\pi l)+F\sin(\frac{2}{3}\pi l) \right]=0 \Rightarrow \begin{cases} E=0 \\ l=\frac{3}{2}n, \quad n=1,2,3\ldots \end{cases} \\ \left[E\cos(\frac{4}{3}\pi l)+F\sin(\frac{4}{3}\pi l) \right]=0 \end{cases}$$

Rewriting the solution,

$$U(r,\theta)=\sum_{n=0}^{\infty} \left[A_n J_{\frac{3}{2}n}(\kappa r)+B_n Y_{\frac{3}{2}n}(\kappa r)+C_n I_{\frac{3}{2}n}(\kappa r)+D_n K_{\frac{3}{2}n}(\kappa r) \right] \sin(\frac{3}{2}n\theta) \tag{4.39}$$

2. The center of the circular plate is bounded, $u(0,\theta,t)=0$, while $Y_n(0 \to \infty)$ and $K_n(0 \to \infty)$. Therefore, $B_n = D_n = 0$. Rewriting the solution, we obtain:

$$U(r,\theta)=\sum_{n=0}^{\infty} \left[A_n J_{\frac{3}{2}n}(\kappa r)+C_n I_{\frac{3}{2}n}(\kappa r) \right] \sin(\frac{3}{2}n\theta), \tag{4.40}$$

$$U(0,\theta)=\sum_{n=0}^{\infty} \left[A_n J_{\frac{3}{2}n}(0)+C_n I_{\frac{3}{2}n}(0) \right] \sin(\frac{3}{2}n\theta)=0,$$

$$\Rightarrow A_n J_{\frac{3}{2}n}(0)+C_n I_{\frac{3}{2}n}(0)=0 \Rightarrow C_n = \frac{J_{\frac{3}{2}n}(0)}{I_{\frac{3}{2}n}(0)} A_n$$

Rewriting the solution,

$$U(r,\theta) \propto \sum_{n=0}^{\infty} \left[J_{\frac{3}{2}n}(\kappa r)+\frac{J_{\frac{3}{2}n}(0)}{I_{\frac{3}{2}n}(0)} I_{\frac{3}{2}n}(\kappa r) \right] \sin(\frac{3}{2}n\theta), \tag{4.41}$$

3. The circular plate is simply supported at three ACS connection points on the edge.

$$M_\theta \Big|_{r=R_1,\theta=0,\frac{2}{3}\pi,\frac{4}{3}\pi} = (\frac{1}{r}\frac{\partial U}{\partial r}+\frac{1}{r^2}\frac{\partial^2 U}{\partial \theta^2}+\nu\frac{\partial^2 U}{\partial r^2})=0 \tag{4.42}$$

$$M_r \Big|_{r=R_1} = \left(\frac{\partial^2 U}{\partial r^2}+\nu\left(\frac{1}{r}\frac{\partial U}{\partial r}+\frac{1}{r^2}\frac{\partial^2 U}{\partial \theta^2} \right) \right)=0 \tag{4.43}$$

when $M_r \Big|_{r=R_1}=0$, we can obtain

$$\frac{d^2 J_{\frac{3}{2}n}(\kappa r)}{dr^2} + \frac{J_{\frac{3}{2}n}(0)}{I_{\frac{3}{2}n}(0)}\frac{d^2 I_{\frac{3}{2}n}(\kappa r)}{dr^2} + \nu\frac{1}{r}\left(\frac{dJ_{\frac{3}{2}n}(\kappa r)}{dr} + \frac{J_{\frac{3}{2}n}(0)}{I_{\frac{3}{2}n}(0)}\frac{dI_{\frac{3}{2}n}(\kappa r)}{dr}\right)$$

$$-\nu\frac{1}{r^2}(\frac{3}{2}n)^2\left[J_{\frac{3}{2}n}(\kappa r) + \frac{J_{\frac{3}{2}n}(0)}{I_{\frac{3}{2}n}(0)} I_{\frac{3}{2}n}(\kappa r)\right]_{r=R_1}\Bigg| = 0 \tag{4.44}$$

Using Maple, we can calculate the constant C_{mn} and obtain the values of κ_{mn} according to the change of n, shown in Table 4.2:

Table 4.2. *Values of* κ_{mn}.

	m=1	m=2
n=1	5.64	25.9
n=2	11.9	30.2
n=3	19.2	38.2
n=4	26.7	47.6

Therefore, the first six mode shapes obtained using the presented analytical solution are shown in Figure 4.37 in three dimensions. The UH Platform is to be used for a Thrust Vector Contol (TVC) (Ghasemi-Nejhad and Doherty, 2002; Doherty and Ghasemi-Nejhad, 2005) application where the range of the frequency under interest and consideration is from 1 to 100 Hz. Our analysis shows that only the first two modes fall in this range. Therefore, for verification purpose an ANSYS finite element analysis was carried out on the same ACCP considered for the analytical solution, and was solved to obtain the first two modes and natural frequencies. In Figure 4.38, the first two mode shapes obtained by our analytical solution as well as those from the ANSYS finite element method are plotted in two dimensions. It is shown that these results obtained from these two techniques are in excellent agreement.

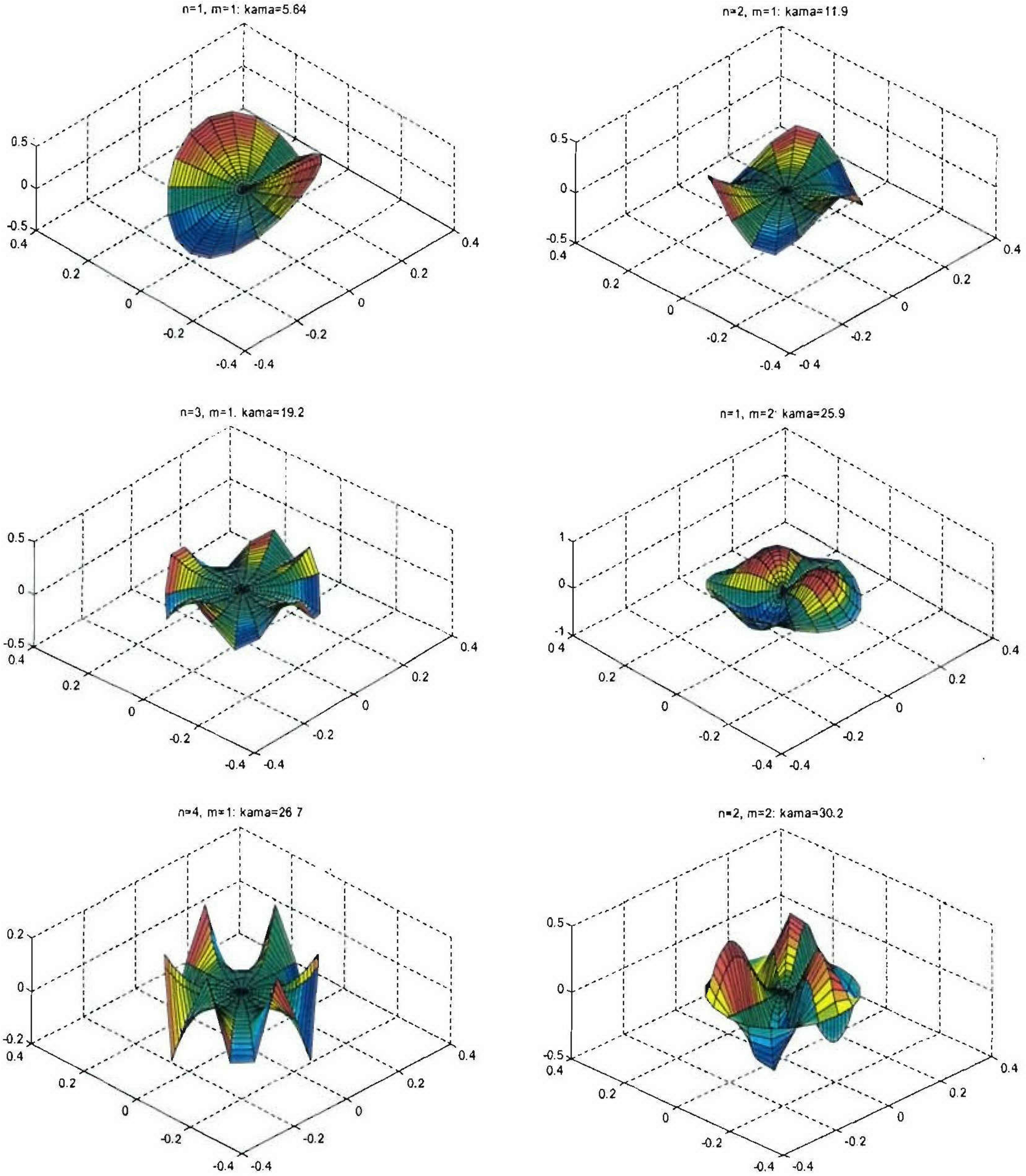

Figure 4.37. *The first six mode shapes obtained analytically.*

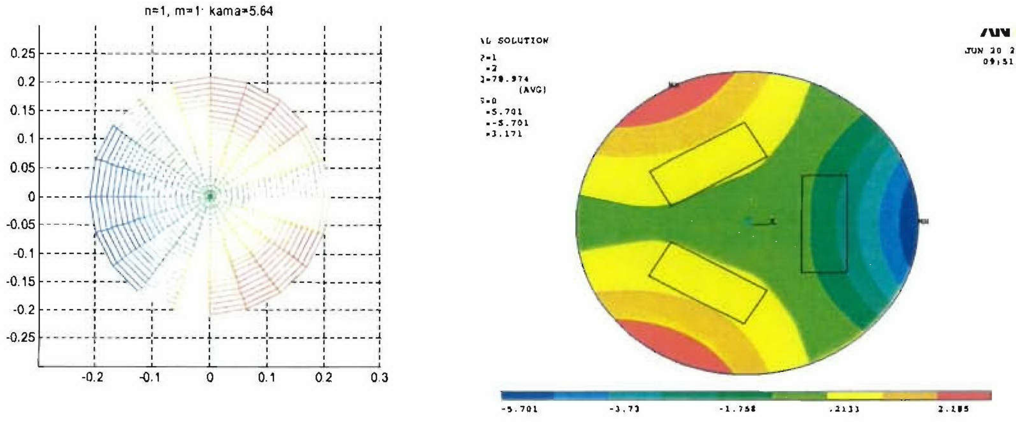

a. First mode shape by analytical.

b. First mode shape by ANSYS FEA.

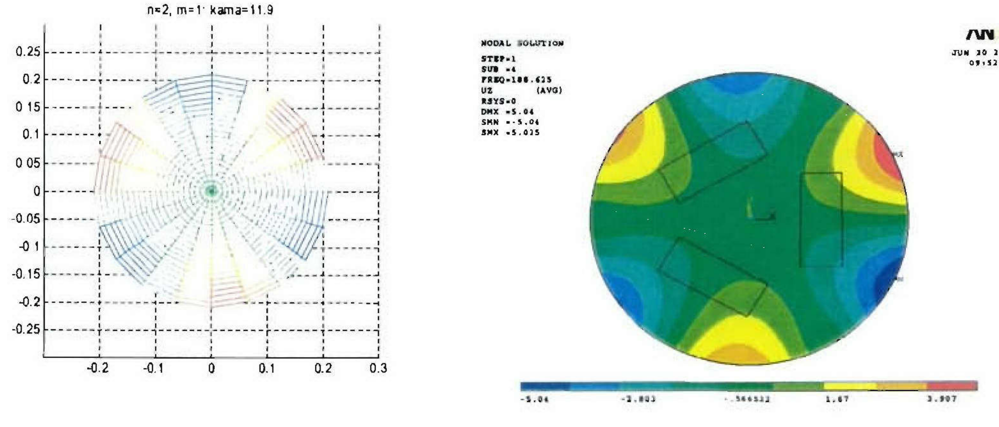

c. Second mode shape by analytical.

d. Second mode shape by ANSYS FEA.

Figure 4.38. *Comparison of the first two mode shapes obtained analytically and numerically.*

4.6.1.2. Optimization

Genetic Algorithms (GAs) are robust search techniques based on Darwin's principles of evolution. A typical GA (Kwak and Shin, 1999; Yan and Ghasemi-Nejhad, 2003, 2004b) consists of a set (population). In each iterated cycle (evolution), the 'stronger' offspring will be chosen to survive and the 'weaker' ones disappear. Through the crossover between the strongers as well as the mutation of the stronger, the new generation is created. In the last generation, the strongest offspring (the optimal value) will be obtained. The binary encoding formula is used in the GA.

As the crucial step in the optimization, some objectives in previous applications for optimal actuator placement were based on structures themselves and overlooked the effects of the applied control law. In fact, the interactions between the controller and the structure exist.

4.6.1.2.1. Actuator Configurations

In this study, considering the dimensions of the ACCP and piezoelectric patches and the boundary condition, there are four positions for each piezoelectric actuator, that is, the actuator in triangle shape (T), in star shape (S), close to the edge (F) and close to the center. Therefore, a total of 16 possible configurations are defined combining the position of the three actuators and they are: TTT, TTS, TST, STT, TSS, STS, SST, SSS, TTTF, TTSF, TSTF, STTF, TSSF, STSF, SSTF, and SSSF. Figure 4.39.a shows the ACCP model with the triangle configuration (called TTT) of the actuators and Figure 4.39.b shows the star configuration (SSS).

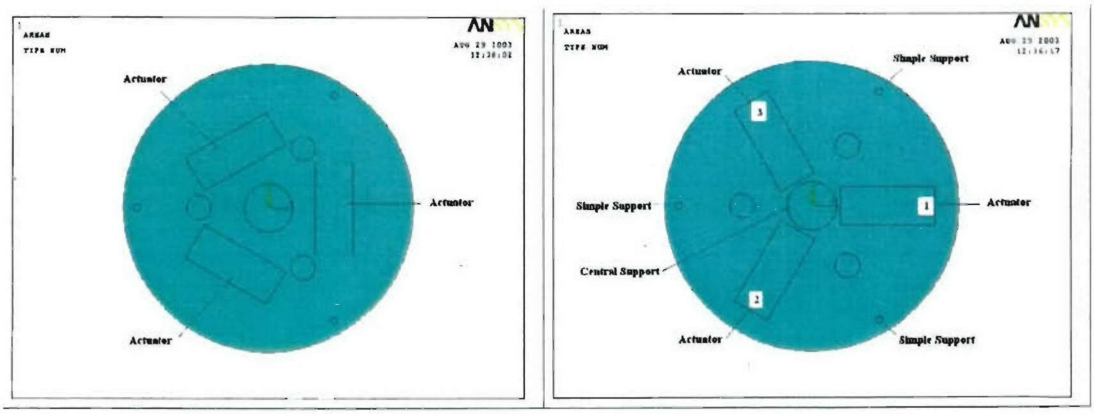

a. Triangular configuration. *b. Star configuration.*

Figure 4.39. *Typical actuator configurations.*

By performing the ANSYS finite element model analysis, the first three natural frequencies of the ACCP with three actuators placed in the 8 possible configurations are found and given in Table 4.3, showing that the natural frequencies vary with different configurations and the relative difference rates of the first three natural frequencies are 9.56%, 9.71%, and 10.28%, respectively. The variation of the natural frequencies demonstrates the effects of the actuators configurations on the dynamics of the system.

Table 4.3. *Natural frequencies of the ACCP for first 3 modes and 8 different conditions.*

Actuator	Mode 1	Mode 2	Mode 3
TTT	75.964	78.974	88.68
TST	75.252	79.248	88.353
TSS	73.946	78.053	87.172
SSS	73.894	76.64	85.66
TTTF	72.059	74.676	83.644
TSTF	71.146	74.482	82.961
SSTF	71.034	72.742	81.348
SSSF	69.337	72.236	80.41
Relative Rate = (Max- Min)/Min	9.56%	9.71%	10.28%

4.6.1.2.2. Objective Function

To obtain the optimal location of the actuator considering the control power for the vibration suppression, an optimal output feedback control scheme (LQR, Kwak and Shin, 1999) is adopted as the objective function. Consider a linear model in terms of the state-space form:

$$\begin{aligned} \dot{x} &= Ax + Bu \\ y &= Cx \end{aligned} \tag{4.45}$$

where x is the state vector, u is the control input, and y is the output. A, B, and C are the state transform matrix, the input matrix, and the output matrix, respectively. We can calculate the optimal gain matrix K such that the state-feedback law $u = -Kx$ minimizes the quadratic cost function, $J(u)$, as:

$$J(u) = \int_0^\infty (x^T Qx + u^T Ru)dt \tag{4.46}$$

where Q and R are the weight matrices. The state-feedback gain K can be derived through the solution S of the associated Riccati equation.

$$A^T S + SA - SBR^{-1}B^T S + Q = 0 \tag{4.47}$$

Therefore, K is

$$K = R^{-1}B^T S \tag{4.48}$$

Since the state-feedback gain matrix K is a vector, Euclidean norm of the feedback matrix is explored as the control index.

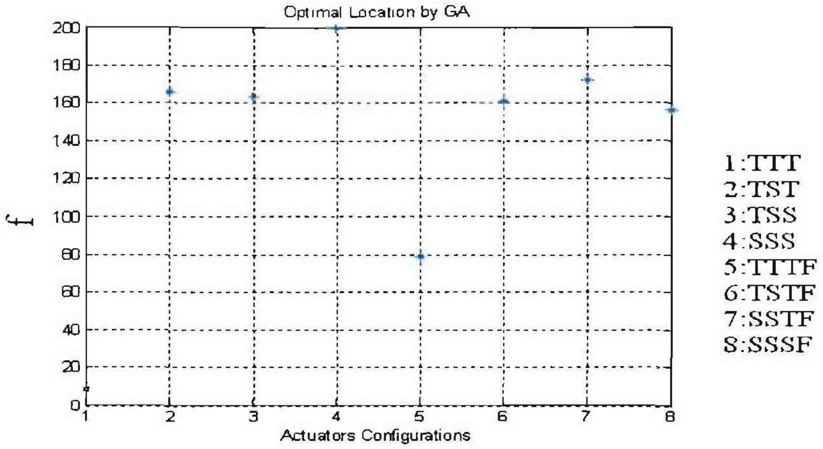

Figure 4.40. *Feedback gains versus actuator configuration.*

The optimal configuration is obtained by GA when the population size is set to 50, the crossover probability to 0.5, and the mutation probability to 0.05. The binary encoding formula is used to code the 8 candidate configurations from 1 to 8.

Figure 4.40 shows the value of the objective for the 8 possible actuators configurations. The minimum value of the objective is at the first configuration, which means that the TTT is the optimal configuration. The second best configuration is TTTF. The worst performing configuration is SSS.

4.6.1.2.3. Simulation

To verify the effectiveness of the proposed actuator configuration optimization and the MIMO LQR control algorithm for the ACCP MIMO system vibration control, the simulations are conducted for five different PZT actuators configurations and they are: TTT, TST, TSS, SSS, and TTTF. In the simulation, the white noise as the disturbance is considered and is given in Equation (4.49).

$$d(t) = sqrt(1/dt) * rand(3, length(t)) \quad (Voltage) \tag{4.49}$$

where $1/dt$ is the sample frequency.

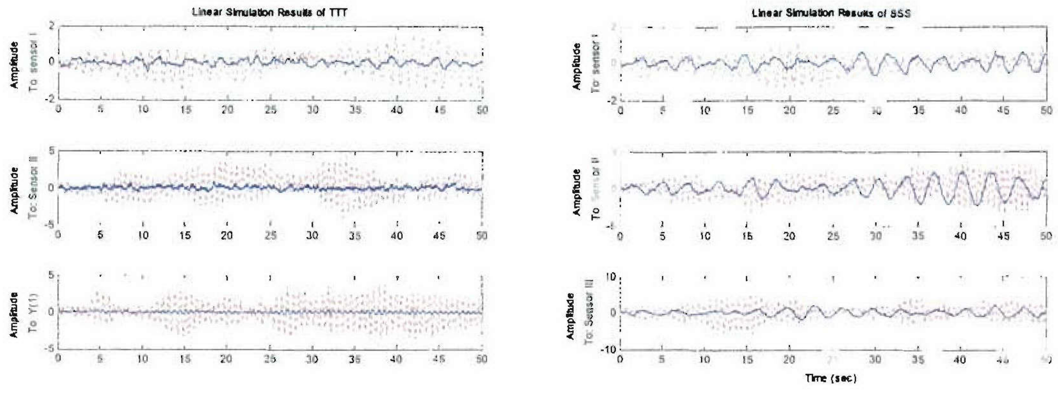

a. TTT

b. SSS

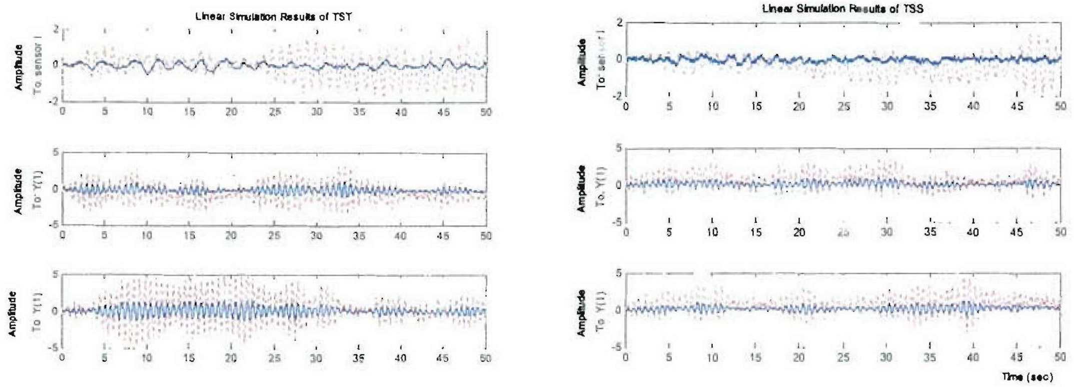

c. TST

d. TSS

Figure 4.41. Controlled and uncontrolled responses of four actuator configuration for the three sensor locations.

In Figure 4.41, the time histories of the controlled and uncontrolled responses are shown with the actuator configuration of TTT, SSS, TST, and TSS, respectively, for the three sensor locations which are placed in between the ACS top connection points to the ACCP. It is easy to see that the vibration amplitude are reduced at all three sensor locations and the control efficiency using the optimized actuators configuration (i.e. TTT) is much higher than using actuators without configuration optimization.

Same results can be obtained when comparing the responses of the TTT actuators configuration with that of the TTTF. Figure 4.42 confirms that placing the actuators close to the central support rather than close to the edge improves the performance of the actuators.

These simulation results fully reveal that substantial saving in the control performance gain can be obtained by placing the piezoelectric actuators in their optimized positions close to the central support with the triangular configuration of TTT for this application.

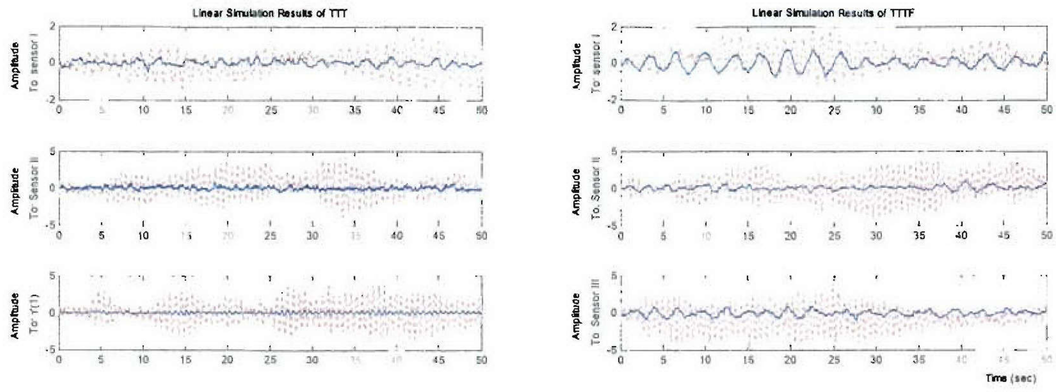

a. TTT b. TTTF

Figure 4.42. Controlled and uncontrolled responses of TTT and TTTF configurations for the three sensor locations.

4.6.3. Conclusions

Two main improvements from the previous works have been achieved in this work. First, two modeling strategies are proposed. Both of them can be applied for ACCP modeling taking the effects of piezoelectric actuators on the dynamic of the adaptive circular composite plate into account. The second improvement lays in the combination of the optimization technique (i.e. GAs) with the control law in the entire optimization process. Finally, the result shows that placing the actuators close to the central support with the triangle shape is the optimal configuration in this application, and it yields the minimal control energy.

As a part of the Adaptive Damping and Positioning using Intelligent Composite Active Structures (ADPICAS) project granted by ONR, the continuous work will focus on vibration suppression experiments and the realization of the simultaneously precision positioning and vibration suppression of the adaptive circular composite plate with the optimal configuration of actuators by LQR and adaptive control schemes in Phase III.

4.6.2. Optimization of the Circular ACP Using FEA and VSS

We have performed a series of analyses on the top circular plate to optimize the configuration, location, size, and number of the piezoelectric sensors and actuators necessary for the top circular device plate of the MSP, employing the Vibration Suppression Schemes (VSS) that we developed in the ADPICAS project and is explained in details in Section 2. The piezo patches considered and utilized in this section are Active Fiber Composite (AFC) piezo patches (CCC, 2002). Based on these analyses, a triangular configuration where the piezo patches are closer to the thruster base locations gave the best results compared with the Star configuration or other triangular configurations where the piezo patches are farther away from the thruster base location for both cases of thruster bolts not being rigidly connected (see Figure 4.43) as well as being rigidly connected (see Figures 4.44). It should be noted that while the Star configuration has only one case, the Triangular configuration has three cases: Triangular 1 where the piezo are close to the thruster location, Triangular 2 where the piezos are close to the edges, and for Triangular 3 the piezos are located in between Triangular 1 and 2. The vibration loading configuration and its displacement results are shown in Figures 4.45 and 4.46 using half-symmetry. The results of vibration suppression of Figure 4.44 with the loading conditions shown in Figure 4.45 employing the Vibration Suppression Schemes are given in Tables 4.4 and 4.5 for Star and Triangular configurations, respectively. These tables show that the Triangular 1 configuration has the lowest level of control voltage and highest level of vibration suppression (see Figures 4.47 and 4.48). The initial version of this work without the thruster rigid link (see Figure 4.43) was reported by Ghasemi-Nejhad and Soon (2003), and a similar work on a cylindrical part (see Figure 4.1.d) was reported by Ghasemi-Nejhad and Sakagawa (2003).

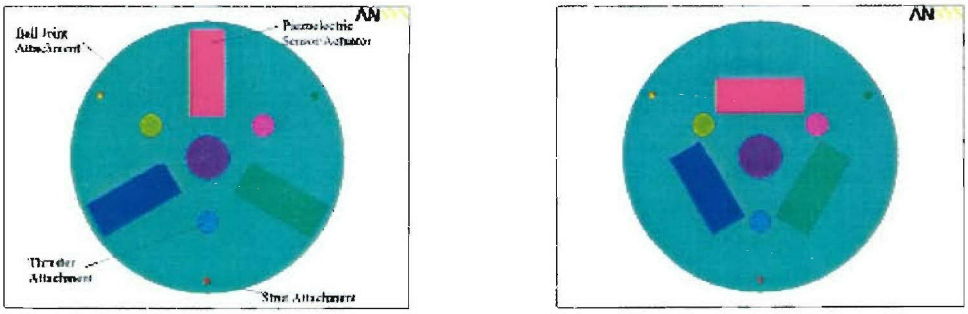

a) Star

b) Triangle

Figure 4.43. *ACP top circular plate without thruster rigid link.*

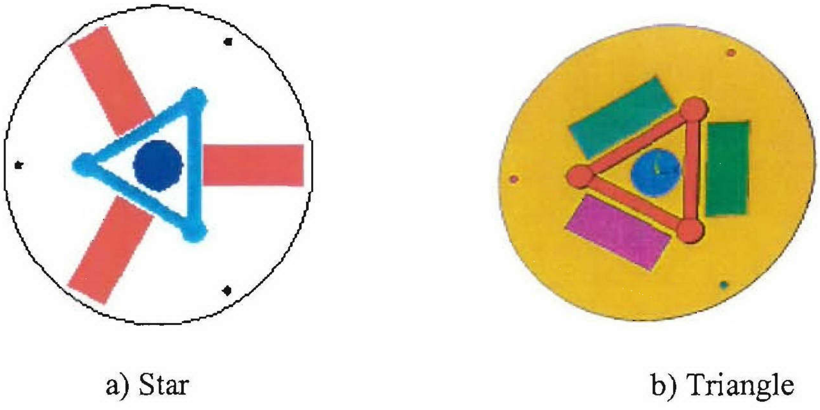
a) Star b) Triangle

Figure 4.44. *ACP top circular plate with thruster rigid link.*

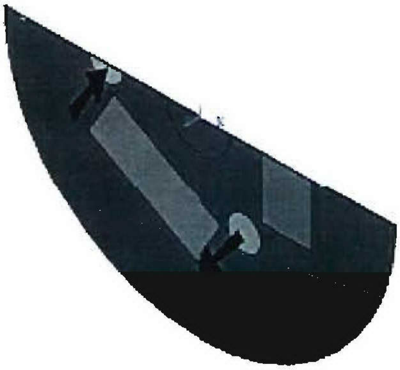

Figure 4.45. *ACP top circular plate vibration loading.*

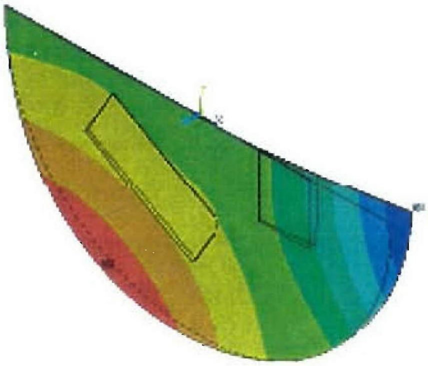

Figure 4.46. *ACP top circular plate vibration, Triangular 1, MX and MN Points.*

Table 4.4. *ACP of Figure 4.44-a.*

Star Actuator Voltages

Freq (Hz)	Act. 1 (V)	Act. 2 (V)
79	3070.89	1267.07
0	83285.41	1234.38
81	3514.56	1200.46
82	4017.75	1269.67
83	3409.29	2479.22
84	4603.03	1184.62
85	5065.90	1178.85

Table 4.5. *ACP of Figure 4.44-b.*

Triangle 1 Actuator Voltages

Freq (Hz)	Act. 1 (V)	Act. 2 (V)
86	745.97	-148.68
87	754.16	-150.59
88	748.66	-151.10
89	837.11	-161.35
90	816.56	-160.33
91	822.81	-162.06
92	826.66	-163.39
93	36.44	-60.90
94	895.41	-174.20
95	902.01	-175.88
96	916.07	-178.57

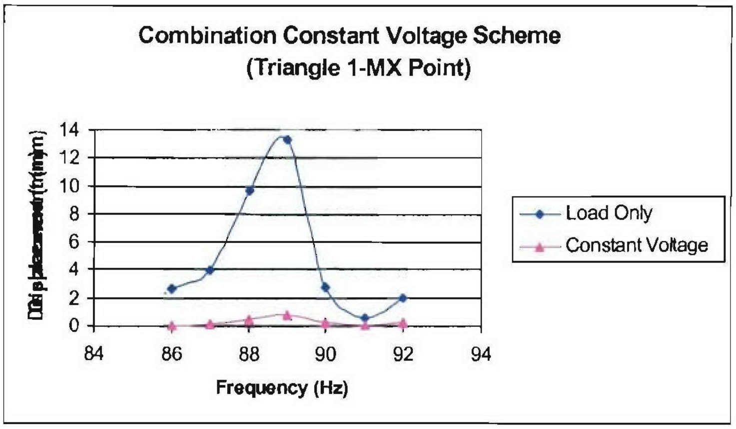

Figure 4.47. *ACP top circular plate vibration, Triangular 1, MX Point.*

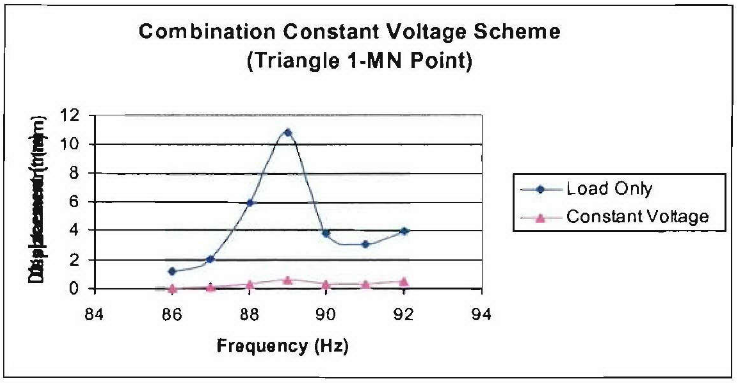

Figure 4.48. *ACP top circular plate vibration, Triangular 1, MN Point.*

4.6.2.1. Circular ACP Modeling without Brackets

Next, two different models are created to simulate the circular ACP ANSYS (2002) Finite Element Model (FEM). Both circular ACPs have a diameter of 42 cm and contain embedded Active Fiber Composite (AFC) CCC (2002) piezoelectric patches. The first circular ACP model contains six piezoelectric patches and the second model contains nine piezoelectric patches. For the first ACP model, three of the piezoelectric patches are embedded in the upper half of the panel and the remaining patches are embedded directly below their counterparts in the bottom half of the panel in a back-to-back configuration. The three piezoelectric patches on the upper half of the panel are used as actuators and the three piezoelectric patches on the bottom half of the panel are used as sensors. For the second ACP model, there is a similar design as the first one where three of the piezoelectric patches are embedded in the upper half of the panel and three patches of similar size are embedded directly below their counterparts in the bottom half of the panel. However, for the second ACP model, the difference comes from the addition of three narrower piezoelectric patches on the bottom half of the panel next to the three bottom piezoelectric patches. These three narrower piezoelectric patches will act as the sensors so that we can utilize the six wider piezoelectric patches as actuators to suppress vibrations as opposed to the use of only three piezoelectric patches as actuators to suppress the vibrations in the first model.

Figure 4.49 shows our Intelligent Composite Platform. The ACSs are joined to the top device circular plate Active Composite Panel (ACP) 2 cm from the perimeter of the plate, to allow the panel to pivot freely about its central support. Therefore, the top device plate can pivot about its central support to give two in-plane rotational degrees of freedom (Ma and Ghasemi-Nejhad, 2004c, 2005e). Since the active composite platform is intended for space applications, the structure must be lightweight yet have a high strength to handle the loading during the thruster firings. For this reason, nearly the entire structure is made of carbon/epoxy composite. This includes the active composite panel. Here, two different models are created to simulate the circular ACP ANSYS (2002) Finite Element Model (FEM). Both circular ACPs have a diameter of 42 cm and contain embedded Active Fiber Composite (AFC) CCC (2002) piezoelectric patches. The first circular ACP model contains six piezoelectric patches and the second model contains nine piezoelectric patches. For the first ACP model, three of the piezoelectric patches are embedded in the upper half of the panel and the remaining patches are embedded directly below their counterparts in the bottom half of the panel in a back-to-back configuration. The three piezoelectric patches on the upper half of the panel are used as actuators and the three piezoelectric patches on the bottom half of the panel are used as sensors. For the second ACP model, there is a similar design as the first one where three of the piezoelectric patches are embedded in the upper half of the panel and three patches of similar size are embedded directly below their counterparts in the bottom half of the panel. However, for the second ACP model, the difference comes from the addition of three narrower piezoelectric patches on the bottom half of the panel next to the three bottom piezoelectric patches. These three narrower piezoelectric patches will act as the sensors so that we can utilize the six wider piezoelectric patches as actuators to suppress vibrations as opposed to the use of only three piezoelectric patches as actuators to suppress the vibrations in the first model. Ghasemi-Nejhad et al. (2005c) introduced three techniques to embed piezoelectric patches into composites.

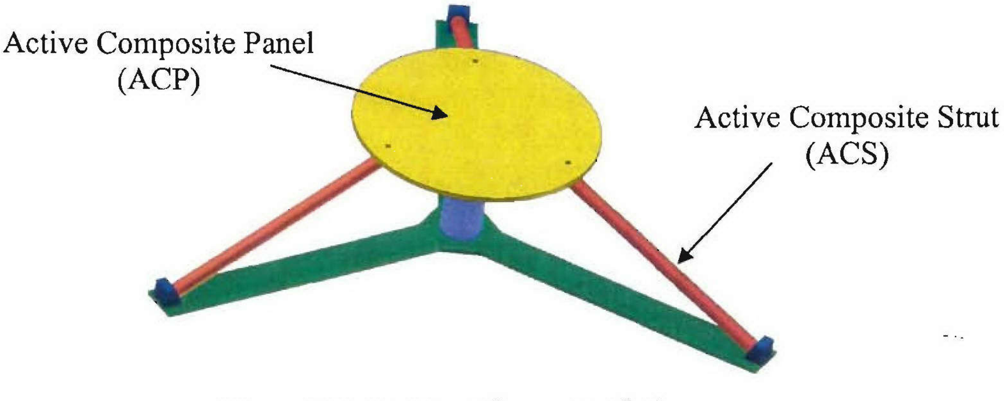

Figure 4.49. Intelligent Composite Platform.

Since some of the mode shapes are not symmetric, a half-plane model such as that shown in Figure 4.45 will miss those modes not symmetric with respect to the half plane line. In addition, it is impossible to independently use all three actuators in a half-plane model. As a result, for completeness full plane models with six piezos (all six piezos are wide back-to-back, see Figure 4.50) and nine piezos (six wide, i.e., 2", piezos as actuators, three upper and three lower back-to-back, and three narrow, i.e., 0.5", piezos as sensors next to the bottom actuators, see Figure 4.51).

The full panel with nine piezoelectric patches model (called nine-patch model) utilized the same Triangle 1 optimize configuration of the piezoelectric patches. The three additional piezoelectric sensor patches were located next to the bottom layer piezoelectric patches (see Figure 4.51). These narrower piezoelectric patches (to be used as sensors) were 0.5" wide, the wider piezoelectric patches (to be used as actuators) were 2" wide, and the other dimensions as well as the material properties of these AFC piezo sensor and actuator patches were the same (see Figure 4.51). With the use of ANSYS Finite Element Analysis (FEA) software, the vibration modes and frequencies of the structure were characterized. The results from the full panel nine-patch analysis were compared with the results from the full panel six-patch analysis to make a comparison before continuing to harmonic analysis. It should be noted that the boundary conditions at the central support and the ACS top ball joint connections are assumed to be simply supported.

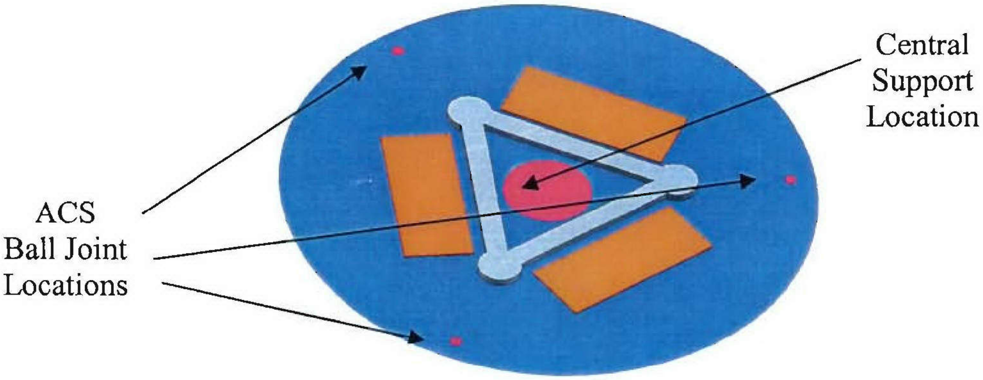

***Figure 4.50**. Full panel six-patch model showing the location of the six wide piezoelectric actuators, central support, and three ACS ball joints.*

Modal analysis is run to determine the first eight vibration modes. Once the natural frequencies for the first bending mode are found, harmonic analysis can be performed with the simulated loading of the thruster. The loading is applied to the thruster attachments as shown in Figure 4.52. For this preliminary analysis, the combined loading on the full panel model is assumed to be ten pounds. Two of the thruster attachments experience a downward loading while the remaining attachment experiences an upward loading. This loading vibrates the structure about its center.

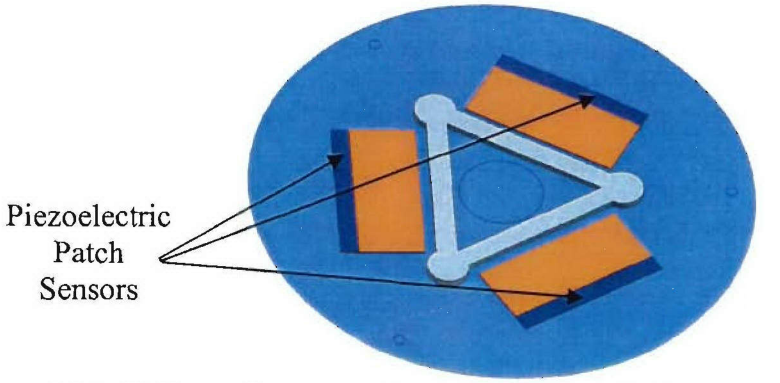

***Figure 4.51**. Full panel nine-patch model showing the location of the three narrower piezoelectric patch sensors.*

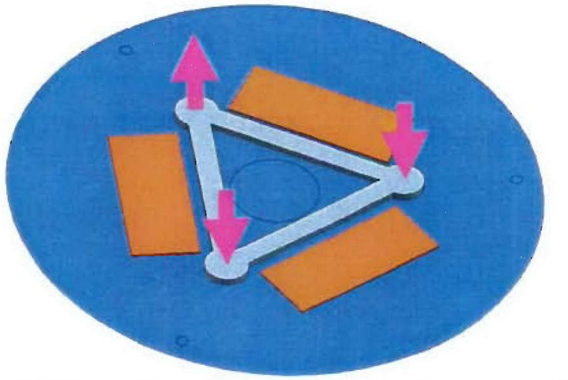

***Figure 4.52**. Full panel model showing the direction of loading applied to the thruster attachments.*

To begin the harmonic analysis three points are selected, where the maximum and minimum displacements occur, from the modal analysis. A frequency interval of 10 Hz with five sub steps is chosen about the first bending natural frequency. The harmonic analysis is performed with load only and the displacement of the three points is observed for each of the five frequency sub steps. The load-only displacement of these three points are denoted as D_{P1}, D_{P2}, and D_{P3}. Next, an arbitrary value of voltage is applied to one of the actuators and the harmonic analysis is run without loading and the displacements of those three points are noted. This step is repeated for the two remaining actuators. Since the relationship between displacement and voltage is nearly linear, ratios for voltage to displacement can be calculated. The configuration has nine ratios, that is, for each actuator there are three ratios, one for point one, one for point two, and the other for point three. The ratios are denoted as $r_{1,P1}$, $r_{1,P2}$, $r_{1,P3}$, $r_{2,P1}$, $r_{2,P2}$, $r_{2,P3}$, $r_{3,P1}$, $r_{3,P2}$, and $r_{3,P3}$. The ratios are calculated by simply dividing displacement of the point by the input voltage. Then dividing the load-only displacement of the corresponding point by each ratio gives the voltage required for suppression of that particular point. The voltage required for suppression is denoted as V_1, V_2, and V_3. These voltages can be applied in a number of different voltage schemes to provide vibration suppression to the structure (Russ and Ghasemi-Nejhad, 2002a; Doherty and Ghasemi-Nejhad, 2005; Ghasemi-Nejhad et al., 2005a); however, the only scheme used for this analysis was the Constant Voltage scheme. The Constant Voltage scheme uses a constant voltage to one or all of the actuators across the frequency interval. The voltage to each of the actuators does not necessarily have to be the same value. The determination of the appropriate value is difficult since the variation of voltages across the frequency range is large and there is no one value that is representative of all the voltages. The voltages are calculated by solving the following set of linear equations simultaneously at each frequency:

$$\begin{bmatrix} r_{1,P1} & r_{2,P1} & r_{3,P1} \\ r_{1,P2} & r_{2,P2} & r_{3,P2} \\ r_{1,P3} & r_{2,P3} & r_{3,P3} \end{bmatrix} \begin{bmatrix} V_1 \\ V_2 \\ V_3 \end{bmatrix} = \begin{bmatrix} -D_{P1} \\ -D_{P2} \\ -D_{P3} \end{bmatrix} \tag{4.50}$$

In Equation (4.50), the right-hand-side is negative to provide out-of-phase displacements for V_1, V_2, and V_3 compared to the external disturbance (Russ and Ghasemi Nejhad, 2002a; Doherty and Ghasemi-Nejhad, 2005; Ghasemi Nejhad et al., 2005a). Applying the calculated voltages, V_1, V_2, and V_3, at each frequency delivers vibration suppression for all three points. Following the same procedure listed above, the upper and bottom piezoelectric patches were used in tandem for comparison with using only the upper three piezoelectric actuator patches.

The next step involved changing the thickness of the panel to find the optimum thickness. The selected thicknesses to run the analysis on were six, eight, ten, twelve, fourteen, sixteen, eighteen, twenty, twenty two, and twenty four total layers of composite. The location of the piezoelectric patches remained the same, being just one layer above the bottom layer and one layer below the upper layer of composite. The change of thickness resulted from changing the number of layers sandwiched in between the piezoelectric patches. The analysis started with modal analysis to determine the vibration modes of the panel for each thickness, then the first symmetric vibration mode was selected for running the harmonic analysis. The voltage required for vibration suppression at the vibration mode was determined employing the Constant Voltage scheme.

The results for comparison of the modal analysis natural frequency from the full panel six-patch and full panel nine-patch models are given in Table 4.6. From the comparison, one can see that the full panel nine-patch model has similar vibration modes as a six-patch panel but at slightly lower frequencies which was expected since the piezoelectric patches are heavier than the composite and an increase in mass results in a decrease in vibration natural frequencies.

The first mode of the full panel nine-patch model was non-symmetric (see Figure 4.53) and the second vibration mode was symmetric (see Figure 4.54). The second vibration mode was used for the comparisons of the Constant Voltage scheme results from the full panel six-patch model analysis. The results obtained from the full panel nine-patch model when using the upper layer piezoelectric patches are given in Table 4.7 and compared with the results from the full panel six-patch model.

Table 4.6. *Comparison of modal analysis natural frequencies for the full panel six-patch and full panel nine-patch models for six and twenty four total layers of composite.*

6 Total Layers		24 Total Layers	
Full Panel Six-Patch	Full Panel Nine-Patch	Full Panel Six-Patch	Full Panel Nine-Patch
85.07	83.96	248.29	244.76
87.73	86.70	263.38	262.20
92.28	91.20	321.74	319.35
203.82	201.70	590.32	582.54
207.49	205.70	690.38	683.66
210.04	208.18	698.92	693.93
235.85	234.88	906.98	906.17
279.62	277.63	998.66	999.60

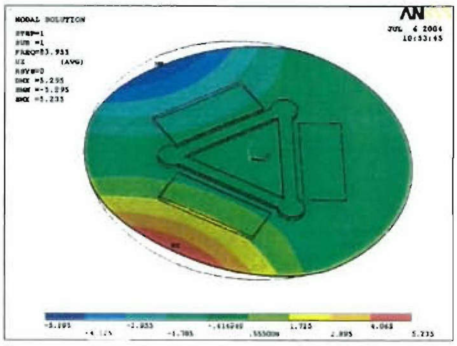

Figure 4.53. *The first vibration mode (non-symmetric), at 83.96Hz, of the full panel nine-patch model with six total layers of composite.*

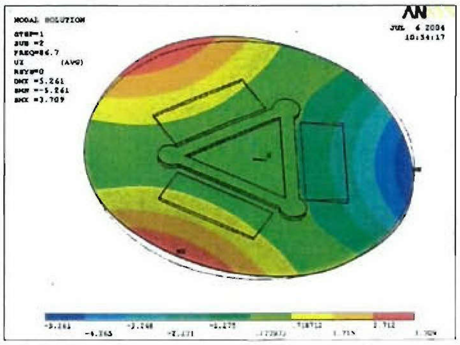

Figure 4.54. *The second vibration mode (symmetric), at 86.70Hz, of the full panel nine-patch model with six total layers of composite.*

Table 4.7. *Comparison of the Constant Voltage scheme results for the full panel six-patch and full panel nine-patch models using only the upper layer actuators.*

Full Panel Six-Patch Results		Full Panel Nine-Patch Results	
	voltage		voltage
V_1	751.92	V_1	777.44
V_2	-148.45	V_2	-159.06
V_3	-134.20	V_3	-151.95

The control voltage results from the full panel nine-patch model are slightly higher than those from the full panel six-patch model. The resulting increase in voltage is due to the reduction in the stiffness of the panel. The piezoelectric patches are more flexible than the cured carbon/epoxy prepreg material and deflect more requiring more voltage to suppress the vibrations. The results for the full panel six-patch and nine-patch models when using the upper and bottom layer piezoelectric patches in tandem are given in Table 4.8. Once again, the results from the full panel nine-patch model are slightly higher than those from the six-patch model.

Table 4.8. *Comparison of the Constant Voltage scheme results for the full panel six-patch and nine-patch models using both the upper and bottom layer piezoelectric patches in tandem.*

Full Panel Six-Patch Results		Full Panel Nine-Patch Results	
	voltage		voltage
V_1	375.29	V_1	383.80
V_2	-77.21	V_2	-84.49
V_3	-70.42	V_3	-79.23

The next step involved varying the thickness of the platform to optimize the number of required composite layers. The results from this analysis are plotted in Figure 4.55. From the Voltage Curve one can see that two of the voltages are similar (i.e., V_2 and V_3) based on the symmetric nature of the vibration mode. The voltages V_2 and V_3 remain similar throughout the thickness variation. The first voltage V_1 steadily decreases as the thickness increases and is what was expected since as the number of layers increases, the structure becomes stiffer meaning there is less displacement (due to the same external disturbance) that needs to be suppressed, and thus leading to lower control voltage requirements.

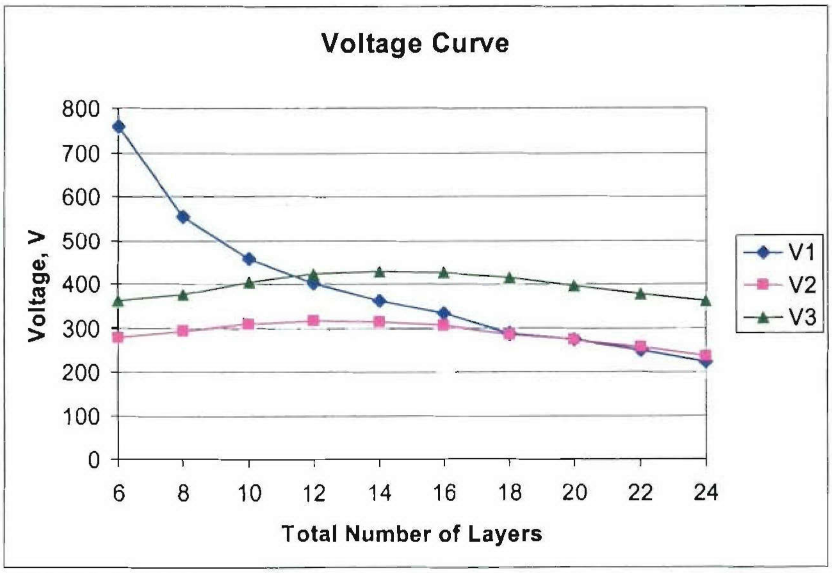

Figure 4.55. *The Voltage Curve, showing the required control voltage, in volts, versus total number of composite layers to obtain vibration suppression.*

4.6.2.2. Circular ACP Modeling with Brackets

The full panel with brackets model utilized the same configuration of the piezoelectric patches as the full panel with nine-patch model with simply supported boundary conditions. The difference in the full panel with brackets and full panel with nine-patche models was the addition of aluminum brackets to represent the central support and ACS ball joints (see Figure 4.56).

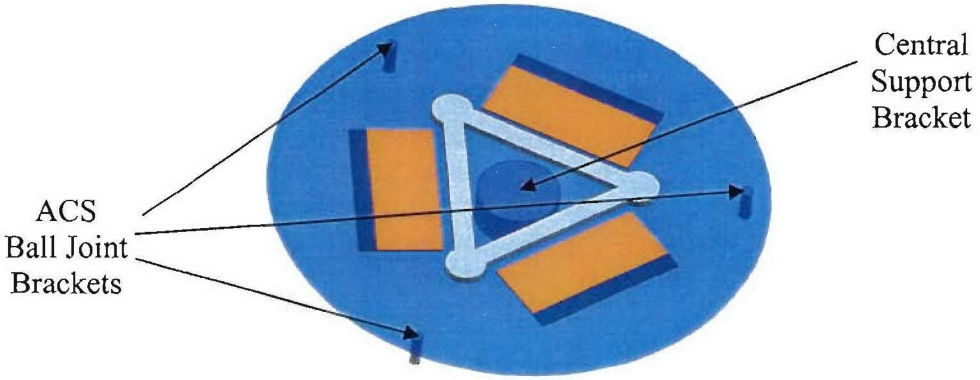

Figure 4.56. *Full panel with brackets model showing the location of the central support and ACS ball joint brackets.*

The addition of brackets was used to model the correct location of pivot points for the central support and ACS ball joints. Another difference is the location of the boundary conditions, instead of being located on the bottom layer of composite, the boundary conditions are now located at the bottom of each bracket. The objective is the thruster vibration suppression and was done by selecting one point within each of the three circular section of the thruster attachment, denoted as D_{P1}, D_{P2}, and D_{P3}.

Harmonic analysis was performed with the simulated loading of the thruster at 25, 50, 75, and 100Hz. The loading is applied to the thruster attachments as shown previously in Figure 4.52. The combined loading on the full panel with brackets model is one pound of force that was calculated from the thruster vector misalignment. The combined loading on the full panel is one pound of force that was estimated from the thruster vector misalignment. The fact is that the thruster static (or DC) loading is at 100 lbs. 10% of this load (i.e., 10 lbs) is estimated to form a dynamic (or AC) component and is primarily the axial vibration that will be suppressed by the components (other than the circular ACP being designed here) of the intelligent composite platform (see Figure 4.49). 10% of the axial dynamic load (i.e., 1 lb) is estimated to form the lateral vibration that should be suppressed using the circular ACP being designed here.

Two of the thruster attachments experience a downward loading while the remaining attachment experiences an upward loading. The harmonic analysis is performed at 25, 50, 75, and 100Hz with load only and the displacement of the three points D_{P1}, D_{P2}, and D_{P3} were noted. The procedure to determine V_1, V_2, and V_3, i.e., the three actuator pair control voltages, was the same as that explained earlier for Equation (4.50).

The next step involved changing the thickness of the panel to find the optimum thickness. The selected thicknesses to run the analyses on were six, ten, fourteen, sixteen, eighteen, and twenty four total layers of composite to obtain the trend. The location of the piezoelectric patches remained the same, being just one layer above the bottom layer and one layer below the upper layer of composite. Therefore, the change of thickness resulted from changing the number of layers sandwiched between the piezoelectric patches.

The control voltage results from this FEA analysis (i.e., V_{FEA}) are smaller when compared to actual needed control voltages (i.e., V_{actual}), since there are three conversion factors that should be applied to the results from ANSYS to obtain the actual control voltage. The three conversion factors are for the (a) piezo fiber effective area, (b) piezo fiber volume fraction, and (c) voltage. (a) The effective area conversion factor (CF_{EA}) is 0.75 and this factor comes from the piezoelectric manufacturer (CCC, 2002), and it implies that the actual effective AFC area within each patch is 75%. (b) The volume fraction conversion factor (CF_{VF}) is 0.55 which is due to the fact that the active piezoelectric fibers in the AFC patch within the effective area only make up 55% of the actual area/volume of the AFC patch (CCC, 2002). (c) The voltage conversion factor (CF_{Vol}) is 0.60 and is found from the comparison of the voltage versus free expansion experimental data supplied by the manufacturer and that obtained from the finite element model taking the effective area and fiber volume fractions also into account, and it was found to be 60%. Therefore, Equation (4.51) given below gives the actual Voltage Conversion Equation.

$$V_{FEA} = V_{actual} * (CF_{EA} = 0.75) * (CF_{VF} = 0.55) * (CF_{Vol} = 0.60) \qquad (4.51)$$

The Voltage Curve for different thicknesses at 25Hz is plotted in Figure 4.57. From the Voltage Curve at 25Hz, one can see that two of the voltages are similar (V_2 and V_3). The trends of all voltages (V_1, V_2, and V_3) are the same and continue to decrease as the thickness increases. The Voltage Curve for different thicknesses at 50Hz is plotted in Figure 4.58.

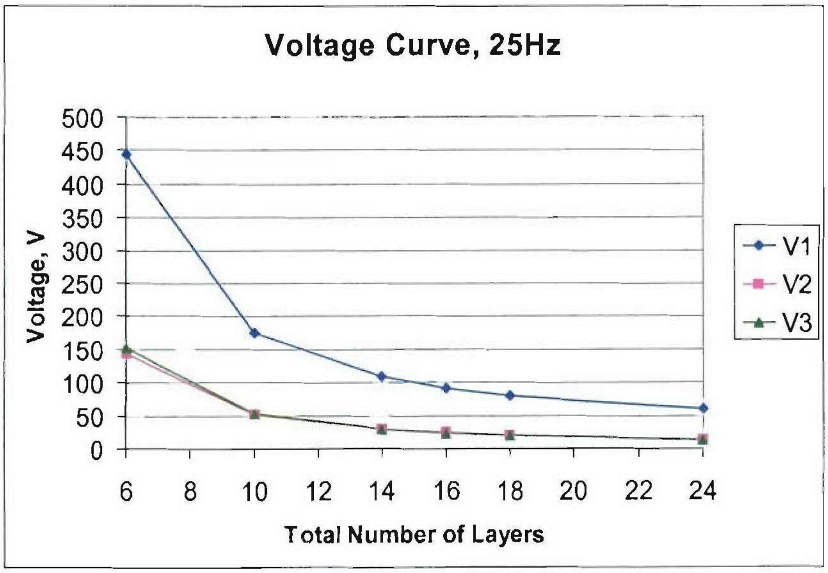

***Figure 4.57**. The Voltage Curve (V_{FEA}), showing the required control voltage versus total number of composite layers to obtain vibration suppression at 25Hz.*

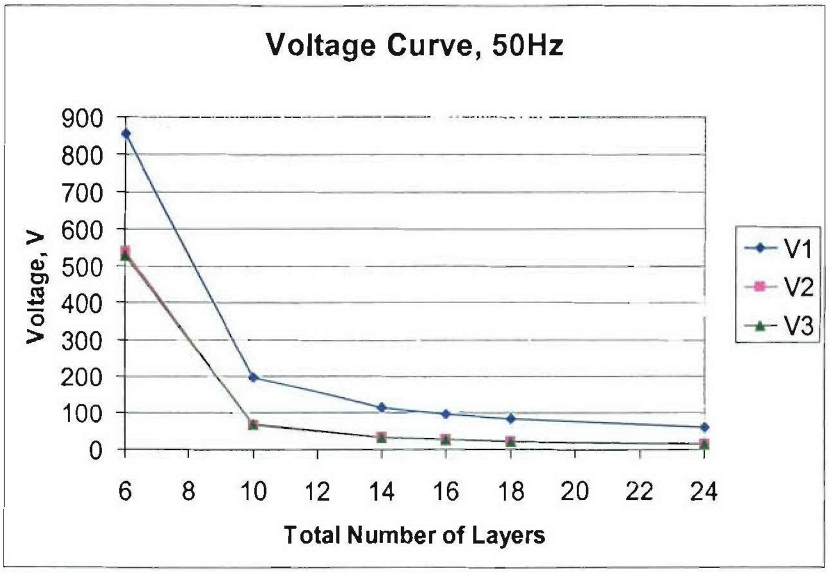

Figure 4.58. *The Voltage Curve (V_{FEA}), showing the required control voltage versus total number of composite layers to obtain vibration suppression at 50Hz.*

From the Voltage Curve at 50Hz we can see that two of the voltages are similar (V_2 and V_3). The trends of all voltages (V_1, V_2, and V_3) are the same and continue to decrease as the thickness increases. The Voltage Curve for different thicknesses at 75Hz is plotted in Figure 4.59.

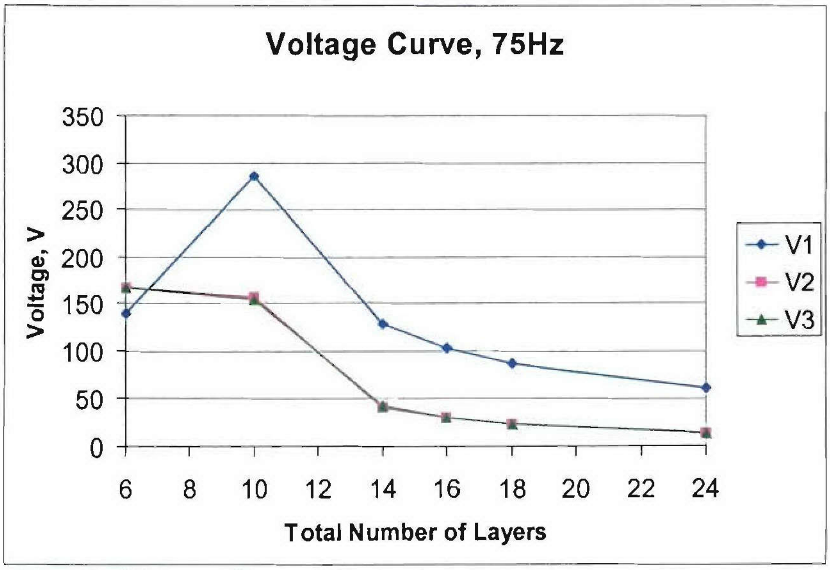

Figure 4.59. *The Voltage Curve(V_{FEA}), showing the required control voltage versus total number of composite layers to obtain vibration suppression at 75Hz.*

From the Voltage Curve at 75Hz, one can see that two of the voltages are similar (V_2 and V_3). With the exception of ten total layers, the trends of all voltages (V_1, V_2, and V_3) are the same and continue to decrease as the thickness increases. The Voltage Curve for different thicknesses at 100Hz is plotted in Figure 4.60.

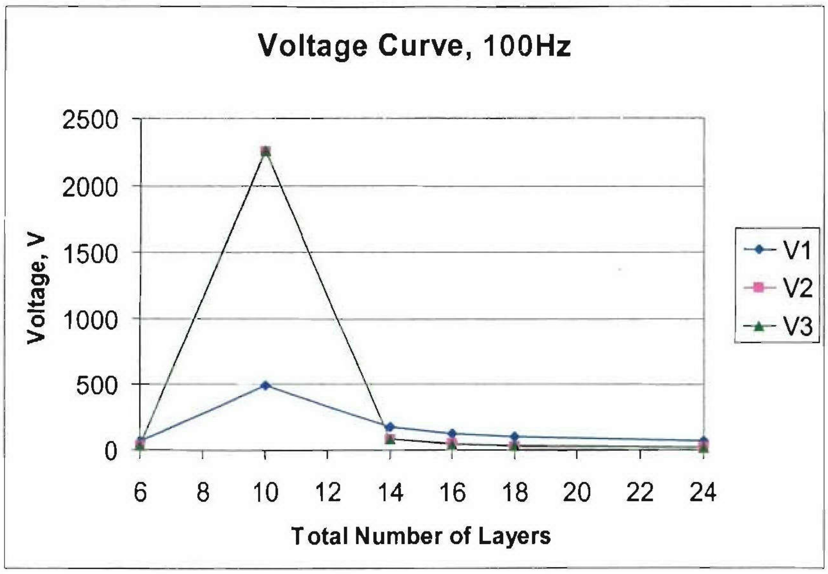

***Figure 4.60**. The Voltage Curve (V_{FEA}), showing the required control voltage versus total number of composite layers to obtain vibration suppression at 100Hz.*

From the Voltage Curve at 100Hz, one can see that two of the voltages are similar (V_2 and V_3). With the exception of ten total layers, the trends of all voltages (V_1, V_2, and V_3) are the same and continue to decrease as the thickness increases. Figures 4.61 through 4.64 contain the same plots of control voltage versus total number of layers for frequencies of 25, 50, 75, and 100Hz with the conversion factors, given in Equation (4.51), applied.

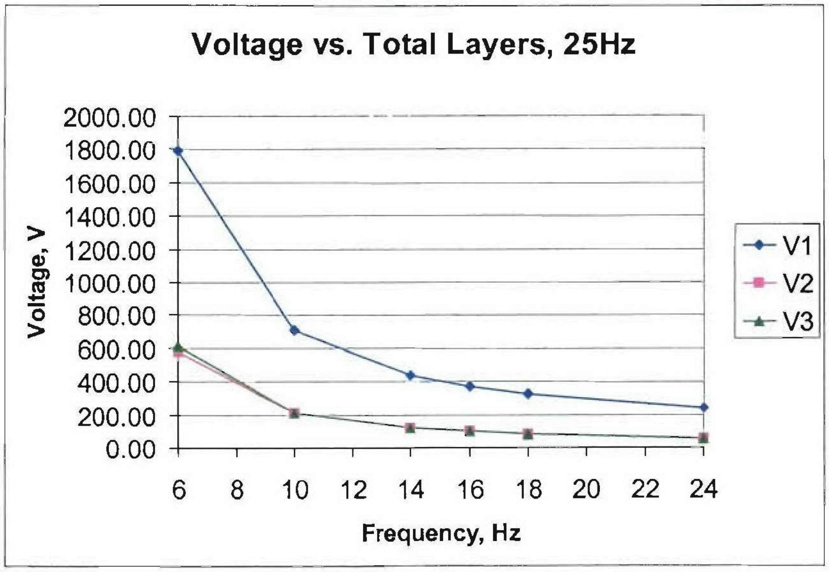

***Figure 4.61**. The Voltage Curve (V_{actual}), showing the required control voltage versus total number of composite layers to obtain vibration suppression at 25Hz.*

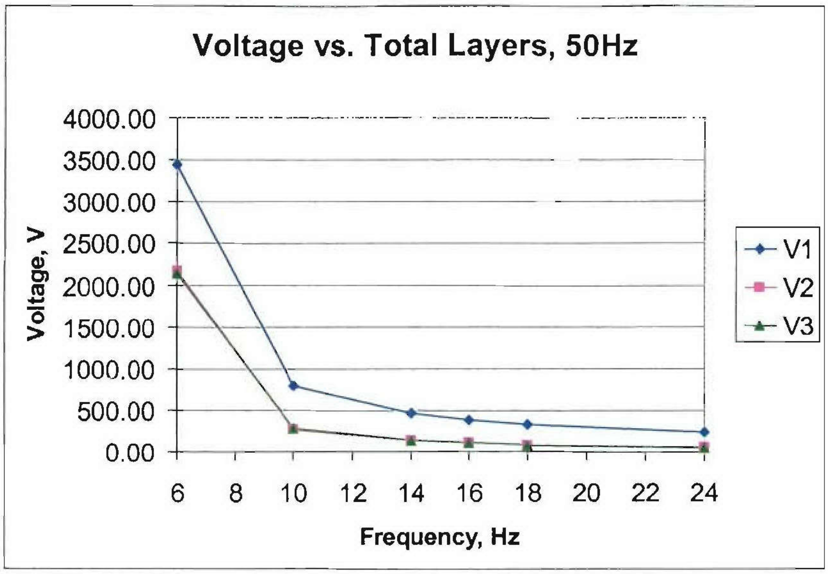

Figure 4.62. *The Voltage Curve (V_{actual}), showing the required control voltage versus total number of composite layers to obtain vibration suppression at 50Hz.*

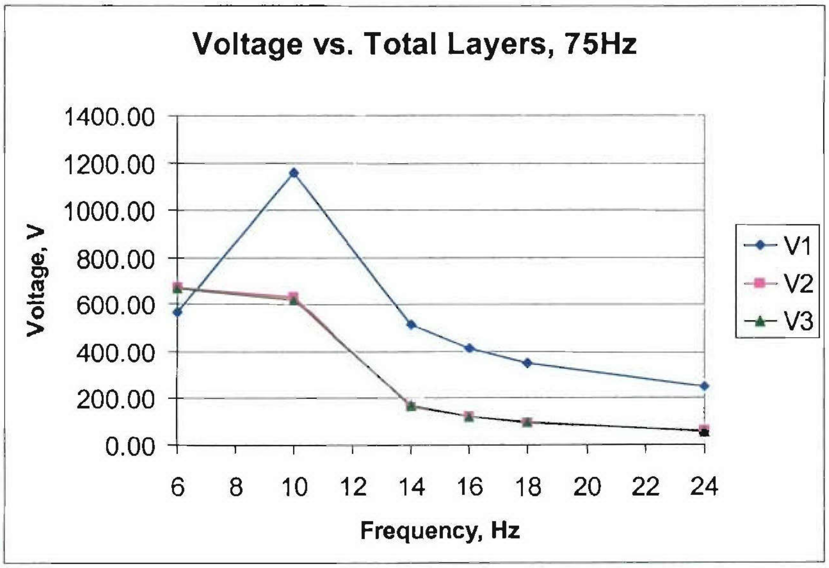

Figure 4.63. *The Voltage Curve (V_{actual}), showing the required control voltage versus total number of composite layers to obtain vibration suppression at 75Hz.*

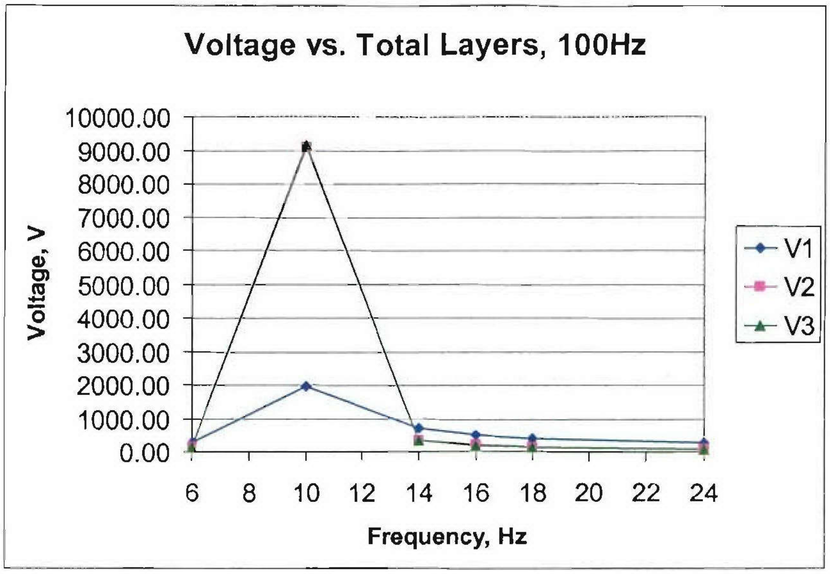

***Figure 4.64**. The Voltage Curve (V_{actual}), showing the required control voltage versus total number of composite layers to obtain vibration suppression at 100Hz.*

4.6.2.3. Circular ACP Modeling with Brackets for 8 Different Actuator Configurations

With the changes to the boundary conditions and the addition of aluminum brackets on the circular panel, there was no certainty that the Triangle 1 configuration would still remain the best possible configuration for the circular ACP. This resulted in the development of eight different configurations of the top circular ACP, i.e., three star configurations and five triangle configurations. (2) Star 2: the diameter of the ACP was increased to 63.6 cm due to the second star configuration which required the piezoelectric patches to be inline with the thruster attachments and the ACS ball joint (see Figure 44.4b). (1) Star 1: this is the first star configuration that has the embedded piezoelectric patches arrayed in a similar design as the Star 2 configuration, but rotated to be non-inline with the thruster attachments and ACS ball joints. (3) Star 3: the third star configuration (Star 2 Optimized) has the same configuration of embedded piezoelectric patches as the Star 2 configuration and removes as much composite material as possible to make the panel lighter (basically removing the composites in between the star piezos, leaving more of a star shape rather than a circle). (4) Triangle 1: the first triangle configuration has the same configuration as all the previous analysis with the embedded piezoelectric patches being the closest to the center of the circular ACP, but with the enlarged circular dimension (i.e., 63.3 cm in diameter). (5) Triangle 2: the second triangle configuration has the same configuration of embedded piezoelectric patches as Triangle 1 with the patches being the furthest away from the center of the circular ACP as possible. (6) Triangle 3: the third triangle configuration has the same configuration of embedded piezoelectric patches as Triangle 1 with the patches located in between the locations of Triangle 1 and Triangle 2. (7) Triangle 4: the fourth triangle configuration (Triangle 1 Optimized) has the same configuration of embedded piezoelectric patches as Triangle 1 and removes as much composite material as possible to make the panel lighter (basically removing all around the panel, and hence making the ACP the smallest circle possible, i.e., 32.5 cm in diameter). (8) Triangle 5: the fifth triangle configuration

(Triangle 1 Current) has the same Triangle 1 configuration of embedded piezoelectric patches and is the model that is currently being used in all previous analyses (i.e., 42 cm in diameter).

Harmonic analysis is performed at 25Hz with the simulated thruster loading of one pound of force calculated from the thruster vector misalignment, as explained earlier. The loading is applied to the thruster attachments as shown previously in Figure 4.52. All analyses in this section for each configuration were performed with six total layers of composite material.

Two scenarios were considered in this section: (a) thruster vibration suppression to perform TVC, and (b) to isolate the vibration coming from the thruster transmitting in the satellite. In case (a), the vibration of the thruster attachment location should be suppressed, i.e., reducing D_{P1}, D_{P2}, and D_{P3} (i.e., the displacements within each of the three circular sections of the thruster attachment) to zero. In case (b), the force resultants at the three locations of the top ACS attachments to the circular ACP (i.e., F_{P1}, F_{P2}, and F_{P3}) should be reduced to zero.

To find V_1, V_2, and V_3, i.e., the three actuator pairs control voltages, for case (a), which is the thruster vibration suppression, an approach similar to the one explained for Equation (4.50) is used. To find V_1, V_2, and V_3, i.e., the three actuator pairs control voltages, for case (b), which vibration suppression at the ACS ball joints by eliminating the vibration transmissibility from the thruster to the satellite, an analogous approach to the one used for equation (4.50) is used, except here the force resultants at the ACS ball joint locations should vanish. This approach is explained in the following. The harmonic analysis is performed at 25Hz with load only and the force resultants at the ACS ball joints are observed. The force resultants of the ball joints are denoted as F_{P1}, F_{P2}, and F_{P3}. Next, an arbitrary value of voltage is applied to one pair of actuators and the harmonic analysis is run without loading and the force resultants at the three ACS ball joints are noted. This step is repeated for the two remaining pairs of actuators. Since the relationship between force resultant and voltage is nearly linear, ratios for voltage to force resultant can be calculated. The configuration has nine ratios, that is, for each actuator there are three ratios, one for point one, one for point two, and the other for point three. The ratios are denoted as $r_{1,P1}$, $r_{1,P2}$, $r_{1,P3}$, $r_{2,P1}$, $r_{2,P2}$, $r_{2,P3}$, $r_{3,P1}$, $r_{3,P2}$, and $r_{3,P3}$. The ratios are calculated by simply dividing force resultant of the point by the input voltage. Then dividing the load-only force resultant of the corresponding point by each ratio gives the voltage required for suppression of that particular point. The voltage required for suppression are denoted as V_1, V_2, and V_3. These voltages can be applied in a number of different voltage schemes to provide vibration suppression to the structure (Russ and Ghasemi-Nejhad, 2002a; Doherty and Ghasemi-Nejhad, 2005; Ghasemi-Nejhad et al., 2005a); however, the Constant Voltage scheme uses a constant voltage to one or all of the actuators across the frequency interval. The voltage to each of the actuators does not necessarily have to be the same value. The determination of the appropriate value is difficult since the variation of voltages across the frequency range is large and there is no one value that is representative of all the voltages. The voltages are calculated by solving the following set of linear equations simultaneously at each frequency:

$$\begin{bmatrix} r_{1,P1} & r_{2,P1} & r_{3,P1} \\ r_{1,P2} & r_{2,P2} & r_{3,P2} \\ r_{1,P3} & r_{2,P3} & r_{3,P3} \end{bmatrix} \begin{bmatrix} V_1 \\ V_2 \\ V_3 \end{bmatrix} = \begin{bmatrix} -F_{P1} \\ -F_{P2} \\ -F_{P3} \end{bmatrix} \tag{4.52}$$

In Equation (4.52), the right-hand-side is negative to provide out-of-phase force resultants for V_1, V_2, and V_3 compared to the external disturbance (Russ and Ghasemi Nejhad, 2002a; Doherty and Ghasemi-Nejhad, 2005; Ghasemi Nejhad et al., 2005a). Applying the calculated voltages, V_1, V_2, and V_3, at each frequency delivers force resultant transmissibility suppression for all three points.

The results from these analyses are plotted in Figures 4.65 and 4.66 with the numerical results tabled in Tables 4.9 and 4.10. Figure 4.65 contains the control voltage curve versus shape configuration for vibration suppression using the force resultant (i.e., Equation (4.52)). The numbers on the x-axis refer to the different eight configurations explained earlier. Number 1 is the Star 1 configuration that has the piezoelectric patches non in-line with the thruster attachments and ACS ball joints (with 63.3 cm in diameter), Number 2 is the Star 2 configuration that has the piezoelectric patches in-line with the thruster attachments and ACS ball joints (with 63.3 cm in diameter), Number 3 is the Triangle 1 configuration that has the piezoelectric patches closest to the central support arranged in a fashion that resembles a triangle (with 63.3 cm in diameter), Number 4 is the Triangle 2 configuration that has the piezoelectric patches furthest away from the central support (with 63.3 cm in diameter), Number 5 is the Triangle 3 configuration that has the piezoelectric patches midway between the Triangle 1 and Triangle 2 configurations (with 63.3 cm in diameter), Number 6 is the Star 2 Optimized configuration that has the same configuration as Star 2 with as much composite material removed from the between the Stars as possible (with 63.3 cm in diameter), Number 7 is the Triangle 1 Optimized configuration that has the same configuration as Triangle 1 with as much composite material removed as possible (with 32.5 cm in diameter), and Number 8 is the Triangle 1 Current configuration that has the same configuration as the analyses being previously conducted (with 42 cm in diameter). The above 8 shape configurations are shown schematically in Figure 4.67. Figure 4.66 contains the control voltage curve versus shape configuration for thruster vibration control (i.e., Equation (4.50)).

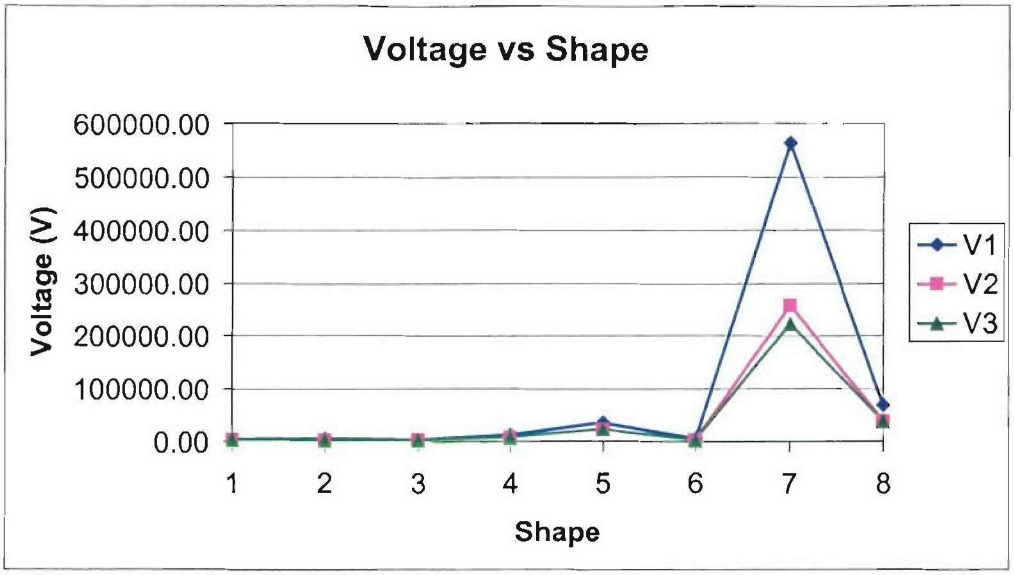

Figure 4.65. *The Voltage Curve, showing the required control voltage versus piezoelectric shape configuration to obtain vibration suppression using the force resultant at the ACS ball joints at 25Hz.*

Table 4.9. *Control voltage values to obtain vibration suppression using the force resultant at the ACS ball joint at 25Hz. The numbers denote the corresponding shape configuration number in Figure 4.65.*

#		V1	V2	V3
1	Star 1	2855.59	2094.46	2180.48
2	Star 2	3824.68	1744.73	1656.24
3	Triangle 1	2413.46	1147.92	1121.38
4	Triangle 2	10181.50	7261.21	7506.58
5	Triangle 3	35696.10	21750.90	22250.20
6	Star 2 Optimized	4893.51	2637.64	2665.88
7	Triangle 1 Optimized	563649.00	256843.00	222257.00
8	Triangle 1 Current	68347.70	37097.70	36321.50

For the case of vibration suppression using the force resultant, the worst case is Triangle 1 Optimized (i.e., Number 7) configuration and the best case is the Triangle 1 (i.e., Number 3) configuration.

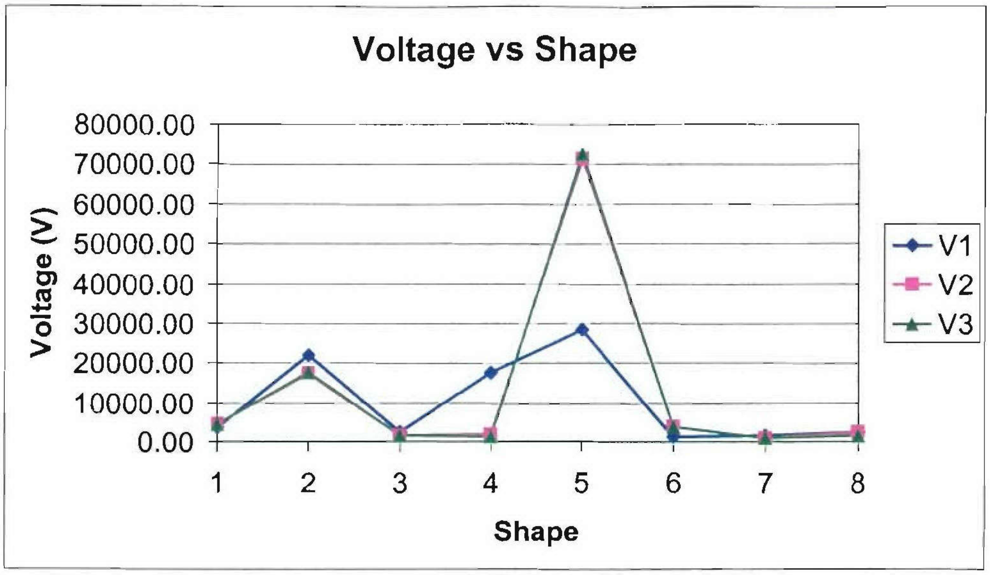

Figure 4.66. *The Voltage Curve, showing the required control voltage versus piezoelectric shape configuration for thruster vibration suppression at 25Hz.*

Table 4.10. *Control voltage values for thruster vibration suppression at 25Hz. The numbers denote the corresponding shape configuration number in Figure 4.66.*

#		V1	V2	V3
1	Star 1	3442.17	4245.10	4337.59
2	Star 2	21880.00	17271.80	17495.10
3	Triangle 1	2378.00	1363.66	1362.55
4	Triangle 2	17566.60	1865.65	1165.11
5	Triangle 3	28342.10	71284.60	72318.10
6	Star 2 Optimized	1077.57	3786.19	3813.48
7	Triangle 1 Optimized	1534.41	993.50	1012.88
8	Triangle 1 Current	2279.16	2290.29	1590.90

For the case of thruster vibration suppression, the worst case is the Triangle 3 (Number 5) configuration and the best case is the Triangle 1 Optimized (Number 7) configuration. It should be noted that if the goal is to isolate the thruster vibration from the satellite, i.e., the use of Equation (4.52), Figure 4.65, and Table 4.9, then the performance of our current plate (Number 8) is relatively worse than others other than the worst one (Number 7). However, if the goal is the Thrust Vector Control (TVC), i.e., the use of Equation (4.50), Figure 4.66, and Table 4.10, then the performance of our current plate (Number 8) is among the bests (Numbers 3, 4, 6, and 7), taking into account that Numbers 3, 4, and 6 are too large for our platform and Number 7 is too small, considering other platform design issues.

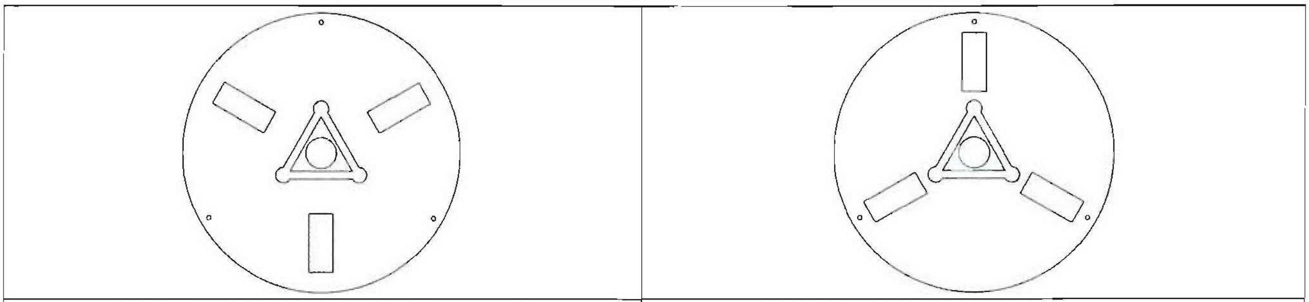

(1) Star 1 (63.3 cm in diameter)

(2) Star 2 (63.3 cm in diameter)

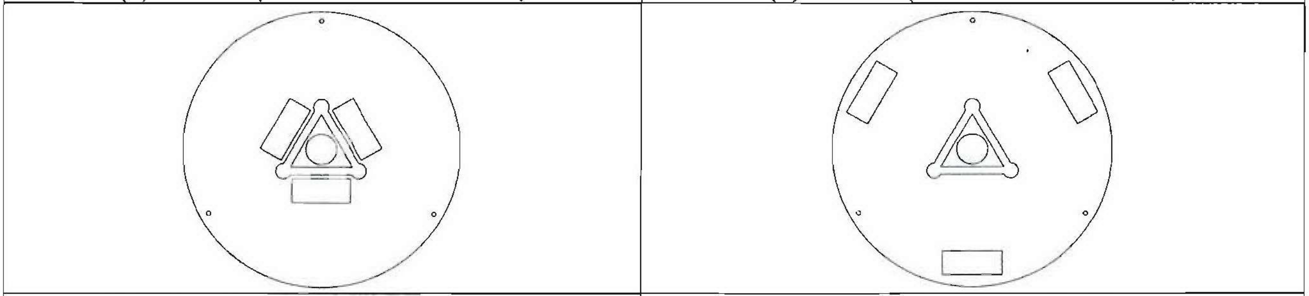

(3) Triangle 1 (63.3 cm in diameter)

(4) Triangle 2 (63.3 cm in diameter)

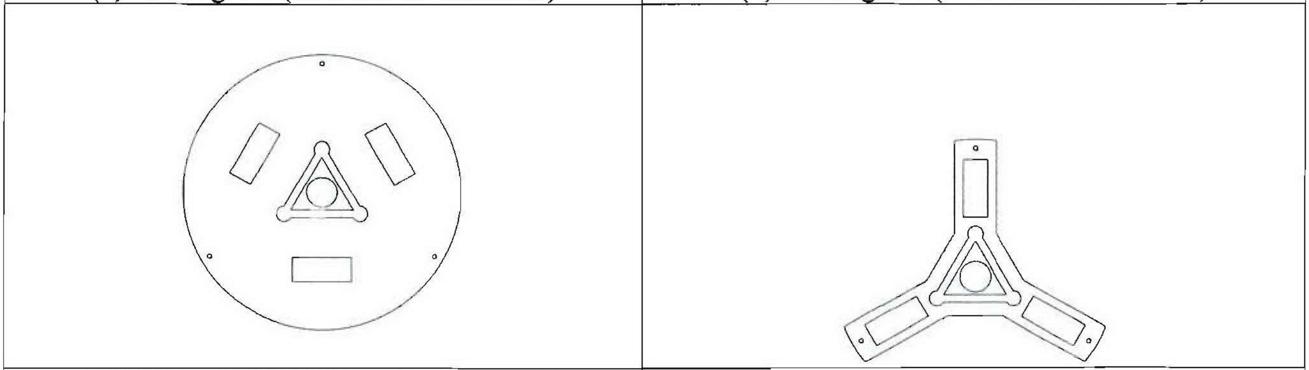

(5) Triangle 3 (63.3 cm in diameter)

(6) Star 3 (63.3 cm in diameter)

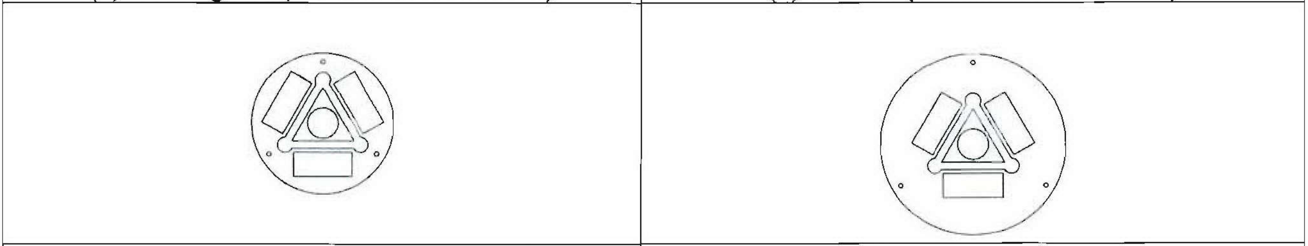

(7) Triangle 1 Optimized (32.5 cm in diameter)

(8) Triangle 1 Current (42 cm in diameter)

***Figure 4.67**. Eight different shape configurations considered for the optimization.*

4.6.2.4. ACP VS Design Considering the Effects of Damping

Since in real life, the satellite will have some level of damping, the next step of the analysis employs the Triangle 1 Current (Number 8) configuration and adds a damping ratio of one percent (i.e., 0.01) to the entire structure. This allows us to find the optimum control voltage and phase required for vibration suppression.

Harmonic analysis is performed at 25Hz with the simulated thruster loading of one pound of force calculated from the thruster vector misalignment, as explained earlier. The loading is applied to the thruster attachments as shown previously in Figure 4.52. The analysis was conducted with six total layers of composite material.

Once again, the two approaches for these analyses were thruster vibration suppression (i.e., Equation (4.50)) and the satellite vibration suppression using the force resultant (i.e., Equation (4.52)). The first analysis was thruster vibration suppression performed by selecting one point within each of the three circular sections of the thruster attachment, denoted as D_{P1}, D_{P2}, and D_{P3}. Next, an arbitrary value of voltage is applied to one pair of the actuators and the harmonic analysis is run without loading and the displacements of those three points are noted, both the real and imaginary values of the displacement. This step is repeated for the two remaining pairs of actuators. These values for real and imaginary displacements are denoted as $D_{P1_r} + D_{P1_i}$, $D_{P2_r} + D_{P2_i}$, and $D_{P3_r} + D_{P3_i}$. Since the relationship between displacement and voltage is nearly linear, ratios for voltage to displacement can be calculated. Each configuration has nine ratios, that is, for each actuator there are three ratios, one for point one, one for point two, and the other for point three. The ratios are denoted as $r_{1,P1r}$, $r_{1,P1i}$, $r_{1,P2r}$, $r_{1,P2i}$, $r_{1,P3r}$, $r_{1,P3i}$, $r_{2,P1r}$, $r_{2,P1i}$, $r_{2,P2r}$, $r_{2,P2i}$, $r_{2,P3r}$, $r_{2,P3i}$, $r_{3,P1r}$, $r_{3,P1i}$, $r_{3,P2r}$, $r_{3,P2i}$, $r_{3,P3r}$ and $r_{3,P3i}$; where r denotes the real part of the ratio and i denotes the imaginary part. The ratios are calculated by simply dividing displacement of the point by the input voltage. The voltage required for suppression will be denoted as V_{1_r}, V_{1_i}, V_{2_r}, V_{2_i}, V_{3_r} and V_{3_i}; where, again, r denotes the real part of the ratio and i denotes the imaginary part. These voltages can be applied in a number of different voltage schemes to provide vibration suppression to the structure (Russ and Ghasemi-Nejhad, 2002a; Doherty and Ghasemi-Nejhad, 2005; Ghasemi-Nejhad et al., 2005a); however, the only scheme used for this analysis was the Constant Voltage scheme. The Constant Voltage scheme uses a constant voltage to one or all of the actuators across the frequency interval. The voltage to each of the actuators does not necessarily have to be the same value. The determination of the appropriate value is difficult since the variation of voltages across the frequency range is large and there is no one value that is representative of all the voltages. The voltages are calculated by solving the following set of linear equations simultaneously at each frequency:

$$\begin{bmatrix} r_{1,P1r} + r_{1,P1i} & r_{2,P1r} + r_{2,P1i} & r_{3,P1r} + r_{3,P1i} \\ r_{1,P2r} + r_{1,P2i} & r_{2,P2r} + r_{2,P2i} & r_{3,P2r} + r_{3,P2i} \\ r_{1,P3r} + r_{1,P3i} & r_{2,P3r} + r_{2,P3i} & r_{3,P3r} + r_{3,P3i} \end{bmatrix} \begin{bmatrix} V_{1_r} + V_{1_i} \\ V_{2_r} + V_{2_i} \\ V_{3_r} + V_{3_i} \end{bmatrix} = \begin{bmatrix} -(D_{P1_r} + D_{P1_i}) \\ -(D_{P2_r} + D_{P2_i}) \\ -(D_{P3_r} + D_{P3_i}) \end{bmatrix} \qquad (4.53)$$

In Equation (4.53), the right-hand-side is negative to provide out-of-phase displacements for V_1, V_2, and V_3 compared to the external disturbance (Russ and Ghasemi Nejhad, 2002a; Doherty and Ghasemi-Nejhad, 2005; Ghasemi Nejhad et al., 2005a). Applying the calculated voltages, V_1, V_2, and V_3, at each frequency delivers vibration suppression for all three points.

An alternative approach to Equation (4.53) where the real and imaginary parts of D and V are calculated, is to determine the magnitude and phase of D and V, and is explained in the following. Therefore, for the first analysis which is the thruster vibration suppression the procedure is performed by selecting one point within each of the three circular sections of the thruster attachment, denoted as D_{P1}, D_{P2}, and D_{P3}. Next, an arbitrary value of voltage is applied to one pair of the actuators and the harmonic analysis is run without loading and the displacements of those three points are noted, both the magnitude and phase. This step is repeated for the two remaining pairs of actuators. The phase of the displacement is accounted for by using the equation of $D_{Px}e^{\phi_d i}$, where D_{Px} is the magnitude of the displacement for point x and ϕ_d is the phase of the displacement. This complex number is used with the assumption that the relationship between displacement and voltage is nearly linear, to obtain ratios for voltage to displacement. Each configuration has nine ratios, that is, for each actuator there are three ratios, one for point one, one for point two, and the other for point three. The ratios are denoted as $r_{1,P1}e^{\phi_r i}$, $r_{1,P2}e^{\phi_r i}$, $r_{1,P3}e^{\phi_r i}$, $r_{2,P1}e^{\phi_r i}$, $r_{2,P2}e^{\phi_r i}$, $r_{2,P3}e^{\phi_r i}$, $r_{3,P1}e^{\phi_r i}$, $r_{3,P2}e^{\phi_r i}$, and $r_{3,P3}e^{\phi_r i}$. The ratios are calculated by simply dividing displacement of the point by the input voltage. Then, dividing the load-only displacement of the corresponding point by each ratio gives the voltage required for suppression of that particular point. The voltage required for suppression will be denoted as $V_1e^{\phi_v i}$, $V_2e^{\phi_v i}$, and $V_3e^{\phi_v i}$; where V_x is the magnitude of the voltage required for suppression of point x and ϕ_v is the phase of the voltage. These voltages can be applied in a number of different voltage schemes to provide vibration suppression to the structure (Russ and Ghasemi-Nejhad, 2002a; Doherty and Ghasemi-Nejhad, 2005; Ghasemi-Nejhad et al., 2005a); however, the only scheme used for this analysis was the Constant Voltage scheme. The Constant Voltage scheme uses a constant voltage to one or all of the actuators across the frequency interval. The voltage to each of the actuators does not necessarily have to be the same value. The determination of the appropriate value is difficult since the variation of voltages across the frequency range is large and there is no one value that is representative of all the voltages. The voltages are calculated by solving the following set of linear equations simultaneously at each frequency:

$$\begin{bmatrix} r_{1,P1}e^{\phi_r i} & r_{2,P1}e^{\phi_r i} & r_{3,P1}e^{\phi_r i} \\ r_{1,P2}e^{\phi_r i} & r_{2,P2}e^{\phi_r i} & r_{3,P2}e^{\phi_r i} \\ r_{1,P3}e^{\phi_r i} & r_{2,P3}e^{\phi_r i} & r_{3,P3}e^{\phi_r i} \end{bmatrix} \begin{bmatrix} V_1e^{\phi_v i} \\ V_2e^{\phi_v i} \\ V_3e^{\phi_v i} \end{bmatrix} = \begin{bmatrix} -D_{P1}e^{\phi_d i} \\ -D_{P2}e^{\phi_d i} \\ -D_{P3}e^{\phi_d i} \end{bmatrix} \tag{4.54}$$

In Equation (4.54), the right-hand-side is negative to provide out-of-phase displacements for V_1, V_2, and V_3 compared to the external disturbance (Russ and Ghasemi Nejhad, 2002a; Doherty and Ghasemi-Nejhad, 2005; Ghasemi Nejhad et al., 2005a). Applying the calculated voltages, $V_1e^{\phi_v i}$, $V_2e^{\phi_v i}$, and $V_3e^{\phi_v i}$, at each frequency delivers vibration suppression for all three points.

The second approach was vibration suppression at the ACS ball joints to suppress the vibration transmissibility from the thruster to the satellite . Similar procedures as explained earlier can be applied to arrive at an equation similar to Equation (4.53) in terms of real and imaginary parts where in the right-hand-side in Equation (4.53), D should be replaced by F. Likewise, if the alternative magnitude and phase approach is used here, one will arrive at an equation similar to Equation (4.54) where in the right-hand-side in Equation (4.54), D should be replaced by F and obviously ϕ_d by ϕ_F.

The results from these analyses are shown numerically in Tables 4.11 and 4.12. These tables show that when there is damping present in the structure, the control voltage for vibration suppression using the force resultant increases by less than one percent and there is no phase change involved. Also, when there is damping present in the structure, the control voltage for thruster vibration suppression increases for V1 and V2 and decreases for V3. The increase in the control voltage for thruster vibration suppression is less than one percent and the decrease in control voltage for thruster vibration suppression is slightly more than one percent. The phase change experienced in the structure with damping is very minimal with most of the control voltages still being applied almost exactly 180 degrees out of phase with the external disturbance.

Table 4.11. *Control voltage values to obtain vibration suppression using the force resultant at 25Hz.*

	V1	V2	V3
Without Damping	68347.70	37097.70	36321.50
With Damping	68389.80	37120.80	36343.80

Table 4.12. *Control voltage values as well as the phase required for thruster vibration suppression at 25Hz.*

	V1	V2	V3
Without Damping	2279.16	2290.29	1590.90
With Damping	2282.55	2297.07	1567.22
Phase for Damping	179.96	179.91	179.58

4.6.2.5. Conclusions

The results from the analyses presented here showed that the Number 8 (Triangle 5, i.e., Current Design, shown in Figure 4.56) configuration satisfies most of the design and performance requirements. Particularly, for TVC application and the vibration suppression that comes from the thruster. Also, Figures 4.61 to 4.64 show that the actual actuator voltage requirement for our case (i.e., a lateral vibration coming from a total force of 1 lbs coming from the thruster) is less than 500 volts for all three pairs of AFC actuators (i.e., six back-to-back AFC actuators) working in tandem for an ACP with 18 total layers of plain weave carbon/epoxy composites (i.e., our circular ACP) (Sakagawa and Ghasemi-Nejhad, 2005).

PART II (Phase II: June 2002 – May 2005)

5. MODIFIED STEWART PLATFORM (MSP)

(Nejhad, Antin, Mitchell, Askari, Bletcha, Russ, Ma)

5.1. MSP Configurations

Phase I was completed in 2002 and showed promising results for the use of ACP and ACS in an adaptive composite platform with simultaneous precision positioning and vibration suppression for their use in a thrust vector control (TVC) application for spacecrafts, in general, and satellites, in particular. Phase II incorporated ACP and ACS technology in the design, analysis, fabrication, and testing of the adaptive composite platform with simultaneous precision positioning and vibration suppression of a satellite thruster TVC application. This platform is now fully designed, analyzed, fabricated, assembled and is in the initial stages of testing. Simulation results show that it can simultaneously suppress thruster vibration and control the thrust vector with a pointing accuracy better than 1 arc minute. It can also suppress the vibration of the satellite by minimizing or eliminating the transmissibility of the vibration from thruster to the satellite. The following explains the use of various piezoelectric stack and patch actuators to achieve the above objectives. a) The top device plate has nine AFC piezo patches. Six of them are wide (2") with a triangular configuration (i.e., the Triangle 1 Current Configuration shown in Figure 4.67, Number 8) of three back-to-back pair actuators and working in tandem to suppress the vibration of the thruster. Three of these actuators are place in a layer just below the top layer and the other three actuators are placed back-to-back, with respect to the top three, in a layer just above the bottom layer. The three narrower (0.5") piezo patch sensors are place just next to the three actuators in the bottom layer and towards the outer edge of the plate (see Figure 4.56). b) The three precision motors with micron accuracies are used to position the top plate. c) The three piezoelectric stack actuators in the three struts (i.e., one in each) and one piezoelectric stack actuator in the central support participate in the vibration suppression of the satellite by minimizing or eliminating the transmissibility of the vibration from the thruster into the satellite.

The ACS, ACP, and MSP have the following attributes:

1. Simultaneous vibration suppression and precision position with SISO/MIMO Controls
2. Power off and hold capability (Struts)
3. Load bearing capability
4. DC-100 Hz band-width
5. Low power consumption
6. Well-integrated sensor/actuator with control system
7. Rapid response time
8. Compact and light weight
9. Milli/micro displacements with micro resolution/accuracy
10. Robust and versatile

The completed platform will be fully tested in the initial stage of the ADPICAS Phase III project. The following explains the MSP development from design and analysis to manufacturing and assembly.

5.2. Modified Stewart Platform (MSP) Design and Analysis

(Nejhad, Antin, Mitchell, Askari, Bletcha)

Figure 5.1 shows the MSP developed in ADPICAS Phase II in the Department of Mechanical Engineering of the University of Hawaii at Manoa (UHM). Figure 5.2 shows the developed UHM MSP with the thruster in place. Figure 5.3 shows the platform in its untilted and tilted positions. The thruster force in this application is 100 lbs which is a static force. It is estimated that the dynamic part of the axial thruster is 10 lbs (i.e., 10% of the static force), and its lateral dynamic component is 1 lb (i.e., 10% of the axial dynamic load). We have shown that in the untilted configuration (see Figure 5.3 a), the lateral and axial vibrations can be controlled by the four piezo stacks in the three struts and the central support. However, if the platform is tilted (see Figure 5.3 b), then while the axial vibration can be suppressed by the four piezo stacks, the lateral vibration cannot. Therefore, the MSP is designed such that the thruster vibration due to the lateral dynamic disturbances (1 lbs, here) are suppressed by three pairs (i.e., a total of six back-to-back) of AFC piezo patches in the top ACCP working in tandem, and the axial dynamic disturbances (10 lbs, here) are suppressed by three ACS and one Central Support piezo stacks. Figure 5.4 shows the UHM Modified Stewart Platform (MSP) with the thruster in place installed on a satellite.

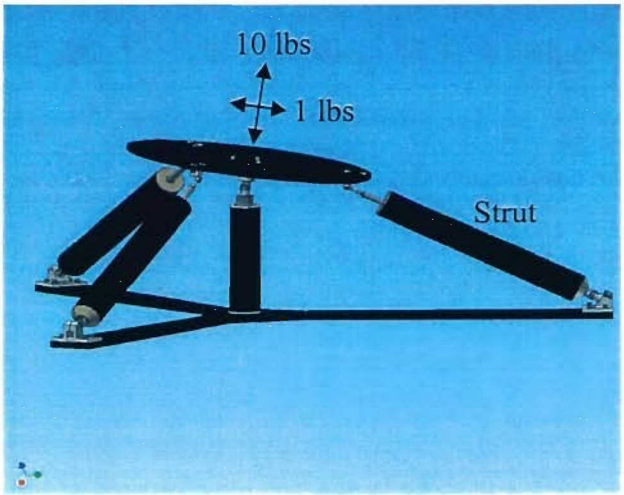

Figure 5.1. *The UHM Modified Stewart Platform (MSP).*

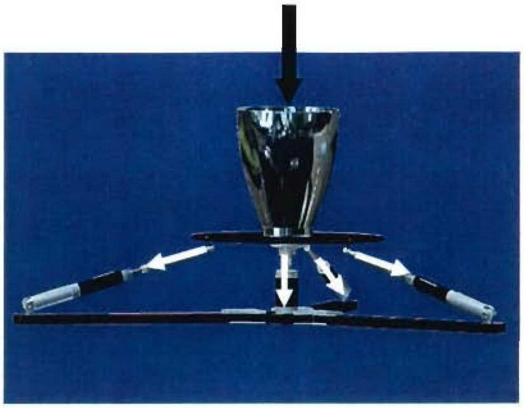

Figure 5.2. *UHM Modified Stewart Platform (MSP) with the thruster in place.*

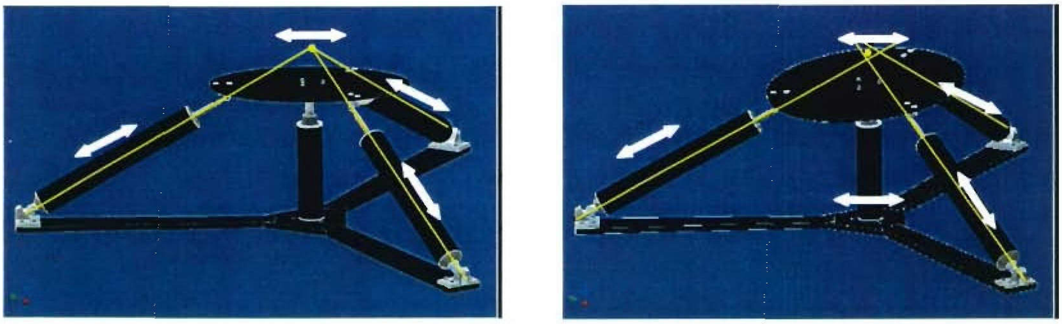

a) Untilted

b) Tilted

Figure 5.3. *UHM MSP in untilted and tilted positions.*

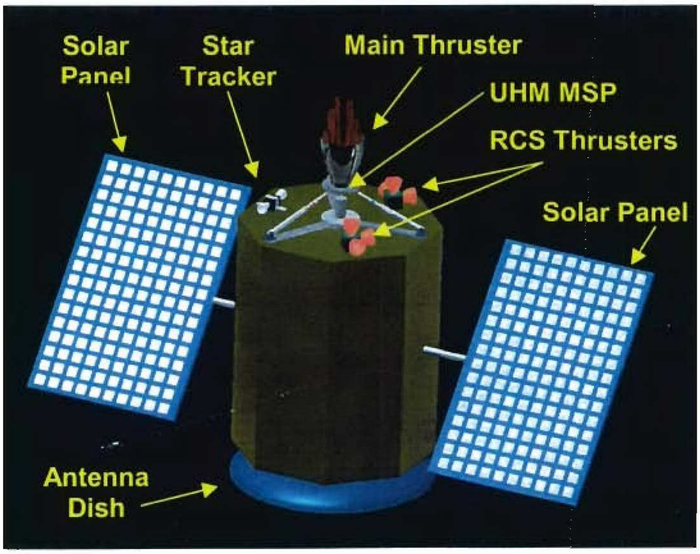

Figure 5.4. *UHM MSP with the thruster in place installed on a satellite.*

5.2.1. UHM MSP ACS Parameters Design and Analysis

To minimize the lateral load transfer to the central support from the thruster, a load analysis was performed and found that the relationship given in Figure 5.5 should exist between the thruster angle and other geometric dimensions of the platform. The following values are used for the parameters given in Figure 5.5: L=8.3", H=3" and H_j=1.3", λ can be found from Equation (5.1) and its value is 32°. Here H_c = 1.85", H_{cb} = 11.65", L_s = 19.5", L_b = 23.46". It should be noted that this configuration gives a zero lateral load to the central support if the top plate is untilted, and some small nonzero lateral load to the central support if the top plate is tilted (see Figure 5.3).

$$\tan\lambda = \frac{H + H_j}{L} \tag{5.1}$$

The worst situation in term of load for the strut appears when a misalignment is created and when the top plate is tilted to correct this misalignment. The maximum estimated misalignment of the thrust vector with respect to the axis of reference is $\Gamma_{max} = 6°$. Therefore, the worst situation for the strut is Γ=6° and Φ = -6° (see Figure 5.6). Here, λ = 32° obtained from Equation (5.1).

In these conditions, $\boxed{F_{strut\ max} = 9.2 \text{ lbs} = 41\text{N} < 100\text{N}}$

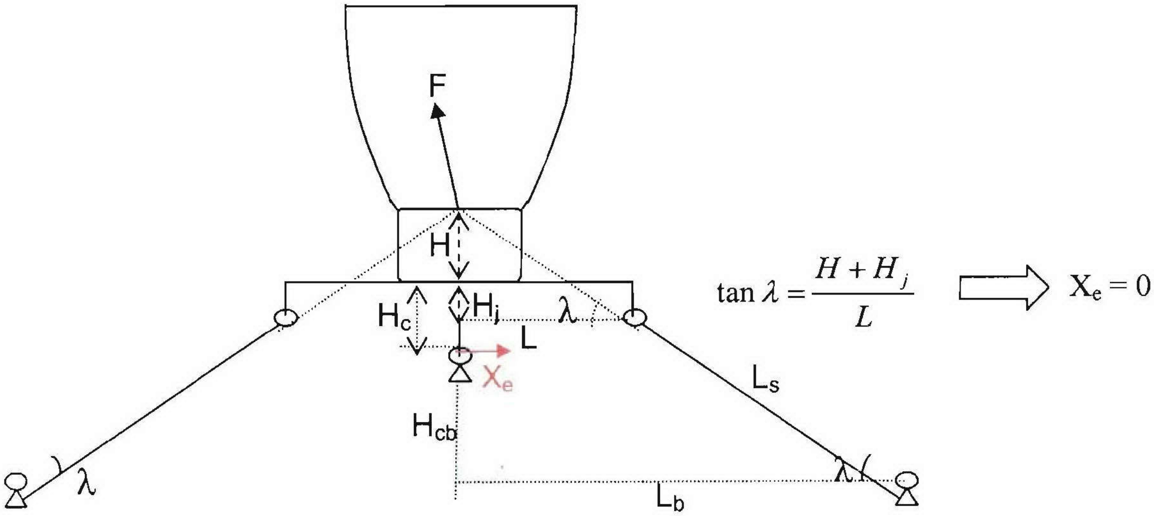

Figure 5.5. UHM MSP optimum ACS angle.

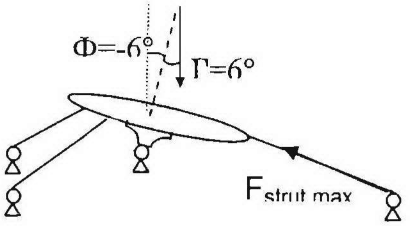

Figure 5.6. UHM MSP worst-case ACS load.

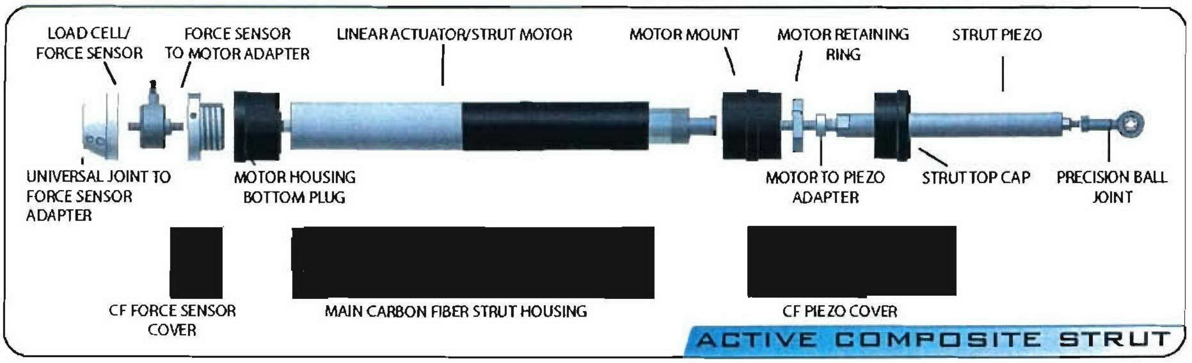

Figure 5.7. ACS exploded view.

Figure 5.7 shows the ACS exploded view with its components in place. The load cell senses vibrations characterized by changes in compressive loading. The ACS piezo stack can use this data to damp the vibration. Since the strut is meant to prevent vibration from reaching the base of the UHM platform and in turn the satellite, the load cell was placed as close to the base end of the strut as possible. The housing is composed of three composite segments, where the motor housing segments, in the ACS middle in Figure 5.7, is the only load bearing composite housing here and allows the motor to be removed without complete disassembly of the strut. The upper (right in Figure 5.7) and lower (left in Figure 5.7) composite housings are removable and serve only to protect the piezo stack actuator and load cell sensor, respectively. All wiring is contained within the main strut housing. The ball joints used for the connection of the top of the strut to the platform top plate are slated to be precision Uniflon® tight bearing fit rod ends to minimize joint play. The base mounted end of the strut pivots on an Apex Military Standard Universal Joints (model MS-20270-B12) which has precise tolerances and allows only a minimal 0.53 degrees of torsional play. Adapters were required to connect the various components together. All composites used in this work are plain weave carbon/epoxy woven prepreg composite.

5.2.2. UHM MSP Composite Component Design and Analysis

ANSYS (2004) FEA was carried out on the top device composite plate and strut composite housing and it was found that the factors of safety were over 100, and hence these structure design were mainly due to their dynamics and geometric requirement conditions rather than static loading. The strut composite housing was in three segments (see Figure 5.7). The central support composite housing does not take any load and is primarily a cover for the central support piezoelectric stack that takes the axial loading due to the thruster firing (see Figure 5.8). The metal-to-metal, composite-to-metal, and composite-to-composite bolted and adhesive joints were analyzed to ensure the performance of the joints and the integrity of the structure. Also accordingly, the composite components stacking sequences were optimized. All composites used in this work are plain weave carbon/epoxy woven prepreg composite.

5.2.3. UHM MSP Active Composite Central Support (ACCS) Design and Analysis

The ACCS serves dual purposes. The first purpose is to provide a stable pivot point for the top plate. The second purpose is to damp axial vibration from reaching the platform base and subsequently the satellite below. The central support is made up of nine individual components. In order for the central support to provide a stable pivot point for the top plate, it must be securely mounted to the base plate. The base mount serves to not only secure the central support to the base plate but also to serve as a mounting point for the protective composite housing which encloses the central support. The support components are stacked on top of the base support. Adapters were required to connect the various components together. The adapter for the load cell to central piezo is a two-piece stainless steel component where the piezo to universal joint adapter is constructed of aluminum to minimize weight. The pivoting responsibilities are taken care of by a custom mil-spec Apex precision universal joint. This precision universal joint allows maximum mobility with minimal joint play. In a similar design to the active strut the central support contains a load cell placed close to the platform base followed by a piezo actuator to actively damp vibration. The central support uses a higher capacity piezo than the three struts. The carbon/epoxy composite housing, here, bears no structural loading and is strictly in place to provide protection for the central support internals. The housing is easily removable and uses a floating rubber seal provide a complete seal while not passing on any vibration. All wiring is contained within the composite housing. Same composite material used for the ACS and ACP is used here, as well. Figure 5.8 shows the exploded view of the ACCS.

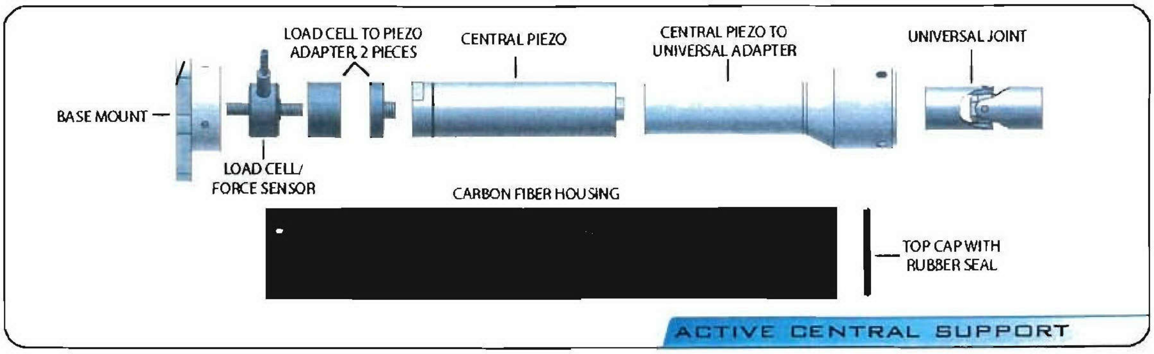

Figure 5.8. *ACCS exploded view.*

5.3. MSP Manufacturing and Assembly

(Nejhad, Askari, Russ, Bletcha)

All composites were made of 250° F and 100 psi curing temperature and pressure, respectively, prepreg in an autoclave. The composite used throughout this work was a plain weave woven carbon/epoxy prepreg with 0.01" thick ply thickness. Figure 5.9 shows the curing cycle for the woven composite prepreg used throughout this work.

5.3.1. ACS and ACCS Composite Tubular Housings

A roll-wrapping technique was used to manufacture the ACS and ACCS composite tubular housing. In this technique carbon/epoxy prepreg composite is rolled around an aluminum mandrel with the outer diameter of the mandrel being the inner diameter of the composite tube (i.e., 1.5 inches for both ACS and ACCS). When sufficient layers of composite prepreg (six layers for all tubing in this work) are wrapped over the mandrel with sufficient pull force, it is wrapped by shrink tape and cured in the autoclave. The mandrels are removed upon curing and cooling of the manufactured parts, and are subsequently trimmed to the final size.

5.3.2. UHM MSP Composite Plates

There are three different composite plates to be used in the UHM MSP. Hand lay-up composite manufacturing technique is utilized and the same Carbon/Epoxy woven prepreg (explained earlier) are used to manufacture the composite plates. These three types of plates were three trapezoidal legs, a hexagonal central-base plate, and an Active Circular Composite Plate (ACCP) with uniform thicknesses (see Figure 5.10). It should be mentioned that the composite cured ply thickness is slightly lower than as received prepreg due to the compaction and consolidation under 100 psi cure pressure.

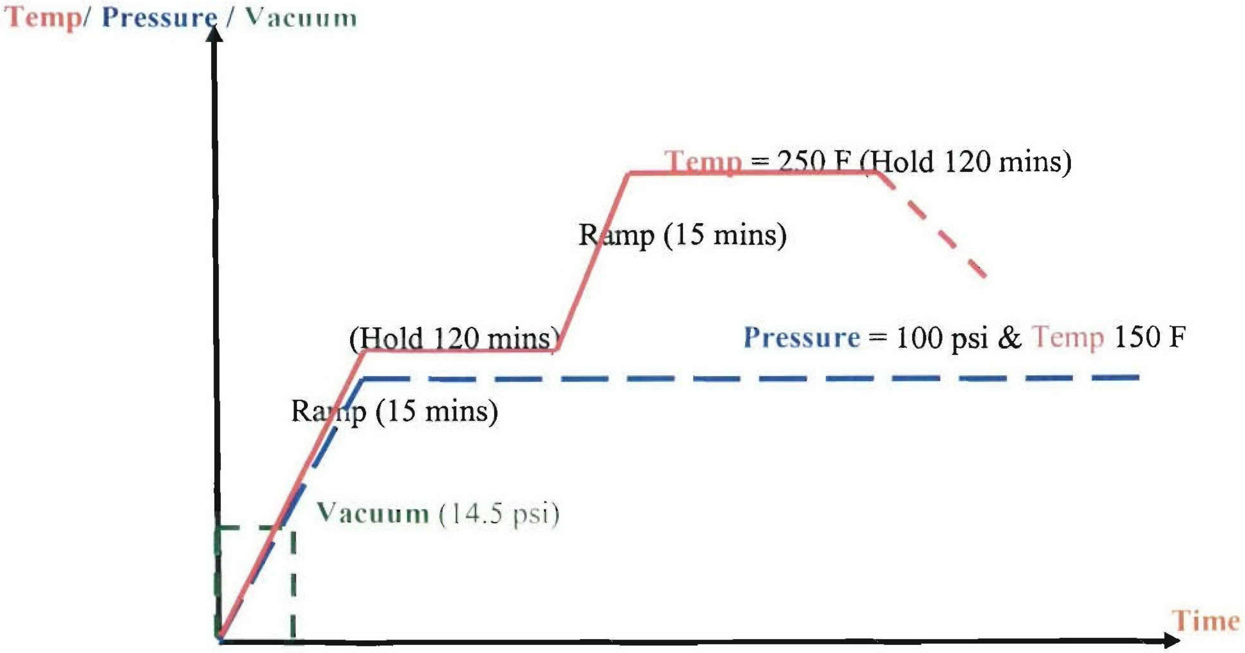

Figure 5.9. Curing cycle for the plain weave carbon/epoxy woven prepreg composite.

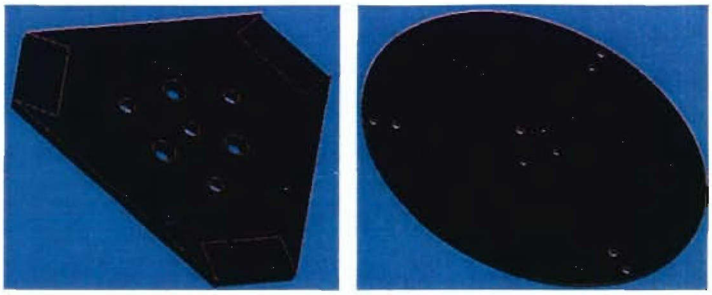

a) Central-base plate b) ACCP

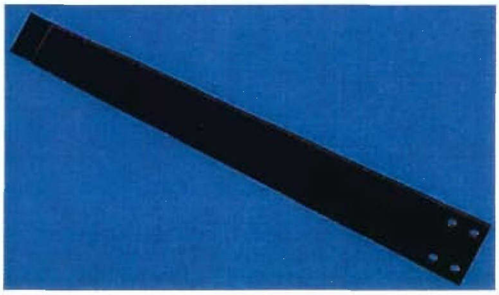

c) Legs

Figure 5.10. *UHM MSP composite plates.*

The central-base plate as well as the legs had 30 layers of woven plies to give a finished thickness of 1/4 inches. The ACCP was manufactured with six back-to-back 2” wide AFC piezoelectric patch actuators and three ½” wide AFC piezoelectric patch sensors (see Figure 4.56). The thickness of the AFCs was about 0.013’. The same Wires out by Drilled-hole technique explained in the ACP Section was used here. This technique was used here since a) the piezo patches are placed just one layer below the surface, and b) the wires had to be taken out from the surface of the ACCP as opposed the edges, since the edges had to be cut into the circular shape. 18 woven layers of 18”x18” were cut and used to manufacture the ACCP. The stacking sequence of $[0/120/240]_{3S}$ was used for the ACCP to provide quasi-isotropic effective properties for the ACCP. Figure 5.11.a shows the ACCP next to the bottom cut-out layer (i.e., the 2nd layer) with three AFC piezo actuators and another three AFC piezo sensors in place. Figure 5.11.b shows the ACCP next to the top cut-out layer (i.e., the 17th layer) with three AFC piezo actuators in place. The platform base utilizes composite construction for rigidity and light weight. The base utilizes a modular four-piece construction with a central base plate and three attached legs. The legs are joined to the central base using a precision lap joint bonded with high strength ceramic epoxy. The modular construction was used to simplify the production here, but in mass production versions of the platform a one piece base could be used.

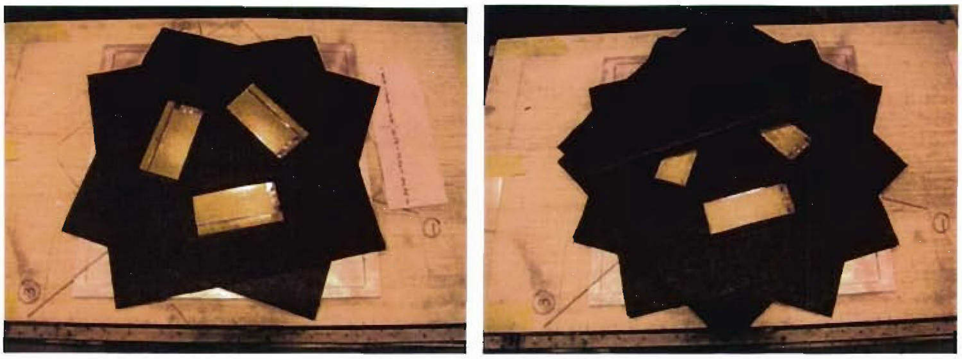

a) Piezos embedded in the 2nd layer b) Piezos embedded in the 17th layer

Figure 5.11. *ACCP embedded with nine AFC piezo actuators (six) and sensors (three).*

Manufacturing of the platform components have primarily been performed in house within the ADPICAS project. The platform consists of both metallic and carbon/epoxy plain weave composite components. The metallic parts are manufactured mainly by the University of Hawaii machine shop. Approximately a third of the parts are manufactured by using ADPICAS facilities, and a few complex parts were manufactured by Bear Machinery of Hawaii. All composite components are manufactured in the ADPICAS composites labs (i.e., AMML and ICML). The flat components such as the base plate, legs, and platform top-plate were then water jet cut by Allied Machinery of Hawaii. The composites tubing were then cut in the ADPICAS labs using a rotary diamond cutting saw. The ball joints used for the connection of the top of the strut to the platform top plate are slated to be precision Uniflon® tight bearing fit rod ends to minimize joint play. The base mounted end of the strut pivots on an Apex Military Standard Universal Joints (model MS-20270-B12) which has precise tolerances and allows only a minimal 0.53 degrees of torsional play. Similar joint but stronger was used for connecting the Central Support to the top circular plate.

5.3.3. UHM MSP Joints

In this section, the UHM MSP joints are explained. Figure 5.12 shows the joint configuration of the ACSs to the ACCP Top Plate. Figure 5.13 shows the joint configuration of the ACSs to the Legs. Figure 5.14 shows the joint configurations of the ACSs and Central Support to the ACCP top plate as well as the bottom Legs. Figure 5.15 shows the adhesive bounding of the Legs to the Central Base Plate, as well as the Central Support bottom bracket and bolts. Figure 5.16 shows the double butt lap joint for the composites (joining the three Legs to the Central Base Plate.

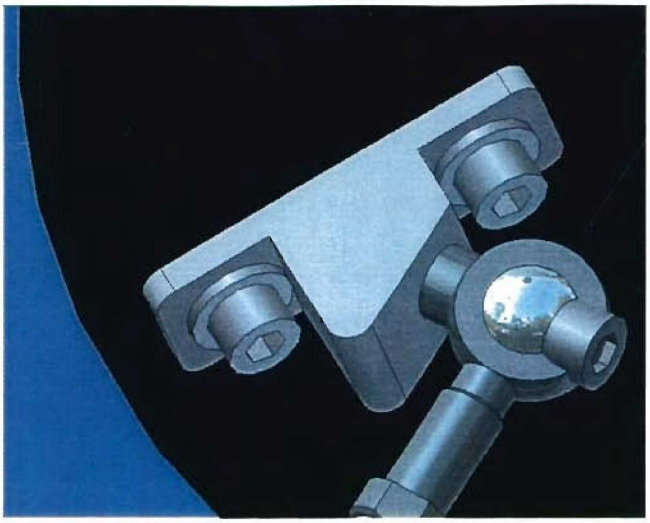

Figure 5.12. *Joint configuration of the ACSs to Top Plate ACCP.*

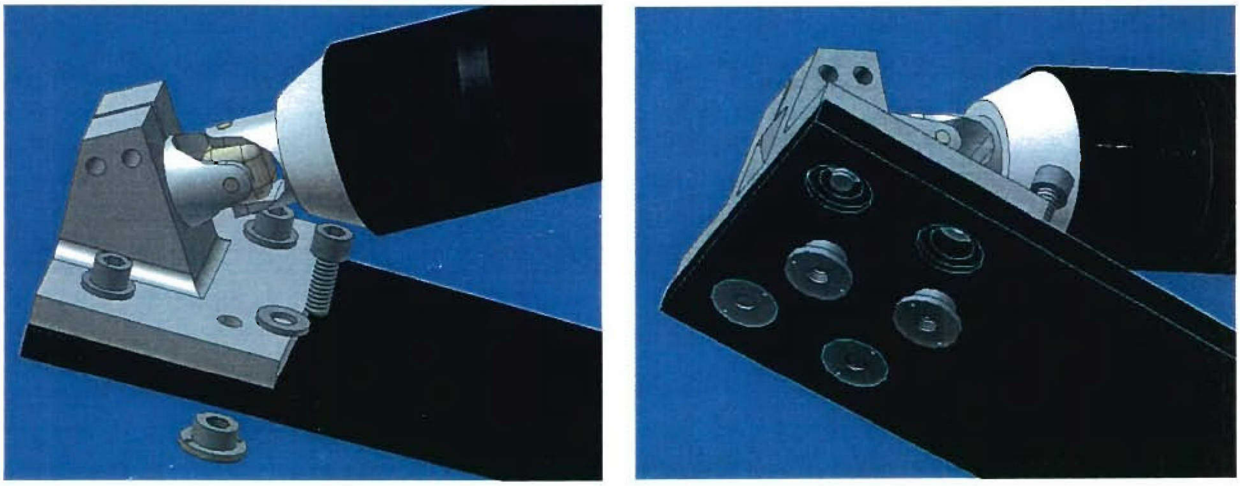

Figure 5.13. *Joint configuration of the ACSs to the bottom Legs.*

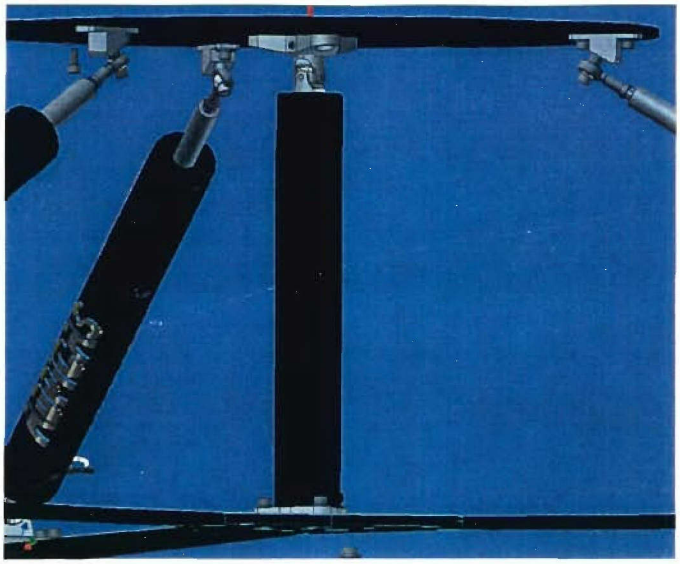

Figure 5.14. *Joint configurations of the ACSs and Central Support to the ACCP top plate as well as the bottom Legs.*

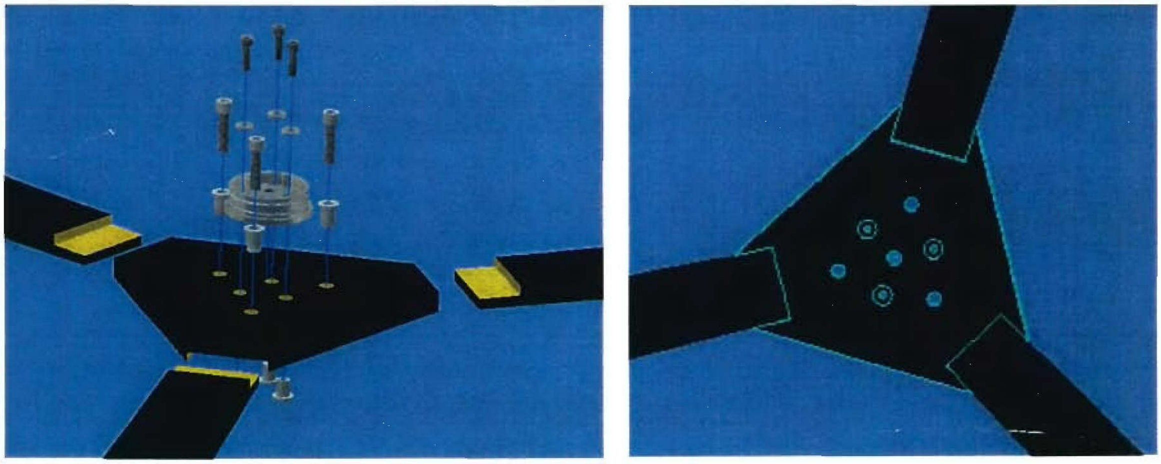

Figure 5.15. *Adhesive bounding of the Legs to the Central Base Plate, as well as the Central Support bottom bracket and bolts.*

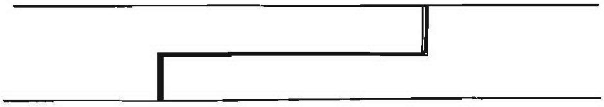

Figure 5.16. *Double butt lap joint for composites.*

5.3.4. UHM MSP Composite Metallic Inserts

Inserts are used to prevent the direct contact of the metallic bolts with the composite laminates. This protects the inner surface of the composite holes from wearing and also increases the bearing strength of the bolted joint. These inserts were machined from stainless. Epoxy is used to glue the inserts into the composite bolt holes in the load bearing areas, while the inserts in the non-load bearing areas were simply press fit in their respective mountings. Figure 5.16 shows the joint configurations of the Central Base Plate to the Central Support as well as the Satellite, where inserts are used for the fastening bolts. Also, Figure 5.17 shows the joint configurations of the Circular Top Plate to the Central Support as well as the Struts, where inserts are used for the fastening bolts. Figure 5.18 shows the stainless steel inserts used in the platform composite legs at the lower mounting point of each strut.

Figure 5.16. *Joint configurations of the Central Base Plate to Central Support and Satellite.*

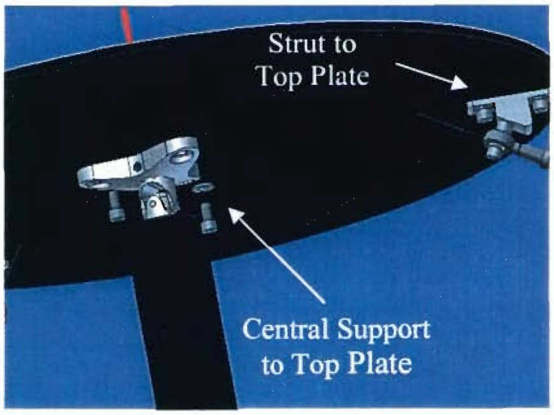

Figure 5.17. *Joint configurations of the Circular Top Plate to Central Support and Strut.*

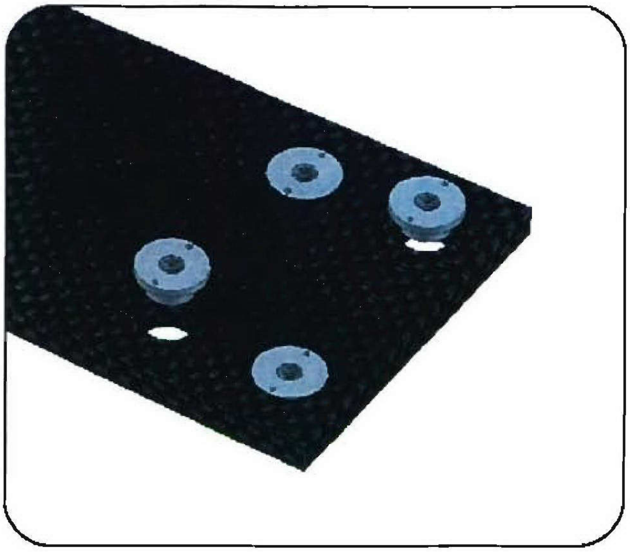

Figure 5.18. Stainless steel inserts used in the platform composite legs at the lower mounting point of each strut.

5.4. MSP Active Vibration Suppression Schemes

(Nejhad, Antin)

This section focuses on a finite element analysis active vibration suppression of UHM platform and its satellite frame. This smart platform connects the thruster to the structure of the satellite and has three active struts and one active central support with one piezoelectric stack in each. Here first, only the four piezo stacks are considered to suppress the four key points under the ACSs and the ACCS to prevent the vibration going from the thruster into the satellite frame. The same technique is then used including the three pairs of the AFC piezo patch actuators in the UHM platform ACCP as well as the four piezo stacks in the UHM platform three ACSs and the ACCS to suppress the vibration of the thruster, using the three piezo pairs in the ACCP, and that of the satellite by using the four piezo stacks mentioned above.

Here, a finite element harmonic analysis is employed to develop a vibration suppression scheme, which is then used to study the vibration control of the satellite structure using the vibration suppression capabilities of the intelligent platform mounted on the satellite. In this approach, the responses of the structure to a unit external force as well as unit internal piezoelectric control voltages are first determined, individually. The responses are then assembled in a system of equation as a coupled system and then solved simultaneously to determine the control voltages and their respective phases for the system actuators for a given external disturbance.

As stated earlier, when the thruster of a satellite fires, it creates 2 problems. The first one is the thrust vector misalignment, and the second one is the vibration created by the thruster that transmits to the satellite (Ghasemi-Nejhad and Doherty, 2002). The ideal thrust vector is such that it is aligned with the center of mass of the satellite to avoid any rotation of the satellite, as shown in Figure 5.19. However, in reality, the thrust vector is not perfectly aligned with the center of mass, which creates a moment and a rotation of the structure. This problem is currently solved by using reaction control system (RCS) thrusters that create the opposite moment and rectify the trajectory to the desired path (see Figure 5.20).

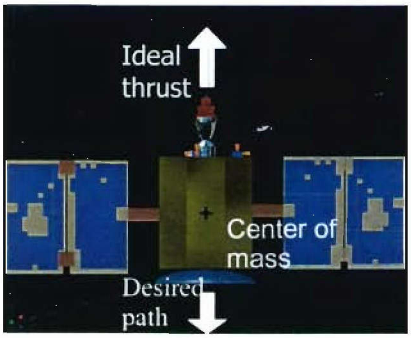

Figure 5.19. *Ideal thrust vector.*

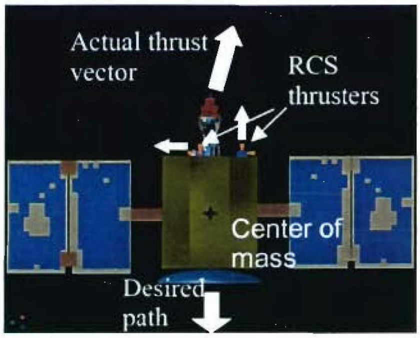

Figure 5.20. *Thrust vector misalignment.*

The second issue is the vibration of the thrust propagating from the thruster to the satellite, as shown schematically in Figure 5.21, where the dominant component of the vibration is due to the thruster compared with that due to the motion of solar panels, antenna, etc. This problem is not currently solved, and is addressed in the ADPICAS project.

Figure 5.21. *Vibration transmission.*

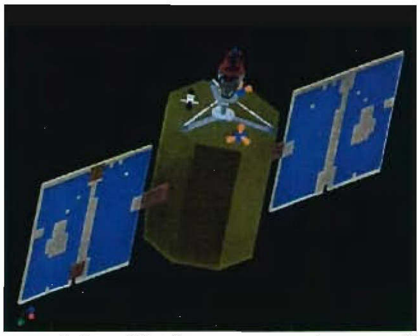

Figure 5.22. *Platform mounted on satellite.*

As stated earlier, it is proposed to solve these two problems, in the ADPICAS project, by adding the UHM platform between the thruster and the satellite for simultaneous precision positioning and vibration suppression (Ghasemi-Nejhad and Doherty, 2002), as shown in Figure 5.22. The ACS precision motors will be used for precision positioning and will be explained in the next section. In the active vibration suppression approach introduced in this section, the main idea is to sense the vibration created by the thruster in each component and apply the opposite vibration using the actuators, i.e., piezoelectrics. Ideally, the two vibrations will cancel each others resulting in zero residual vibration. Figures 5.23 and 5.24 give the primary elements of the platform and strut, respectively.

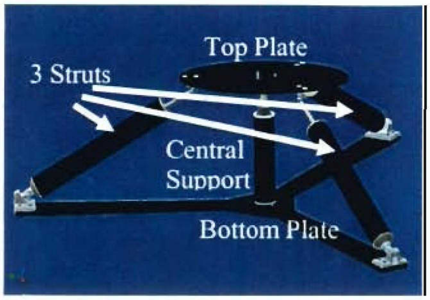

Figure 5.23. Elements of the Platform.

Figure 5.24. Elements of the struts.

The work presented here only aims at vibration suppression. A finite element harmonic analysis (ANSYS, 2004) was employed to develop a vibration suppression scheme, which was then used to study the vibration control of the satellite structure using the vibration suppression capabilities of the intelligent UHM platform mounted on the satellite.

5.4.1. Harmonic Analysis

When the thruster fires, a vibration is created. This vibration is normally transmitted to the satellite. One of the objectives of the platform is to isolate the satellite from this unwanted vibration. In other words, the aim is to suppress the vibration of the satellite by reducing the transmissibility between the thruster and the satellite. To achieve this goal, 4 displacement/force sensors and 4 piezoelectric stack actuators are installed in the platform, i.e., 1 sensor and 1 actuator in each strut as well as in the central support. The objective of this study is to find a scheme for suppressing the vibration using these sensors and actuators (Russ and Ghasemi-Nejhad, 2002a, 2002b; Doherty and Ghasemi-Nejhad, 2005; Ghasemi-Nejhad et al., 2005a). The main idea is to sense the vibration created by the thruster in each component (i.e., struts and central support, here) and apply the opposite vibration using the actuators to actively suppress the vibration. Ideally, the two vibrations will cancel each other leading to a zero residual vibration.

By applying a voltage to a piezoelectric, the piezo contracts or extends. This extension is linearly related to the applied voltage; for example, to create a harmonic vibration, a harmonic voltage has to be applied. A scheme for the determination of the control voltages to apply to the 4 actuators has been developed in this work. This method determines the actuators control voltages for total vibration suppression of the entire structure of the satellite.

The vibration created by the thruster has two components. First, the amplitude of the thrust is not perfectly constant which creates some axial vibration (z-direction). It is evaluated that the thruster has a variation of the thrust force of 10%. Therefore, for the considered thrust of 100 lbs, the axial variation of load is estimated at 10 lbs. The thrust orientation is also not perfectly constant. The maximum angle of variation is estimated at 1° which leads to a lateral variation of load of $100*\sin(1) \approx 1$ lb. Therefore, the system is subjected to an axial and a lateral vibration (see Figure 5.25). When these vibrations are not controlled by the platform, they are transmitted through the central support and struts to the satellite (see Figure 5.26).

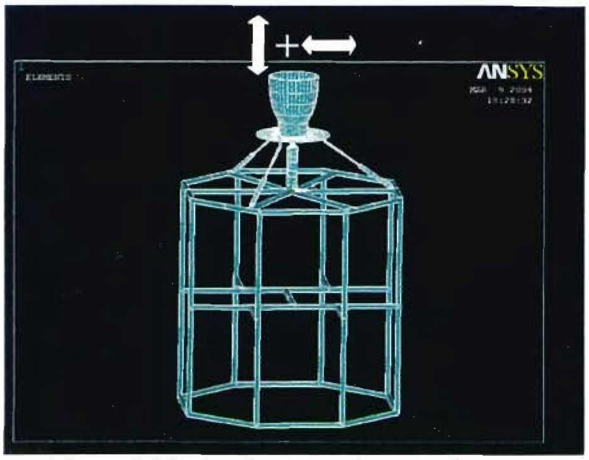

Figure 5.25. *Axial + Lateral input vibrations.*

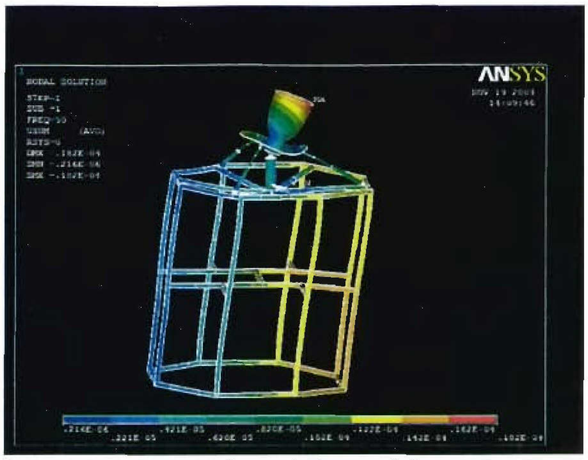

Figure 5.26. *Deformed shape of the structure.*

The range of frequency considered here is from 0 to 100Hz. In this range, a modal analysis using ANSYS shows that the satellite-platform-thruster system has a few natural frequencies. First, since no boundary condition is applied (i.e., the system is in space: free floating situation), f=0 is a natural frequency, i.e., rigid body motion. The main natural frequencies to be considered are 33, 43, 63, 67, 83, 89, and 95 Hz (see Figure 5.27).

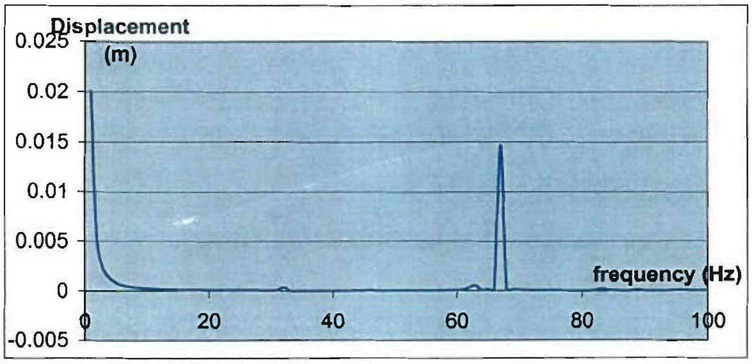

Figure 5.27. *Natural frequencies of the system.*

The vibration suppression scheme has been developed and applied using ANSYS Finite Element Analysis (FEA) by running harmonic analyses. For a general harmonic analysis, ANSYS FEA solves the following equation:

$$MU^{\bullet\bullet} + CU^{\bullet} + KU = F_a \qquad (5.2)$$

where, M: mass matrix, C: damping matrix, K: stiffness matrix, and F_a: thruster load. At a pulsation ω, this equation is transformed to:

$$(-\omega^2 M + i\omega C + K)U_{max}e^{i\varphi_U} = F_{max}e^{i\varphi_F} \qquad (5.3)$$

For a vibration suppression using piezoelectric elements, this equation becomes (ANSYS, 2004):

$$\begin{bmatrix} M & 0 \\ 0 & 0 \end{bmatrix}\begin{bmatrix} U^{\bullet\bullet} \\ V^{\bullet\bullet} \end{bmatrix}+\begin{bmatrix} C & 0 \\ 0 & 0 \end{bmatrix}\begin{bmatrix} U^{\bullet} \\ V^{\bullet} \end{bmatrix}\begin{bmatrix} K & K_z \\ K_z^{\,T} & K_d \end{bmatrix}\begin{bmatrix} U \\ V \end{bmatrix}=\begin{bmatrix} F_a \\ L_a \end{bmatrix} \tag{5.4}$$

where L_a is the applied nodal charge vector and V is the nodal electric potential vector.

The material properties are as the following:

a) Satellite frame: Aluminum, $E = 6.8e10$ Pa, $\upsilon = 0.3$, $A = 1" \times 1"$
b) Thruster: Quasi-isotropic woven Carbon/Carbon Composite, $E = 7.75e10$ Pa, $\upsilon = 0.3$, lower radius = 3.25", upper radius = 5.11", thickness = 0.39"
c) Piezoelectric, PZT-5A (PI, 2004; Doherty and Ghasemi-Nejhad, 2005; Ghasemi-Nejhad et al., 2005a, 2005b, 2005c):

$$\text{Stiffness matrix:} \quad C = \begin{bmatrix} 12.6 & 8.41 & 7.95 & 0 & 0 & 0 \\ 8.41 & 12.6 & 7.95 & 0 & 0 & 0 \\ 7.95 & 7.95 & 1 & 0 & 0 & 0 \\ 0 & 0 & 0 & 2.325 & 0 & 0 \\ 0 & 0 & 0 & 0 & 2.325 & 0 \\ 0 & 0 & 0 & 0 & 0 & 2.325 \end{bmatrix} * 10^{10}\,\text{Pa}$$

$$\text{Piezoelectric matrix:}\ e = \begin{bmatrix} 0 & 0 & -6.62 \\ 0 & 0 & -6.62 \\ 0 & 0 & 23.2 \\ 0 & 0 & 0 \\ 0 & 17 & 0 \\ 17 & 0 & 0 \end{bmatrix} \text{C/m}^2; \quad \text{Permittivity:}\ \varepsilon = \begin{bmatrix} 15.04 & 0 & 0 \\ 0 & 15.04 & 0 \\ 0 & 0 & 15.04 \end{bmatrix} * 10^{-9}\ \text{F/m} \tag{5.5}$$

5.4.2. Vibration Suppression Scheme for the Satellite

The fundamentals of this approach are explained in details for a one-dimensional case of a strut by Antin and Ghasemi-Nejhad (2005). Here, this approach is directly applied to the satellite-platform thruster system for the isolation of the thruster vibration from the satellite structure using the 4 sensors and actuators in the ACSs and ACCS (see Figure 5.28). Therefore, here, for vibration suppression in the satellite, four sensors and four actuators are installed in the platform, i.e., 1 sensor and 1 actuator in each strut as well as in the central support. The sensors are installed at the 4 points of the connections between the platform and the satellite (see Figure 5.28).

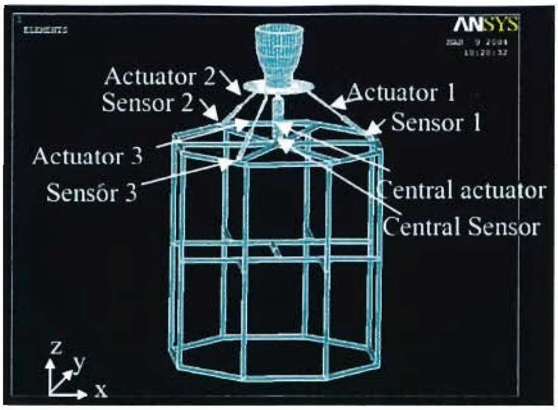

Figure 5.28. *Components of the platform installed on the satellite with thruster in place.*

The problem, here, is more complex to solve compared with a simple one-dimensional case due to the coupling effects. For example, the actuator in strut 1 not only has an influence in the strut 1 but also on the entire structure. In other words, it is not possible to control connection 1 by only using actuator 1. The control voltage of the 4 actuators is determined by solving a linear system in the complex domain. The following presents the vibration suppression scheme.

5.4.2.a) Influence of the thruster (or external load)

When the thruster vibrates (see Figure 5.29), the vibration propagates through the struts and central support and is transmitted into the satellite. First, the four sensors sense the vibration at the points of connections (see Figure 5.30).

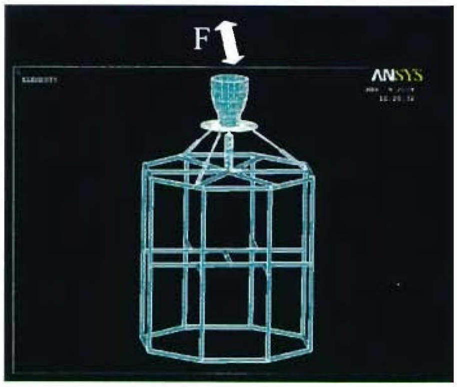

Figure 5.29. *Axial +lateral thruster vibration.*

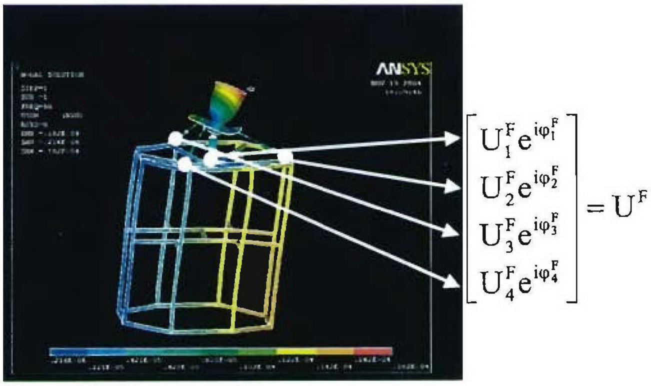

Figure 5.30. *Deformed shape and displacements.*

The Finite Element Analysis gives 4 harmonic displacements (see Figure 5.30) stored in a complex vector:

$$U^F = \begin{bmatrix} U_1^F e^{i\varphi_1^F} \\ U_2^F e^{i\varphi_2^F} \\ U_3^F e^{i\varphi_3^F} \\ U_4^F e^{i\varphi_4^F} \end{bmatrix} \tag{5.6}$$

5.4.2.b) Influence of the actuators (or internal load)

Each actuator has its own influence on the entire structure. Therefore, a unit voltage is applied to one actuator, one at a time, and the vibration caused by each actuator is sensed at the sensing points.

- central piezo: $U^C = \begin{bmatrix} U_1^C e^{i\varphi_1^C} \\ U_2^C e^{i\varphi_2^C} \\ U_3^C e^{i\varphi_3^C} \\ U_4^C e^{i\varphi_4^C} \end{bmatrix}$ (5.7)
- piezo strut 1: $U^{S_1} = \begin{bmatrix} U_1^{S_1} e^{i\varphi_1^{S_1}} \\ U_2^{S_1} e^{i\varphi_2^{S_1}} \\ U_3^{S_1} e^{i\varphi_3^{S_1}} \\ U_4^{S_1} e^{i\varphi_4^{S_1}} \end{bmatrix}$ (5.8)
- piezo strut 2: $U^{S_2} = \begin{bmatrix} U_1^{S_2} e^{i\varphi_1^{S_2}} \\ U_2^{S_2} e^{i\varphi_2^{S_2}} \\ U_3^{S_2} e^{i\varphi_3^{S_2}} \\ U_4^{S_2} e^{i\varphi_4^{S_2}} \end{bmatrix}$ (5.9)
- piezo strut 3: $U^{S_3} = \begin{bmatrix} U_1^{S_3} e^{i\varphi_1^{S_3}} \\ U_2^{S_3} e^{i\varphi_2^{S_3}} \\ U_3^{S_3} e^{i\varphi_3^{S_3}} \\ U_4^{S_3} e^{i\varphi_4^{S_3}} \end{bmatrix}$ (5.10)

5.4.2.c) Determination of the control voltage

Let us store U^C, U^{S1}, U^{S2}, and U^{S3} in matrix *A*, which represents the influence of the 4 actuators:

$$A = \begin{bmatrix} U_1^C e^{i\varphi_1^C} & U_1^{S_1} e^{i\varphi_1^{S1}} & U_1^{S_2} e^{i\varphi_1^{S2}} & U_1^{S_3} e^{i\varphi_1^{S3}} \\ U_2^C e^{i\varphi_2^C} & U_2^{S_1} e^{i\varphi_2^{S1}} & U_2^{S_2} e^{i\varphi_2^{S2}} & U_2^{S_3} e^{i\varphi_2^{S3}} \\ U_3^C e^{i\varphi_3^C} & U_3^{S_1} e^{i\varphi_3^{S1}} & U_3^{S_2} e^{i\varphi_3^{S2}} & U_3^{S_3} e^{i\varphi_3^{S3}} \\ U_4^C e^{i\varphi_4^C} & U_4^{S_1} e^{i\varphi_4^{S1}} & U_4^{S_2} e^{i\varphi_4^{S2}} & U_4^{S_3} e^{i\varphi_4^{S3}} \end{bmatrix} \qquad (5.11)$$

The vibration created by *F* is given by U^F in Equation (5.6). Let *V* be the unknown vector representing the control voltage to be applied to the 4 piezos to control the vibration, and is given in Equation (5.12).

$$V = \begin{bmatrix} V^C e^{i\varphi^C} \\ V^{S_1} e^{i\varphi^{S_1}} \\ V^{S_2} e^{i\varphi^{S_2}} \\ V^{S_3} e^{i\varphi^{S_3}} \end{bmatrix} \qquad (5.12)$$

V^C and ϕ^C are the amplitude and phase to be applied to the central piezo and V^{Si} and ϕ^{Si} are the amplitudes and phases to be applied to the struts S_i (where i = 1 to 3). If these voltages are applied to the actuators at the same time, the resulting vibration can be calculated by multiplying *A* and *V*. Therefore, if these voltages are applied simultaneously with the force *F*, the total vibration becomes $A*V+U^F$. The objective is to obtain zero vibration which leads to Equation (5.13):

$$A*V+U^F=0 \qquad (5.13)$$

This equation is solved by predotting it by A^{-1}, hence:

$V=-A^{-1}*U^F$:

$$\boxed{V=\begin{bmatrix} V^C e^{i\varphi^C} \\ V^{S_1} e^{i\varphi^{S_1}} \\ V^{S_2} e^{i\varphi^{S_2}} \\ V^{S_3} e^{i\varphi^{S_3}} \end{bmatrix} = -\begin{bmatrix} U_1^C e^{i\varphi_1^C} & U_1^{S_1} e^{i\varphi_1^{S_1}} & U_1^{S_2} e^{i\varphi_1^{S_2}} & U_1^{S_3} e^{i\varphi_1^{S_3}} \\ U_2^C e^{i\varphi_2^C} & U_2^{S_1} e^{i\varphi_2^{S_1}} & U_2^{S_2} e^{i\varphi_2^{S_2}} & U_2^{S_3} e^{i\varphi_2^{S_3}} \\ U_3^C e^{i\varphi_3^C} & U_3^{S_1} e^{i\varphi_3^{S_1}} & U_3^{S_2} e^{i\varphi_3^{S_2}} & U_3^{S_3} e^{i\varphi_3^{S_3}} \\ U_4^C e^{i\varphi_4^C} & U_4^{S_1} e^{i\varphi_4^{S_1}} & U_4^{S_2} e^{i\varphi_4^{S_2}} & U_4^{S_3} e^{i\varphi_4^{S_3}} \end{bmatrix}^{-1} \begin{bmatrix} U_1^F e^{i\varphi_1^F} \\ U_2^F e^{i\varphi_2^F} \\ U_3^F e^{i\varphi_3^F} \\ U_4^F e^{i\varphi_4^F} \end{bmatrix}} \qquad (5.14)$$

By inverting the A matrix in the complex domain, we obtain the control voltage in terms of amplitudes and phases to be applied to the 4 piezos (see Figure 5.31).

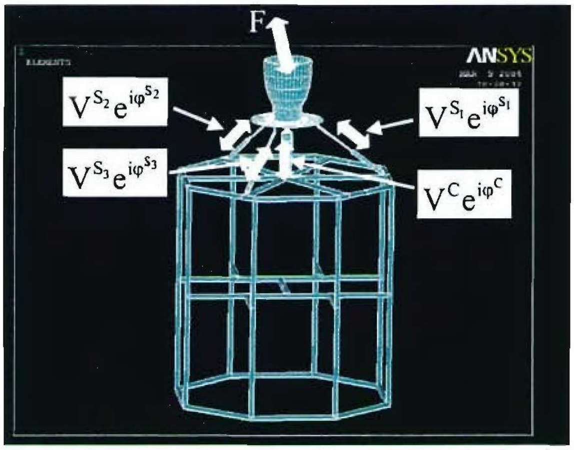

Figure 5.31. *Control voltages simultaneously applied with the load.*

5.4.2.d) Results:

Figure 5.32 presents the deformed shape of the entire structure. The vibration of the thruster is suppressed by the platform and is not transmitted to the satellite. The uncontrolled and controlled vibrations of the center of mass of the satellite are plotted in Figure 5.33 as a function of time for a given frequency. The struts and central support piezos contract and expand such that the vibration caused by the thruster is "absorbed" by the motion of these actuators. At the connection points between the platform and the satellite, the transmissibility is reduced to zero. Therefore, this control scheme leads to complete vibration suppression in the entire satellite. Sometimes, for numerical imperfection issues in an FEA, the sensed displacements are not accurate enough to lead to complete vibration suppression. This usually occurs for frequencies close to the natural frequencies of the structure. In such events, an iteration procedure can be applied by re-sensing the residual vibration and determining a new control voltage, as explained by the following relationships.

$$\begin{aligned} V_1 &= -A^{-1}.U_1^F \\ V_{i+1} &= V_i - A^{-1}.U_i^F \end{aligned} \qquad (5.15)$$

where: $\left.\begin{array}{l} U_i^F \text{ is the sensed vibration} \\ V_i \text{ is the control voltage} \end{array}\right\}$ at iteration i

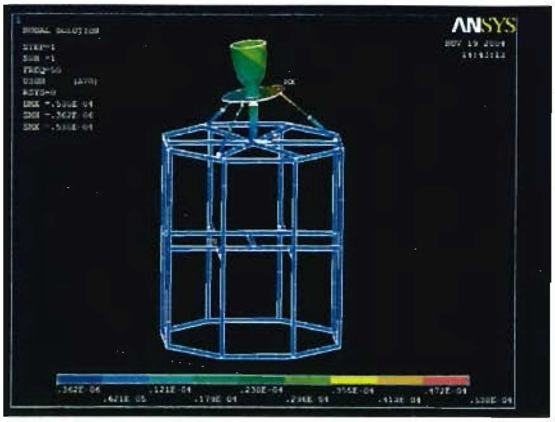

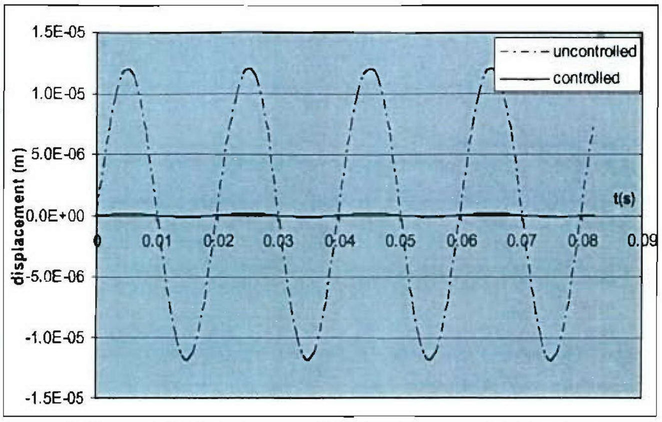

Figure 5.32. Vibration suppression of the satellite.

Figure 5.33. Uncontrolled and controlled vibration of the center of mass of the satellite (frequency = 50Hz).

5.4.2.e) Influence of the frequency:

The following presents the influence of the frequency of the harmonic thrust on the vibration suppression results. The range of frequency under consideration is 0-100Hz. 10 lbs are applied axially simultaneously with 1lb laterally in the direction of Strut 1 (see Figure 5.25). For each frequency, the vibration suppression scheme has been applied and a control voltage has been computed. Figure 5.34 shows the control voltage (amplitude + phase) of each actuator as a function of frequency.

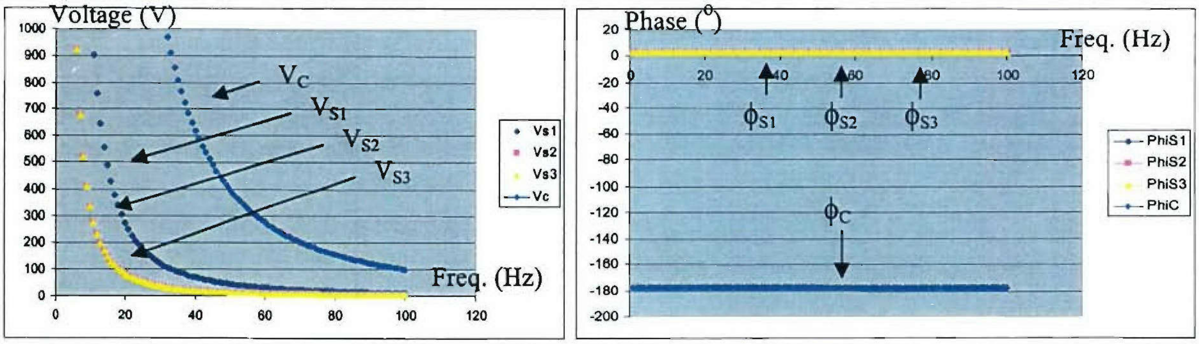

***Figure 5.34.** Amplitudes and phases of the 4 control voltages vs. frequency.*

Here, the control voltage is a decreasing function of the frequency. When the frequency decreases, the amplitudes of the displacements created by a load with given constant amplitude, increases. Therefore, the piezoelectric actuators have to suppress more vibration which implies a higher control voltage. Moreover, the control voltage does not depend on the natural frequencies of the satellite, i.e., the voltage does not have any pick for $f = f_{nat}$. A simpler case of one-dimensional problem can explain this result, and is presented in the following.

Let us assume that two one-dimensional struts exist, one with a mass (see Figure 5.35 (a)) and one without a mass (see Figure 5.35 (b)). The vibration suppression scheme introduced here is applied to both strut systems shown in Figure 5.35, and it was found that the control voltages found from these two struts were identical. Therefore, attaching the mass first and suppressing the vibration after, or suppressing the vibration first and attaching the mass after, actually produces the same results. In other words, if the mass is attached to a non-vibrating point, the mass will not vibrate either. Therefore, the control voltage does not depend on the satellite, i.e., the mass, the shape, or the material properties of the satellite do not affect the control voltage. Since the transmissibility between the thruster and the satellite is prevented by the platform, the satellite is not vibrating, and therefore it does not have any influence. However, in reality, for inaccuracy of sensors or for other practical reasons, the exact control voltage may not be possible to be determined and applied with absolute precision. Therefore, some residual vibration will remain in the structure and this residual vibration will depend on the natural frequencies of the entire structure. To show this, at each frequency between 0 and 100Hz, the control voltage (CV) is applied to the actuators with an error, and is shown in the following:

$$\begin{aligned} &V = CV \Rightarrow U = 0 \\ &V = CV + \Delta V \Rightarrow U = U(f_{nat}) \neq 0 \end{aligned} \tag{5.16}$$

Figure 5.36 presents the residual vibration as a function of the frequency. At the natural frequencies of the structure, the residual vibration has some maximum. Therefore, at a frequency away from a natural frequency (e.g., 50Hz), the control voltage does not need to be applied with perfect accuracy. However, at $f = f_{nat}$ (e.g., 67Hz), the residual vibration may not be negligible. In other words, since the control voltage is not perfectly applied, transmissibility remains between the platform and the satellite leading to some residual vibration that depends on the natural frequencies. This approach has also been successfully applied to transient analyses with various applied vibrations, e.g., harmonic, non-harmonic, random, etc.

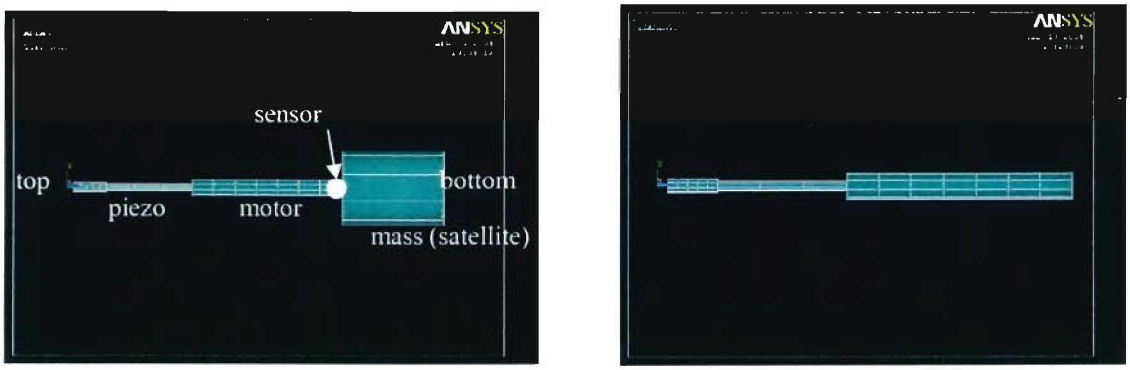

(a) Strut with a Mass (b) Strut without a Mass

Figure 5.35. *Struts with and without mass.*

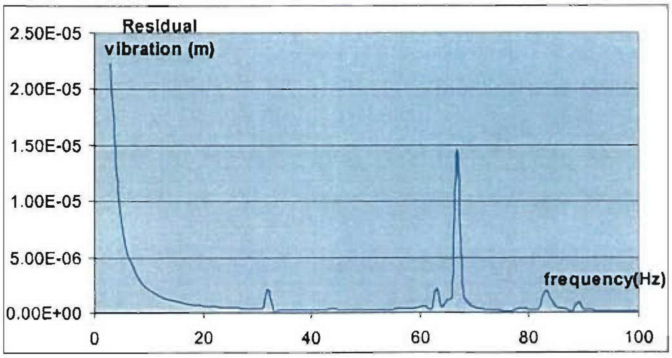

Figure 5.36. *Residual vibration vs. frequency of the system.*

5.4.3. Simultaneous Satellite Vibration Suppression and Thruster Precision Pointing

When a lateral vibration is applied, the struts expand and contract in such a way that they tilt the top plate. Therefore, the static thrust is not perfectly pointed at the same direction during the vibration suppression procedure. To solve this problem, the top plate of the platform is embedded by 3 flat back-to-back pairs of patch piezoelectrics (see Figures 4.56 and 5.37). Ghasemi-Nejhad and Soon (2003), and Yan and Ghasemi-Nejhad (2004b, 2005) showed that a triangular (as opposed to a star where the piezo patches are placed radially) configuration with piezo patches located close to the central support is the optimized configuration for the placement of the piezo patch actuators on the top plate. In addition, various cases shown in Figure 4.67 were considered and it was found that Case 8 of Figure 4.67 which is the Triangle 1 Current case taking into account the size limitations was the optimum actuator configuration. Also, Ghasemi-Nejhad et al. (2005b) introduced techniques to embedded active fiber composite piezo patches inside composite structures. The objective is to keep the thruster pointed at the same direction without vibration, and at the same time, allowing the struts to expand and contract to suppress the vibration of the satellite. To achieve this, the piezoelectric patches will create a bending vibration of the top plate to suppress the vibration of the thruster.

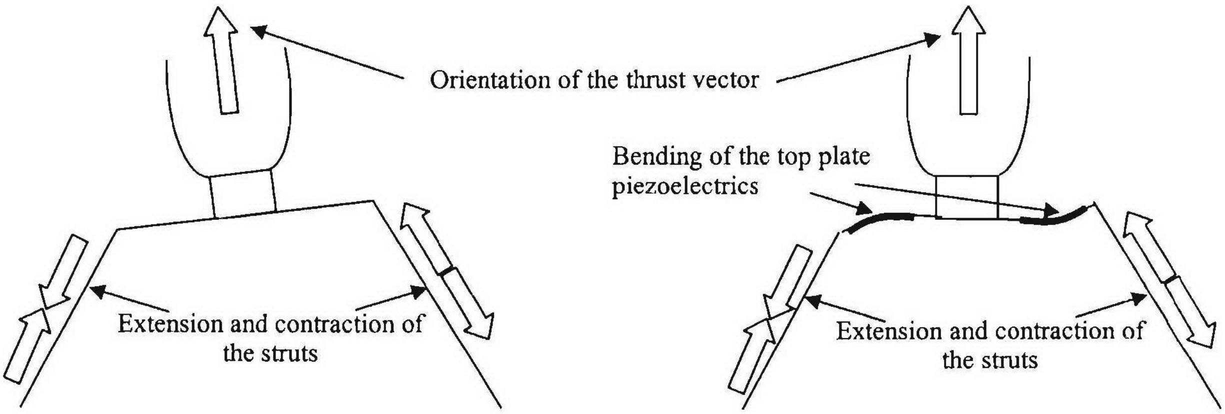

Figure5.37. *Influence of the piezoelectric integrated in the top plate.*

The approach here is similar to the scheme described in the previous section. Here, the A matrix is a 7 x 7 matrix. The sensed degrees of freedom are not only the displacements at the connection between the platform and the satellite but also the angles of tilt of the thruster. This tilt can be sensed by taking the difference of the z-displacements between the 3 points of the thruster connections, i.e., *tp1*, *tp2*, and *tp3*, and the z-displacement of the center of the top plate, *tp0* (see Figure 5.38). Therefore, the vector to be control is the following:

$$\begin{bmatrix} U_1 \\ U_2 \\ U_3 \\ U_4 \\ U_5 \\ U_6 \\ U_7 \end{bmatrix} = \begin{bmatrix} U_Z^C \\ U_Z^{S_1} \\ U_Z^{S_2} \\ U_Z^{S_3} \\ U_Z^{tp_1} - U_Z^{tp_0} \\ U_Z^{tp_2} - U_Z^{tp_0} \\ U_Z^{tp_3} - U_Z^{tp_0} \end{bmatrix} \tag{5.17}$$

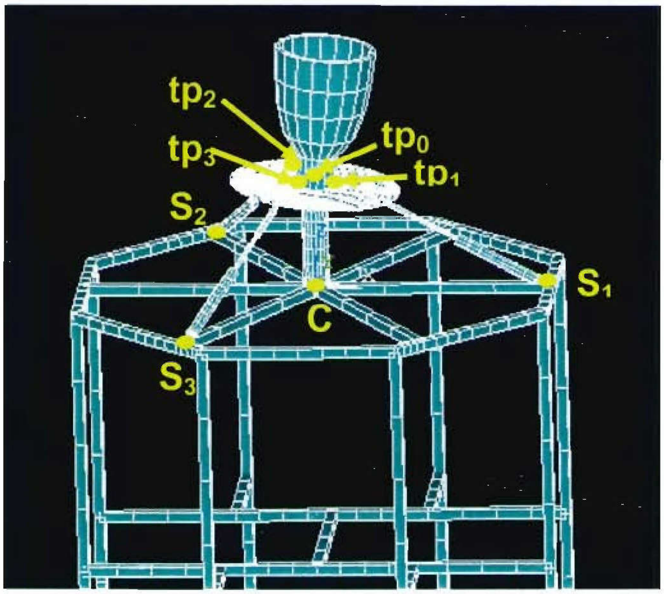

Figure 5.38. *Locations of the sensed displacements.*

The actuators control voltages are obtained by solving a linear system $V = -A^{-1} * U^F$ where V is a vector composed by the 7 control voltages of the 7 piezoelectrics of the platform (3 piezo patch pairs in the top plate and 4 piezo stacks, one in each three struts and one in the central support). Equations (5.18) to (5.20) give the formulations of U^F, V, and A, respectively.

$$V=\begin{bmatrix} V^{C}e^{i\varphi^{C}} \\ V^{S_1}e^{i\varphi^{S_1}} \\ V^{S_2}e^{i\varphi^{S_2}} \\ V^{S_3}e^{i\varphi^{S_3}} \\ V^{tp_1}e^{i\varphi^{tp_1}} \\ V^{tp_2}e^{i\varphi^{tp_2}} \\ V^{tp_3}e^{i\varphi^{tp_3}} \end{bmatrix} \qquad (5.18) \qquad\qquad U^{F}=\begin{bmatrix} U_1^{F}e^{i\varphi_1^{F}} \\ U_2^{F}e^{i\varphi_2^{F}} \\ U_3^{F}e^{i\varphi_3^{F}} \\ U_4^{F}e^{i\varphi_4^{F}} \\ U_5^{F}e^{i\varphi_5^{F}} \\ U_6^{F}e^{i\varphi_6^{F}} \\ U_7^{F}e^{i\varphi_7^{F}} \end{bmatrix} \qquad (5.19)$$

$$A=\begin{bmatrix}
U_1^{C}e^{i\varphi_1^{C}} & U_1^{S_1}e^{i\varphi_1^{S_1}} & U_1^{S_2}e^{i\varphi_1^{S_2}} & U_1^{S_3}e^{i\varphi_1^{S_3}} & U_1^{tp_1}e^{i\varphi_1^{tp_1}} & U_1^{tp_2}e^{i\varphi_1^{tp_2}} & U_1^{tp_3}e^{i\varphi_1^{tp_3}} \\
U_2^{C}e^{i\varphi_2^{C}} & U_2^{S_1}e^{i\varphi_2^{S_1}} & U_2^{S_2}e^{i\varphi_2^{S_2}} & U_2^{S_3}e^{i\varphi_2^{S_3}} & U_2^{tp_1}e^{i\varphi_2^{tp_1}} & U_2^{tp_2}e^{i\varphi_2^{tp_2}} & U_2^{tp_3}e^{i\varphi_2^{tp_3}} \\
U_3^{C}e^{i\varphi_3^{C}} & U_3^{S_1}e^{i\varphi_3^{S_1}} & U_3^{S_2}e^{i\varphi_3^{S_2}} & U_3^{S_3}e^{i\varphi_3^{S_3}} & U_3^{tp_1}e^{i\varphi_3^{tp_1}} & U_3^{tp_2}e^{i\varphi_3^{tp_2}} & U_3^{tp_3}e^{i\varphi_3^{tp_3}} \\
U_4^{C}e^{i\varphi_4^{C}} & U_4^{S_1}e^{i\varphi_4^{S_1}} & U_4^{S_2}e^{i\varphi_4^{S_2}} & U_4^{S_3}e^{i\varphi_4^{S_3}} & U_4^{tp_1}e^{i\varphi_4^{tp_1}} & U_4^{tp_2}e^{i\varphi_4^{tp_2}} & U_4^{tp_3}e^{i\varphi_4^{tp_3}} \\
U_5^{C}e^{i\varphi_5^{C}} & U_5^{S_1}e^{i\varphi_5^{S_1}} & U_5^{S_2}e^{i\varphi_5^{S_2}} & U_5^{S_3}e^{i\varphi_5^{S_3}} & U_5^{tp_1}e^{i\varphi_5^{tp_1}} & U_5^{tp_2}e^{i\varphi_5^{tp_2}} & U_5^{tp_3}e^{i\varphi_5^{tp_3}} \\
U_6^{C}e^{i\varphi_6^{C}} & U_6^{S_1}e^{i\varphi_6^{S_1}} & U_6^{S_2}e^{i\varphi_6^{S_2}} & U_6^{S_3}e^{i\varphi_6^{S_3}} & U_6^{tp_1}e^{i\varphi_6^{tp_1}} & U_6^{tp_2}e^{i\varphi_6^{tp_2}} & U_6^{tp_3}e^{i\varphi_6^{tp_3}} \\
U_7^{C}e^{i\varphi_7^{C}} & U_7^{S_1}e^{i\varphi_7^{S_1}} & U_7^{S_2}e^{i\varphi_7^{S_2}} & U_7^{S_3}e^{i\varphi_7^{S_3}} & U_7^{tp_1}e^{i\varphi_7^{tp_1}} & U_7^{tp_2}e^{i\varphi_7^{tp_2}} & U_7^{tp_3}e^{i\varphi_7^{tp_3}}
\end{bmatrix} \qquad (5.20)$$

Figure 5.39 presents the deformed shape of the entire structure. The vibration in the satellite is suppressed while the thruster keeps its orientation fixed. Figure 5.40 shows the deformed shape of the top plate only. The piezo patches bend the top plate to suppress the vibration of the thruster and allow the motion of the struts without affecting the tilt of the thruster. The tilt of the thruster is plotted as a function of time for 3 cases: uncontrolled vibration, controlled vibration without using the top plate piezo patches, and controlled vibration using the top plate piezo patches as well (see Figure 5.41).

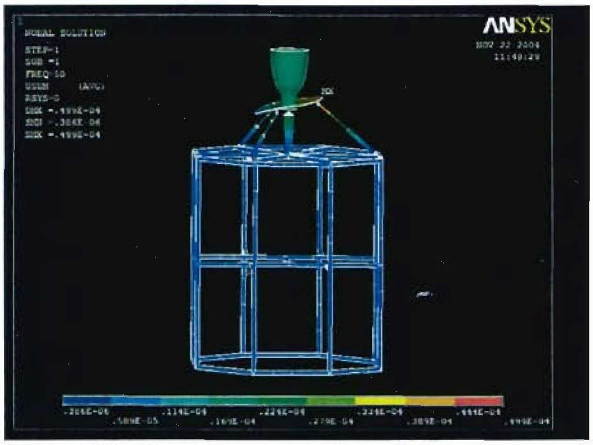

Figure 5.39. *Simultaneous satellite vibration suppression and thruster precision pointing.*

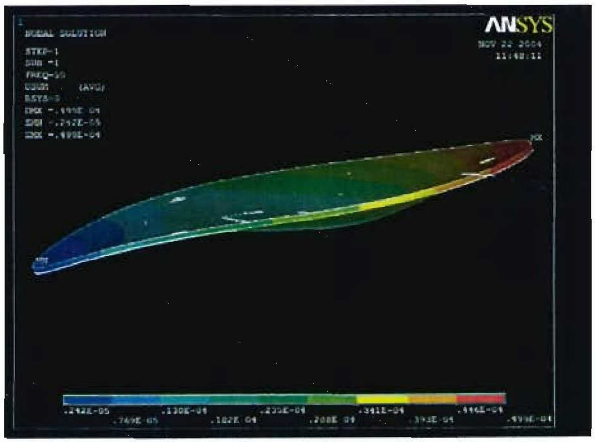

Figure 5.40. *Deformed shape of the top plate.*

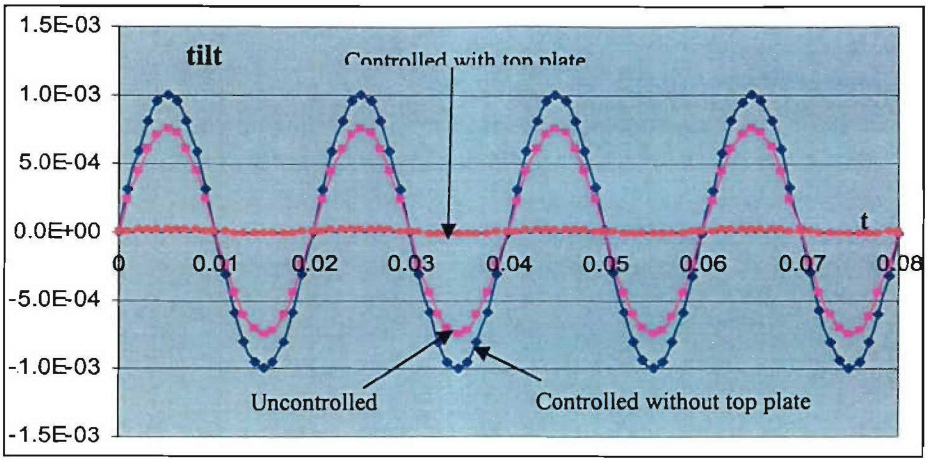

Figure 5.41. *Tilt of the thruster (frequency = 50Hz).*

The following presents the influence of the frequency on the control voltage of the top plate piezoelectric patches.

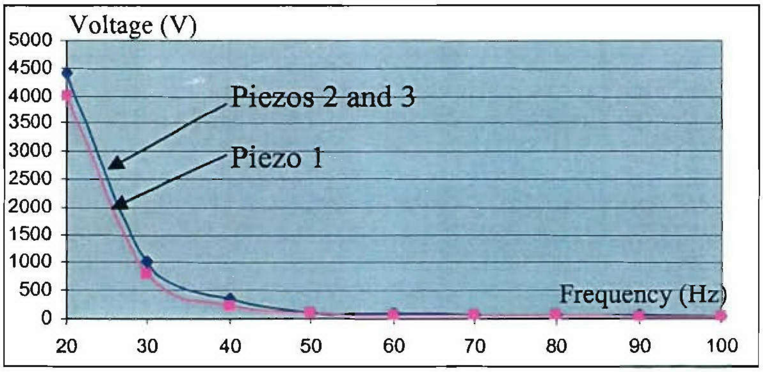

Figure 5.42. *Top plate piezo patches actuators control voltages vs. frequency.*

For a similar reason as for Figure 5.34, the control voltages are decreasing functions of the frequency. For low frequency, these voltages are very high but become more reasonable after 33Hz. These values represent the voltages for a given design of the top plate but can be modified by changing the diameter, the thickness, or the shape of the top plate. The control voltages of the central support and the struts are not presented here, but are very close to the control voltages without the inclusion of the top plate piezos, i.e., they only vary by less than 3%. Therefore, the use of the top plate piezoelectric patches does not have a major effect on the control voltages of the central support and struts piezoelectric stacks.

5.5. MSP Control Strategies

(Nejhad, Ma)

This section briefly explains the control strategies employed for the UHM MSP (Ghasemi-Nejhad and Doherty, 2002; Ghasemi-Nejhad, 2004). It should be noted that the platform has been assembled by the end of Phase I & Phase II and the extensive testing and application of the developed control strategies on the UHM MSP is planned for the initial stages of Phase III.

5.5.1. MSP Integrated Controllers, Actuators, and Sensors

One of the attribute of the UHM intelligent platform is in its integrated controllers, actuators, and sensors to provide simultaneous precision positioning and vibration suppression using MIMO or Multi-SISO control approaches. The following briefly explains the UHM platform characteristics to provide the above mentioned attributes.

5.5.1.1. MSP Integrated Controllers

Basically, the Fuzzy Logic Control (FLC) (Ma and Ghasemi-Nejhad, 2004a, 2005a, 2005b) approach is used for the simultaneous precision positioning (using the precision motor) and vibration suppression (using the piezo stacks) (SPPVS) in the struts, FLC for the VS using the piezo stack in the central support, and Hybrid Adaptive Control (HAC) (Ma and Ghasemi-Nejhad, 2002a, 2004b, 2005c) for the VS using the AFC piezo patches in the top plate.

5.5.1.2. MSP Integrated Actuators

The three pairs of back-to-back piezo patches in the top plate (Active Circular Composite Plate, ACCP) are used to suppress the vibration of the thruster and the four piezo stacks, i.e., one in each of the three struts (Active Composite Strut, ACS) and one in the central support (Active Composite Central Support, ACCS), are used to effectively minimize the transmissibility of vibration from the thruster to the satellite, and hence to suppress the vibration of the satellite. Also, the three precision motors, one in each ACS, are used for the precision positioning of the thruster. All these Precision Positioning (PP) and Vibration Suppression (VS) are performed Simultaneously (S) to give Simultaneous Precision Positioning and Vibration Suppression (SPPVS).

5.5.1.3. MSP Integrated Sensors

Each of the three struts (ACS) and the central support (ACCS) has a force sensor at its lower end to be used for vibration suppression (VS). The top plate (ACCP) has three AFC piezo patch sensor to be used for vibration suppression (VS). The top plate has a tilt sensor to be used for precision positioning (PP). In addition to these integrated structural sensors, laser sensors and accelerometers are also used on the top plate for its SPPVS as well as the satellite structure for its VS.

5.5.2. Precision Positioning Experiments of the UHM MSP (Ma and Ghasemi-Nejhad, 2005e)

The PP experiments of the UHM platform are performed. The experimental configurations of the local control strategy and the global control strategy are shown in Figures 5.43 and 5.44, respectively (Ghasemi-Nejhad and Ma, 2004; Ma and Ghasemi-Nejhad, 2004c). In the local mode control, the control goal (command) is firstly separated to sub-commands, which are responded by the output of sub-systems. Each sub-controller uses local information and actuates locally, resulting in a combination of multi-SISO sub-systems. For example, in order to precisely position the platform, each ACS can be controlled individually, i.e., the displacement of each ACS is measured and the error between the desired and measured displacements is used to drive the controller to correct the error. To determine the desired displacement of each ACS, a mapping between the tilt and the strut expansion/contraction has to be used (i.e., the inverse kinematics given below). In global mode control, the controller will be designed in MIMO case. All sensor signals come together to be used to design a MIMO controller, and control signals are distributed to actuators. Global system sensors may be employed in this case. For example, a tilt sensor is used to measure the tilt of the thrust vector and the measured tilt signals are fed back to the controller directly. This approach does not need any kinematics analysis of the platform, and may provide much more accurate position; however, the controller design is more complex. Fuzzy logic control is employed in both control modes here. The typical control signal to the strut in the UHM platform is given in Figure 5.45.

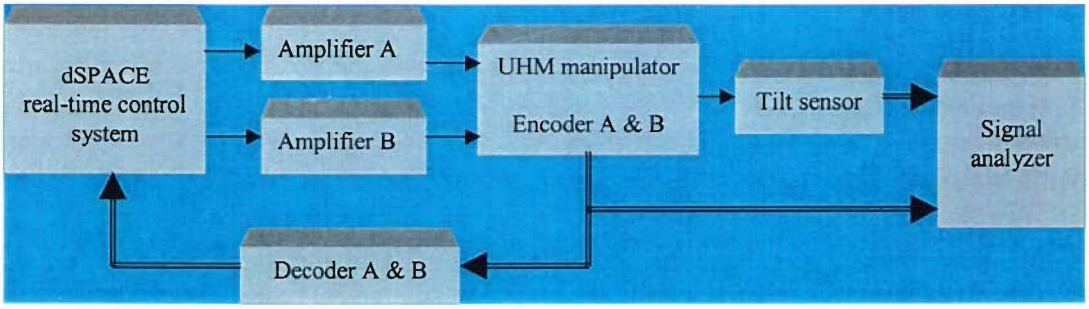

***Figure 5.43**. Local Control Strategy (Multi-SISO).*

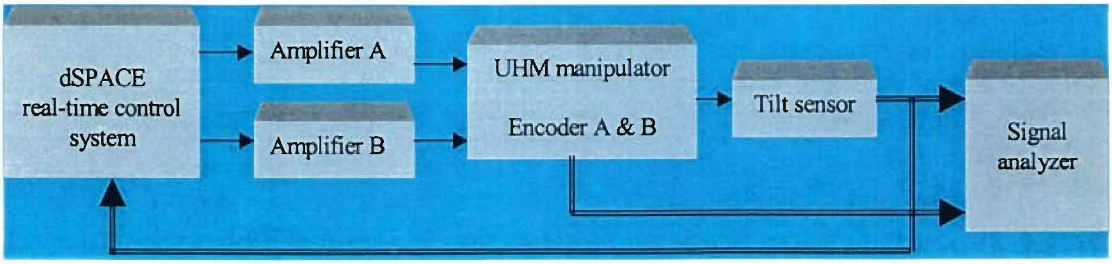

***Figure 5.44**. Global Control Strategy (MIMO).*

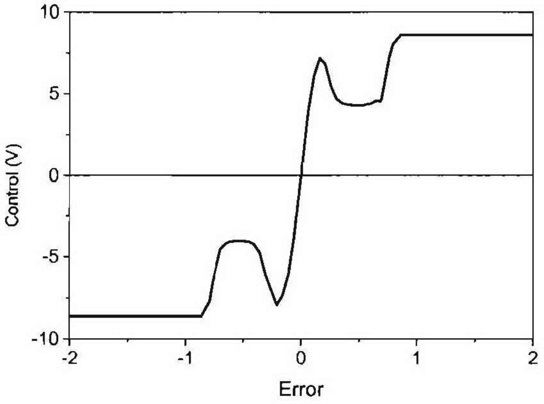

Figure 5.45. *Typical control signals.*

The following explains the inverse kinematics that is used in the local control strategy using multi-SISO approach. Figure 5.46 shows the schematic of the UHM platform where the distance between the top plate and the central joint is considered. The inverse kinematics of the UHM platform is given in the relationships given in Equation (5.21). Figure 5.47 shows the length changes of the three struts while the ACCP tilt angle varies within [-1, 1] degree.

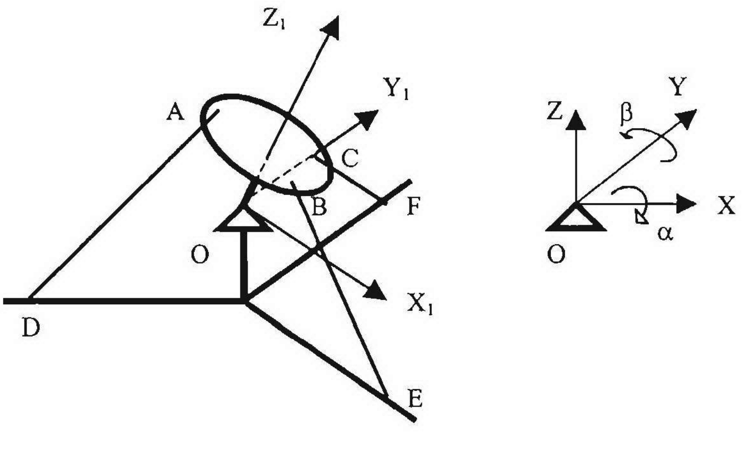

Figure 5.46. *Schematic of UHM MSP.*

(5.21)

$$\Delta L_{AD} = L_{AD} - L_{AD}^{0} \qquad \Delta L_{BE} = L_{BE} - L_{BE}^{0} \qquad \Delta L_{CF} = L_{CF} - L_{CF}^{0}$$

$$L_{AD}^{0} = L_{BE}^{0} = L_{CF}^{0} = \sqrt{(R-r)^2 + (h_1 + h_2)^2}$$

$$L_{AD} = \sqrt{(X_A - X_D)^2 + (Y_A - Y_D)^2 + (Z_A - Z_D)^2}$$

$$L_{BE} = \sqrt{(X_B - X_E)^2 + (Y_B - Y_E)^2 + (Z_B - Z_E)^2}$$

$$L_{CF} = \sqrt{(X_C - X_F)^2 + (Y_C - Y_F)^2 + (Z_C - Z_F)^2}$$

$$\begin{Bmatrix} X_A \\ Y_A \\ Z_A \end{Bmatrix} = \begin{Bmatrix} -r\cos\beta + h_1 \cos\alpha \sin\beta \\ -h_1 \sin\alpha \\ r\sin\beta + h_1 \cos\alpha \cos\beta \end{Bmatrix}$$

$$\begin{Bmatrix} X_B \\ Y_B \\ Z_B \end{Bmatrix} = \begin{Bmatrix} (r\cos\beta)/2 - (r\sqrt{3}\sin\alpha \sin\beta)/2 + h_1 \cos\alpha \sin\beta \\ -(r\sqrt{3}\cos\alpha)/2 - h_1 \sin\alpha \\ -(r\sin\beta)/2 - (r\sqrt{3}\sin\alpha \cos\beta)/2 + h_1 \cos\alpha \cos\beta \end{Bmatrix}$$

$$\begin{Bmatrix} X_C \\ Y_C \\ Z_C \end{Bmatrix} = \begin{Bmatrix} (r\cos\beta)/2 + (r\sqrt{3}\sin\alpha \sin\beta)/2 + h_1 \cos\alpha \sin\beta \\ (r\sqrt{3}\cos\alpha)/2 - h_1 \sin\alpha \\ -(r\sin\beta)/2 + (r\sqrt{3}\sin\alpha \cos\beta)/2 + h_1 \cos\alpha \cos\beta \end{Bmatrix}$$

$$\begin{Bmatrix} X_D \\ Y_D \\ Z_D \end{Bmatrix} = \begin{Bmatrix} -R \\ 0 \\ -h_2 \end{Bmatrix} \qquad \begin{Bmatrix} X_E \\ Y_E \\ Z_E \end{Bmatrix} = \begin{Bmatrix} R/2 \\ -R\sqrt{3}/2 \\ -h_2 \end{Bmatrix} \qquad \begin{Bmatrix} X_F \\ Y_F \\ Z_F \end{Bmatrix} = \begin{Bmatrix} R/2 \\ R\sqrt{3}/2 \\ -h_2 \end{Bmatrix}$$

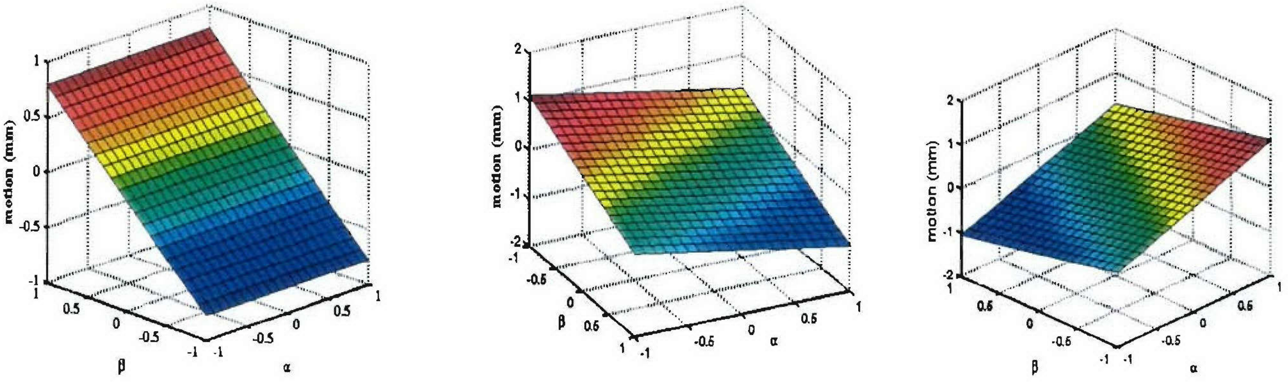

(a) *Strut AD* (b) *Strut BE* (c) *Strut CF*

Figure 5.47. *Length changes of Struts AD, BE, and CF for [-1, 1] degree of ACCP tilt.*

Figures 5.48 and 5.49 illustrate the desired tilt angles, which are in square wave with amplitude of one degree and frequency of 0.05 Hz for both α and β, as well as the actual tilt angles of the top device-plate for the local and global control strategies, respectively. Figure 5.50 shows the steady state errors of the tilt angles for the local and global control strategies, respectively. The steady state errors of α are 0.022 degrees in the positive tilt angle and 0.044 degrees in the negative tilt angle for the case of the local control strategy, and these values decrease to 0.003 degrees and 0.015 degrees for the case of the global control strategy. Since the amplitudes of the commands are one degree, the steady state relative errors of α are 2.2% in the positive tilt angle and 4.4% in the negative tilt angle, resulting in a average steady state relative error of 3.3%, for the case of the local control strategy, and 0.3% in the positive tilt angle and 1.5% in the negative tilt angle, resulting in a average steady state relative error of 0.9%, for the case of the global control strategy. Similarly, the steady state errors of β are 0.007 degrees in the positive tilt angle and 0.035 degrees in the negative tilt angle for the case of the local control strategy, and these values decrease to 0.007 degrees and 0.009 degrees for the case of the global control strategy, i.e., the steady state relative errors of β are 0.7% in the positive tilt angle and 3.5% in the negative tilt angle, resulting in a average steady state relative error of 2.1%, for the case of the local control strategy, and 0.7% in the positive tilt angle and 0.9% in the negative tilt angle, resulting in a average steady state relative error of 0.8%, for the case of the global control strategy. Setting a steady state relative error tolerance of 2% and checking the settling time with the two control strategies, it can be observed that all average steady state relative errors of α and β for the local control strategy are greater than 2%, and the settling times are about 4 seconds for α and 4.5 seconds for β, for the global control strategy. Table 5.1 summarizes the above-mentioned experimental results.

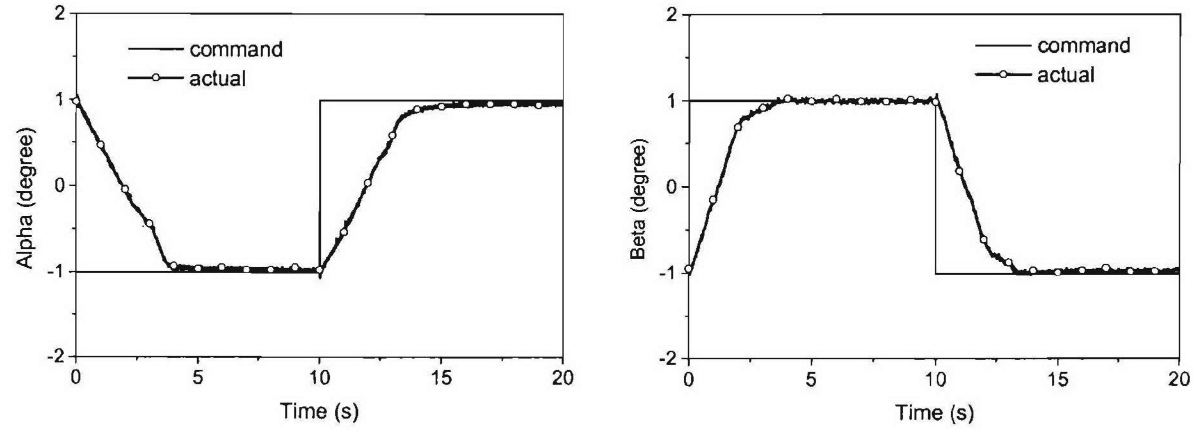

(a) α *(b) β*

Figure 5.48. *Commands and tilt angles (Local).*

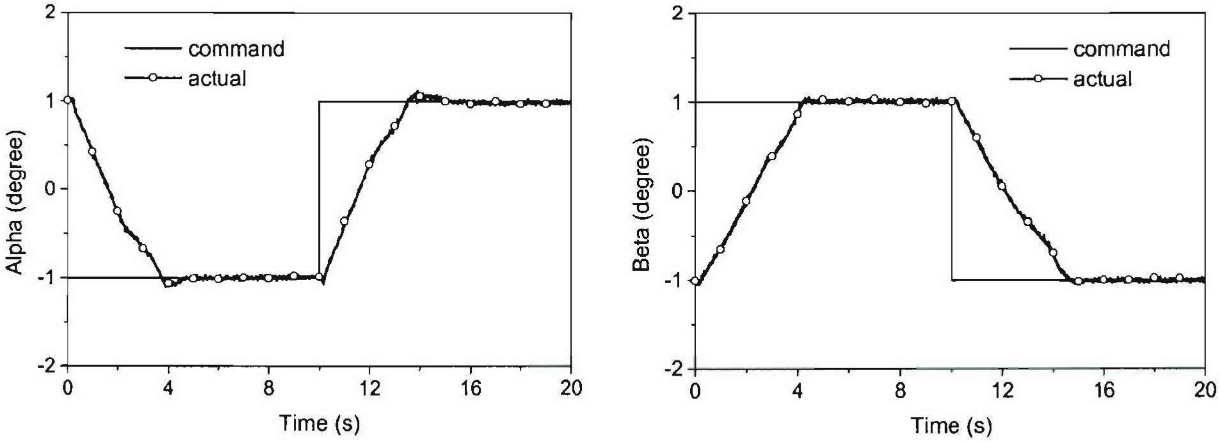

(a) α *(b) β*

Figure 5.49. *Commands and tilt angles (Global).*

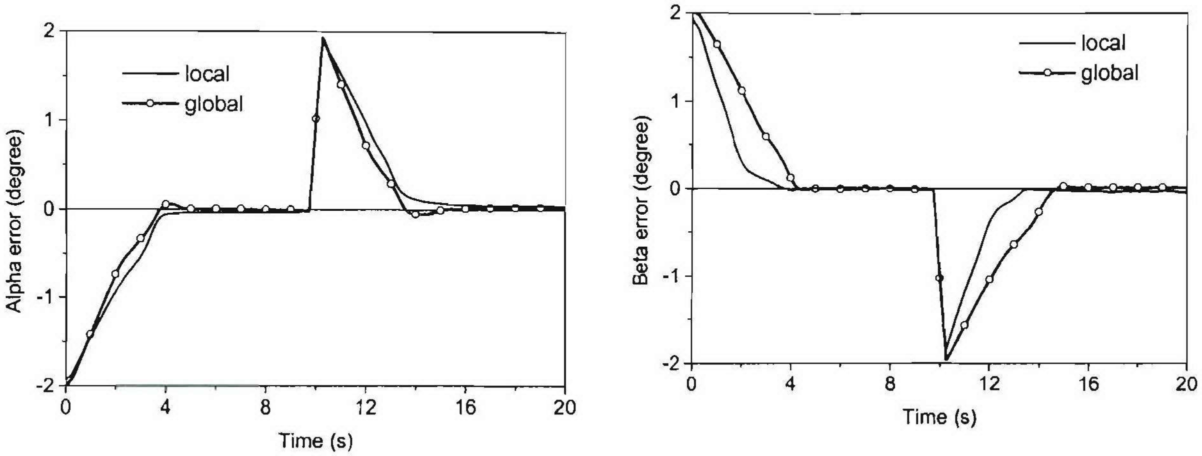

(a) α *(b) β*

Figure 5.50. *Steady state errors.*

Table 5.1. *Summary of the UHM platform PP experiments.*

		α		β	
		Positive tile	Negative tile	Positive tile	Negative tile
Global control	Steady state error (degree)	0.003	0.015	0.007	0.009
	Steady state relative error	0.3%	1.5%	0.7%	0.9%
	Average steady state relative error	0.9%		0.8%	
	Settling time (second) (2% relative error tolerance)	4.5	3.5	4.2	4.9
Local control	Steady state error (degree)	0.022	0.044	0.007	0.035
	Steady state relative error	2.2%	4.4%	0.7%	3.5%
	Average steady state relative error	3.3%		2.1%	
	Settling time (second) (2% relative error tolerance)	Relative error>2 %	Relative error>2 %	3.6	Relative error>2 %

Figure 5.51 shows the strut motions of the two struts and control signals in both the local and global control strategies indicating that the struts AD and BE have to move 0.8 *mm* and 1.5 *mm*, respectively, to achieve the tilt angle Φ=1.4142 degrees and θ=+/- 45 degrees (equivalently, $\alpha=\beta$=+/-1 degree). These strut motions are consistent with the inverse kinematics analysis mentioned earlier.

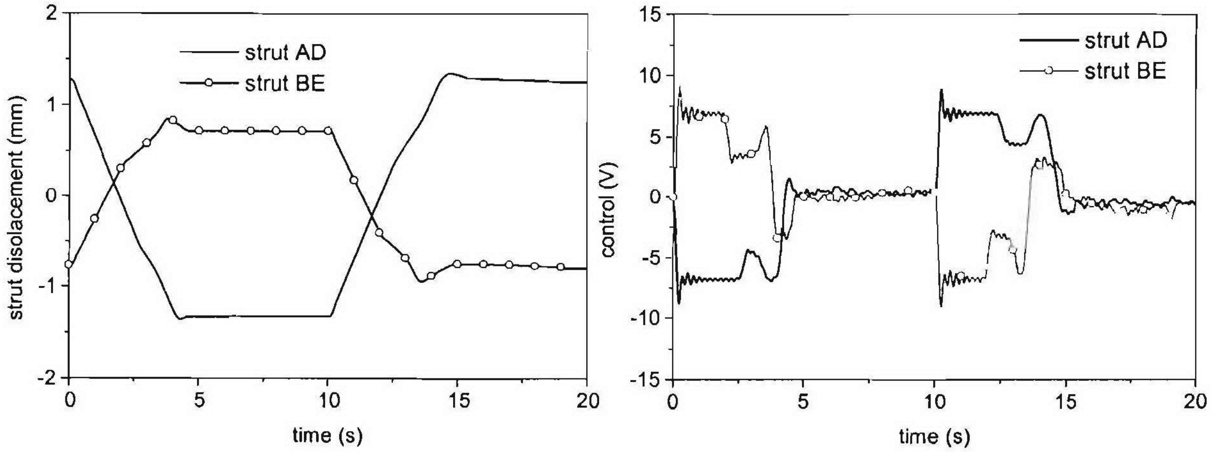

(a) strut motion

(b) control signals

Figure 5.51. *Strut motions and control signals.*

The experimental results reveal that the local control strategy delivers lower positioning accuracy compared with the global control strategy, especially for α. A sensitivity analysis on the tilt angles α and β, with respect to the strut motions explains this feature (Ma and Ghasemi-Nejhad, 2005e). The inverse sensitivities of the strut motions over α and β, i.e., $\partial\Delta L_{AD}/\partial\alpha$, $\partial\Delta L_{BE}/\partial\alpha$, $\partial\Delta L_{AD}/\partial\beta$, and $\partial\Delta L_{BE}/\partial\beta$, can be obtained by calculating the partial derivatives of the strut motions with respect to α and β. Then, the sensitivity of α and β over the strut motions ---- the reciprocals of the inverse sensitivities, i.e., $\partial\alpha/\partial\Delta L_{AD}$, $\partial\alpha/\partial\Delta L_{BE}$, $\partial\beta/\partial\Delta L_{AD}$, and $\partial\beta/\partial\Delta L_{BE}$ can easily be calculated. Figures 5.52 and 5.53 are the sensitivity analysis results showing that $\partial\alpha/\partial\Delta L_{BE}$, $\partial\beta/\partial\Delta L_{AD}$, and $\partial\beta/\partial\Delta L_{BE}$ are about 1.25, -1.45, and –2.55 degree/mm, respectively, in the given ranges of α and β, but the sensitivity $\partial\alpha/\partial\Delta L_{AD}$ is much greater than the other three ones. This means that the small change of the length of the strut AD will produce a large tilt angle change of α. As mentioned above, the local control strategy only measures and controls each strut motion individually; inevitably, the existing tolerances of the joints cannot be counted and compensated. These existing tolerances of the joints directly cause positioning error of the entire parallel manipulator, which is a problem in local control strategy but is not in the global one. It should be noted that the motions of struts BE and CF are similar.

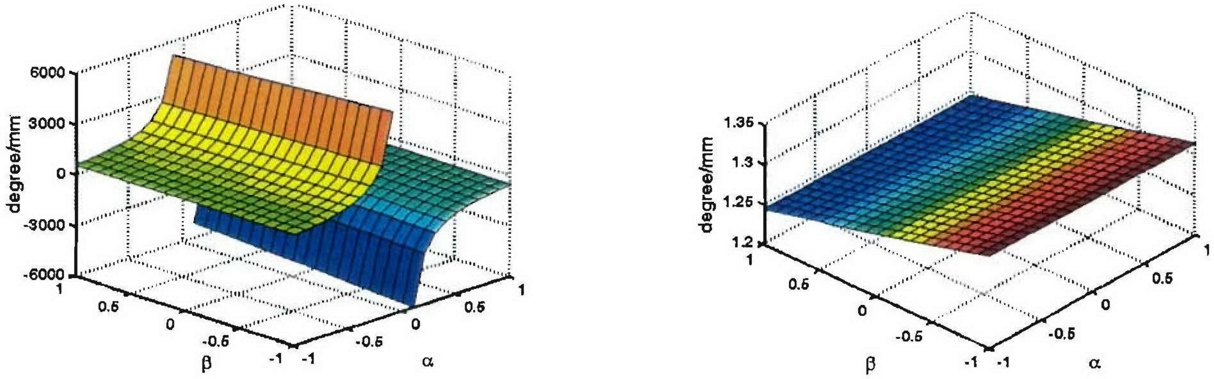

(a) $\partial\alpha / \partial\Delta L_{AD}$ (b) $\partial\alpha / \partial\Delta L_{BE}$

Figure 5.52. *The α-angle sensitivities with respect to the strut motions.*

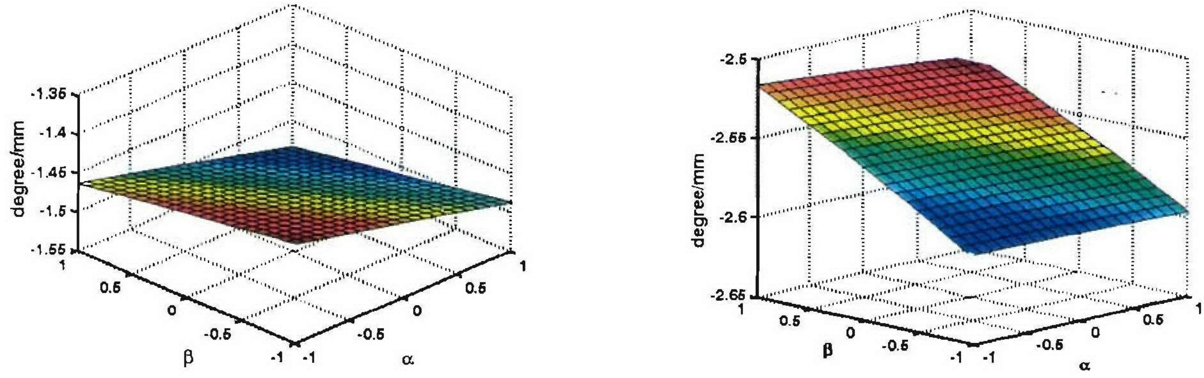

(a) $\partial\beta / \partial\Delta L_{AD}$ (b) $\partial\beta / \partial\Delta L_{BE}$

Figure 5.53. *The β-angle sensitivities with respect to the strut motions.*

5.5.3. Thrust Vector Control of a Satellite using the UHM Platform

Figure 5.54 shows TVC using the UHM platform. The spacecraft inertias are $I_{xx}=I_{yy}=200$ kg-m^2 and $I_{zz}=300$ kg-m^2. Thrust level is 445 N (100 lb) that is turned on in 5 seconds. The axial offset of the center of mass is 0.5 m, and the transverse offsets are $d_1=10$ mm and $d_2=10$ mm, and the result in the commanded platform angles are ± 1.146 degrees.

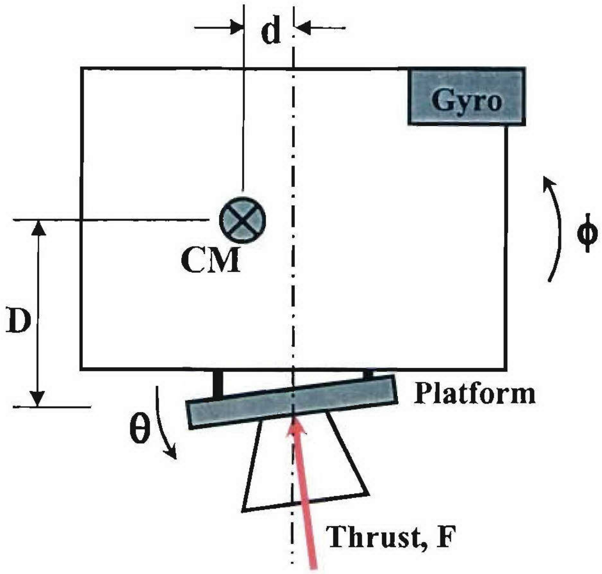

Figure 5.54. TVC using the UHM platform.

Figure 5.55 illustrates the block diagram of the thrust vector control system using the platform. It includes the following main blocks: spacecraft controller, spacecraft dynamic model, and platform controller. In this simulation, the spacecraft controller is a lag-lead compensator. The platform controller is fuzzy logic controller.

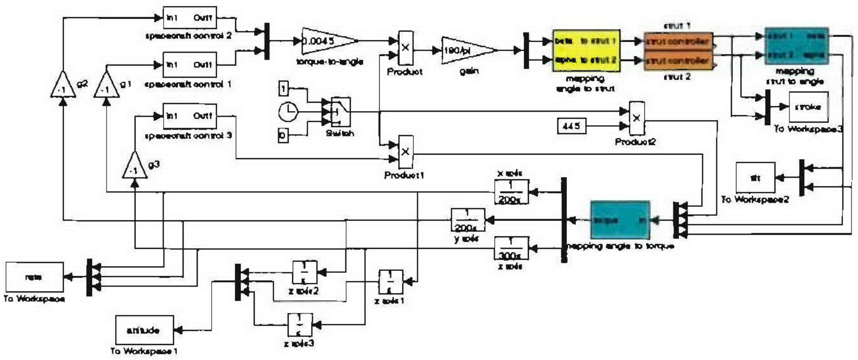

Figure 5.55. Block diagram of the thrust vector control system using the platform.

Figure 5.56 shows the attitude, rate, and torque of the spacecraft. It depicts that the attitudes, rate, and torque of the spacecraft are nullized after the thruster fires at the 5th second, indicating perfect alignment of the thrust with the centre of mass. Figure 5.57 shows the displacements of the struts and the tilt angles of the platform, showing that the required maximum displacement is 0.8 mm and the final displacements are 0.5 mm and -0.6 mm.

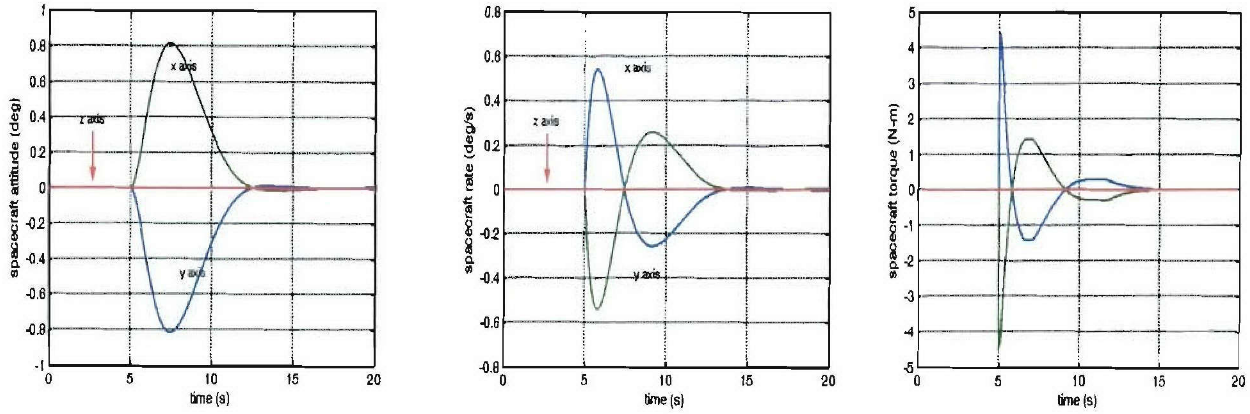

(a) attitude *(b) rate* *(c) torque*

Figure 5.56. *Attitude, rate, and torque of spacecraft.*

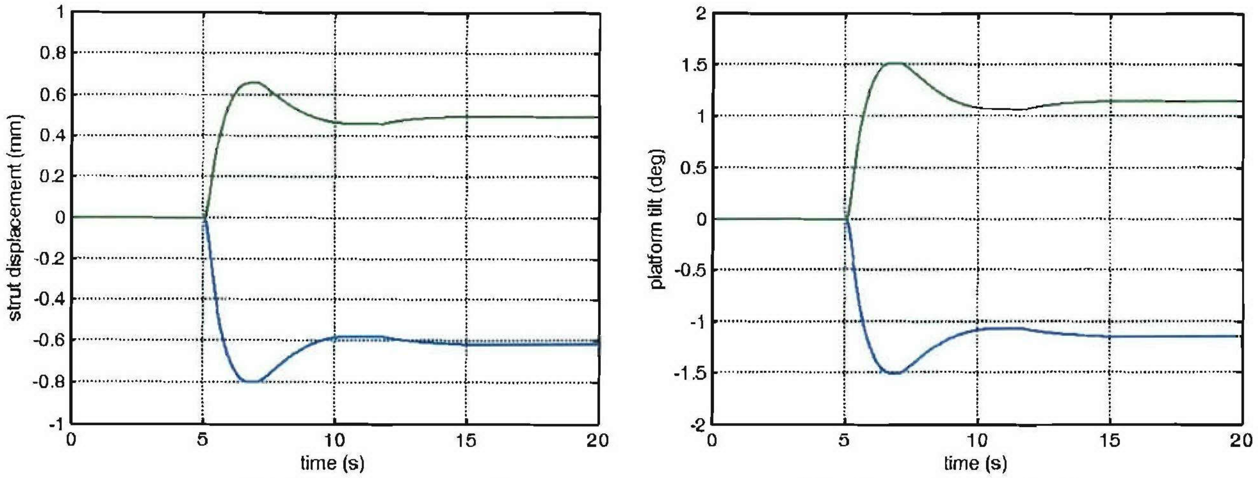

(a) displacements of struts *(b) tilt angles of platform*

Figure 5.57. *Displacements of struts and tilt angles of the platform.*

5.5.4. Vibration Control of the Satellite Frame and Thruster with the UHM Platform

A control strategy is developed and used to simulate the vibration suppression of the thruster-firing-induced vibration of satellites (Ma and Ghasemi-Nejhad, 2005f). A satellite-like frame with the platform is analyzed, and the predominant modes of the frame are determined. A MIMO adaptive control scheme is then developed to suppress the satellite frame and the thruster vibration, and a convergence factor vector concept is introduced to ease the multi-channel convergence rate control. The entire system has ten actuators: four piezoelectric stack actuators and six piezoelectric patch actuators. Eleven vibration components of the frame and platform are controlled. Nine components are in the frame for the satellite vibration suppression, and two are in the top-device plate of the platform for the thruster vibration suppression. Finally, simulations are performed to suppress the vibration of the frame and thruster for three platform positions to simulate the misalignment correction of the satellite thrust vector. The results demonstrate that the entire frame vibration at its dominant frequency decreases to 7-10% of its uncontrolled value in the three platform positions, and the thruster vibration decreases to 7.5% of its uncontrolled value.

The following specifications were used. The dimensions of this platform are as follows: the diameters of the top device-plate and the base are 420 mm and 1,220 mm, respectively, and its height is 510 mm. The DC locomotion motor has high resolution and low power consumption, which is very good for precision positioning. Its maximum velocity is greater than 30 mm/s, its unidirectional repeatability is 0.5 μm, its maximum stroke is 50 mm, and its maximum push/pull force is about 100 *N*. The push force capability, pull force capability, resolution, maximum stroke, and maximum input voltage of the piezoelectric stack actuator in the three struts are 800 N, 300 N, 0.9 nm, 90 μm, and 100 V, respectively. The maximum stroke, maximum input voltage, and push/pull force-carrying capability of the piezoelectric stack actuator in the central support are 80 μm, 1,000 V, and 30,000/3,500 N, respectively. The high-load carrying capability of the piezoelectric stack actuator in the central support ensures the thrust transmission of the main thruster to the satellite in the application of the platform in satellites. All piezoelectric stack actuators used in the UHM platform are PZT-5A type piezoceramics. The intelligent composite top-device plate is made of W3F 282 42" F593 graphite plain weave fabric prepreg with epoxy resin. The piezoelectric patch actuators embedded into the plate are active fiber composite piezoelectric ceramic patches with the dimension of 0.33 mm in thickness, 55 mm in width, and 135 mm in length. These patches employ PZT-5A piezoelectric material and perform as an extension motor. The six piezoelectric patches are placed back-to-back and can be used in pair to enhance the vibration suppression capability. Three narrow piezoelectric patch sensors are also embedded into the plate and are parallel to the piezoelectric patch actuators in the bottom side of the plate. The sensors have the similar material and dimensions as the active fiber composite actuator patches (width = 2"), except for their width (width = 0.5") that is a quarter of that for the patch actuators.

5.5.4.1. Dynamics of the Combined Satellite Frame and the Platform

Figure 5.58 (a) shows the schematic of a satellite. As mentioned in the previous section, the position control of the thruster is achieved by the precision motors inside the ACSs. The three pairs of AFC piezo actuators in the ACCP control the vibration of the thruster (i.e., points G, H, and I in Figure 5.58 (b)). Finally, the four piezo stacks in the three ACSs and the ACCS control the vibration from going into the satellite frame (e.g., points *A*, *B*, *C*, *D*, *E*, and *F* in Figure 5.58 (b)). Figure 5.58 (b) shows the test structure that consists of an aluminum frame simulating the satellite body, the UHM platform, and a thruster. The frame is octagonal with 480 mm long each side, and its height is 1,070 mm. A parametric finite element model was developed and the dynamics of the combined structure was analyzed (Antin and Ghasemi-Nejhad, 2005). The dynamic analysis implies that the first three modal frequencies of the combined structure are 38, 48, and 80 Hz, and the dominant mode of the frame is at 48 Hz.

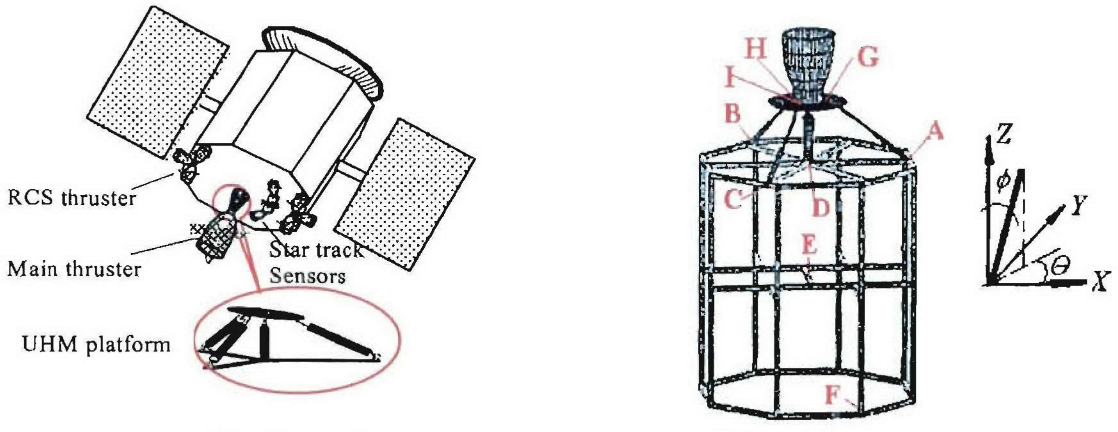

(a) schematic (b) test structure

Figure 5.58. *Satellite with UHM platform.*

5.5.4.2. MIMO Adaptive Vibration Control

There are four piezoelectric stack actuators and three pairs of piezoelectric patch actuators in the UHM platform. In order to control the vibration of the combined structure, displacements at nine points are measured resulting in a multi-input-multi-output (MIMO) control problem. These points are the connecting points (i.e., *A*, *B*, *C*, and *D*) of the UHM platform and the frame, the mass center of the combined structure, *E*, the bottom of the frame, *F*, and the three connecting points (i.e., *G*, *H*, and *I*) of the thruster and the top-device plate of the UHM platform, as marked in Figure 5.58 (b). Adaptive feedforward vibration control (Ma and Ghasemi-Nejhad, 2005f) is chosen here to suppress the combined structure vibration. The basic idea of the adaptive feedforward control is "cancellation", i.e., the adaptive controller tries to adjust its parameters in real time such that the vibration due to the controller tends to be the same in magnitude as the vibration due to the external disturbance but with opposite phase, thus the vibration due to the external disturbance is cancelled by the vibration due to the control. The block diagram of adaptive feedforward MIMO controller is shown in Figure 5.59. This controller is fully explained by Ma and Ghasemi-Nejhad (2005f).

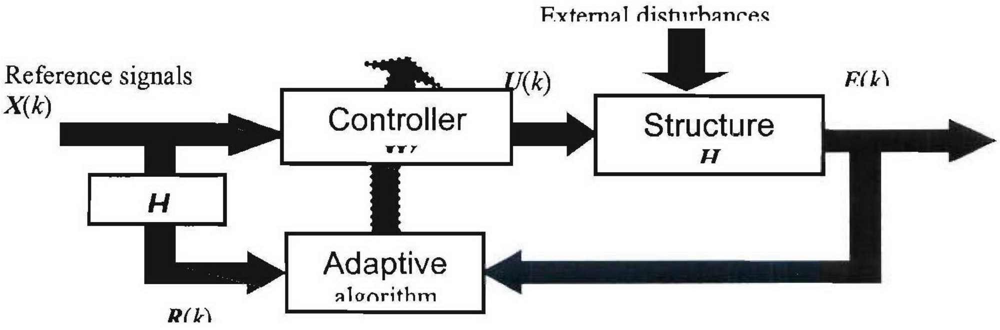

Figure I.68. *Multi-channel filtered-x adaptive algorithm.*

For the controller considered here, an accurate estimate of the finite impulse response of the controlled structure is not required, since this adaptive control scheme is tolerant of error in the estimation of finite impulse response of the controlled structures. Besides the filtered-x LMS algorithm, other adaptive filtering algorithms, such as Recursive Least Square (RLS), Fast Transversal Filtering (FTF), and Gradient-based Least Square (GLS) can also be considered. The choice of algorithms depends on controlled structures, disturbances, the complexity and characteristics of algorithms, and hardware. The LMS algorithm has smallest calculation, but the normal LMS algorithm converges slowly. The RLS algorithm converges faster, but its computation complexity is high, especially while the length of the filter is large. The FTF is complex in calculation, and the GLS has almost the same computation as the LMS but converges faster (Ma, 2003a). Other means to expedite the adaptation process were also explored such as employing combined feedback and adaptive feedforward control (Ma, 2003b; Ma and Melcher, 2003). Another important issue of adaptive feedforward control is the selection of the reference signal. The selection depends on the availability of the external disturbance, the nature of the external disturbance, and the dynamics of the controlled structures. Generally, reference signals must correlate with the uncontrolled response of structures. The external disturbance that causes structural vibrations is the best reference signal, because the disturbance strongly correlates with uncontrolled responses. Unfortunately, it is hard to obtain the disturbance in many situations. One of the alternatives is a so-called "virtual signal", which contains the characteristics of the disturbance. For example, for rotor vibration control, the predominant frequencies of uncontrolled response spectra are the rotating rate. Therefore, a virtual signal can be constructed using the rotating rate that can easily be measured. For wind-induced building vibration control, the virtual sinusoidal signal with the first natural frequency of the controlled building can be used as the reference signal, because the frequency bandwidth of wind is very low and the dominant frequency in the building response is its first natural frequency (Ma et al., 1998). The virtual reference signal was also used to suppress the nonlinear vibration of smart structures (Ma, 2003b). Another method is to use estimated uncontrolled responses by employing an internal model (Ma and Ghasemi-Nejhad, 2003a). In these choices, the first one is direct and efficient. The second one is also very good in some cases. The last choice would be used here with care, since it may cause the control system to become unstable.

5.5.4.3. Simulations and Discussions

First of all, the response of the combined test structure under 10 lbs dynamic thrust at 48 Hz in the *z*-direction has been carried out. The results show that the satellite frame vibration in *y*-direction is negligible compared to the vibrations in *x*- and *z*-directions, and the vibration of the top-device plate is predominantly in *z*-direction. Therefore, the following vibrations are measured: *x*- and *z*-directions of points *A*, *B*, and *C*, and *z*-direction of points *D*, *E*, *F*, *G*, *H*, and *I* shown in Figure 5.58 (b). The objective is defined as the following:

$$J_e(k) = J_e^1(k) + J_e^2(k) \tag{5.22}$$

$$J_e^1(k) = \frac{1}{2}[e_{Ax}^2(k) + e_{Az}^2(k) + e_{Bx}^2(k) + e_{Bz}^2(k) + e_{Cx}^2(k) + e_{Cz}^2(k) + e_{Dz}^2(k) + e_{Ez}^2(k) + e_{Fz}^2(k)] \tag{5.23}$$

$$J_e^2(k) = \frac{1}{2}[e_{Gz}(k) - e_{Hz}(k)]^2 + \frac{1}{2}[e_{Gz}(k) - e_{Iz}(k)]^2 \tag{5.24}$$

where $J_e^1(k)$ and $J_e^2(k)$ are different. $J_e^1(k)$ is targeted at the vibrations at points *A*, *B*, *C*, *D*, *E*, and *F* on the satellite frame, and $J_e^2(k)$ is targeted at the difference between the vibrations of the points *G*, *H*, and *I* in *z*-direction on the thruster connection on the top-device plate of the UHM platform. This is due to the fact that the thrust vector of the main thruster must be accurately kept in a given direction to provide a given propulsion direction. According to the objective in Equations (5.23) and (5.24), there are 11 outputs in this control system. The control system also has seven inputs form seven actuators in the UHM platform: the three piezoelectric stack actuators in the three struts, the piezoelectric stack actuator in the central support, and three piezoelectric patch pairs in the top-device plate. Therefore, the system is a seven-inputs-eleven-outputs (i.e., a 7-11 MIMO) system.

Prior to the simulations, the harmonic analyses of the combined structure are performed to collect the dynamics of each control path (Ma and Ghasemi-Nejhad, 2005f). Then, the simulations are conducted. In the simulations, three thrust vector positions are considered: Case 1, the thrust angle ϕ=0, and the azimuth Θ=0 in Figure 5.58 (b); Case 2, $\phi = 6^0$ and Θ=0; and Case 3, $\phi = 6^0$ and $\Theta = 180^0$. As mentioned earlier, the dominant modal frequency of the frame is 48 Hz; therefore, a sinusoidal signal at 48 Hz is picked up as the reference signal. The length of the finite impulse response of the controller is two and the sampling rate is 10,000 Hz (Ma and Ghasemi-Nejhad, 2005f).

Since there are significant differences in the dynamics of each control path, a multi-convergence factor method is proposed here. Instead of having a convergence factor, the multi-convergence factor method introduces a convergence factor vector. The convergence factor vector is [5×10^7, 2×10^6, 2×10^6, 2×10^6, 1×10^5, 1×10^5, 1×10^5]. The first element in the convergence factor vector is associated with the piezoelectric stack actuator in the central support, the second to the fourth elements are with the three piezoelectric stack actuators in the three struts, and the other three are with the three piezoelectric patch actuator pairs in the top-device plate of the platform.

Figures 5.60, 5.61, and 5.62 illustrate the objective and vibration suppression of the combined test structure in Cases of ϕ=0, Θ=0; $\phi = 6^0$, Θ=0; and $\phi = 6^0$, $\Theta = 180^0$, respectively. Table 5.2 tabulates the percentage of the controlled over uncontrolled displacements after 300 minutes, demonstrating that the objective decreases to 0.7% of its uncontrolled value on an average. The vibration of the test structure is reduced 20.33 dB for Case 1, 23.24 dB for Case 2, and 23.67 dB for Case 3. Table 5.3 lists the control voltages for each actuator.

Table 5.2. *The ratio of controlled displacement after 300 seconds over uncontrolled displacement in % and dB.*

	Case 1 $\phi=0$, $\Theta=0$ % (dB)	Case 2 $\phi=6^0$, $\Theta=0$ % (dB)	Case 3 $\phi=6^0, \Theta=180^0$ % (dB)
J_e	0.79	0.6	0.69
e_{Az}	6.2 (-24.15)	5.7 (-24.88)	7.1 (-22.98)
e_{Ax}	8.6 (-21.30)	5.5 (-25.19)	6.1 (-24.29)
e_{Bz}	11.3 (-18.94)	5.9 (-24.58)	6.1 (-24.29)
e_{Bx}	8.3 (-21.62)	6.9 (-23.22)	5.6 (-25.04)
e_{Cz}	11.7 (-18.64)	6.7 (-23.48)	6.9 (-23.22)
e_{Cx}	7.7 (-22.27)	5.6 (-25.04)	5.7 (-24.85)
$e_{Gz} - e_{Hz}$	9.2 (-20.72)	5.8 (-24.73)	7.0 (-23.10)
$e_{Gz} - e_{Iz}$	9.3 (-20.63)	6.7 (-23.48)	6.8 (-23.35)
e_{Ez}	10.2 (-19.83)	7.8 (-22.16)	8.5 (-21.41)
e_{Fz}	8.6 (-21.31)	6.2 (-24.15)	5.9 (-24.58)
e_{Dz}	19.4 (-14.24)	18.3 (-14.75)	6.8 (-23.35)

Table 5.3. *Amplitudes of control signals after 300 seconds (in Volts).*

	Case 1 $\phi=0$, $\Theta=0$	Case 2 $\phi=6^0$, $\Theta=0$	Case 3 $\phi=6^0, \Theta=180^0$
Actuator in central support	267.83	289.45	212.13
Actuator in strut linked to A	3.15	61.41	18.69
Actuator in strut linked to B	14.38	4.28	51.52
Actuator in strut linked to C	21.14	7.56	53.29
Patch actuator in top plate 1	1811.76	2057.36	1263.47
Patch actuator in top plate 2	1682.05	1711.44	1075
Patch actuator in top plate 3	1623.23	1782.36	1118.19

Here, a MIMO adaptive control scheme with newly introduced convergence factor vector concept is developed to suppress the satellite frame and thruster vibrations. The convergence factor vector is very useful for multi-channel control, especially for the systems where there are substantial differences in the dynamics of each channel. Two objectives are introduced for vibration suppression of the frame and the thrust vector. The control system has seven inputs and eleven outputs (i.e., a 7-11 MIMO system). Simulations are performed to suppress the vibration of the frame for three platform positions to simulate the misalignment correction of the satellite thrust vector. The results demonstrate that the entire satellite frame vibration at its dominant frequency can decrease to 7-10% of its uncontrolled value in various platform positions, and that, on the average, 22.62 dB vibration reductions are achieved. In addition, the thruster vibration decreases to 7.5% of its uncontrolled value, and that, on the average, 22.69 dB vibration reductions are achieved.

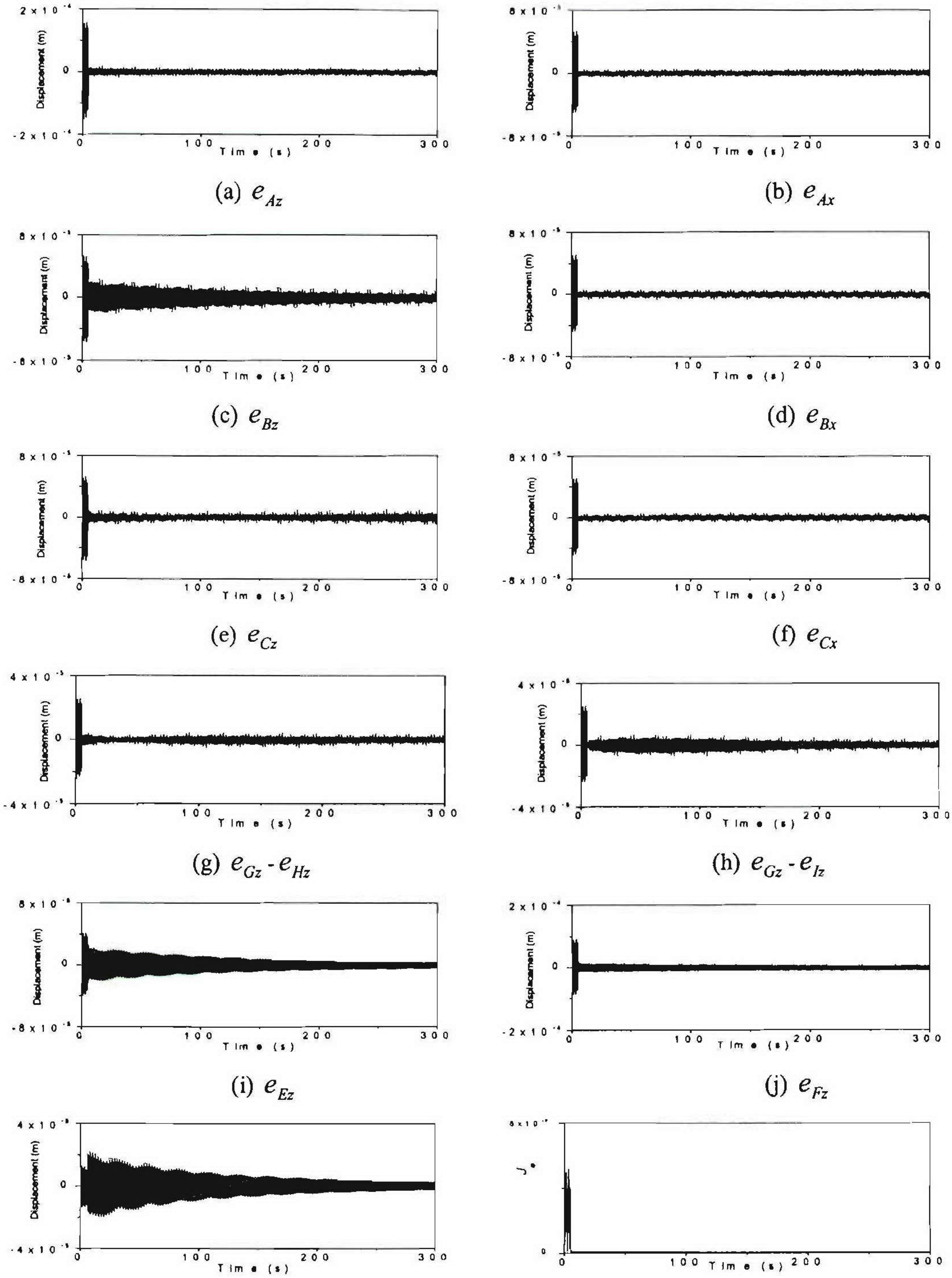

(a) e_{Az} (b) e_{Ax}

(c) e_{Bz} (d) e_{Bx}

(e) e_{Cz} (f) e_{Cx}

(g) $e_{Gz} - e_{Hz}$ (h) $e_{Gz} - e_{Iz}$

(i) e_{Ez} (j) e_{Fz}

(k) e_{Dz} (l) J_e

Figure 5.60. *Vibration suppression and objective for Case 1: $\phi = 0$, $\Theta = 0$.*

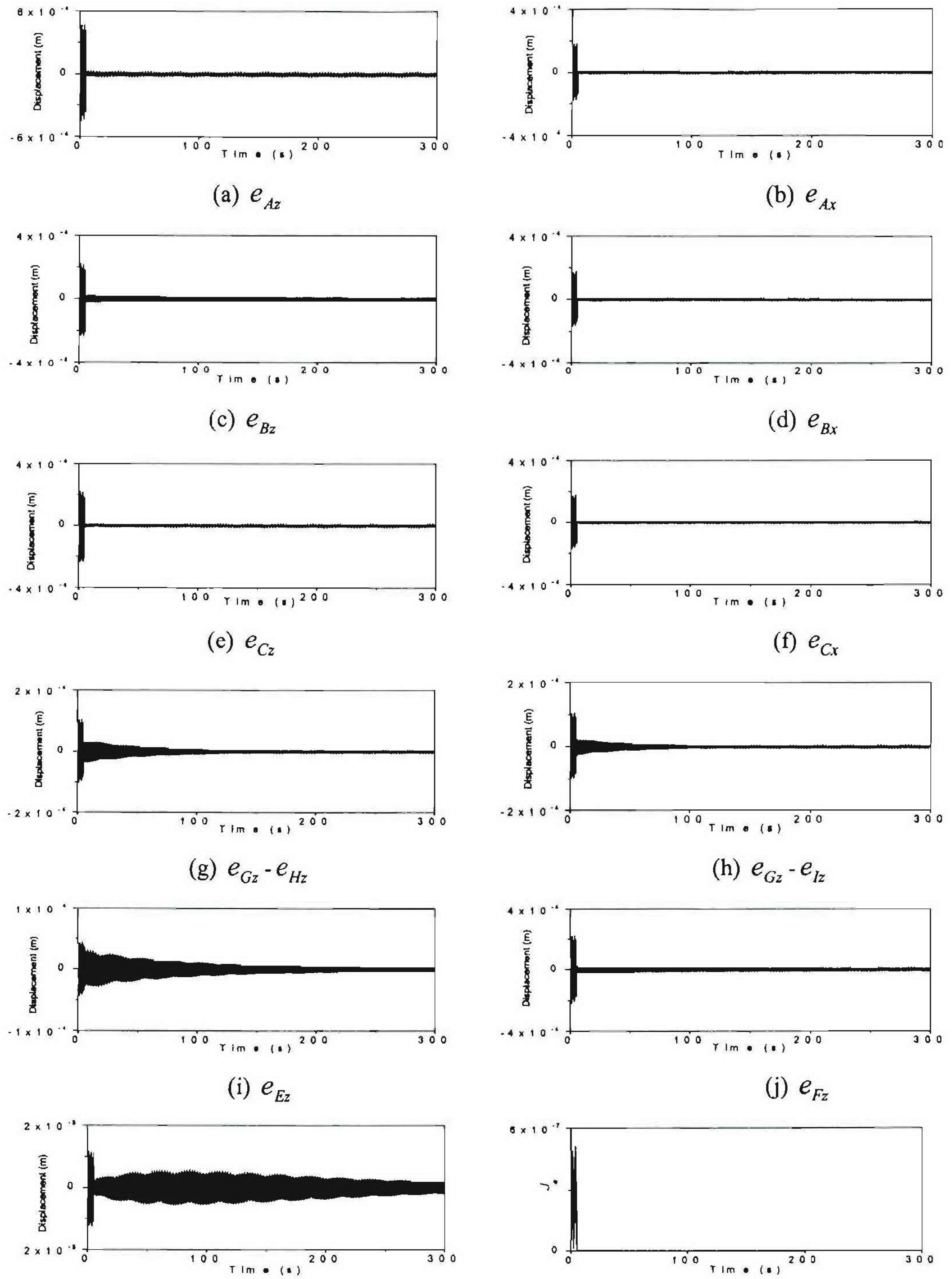

(a) e_{Az}

(b) e_{Ax}

(c) e_{Bz}

(d) e_{Bx}

(e) e_{Cz}

(f) e_{Cx}

(g) e_{Gz} - e_{Hz}

(h) e_{Gz} - e_{Iz}

(i) e_{Ez}

(j) e_{Fz}

(k) e_{Dz}

(l) J_e

Figure 5.61. *Vibration suppression and objective for Case 2:* $\phi = 6^0$, $\Theta = 0$.

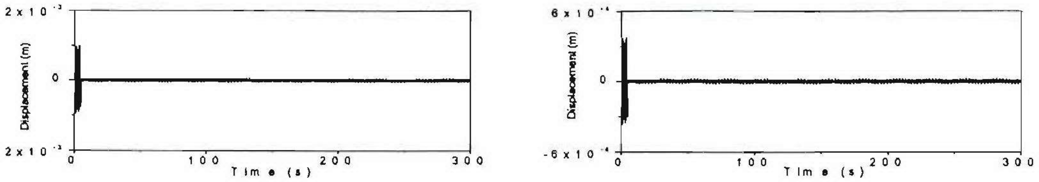

(a) e_{Az} (b) e_{Ax}

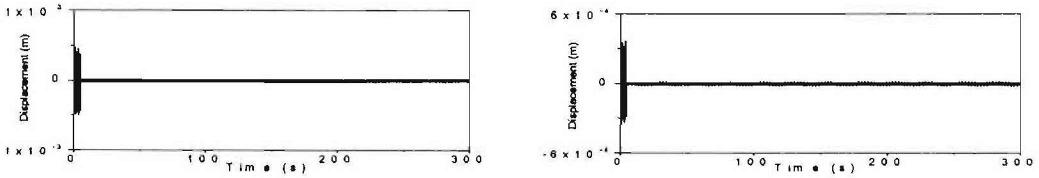

(c) e_{Bz} (d) e_{Bx}

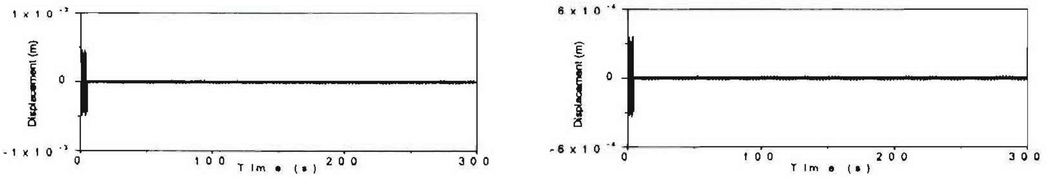

(e) e_{Cz} (f) e_{Cx}

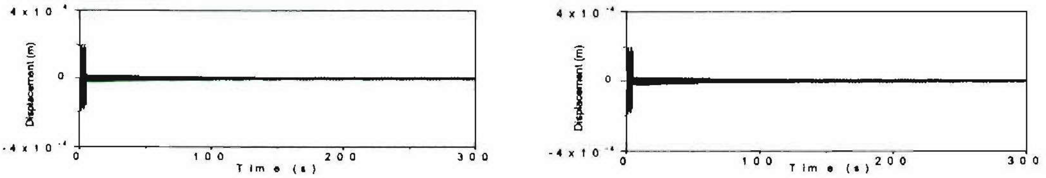

(g) $e_{Gz} - e_{Hz}$ (h) $e_{Gz} - e_{Iz}$

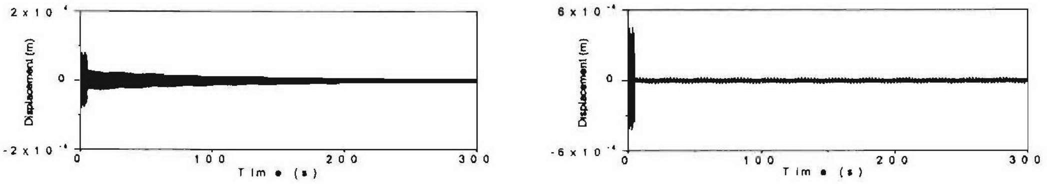

(i) e_{Ez} (j) e_{Fz}

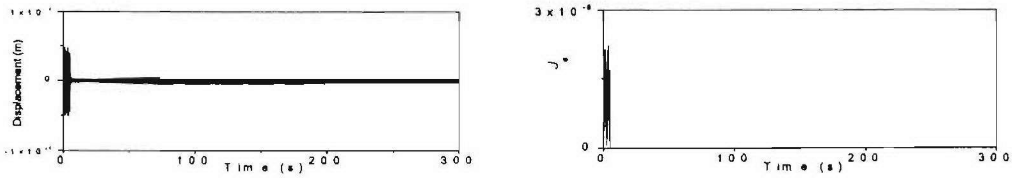

(k) e_{Dz} (l) J_e

Figure 5.62. *Vibration suppression and objective for Case 3:* $\phi = 6^0, \Theta = 180^0$.

5.6. MSP Testing

(Nejhad, Mitchell, Bletcha, Yan, Russ, Ma)

The MSP is fully fabricated and assembled. A satellite frame is also fabricated. The MSP will be tested individually for its functionality both as whole and for its components functionality, e.g., the ACSs, ACCS, and ACCP. Next, a simulated thruster will be mounted onto the MSP, and then this assembled system will be mounted on the fabricated satellite frame. First, the thruster vector positioning capability of the MSP will be tested. Next, the vibration suppression capability satellite frame will be tested. Finally, the simultaneous vibration suppression capability of the satellite as well as the precision pointing of the thruster, i.e., its vibration suppression will be tested simultaneously, to give the required Simultaneous Precision Positioning and Vibration Suppression (SPPVS) capability of the MSP. Finite element analysis vibration suppression schemes as well as control theories will employed to simulate a) the vibration suppression capability of the ACCP, b) the satellite frame vibration suppression, and c) the satellite and thruster simultaneous vibration suppression and precision pointing. These simulations will then be verified by the corresponding experimental results. Both horizontal (see Figure 5.63) and vertical (see Figure 5.64) MSP-Satellite system test set-ups will be considered.

The full simulations and experimental testing of MSP and MSP-Satellite frame system are a part of ADPICAS Phase III, and hence these results will be reported in the ADPICAS Phase III Reports.

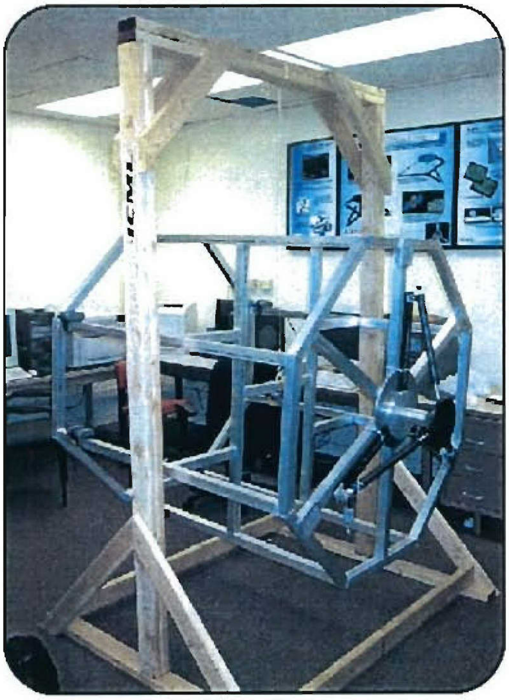

Figure 5.63. *MSP-Satellite system horizontal test set-up.*

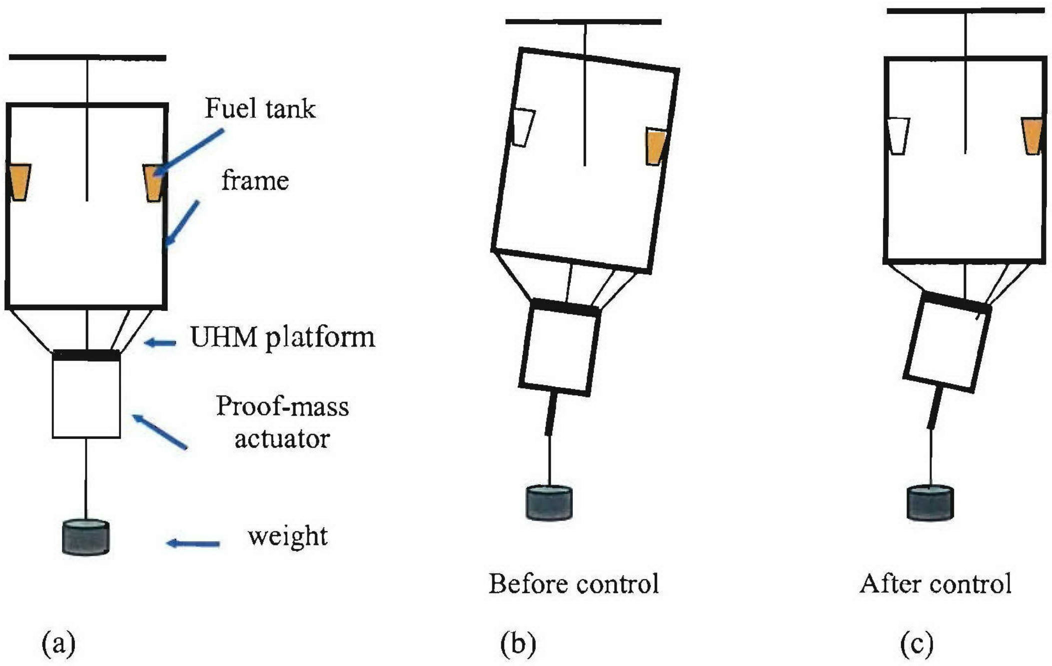

Figure 5.64. *MSP-Satellite system vertical test set-up.*

6. PUBLICATIONS/PATENTS BASED ON ADPICAS PHASES I & II

The following gives a list of all ADPICAS publications/patents (i.e., published/in-press, in-review, in-preparation) for journals, conferences, book chapters, and patents.

6.1. ADPICAS Phase I & Phase II Journal Publications

6.1.1. Journal Publications, Published/In-press (7 Papers)

1. Ghasemi Nejhad, M. N., Pourjalali, S., Uyema, M., and Yousefpour, A., "Finite Element Method for Active Vibration Suppression of Smart Composite Structures using Piezoelectric Materials," *Journal of Thermoplastic Composite Materials*, 2005, in press

2. Ma, K. and Ghasemi Nejhad, M. N., "Precision Positioning of a Parallel Manipulator for Spacecraft Thrust Vector Control," *AIAA Journal of Guidance, Control, and Dynamics*, 2005, Vol. 28, No. 1, pp. 185-188.

3. Doherty, K. M. and Ghasemi Nejhad, M. N., "Performance of an Active Composite Strut for an Intelligent Composite Modified Stewart Platform for Thrust Vector Control" *Journal of Intelligent Material Systems and Structures*, Vol. 16, No. 4, 2005, pp. 335-354.

4. Ghasemi Nejhad, M. N., Russ, R., and Pourjalali, S., "Manufacturing and Testing of Active Composite Panels with Embedded Piezoelectric Sensors and Actuators," *Journal of Intelligent Material Systems and Structures*, Vol. 16, No. 4, 2005, pp. 319-334, **(invited by the associate editor)**.

5. Ma, K. and Ghasemi Nejhad, M. N. "Simultaneous Precision Positioning and Vibration Suppression of Reciprocating Flexible Manipulators," *Journal of Smart Structures and Systems*, January 2005, Vol. 1, No. 1, pp. 13-27, **(invited by the editor-in-chief for the first issue)**.

6. Ma, K. and Ghasemi Nejhad, M. N. "Adaptive Simultaneous Precision Positioning and Vibration Control of Intelligent Composite Structures," *Journal of Intelligent Material Systems and Structures*, February 2005, Vol. 16, No. 2, pp. 163-174.

7. Ma, K. and Ghasemi Nejhad, M. N. "Frequency-Weighted Adaptive Control for Simultaneous Precision Positioning and Vibration Suppression of Smart Structures," *Journal of Smart Materials and Structures*, 2004, Vol. 13, No. 5, pp. 1143-1154.

6.1.2. Journal Publications, In-review (5 Papers)

1. Yan, S. and Ghasemi Nejhad, M. N., "Modeling, Optimization, and Active Vibration Suppression of Adaptive Composite Panels with PZT Patches," *Journal of Intelligent Materials Systems and Structures*, 2005, in review

2. Yan, S. and Ghasemi Nejhad, M. N., "Analytical Modeling and Active Vibration Suppression of Adaptive Composite Panels with Optimal Actuator Configurations," *Journal of Smart Materials and Structures*, 2005, in review

3. Ghasemi Nejhad, M. N., Russ, R., and Ma, K., "Finite Element Charts and Active Vibration Suppression Schemes for Smart Structures Design," *Journal of Intelligent Material Systems and Structures*, 2005, in review

4. Ma, K. and Ghasemi Nejhad, M. N. "Adaptive Precision Positioning of Smart Composite Panels Subjected to External Disturbances," *International Journal of Mechatronics*, 2005, in review

5. Ma, K. and Ghasemi Nejhad, M. N. "Adaptive Control of Flexible Active Composite Manipulators Driven by Piezoelectric Patches and Active Struts with Dead Zones," *ASME/IEEE Transactions on Mechatronics*, 2005, in review

6.1.3. Journal Publications, In-preparation (2 Papers)

1. Russ, R., Ma, K., and Ghasemi Nejhad, M. N., "Piezoelectric Actuator Performance Effectiveness for Active Composite Panels with Surface-Mounted and Embedded Sensors and Actuators," *Journal of Smart Structures and Systems*, 2005, in preparation

2. Sakagawa, R. and Ghasemi Nejhad, M. N., "Finite Element Analysis Design and Optimization of an Adaptive Circular Composite Panel for Vibration Suppression," *Journal of Smart Structures and Systems*, 2005, in preparation

6.2. ADPICAS Phase I & Phase II Conference Publications

6.2.1. Conference Publications, Published (25 Papers)

1. Antin, N. and Ghasemi Nejhad, M. N., "Active Vibration Suppression of a Satellite Frame using an Adaptive Composite Thruster Platform," Smart Structures and Integrated Systems, Alison B. Flatau, SPIE's 12th Annual International Symposium on Smart Structures and Materials, March 6-10, 2005, San Diego, CA, Vol. 5764, No. 47, pp. 390-401.

2. Ma, K. and Ghasemi Nejhad, M. N., "MIMO Adaptive Control of Thruster Firing Induced Vibration of Satellites using Multifunctional Platforms," Modeling, Signal Processing and Control, Ralph C. Smith, Proc. Of SPIE's 12th International Symp. on Smart Structures and Materials, March 6-10, 2005, San Diego, CA, Vol. 5757, No. 46, pp. 459-470.

3. Yan, S. and Ghasemi Nejhad, M. N., "Analytical Modeling and Active Vibration Suppression of an Adaptive Circular Composite Plate with Asymmetric Constraints," Modeling, Signal Processing and Control, Ralph C. Smith, Proc. of SPIE's 12th Annual International Symposium on Smart Structures and Materials, March 6-10, 2005, San Diego, CA, Vol. 5757, No. 5, pp. 42-52.

4. Ghasemi Nejhad, M. N., "Inverse Kinematics and Geometric Relations of an Intelligent Modified Stewart Platform for Thruster Vector Control," Aerospace Division, Adaptive Structures and Material Systems, ASME International Mechanical Engineering Congress and Exposition, Nov. 13-19, 2004, Anaheim, CA, Paper No. IMECE2004-61465, pp.1-8

5. Ghasemi Nejhad, M. N. and Ma, K., "Adaptive Damping and Positioning using Intelligent Composite Active Structures (ADPICAS)," 2004 International Symposium on Active Control of Sound and Vibration, Active 04, September 20-22, 2004, Williamsburg, VA, Paper No. a04-019, pp.1-12

6. Ma, K. and Ghasemi Nejhad, M. N., "Two-DOF Precision Platform for Spacecraft Thrust Vector Control: Control Strategies and Simulations," Smart Structures and Integrated Systems, Alison B. Flatau, Proc. Of SPIE's 11th International Symp. on Smart Structures and Materials, Vol. 5390, March 14-18, 2004, San Diego, CA, pp. 46-57

7. Russ, R. and Ghasemi Nejhad, M. N., "Piezoelectric Actuator Performance Effectiveness for Active Composite Panels with Surface-Mounted and Embedded Sensors and Actuators using Direct Constant Voltage Scheme," Smart Structures and Integrated Systems, Alison B. Flatau, Proc. of SPIE's 11th Annual International Symposium on Smart Structures and Materials, Vol. 5390, March 14-18, 2004, San Diego, CA, pp. 66-77

8. Yan, S. and Ghasemi Nejhad, M. N., "Modeling and Genetic Algorithms based Piezoelectric Actuator Configuration Optimization of an Adaptive Circular Composite Plate," Modeling, Signal Processing and Control, Ralph C. Smith, Proc. of SPIE's 11th Annual International Symposium on Smart Structures and Materials, Vol. 5383, March 14-18, 2004, San Diego, CA, pp. 255-264

9. Yan, S. and Ghasemi Nejhad, M. N., "Simultaneous Vibration Suppression and Precision Position of an Adaptive Composite Panel," Proceedings of the 1st International Workshop on Advanced Smart Materials and Smart Structures Technology, Eds. F.-K. Chang, C.-B. Yun, B. F. Spencer, Jr., DES*tech* Publications, Inc., January 12-14, 2004, Honolulu, Hawaii, pp. 119-126

10. Russ, R. and Ghasemi Nejhad, M. N., "Effect of Constraint Layers on Piezoelectric Actuator Effectiveness for Active Composite Panels with Embedded Sensors and Actuators," Proceedings of the 1st International Workshop on Advanced Smart Materials and Smart Structures Technology, Eds. F.-K. Chang, C.-B. Yun, B. F. Spencer, Jr., DES*tech* Publications, Inc., January 12-14, 2004, Honolulu, Hawaii, pp. 547-556

11. Ma, K. and Ghasemi Nejhad, M. N., "Simultaneous Precision Positioning and Vibration Suppression of Flexible Manipulators," Proceedings of the 1st International Workshop on Advanced Smart Materials and Smart Structures Technology, Eds. F.-K. Chang, C.-B. Yun, B. F. Spencer, Jr., DES*tech* Publications, Inc., January 12-14, 2004, Honolulu, Hawaii, pp. 636-643

12. Ma, K. and Ghasemi Nejhad, M. N., "Simultaneous Precision Positioning and Vibration Suppression of Smart Structures: Adaptive Control Methods and Comparisons," Proceedings of 42nd IEEE Conference on Decision and Control, December 9-12, 2003, Maui, Hawaii, Vol. 6, pp. 6386-6391

13. Ghasemi Nejhad, M. N. and Russ, R., "Manufacturing and Active Control Testing of Active Composite Panels with Embedded Piezoelectric Sensors and Actuators: Wires out by cut-holes and embedding," Aerospace Division, Adaptive Structs. and Mat. Sys., ASME Int. Mechanical Engineering Congress and Exposition, Nov. 16-21, 2003, Washington DC, Paper No. IMECE2003-43017, pp. 1-8

14. Russ, R. and Ghasemi Nejhad, M. N., "A Comparative Study on the Effectiveness of Piezoelectric Patches for Active Composite Panels With Surface-Mounted and Embedded Sensors and Actuators," Smart Structures and Integrated Systems, Amr M. Baz, SPIE's 10th Annual International Symposium on Smart Structures and Materials, March 3-6, 2003, San Diego, CA, Vol. 5056, pp. 163-174

15. Ghasemi Nejhad, M. N. and Pourjalali, S., "Manufacturing and Testing of Active Composite Panels with Embedded Piezoelectric Sensors and Actuators: Wires out by molded-in holes," Smart Structures and Integrated Systems, Amr M. Baz, SPIE's 10th Annual International Symposium on Smart Structures and Materials, March 3-6, 2003, San Diego, CA, Vol. 5056, pp. 373-383

16. Ma, K. and Ghasemi Nejhad, M. N., "Adaptive Internal Model Control for Simultaneous Precision Positioning and Vibration Suppression of Smart Structures," Modeling, Signal Processing and Control, Ralph C. Smith, SPIE's 10th Annual International Symposium on Smart Structures and Materials, March 3-6, 2003, San Diego, CA, Vol. 5049, pp. 252-263

17. Yan, S. and Ghasemi Nejhad, M. N., "Optimization and Vibration Suppression of Adaptive Composite Panels Using Genetic Algorithm and Disturbance Observer Technique," Modeling, Signal Processing and Control, Ralph C. Smith, SPIE's 10th Annual International Symposium on Smart Structures and Materials, March 3-6, 2003, San Diego, CA, Vol. 5049, pp. 381-392

18. Ghasemi Nejhad, M. N., and Sakagawa, R., "Design and Analysis of an Adaptive Tubular Composite Housing for Active Vibration Suppression," Fourth Canadian International Composites Conference (CANCOM 2003), Aug. 19-22, 2003, Ottawa, Canada, Paper No. 045, pp.1-11

19. Ghasemi Nejhad, M. N., and Soon, C., "Design and Analysis of an Adaptive Circular Composite Panel with Embedded Sensors/Actuators for Active Vibration Suppression," Fourth Canadian International Composites Conference (CANCOM 2003), Aug. 19-22, 2003, Ottawa, Canada, Paper No. 046, pp.1-10

20. Ghasemi Nejhad, M. N. and Doherty, K. M., "Modified Stewart Platform for Spacecraft Thruster Vector Control," Aerospace Division, Adaptive Structures and Material Systems, ASME International Mechanical Engineering Congress and Exposition, Nov. 17-22, 2002, New Orleans, LA, Paper No. IMECE2002-34032, pp. 1-8

21. Ghasemi Nejhad, M. N., "Active Composite Panels and Active Composite Struts as Building Blocks of Adaptive Structures," JSME/ASME International Conference on Materials and Processing, Smart Materials and Structures, Oct. 15-18, 2002, Honolulu, HI, pp. 432-440

22. Russ, R. and Ghasemi Nejhad, M. N., "Active Composite Beam With Three Piezoelectric Patches as a New Model For the Verification of the Four Introduced Direct Vibration Suppression Schemes," JSME/ASME International Conference on Materials and Processing, Smart Materials and Structures, Oct. 15-18, 2002, Honolulu, HI, pp. 372-377

23. Ma, K. and Ghasemi Nejhad, M. N., "Development of Smart Composite Structural Systems with Simultaneous Precision Positioning and Vibration Control," JSME/ASME International Conference on Materials and Processing, Smart Materials and Structs., Oct. 15-18, 2002, Honolulu, HI, pp. 396-401

24. Russ, R. and Ghasemi Nejhad, M. N., "Vibration Suppression Schemes for Active Composite Strut and Panel," Modeling, Signal Processing and Control, Vittal S. Rao, SPIE's 9th Annual International Symp. on Smart Structs. and Materials, March 17-21, 2002, San Diego, CA, Vol. 4693, pp. 418-429

25. Ma, K., Pourjalali, S., and Ghasemi Nejhad, M. N., "Hybrid Adaptive Control of Smart Structures with Simultaneous Precision Positioning and Vibration Suppression," Modeling, Signal Processing and Control, Vittal S. Rao, SPIE's 9th Annual International Symposium on Smart Structures and Materials, March 17-21, 2002, San Diego, CA, Vol. 4693, pp. 13-24

6.3. ADPICAS Phase I & Phase II Book Chapter (1 Book Chapter)

1. Ma, K., and Ghasemi Nejhad, M. N., "Smart Composite Platforms for Satellite Thrust Vector Control and Vibration Suppression," *Progress in Smart Materials and Structures Research*, Nova Science Publishers, Inc., 2005 (abstract accepted) **(Invited)**

6.4. ADPICAS Phase I & Phase II Provisional Patents (1 Book Chapter)

1. Ghasemi Nejhad, M.N., and Russ, R., "Manufacturing of Active Composite Panel Smart Structures with Simultaneous Precision Positioning and Vibration Control by Embedded Piezoelectric Patches as Sensors and Actuators: I-Wires out by Cut-Holes, III-Wires out by Embedding," patent application pending

2. Ghasemi Nejhad, M.N., and Pourjalali, S., "Manufacturing of Active Composite Panel Smart Structures with Simultaneous Precision Positioning and Vibration Control by Embedded Piezoelectric Patches as Sensors and Actuators: II-Wires out by Molded-in Holes," patent application pending

7. PERSONNEL SUPPORTED ON ADPICAS PHASES I & II

The following gives a list of all personnel (i.e., post-docs; graduate, undergraduate, and high school students; engineers, administrative assistants) supported by the ADPICAS project. It also gives the graduation (or expected graduation) dates of the students, plus the personnel gender.

7.1. List of Post-Docs (2 PDs)

1. Dr. Kougen Ma (June 2001-pres.; Male)
2. Dr. Richard Russ (June 2001-pres.; Male)

7.2. List of PhD Students (3 PhDs)

1. Su Yan (May 2006, Expected; Female)
2. Vinod P. Veedu (May 2007, Expected; Male)
3. Davood Askari (May 2007, Expected; Male)

7.3. List of MS Students (5 MSs)

1. Saeid Pourjalali (December 2001; Male)
2. Nicolas Antin (August 2004; Male)
3. Chad Mitchel (August 2005; Male)
4. Tai W. Bletcha (May 2006, Expected; Male)
5. Randy K. H. Sakagawa (May 2006, Expected; Male)

7.4. List of BS Students (10 BSs)

1. Melanie Yamauchi (2001; Female)
2. Reid Takamiya (2001; Male)
3. Cory M. Soon (2003; Male)
4. Randy K. H. Sakagawa (2003; Male)
5. Karl J. Santa (2003; Male)
6. Weston Fujii (2003; Male)
7. Lance K. Yoneshige (2004; Male)
8. Zensho Heshiki (2005; Male)
9. David T. Narahara (2006; Male)
10. Stuart Akagi (2008; Male)

7.5. List of High School (HS) Student-Interns (SIs) (4 HS-SIs)

1. Stuart Akagi (Kailua HS, Class of 2003; Male)
2. Matthew S-H. Kasaoka (Mililani HS, Class of 2004; Male)
3. Ryan Balais (Waipahu HS, Class of 2004; Male)
4. Reid Ginoza (Pearl City HS, Class of 2005; Male)

7.6. List of High School Student-Projects (SPs) (3 HS-SPs)

1. Stuart Akagi (Kailua HS, Class of 2003; Male)
2. Tracie Le (Mckinley HS, Class of 2006; Female)
3. Jumy Tong (Mckinley HS, Class of 2006; Female)

7.7. List of Engineers (3 Engineers)

1. Mark Uyema (UHM ME Graduate, B.S.) (Jan. 2000 – May 2001, & Aug. 2001 – December 2001):
   "Design, Analysis, Fabrication, and Assembly of Preliminary Active Composite Struts and their Joints for a Modified Stewart Platform"

2. Luke Beaver (UHM ME Graduate, B.S.) (Aug. 2003 – Dec. 2003):
   "Design, Fabrication, and Assembly of Preliminary Active Composite Struts and their Joints for a Modified Stewart Platform"

3. Nicolas Antin (UHM ME Graduate, M.S.) (Oct. 2004 – Feb. 2005):
   "Design and Analysis of a Modified Stewart Platform"

7.8. List of Administrative Assistants (2 AAs)

1. Wesley Sugimoto, 50%, (Summer. 2000 – Summer 2003):
2. Stacie Shiroma, 50%, (Fall. 2003 – pres.):

8. OTHER PI GRANTS AS PI, CO-PI, & Co-I

The following gives a list of all other PI's grants (i.e., as PI, Co-PI, and Co-I).

8.1. PI's Other Grants as PI (7 Grants)

1. "Application of Composite and Smart Materials to Space Structures-Testing of Active Struts," *Allied-Signal Aerospace Co./Naval Research Laboratory*, 1998 (2 years), $14,598

2. "A Web-Based Crashworthiness Study and Design Software for Composite Materials," Hawaii Electric Vehicle Demonstration Project (HEVDP), National Data Center (NDC), *Defense Advanced Research Projects Agency (DARPA)*, 1998 (1.5 years), $40,599

3. "Composite Materials and Structures Modeling for Hawaii Electric Vehicle Demonstration Project (HEVDP)," Hawaii Electric Vehicle Demonstration Project (HEVDP), National Data Center (NDC), *Defense Advanced Research Projects Agency (DARPA)*, 1995 (2 years), $90,632

4. "Design, Manufacture, and Characterization of Utility Poles Using In-Situ Composite Filament Winding with Recycled Thermoplastic Powder Impregnation of Fibers," *Office of Technology Transfer and Economic Development (OTTED),* University of Hawaii, 1995 (1 year), $18,500

5. "Crashworthiness Study for Candidate Materials and Structures for Hawaii Electric Vehicle Demonstration Program (HEVDP)," *Defense Advanced Research Projects Agency (DARPA)*, 1994 (1.5 years), $39,903

6. "Design of a System for the Filament Winding Manufacturing of Preceramic Polymer Composites-A Novel Approach," University of Hawaii, *University Research Council*, 1993 (1 year), $12,000

7. "Application of Composite and Smart Materials to Space Structures," *Allied-Signal Aerospace Co./Naval Research Laboratory,* 1993 (4.5 years), $298,430

8.2. PI's Other Grants as Co-PI (2 Grants)

1. "Development of a Semi-Autonomous Underwater Vehicle for Intervention Missions (SAUVIM)," *ONR,* Undersea Weapons Technology Program, Phase I, 1997 (3 years), $2,250,000, (PI: J. Yuh) (prorated: ~ $225,000)

2. "Virtual Rapid Prototyping System for Piezoelectric Micro Systems," Rapid Prototyping Initiative, 1995 (3 years), *National Science Foundation-* $460,000 and *The University of Hawaii College of Engineering* $29,000 (PIs: E. S. Kim, Co-PIs: M. G. Nejhad, J. Yuh, and S. Itoga) (Prorated: ~ $122,250)

8.3. PI's Other Grants as Co-I (2 Grants)

1. "Pacific Rim Corrosion Research Program," *US Army, TACOM-ARDEC*, 2003 (2.5 years) $3,215,672 (PI: L.H. Hihara) (Prorated: ~ $150,000)
2. "Hawaii Corrosion Project, Phase I" *Concurrent Technology Corporation/Army Research Laboratory*, Largo, FL, 2001 (1 year), $250,000 (PI: L. H. Hihara) (Prorated: ~ $25,000)

9. ACKNOWLEDEMENTS

We acknowledge the financial and technical support of ONR & Dr. Ng as well as NRL & NRL staff, especially Mr. Ed Senasack, Dr. Glenn Creamer, Dr. Al Bosse, and Dr. Tae Lim, for the ADPICAS (Adaptive Damping and Positioning using Intelligent Composite Active Structures) project.

10. REFERENCES

ACX, Active Control eXperts, *"Product data"*, www.acx.com, 2002.

ANSYS User's Manual, ANSYS, Inc., Canonsburg, PA, 2002.

ANSYS User's Manual, ANSYS, Inc., Canonsburg, PA, 2004.

Antin, N. and Ghasemi Nejhad, M. N., "Active Vibration Suppression of a Satellite Frame using an Adaptive Composite Thruster Platform," Smart Structures and Integrated Systems, Alison B. Flatau, SPIE's 12th Annual International Symposium on Smart Structures and Materials, March 6-10, 2005, San Diego, CA, Vol. 5764, No. 47, pp. 390-401.

Asik, M. Z., "Behavior of laminated circular glass plates," ANZIAM J. 45(E), pp. C338-C349, 2004.

CCC, Continuum Photonics, Inc., *Product data*, Billerica, MA, 2002.

Choi, S. K. and Yuh, J., "Experimental Study on a Learning Control System with Bound Estimation for Under Water Robolts" *International J. of Autonomous Robots*, July 1996.

Doherty, K. M. and Ghasemi Nejhad, M. N., "Performance of an Active Composite Strut for an Intelligent Composite Modified Stewart Platform for Thrust Vector Control" *Journal of Intelligent Material Systems and Structures*, 2005, Vol. 16, No. 4, 2005, pp. 335-354.

Ghasemi Nejhad, M. N., and T-W. Chou, "Compression Behavior of Woven Carbon Fibre-Reinforced Epoxy Composites with Moulded-in and Drilled holes," *Composites*, 1990a, 21(1):33-40.

Ghasemi Nejhad, M. N., and T-W. Chou, "A Model for the Prediction of Compressive Strength Reduction of Composite Laminates with Molded-in Holes," *Journal of Composite Materials,* 1990b, 24(3):236-255.

Ghasemi Nejhad, M. N., "Active Composite Panels and Active Composite Struts as Building Blocks of Adaptive Structures," JSME/ASME International Conference on Materials and Processing, Smart Materials and Structures, Oct. 15-18, 2002, Honolulu, HI, pp. 432-440

Ghasemi Nejhad, M. N. and Doherty, K. M., "Modified Stewart Platform for Spacecraft Thruster Vector Control," Aerospace Division, Adaptive Structures, ASME International Mechanical Engineering Congress and Exposition, Nov. 17-22, 2002, New Orleans, LA, Paper No. IMECE2002-34032, pp. 1-8

Ghasemi Nejhad, M. N. and Pourjalali, S., "Manufacturing and Testing of Active Composite Panels with Embedded Piezoelectric Sensors and Actuators: Wires out by molded-in holes," Smart Structures and Integrated Systems, Amr M. Baz, SPIE's 10th Annual International Symposium on Smart Structures and Materials, March 3-6, 2003, San Diego, CA, Vol. 5056, pp. 373-383

Ghasemi Nejhad, M. N. and Russ, R., "Manufacturing and Active Control Testing of Active Composite Panels with Embedded Piezoelectric Sensors and Actuators: Wires out by cut-holes and embedding," Aerospace Division, Adaptive Structures, ASME International Mechanical Engineering Congress and Exposition, Nov. 16-21, 2003, Washington DC, Paper No. IMECE2003-43017, pp. 1-8

Ghasemi Nejhad, M. N., and Soon, C., "Design and Analysis of an Adaptive Circular Composite Panel with Embedded Sensors/Actuators for Active Vibration Suppression," Fourth Canadian International Composites Conference (CANCOM 2003), August 19-22, 2003, Ottawa, Canada, Paper No. 046, pp.1-10

Ghasemi Nejhad, M. N., and Sakagawa, R., "Design and Analysis of an Adaptive Tubular Composite Housing for Active Vibration Suppression," Fourth Canadian International Composites Conference (CANCOM 2003), August 19-22, 2003, Ottawa, Canada, Paper No. 045, pp.1-11

Ghasemi Nejhad, M. N. , "Inverse Kinematics and Geometric Relations of an Intelligent Modified Stewart Platform for Thruster Vector Control," Aerospace Division, Adaptive Materials and Systems, ASME International Mechanical Engineering Congress and Exposition, Nov. 13-19, 2004, Anaheim, CA, Paper No. IMECE2004-61465, pp.1-8

Ghasemi Nejhad, M. N. and Ma, K., "Adaptive Damping and Positioning using Intelligent Composite Active Structures (ADPICAS)," 2004 International Symposium on Active Control of Sound and Vibration, Active 04, September 20-22, 2004, Williamsburg, VA, Paper No. a04-019, pp.1-12

Ghasemi-Nejhad, M. N., and S. Pourjalali, "Manufacturing of Active Composite Panel Smart Structures with Simultaneous Precision Positioning and Vibration Control by Embedded Piezoelectric Patches as Sensors and Actuators: II-Wires out by Molded-In Holes," patent applications pending, 2005.

Ghasemi-Nejhad, M. N., and R. Russ, "Manufacturing of Active Composite Panel Smart Structures with Simultaneous Precision Positioning and Vibration Control by Embedded Piezoelectric Patches as Sensors and Actuators: I-Wires out by Drilled Holes, III-Wires out by Embedding" patent applications pending, 2005.

Ghasemi Nejhad, M. N., Russ, R., and Ma, K., "Finite Element Charts and Active Vibration Suppression Schemes for Smart Structures Design," *Journal of Intelligent Material Systems and Structures*, 2005a, in review

Ghasemi Nejhad, M. N., Pourjalali, S., Uyema, M., and Yousefpour, A., "Finite Element Method for Active Vibration Suppression of Smart Composite Structures using Piezoelectric Materials," *Journal of Thermoplastic Composite Materials*, 2005b, in press

Ghasemi Nejhad, M. N., Russ, R., and Pourjalali, S., "Manufacturing and Testing of Active Composite Panels with Embedded Piezoelectric Sensors and Actuators," *Journal of Intelligent Material Systems and Structures*, 2005c, Vol. 16, No. 4, 2005, pp. 319-334

Kirchhoff, G., "Uber das gleichgewicht und die bewegung einer elastischen scheibe," Mathematical Journal 40, pp. 51-58, 1850.

Kwak, M. K., and Shin, T., "Real-Time Automatic Tuning of Vibration Controller for Smart Structures by Genetic Algorithm," SPIE, Vol.3667, pp. 679-690, 1999.

Leissa, A. W., "Vibration of Plates," NASA SP-160, Washington, DC, 1965.

Ma, K., "Vibration control of smart structures with bonded PZT patches: novel adaptive filtering algorithm and hybrid control scheme," *Smart Materials and Structures*, 2003a, **12**(3), pp. 473-482.

Ma, K., "Adaptive nonlinear control of a rectangular-clamped plate with PZT patches," *Journal of Sound and Vibration*, 2003b, **264**(4), pp. 835-850.

Ma, K., and Melcher, J., "Adaptive control of structural acoustics using intelligent structures with embedded PZT patches," *Journal of Vibration and Control*, 2003, **9**(11), pp.1285-1302.

Ma, K., Chen, X., and Gu, Z. Q., "Adaptive control of wind-induced vibration of flexible structures---methods and experiments," *Journal of Vibration Engineering*, 1998, **11**(2), pp.131-137.

Ma, K., J. Melcher, and H.P. Monner, "Study on adaptive control strategies for smart structure vibration suppression" In: *Proceedings of the 11th International Conference on Adaptive Structures and Technologies*, Nagoya, Japan, 2000, 447-454.

Ma, K., Pourjalali, S., and Ghasemi Nejhad, M. N., "Hybrid Adaptive Control of Smart Structures with Simultaneous Precision Positioning and Vibration Suppression," Modeling, Signal Processing and Control, Vittal S. Rao, SPIE's 9th Annual International Symposium on Smart Structures and Materials, March 17-21, 2002a, San Diego, CA, Vol. 4693, pp. 13-24

Ma, K. and Ghasemi Nejhad, M. N., "Development of Smart Composite Structural Systems with Simultaneous Precision Positioning and Vibration Control," JSME/ASME International Conference on Materials and Processing, Smart Materials and Structures, Oct. 15-18, 2002b, Honolulu, HI, pp. 396-401

Ma, K. and Ghasemi Nejhad, M. N., "Adaptive Internal Model Control for Simultaneous Precision Positioning and Vibration Suppression of Smart Structures," Modeling, Signal Processing and Control, Ralph C. Smith, SPIE's 10th Annual International Symposium on Smart Structures and Materials, March 3-6, 2003a, San Diego, CA, Vol. 5049, pp. 252-263

Ma, K. and Ghasemi Nejhad, M. N., "Simultaneous Precision Positioning and Vibration Suppression of Smart Structures: Adaptive Control Methods and Comparisons," Proceedings of 42nd IEEE Conference on Decision and Control, December 9-12, 2003b, Maui, Hawaii, Vol. 6, pp. 6386-6391

Ma, K. and Ghasemi Nejhad, M. N., "Simultaneous Precision Positioning and Vibration Suppression of Flexible Manipulators," Proceedings of the 1st International Workshop on Advanced Smart Materials and Smart Structures Technology, Eds. F.-K. Chang, C.-B. Yun, B. F. Spencer, Jr., DES*tech* Publications, Inc., January 12-14, 2004a, Honolulu, Hawaii, pp. 636-643

Ma, K. and Ghasemi Nejhad, M. N. "Frequency-Weighted Adaptive Control for Simultaneous Precision Positioning and Vibration Suppression of Smart Structures," *Journal of Smart Materials and Structures*, 2004b, Vol. 13, No. 5, pp. 1143-1154

Ma, K. and Ghasemi Nejhad, M. N., "Two-DOF Precision Platform for Spacecraft Thrust Vector Control: Control Strategies and Simulations," Smart Structures and Integrated Systems, Alison B. Flatau, Proc. of SPIE's 11th International Symp. on Smart Structures and Materials, Vol. 5390, March 14-18, 2004c, San Diego, CA, pp. 46-57

Ma, K. and Ghasemi Nejhad, M. N. "Simultaneous Precision Positioning and Vibration Suppression of Reciprocating Flexible Manipulators using Intelligent Controllers and Multifunctional Active Struts," *Journal of Smart Structures and Systems*, 2005a, January 2005, Vol. 1, No. 1, pp. 13-27

Ma, K. and Ghasemi Nejhad, M. N. "Adaptive Control of Flexible Active Composite Manipulators Driven by Piezoelectric Patches and Active Struts with Dead Zones," *ASME/IEEE Transactions on Mechatronics*, 2005b, in review

Ma, K. and Ghasemi Nejhad, M. N. "Adaptive Simultaneous Precision Positioning and Vibration Control of Intelligent Composite Structures," *Journal of Intelligent Material Systems and Structures*, 2005c, February 2005, Vol. 16, No. 2, pp. 163-174

Ma, K. and Ghasemi Nejhad, M. N. "Adaptive Filtering-based Feedback Control for Simultaneous Precision Positioning and Vibration Suppression of Smart Structures," *AIAA Journal of Guidance Dynamics and Control*, 2005d, in review

Ma, K. and Ghasemi Nejhad, M. N., "Precision Positioning of a Parallel Manipulator for Spacecraft Thrust Vector Control," *AIAA Journal of Guidance, Control, and Dynamics*, 2005e, Vol. 28, No. 1, pp. 185-188.

Ma, K. and Ghasemi Nejhad, M. N., "MIMO Adaptive Control of Thruster Firing Induced Vibration of Satellites using Multifunctional Platforms," Modeling, Signal Processing and Control, Ralph C. Smith, Proc. Of SPIE's 12th International Symp. on Smart Structures and Materials, March 6-10, 2005f, San Diego, CA, Vol. 5757, No. 46, pp. 459-470.

Mall, S., "Integrity of Graphite/Epoxy Laminate Embedded with Piezoelectric Sensor/Actuator under Monotonic and Fatigue Loads," *Journal of Smart Materials and Structures*, 2002, 11(4):527-533.

Mathews, J., and Walker, R. L., "Mathematical Methods of Physics," Second Edition, pp. 217-238, 1970.

Meirovitch, L., "Analytical Methods in Vibrations," The Macmillan Company, New York, NY, 1967.

MSI, Materials Systems Incorporation, 2003, "*Product data*", www.matsysinc.com.

PI (Physik Instrumente), 16 Albert St.Auburn, MA 01501, 2004, http://www.pi-usa.us

Piefort, V., "Finite Element Modeling of Piezoelectric Active Structures," University Libre De Bruxelles, 2000.

Poisson, S. D., "Memoires de l'Academie Royale des Sciences de l'Institut de France," ser. 2, VIII, 357, 1829.

Ruggiero, E. J., Singler, J., Burns, J., and Inman, D., "Robust Shape Control of a Thin Euler-Bernoulli Beam Using Piezoelectric Actuators and Sensors," ASME Adaptive Structures and Materials Conference, Nov. 13-19, Anaheim, CA, 2004.

Russ, R. and Ghasemi Nejhad, M. N., "Vibration Suppression Schemes for Active Composite Strut and Panel," Modeling, Signal Processing and Control, Vittal S. Rao, SPIE's 9th Annual International Symposium on Smart Structures and Materials, March 17-21, 2002a, San Diego, CA, Vol. 4693, pp. 418-429

Russ, R. and Ghasemi Nejhad, M. N., "Active Composite Beam With Three Piezoelectric Patches as a New Model For the Verification of the Four Introduced Direct Vibration Suppression Schemes," JSME/ASME International Conference on Materials and Processing, Smart Materials and Structures, Oct. 15-18, 2002b, Honolulu, HI, pp. 372-377

Russ, R. and Ghasemi Nejhad, M. N., "A Comparative Study on the Effectiveness of Piezoelectric Patches for Active Composite Panels With Surface-Mounted and Embedded Sensors and Actuators," Smart Structures and Integrated Systems, Amr M. Baz, SPIE's 10th Annual International Symposium on Smart Structures and Materials, March 3-6, 2003, San Diego, CA, Vol. 5056, pp. 163-174

Russ, R. and Ghasemi Nejhad, M. N., "Effect of Constraint Layers on Piezoelectric Actuator Effectiveness for Active Composite Panels with Embedded Sensors and Actuators," Proceedings of the 1st International Workshop on Advanced Smart Materials and Smart Structures Technology, Eds. F.-K. Chang, C.-B. Yun, B. F. Spencer, Jr., DES*tech* Publications, Inc., January 12-14, 2004a, Honolulu, Hawaii, pp. 547-556

Russ, R. and Ghasemi Nejhad, M. N., "Piezoelectric Actuator Performance Effectiveness for Active Composite Panels with Surface-Mounted and Embedded Sensors and Actuators using Direct Constant Voltage Scheme," Smart Structures and Integrated Systems, Alison B. Flatau, Proc. of SPIE's 11th Annual International Symposium on Smart Structures and Materials, Vol. 5390, March 14-18, 2004b, San Diego, CA, pp. 66-77

Sakagawa, R. and Ghasemi Nejhad, M. N. "Finite Element Analysis Design and Optimization of an Adaptive Circular Composite Panel for Vibration Suppression," *Journal of Smart Structures and Systems*, 2005a, in preparation

Saunders, W.R., H.R. Harry, and A.B. Ricardo, "A hybrid structural control approach for narrow-band and impulsive disturbance rejection," *Noise Control Engineering Journal,* 1996, 44:11-21

Thomson, W. T., "Theory of Vibration with Applications," Printice Hall, 1988, New York, NY.

Tseng, W.K., B. Rafaely, and S.J. Elliott, "Combined feedback-feedforward active control of sound in a room," *Journal of Acoustic Society of America,* 1998, 104:3417-3425.

Yan, S. and Ghasemi Nejhad, M. N., "Optimization and Vibration Suppression of Adaptive Composite Panels Using Genetic Algorithm and Disturbance Observer Technique," Modeling, Signal Processing and Control, Ralph C. Smith, SPIE's 10th Annual International Symposium on Smart Structures and Materials, March 3-6, 2003, San Diego, CA, Vol. 5049, pp. 381-392

Yan, S. and Ghasemi Nejhad, M. N., "Simultaneous Vibration Suppression and Precision Position of an Adaptive Composite Panel," Proceedings of the 1st International Workshop on Advanced Smart Materials and Smart Structures Technology, Eds. F.-K. Chang, C.-B. Yun, B. F. Spencer, Jr., DES*tech* Publications, Inc., January 12-14, 2004a, Honolulu, Hawaii, pp. 119-126

Yan, S. and Ghasemi Nejhad, M. N., "Modeling and Genetic Algorithms based Piezoelectric Actuator Configuration Optimization of an Adaptive Circular Composite Plate," Modeling, Signal Processing and Control, Ralph C. Smith, Proc. of SPIE's 11th Annual International Symposium on Smart Structures and Materials, Vol. 5383, March 14-18, 2004b, San Diego, CA, pp. 255-264

Yan, S. and Ghasemi Nejhad, M. N., "Analytical Modeling and Active Vibration Suppression of an Adaptive Circular Composite Plate with Asymmetric Constraints," Modeling, Signal Processing and Control, Ralph C. Smith, Proc. of SPIE's 12th Annual International Symposium on Smart Structures and Materials, March 6-10, 2005, San Diego, CA, Vol. 5757, No. 5, pp. 42-52